Towards Quantum Information Processing with Cr^{3+} based Heterometallic Clusters

A thesis submitted to The University of Manchester for the degree of Doctor of Philosophy in the Faculty of Engineering and Physical Sciences

2013

Morten Albring

School of Chemistry

Table of Contents

Word Count : 42,008

Page Count : 240

List of Figures

List of Tables

Abbreviations Used

Acac   acetylacetone

bit   binary digit

EPR   Electron Paramagnetic Resonance

FID   Free Induction Decay

FT   Fourier Transform

Hfac   hexafluoroacetylacetone

INS   Inelastic Neutron Scattering

NSSC-1   NASA Standard Spacecraft Computer 1

QIP   Quantum Information Processing

Qubit   Quantum bit

QUBO   quadratic unconstrained binary optimization

RT   Room Temperature

SQUID   Superconducting Quantum Interference Device

VT   Variable Temperature

ZFS   Zero Field Splitting

List of Compounds

1 $[H_2NMe_2][Cr_7ZnF_8(O_2C^tBu)_{16}]$

2 $[H_2NMe_2][Cr_7MnF_8(O_2C^tBu)_{16}]$

3 $[H_2NMe_2][Cr_7NiF_8(O_2C^tBu)_{16}]$

4 $[Cr_7ZnF_3(Etglu)(O_2C^tBu)_{15}(Phpy)]$

5 $[Cr_7MnF_3(Etglu)(O_2C^tBu)_{15}(Phpy)]$

6 $[Cr_7NiF_3(Etglu)(O_2C^tBu)_{15}(Phpy)]$

7 $[Cr_7ZnF_3(C_8H_{14}NO_5)(O_2C^tBu)_{15}](NC_5H_4CO_2)\,[\{Cr_7ZnF_8(O_2C^tBu)_{15}\}\{(C_3H_7)_2NH_2\}]$

8 $[Cr_7MnF_3(C_8H_{14}NO_5)(O_2C^tBu)_{15}](NC_5H_4CO_2)\,[\{Cr_7ZnF_8(O_2C^tBu)_{15}\}\{(C_3H_7)_2NH_2\}]$

9 $[Cr_7NiF_3(C_8H_{14}NO_5)(O_2C^tBu)_{15}](NC_5H_4CO_2)\,[\{Cr_7ZnF_8(O_2C^tBu)_{15}\}\{(C_3H_7)_2NH_2\}$

10 $[Cr_7ZnF_3(C_8H_{14}NO_5)(O_2C^tBu)_{15}](NC_5H_4CO_2)\,[\{Cr_7MnF_8(O_2C^tBu)_{15}\}\{(C_3H_7)_2NH_2\}]$

11 $[Cr_7MnF_3(C_8H_{14}NO_5)(O_2C^tBu)_{15}](NC_5H_4CO_2)\,[\{Cr_7MnF_8(O_2C^tBu)_{15}\}\{(C_3H_7)_2NH_2\}]$

12 $[Cr_7NiF_3(C_8H_{14}NO_5)(O_2C^tBu)_{15}](NC_5H_4CO_2)\,[\{Cr_7MnF_8(O_2C^tBu)_{15}\}\{(C_3H_7)_2NH_2\}]$

13 $[Cr_7ZnF_3(C_8H_{14}NO_5)(O_2C^tBu)_{15}](NC_5H_4CO_2)\,[\{Cr_7NiF_8(O_2C^tBu)_{15}\}\{(C_3H_7)_2NH_2\}]$

14 $[Cr_7MnF_3(C_8H_{14}NO_5)(O_2C^tBu)_{15}](NC_5H_4CO_2)\,[\{Cr_7NiF_8(O_2C^tBu)_{15}\}\{(C_3H_7)_2NH_2\}]$

15 $[Cr_7NiF_3(C_8H_{14}NO_5)(O_2C^tBu)_{15}](NC_5H_4CO_2)\,[\{Cr_7NiF_8(O_2C^tBu)_{15}\}\{(C_3H_7)_2NH_2\}]$

16 $(C_3H_7)_2NH_2Cr_7MnF_8(O_2CCMe_3)_{14}(O_2CC_5H_4N)_2\,[Cr_7NiF_3(O_2CCMe_3)_{15}C_8H_{14}NO_5]_2$

17 $(C_3H_7)_2NH_2Cr_7ZnF_8(O_2CCMe_3)_{14}(O_2CC_5H_4N)_2\,[Cr_7NiF_3(O_2CCMe_3)_{15}C_8H_{14}NO_5]_2$

18 $(C_3H_7)_2NH_2Cr_7MnF_8(O_2CCMe_3)_{14}(O_2CC_5H_4N)_2\,[Cr_7ZnF_3(O_2CCMe_3)_{15}C_8H_{14}NO_5]_2$

19 $(C_3H_7)_2NH_2Cr_7ZnF_8(O_2CCMe_3)_{14}(O_2CC_5H_4N)_2\,[Cr_7MnF_3(O_2CCMe_3)_{15}C_8H_{14}NO_5]_2$

Abstract

An investigation of the electronic structure of some transition metal clusters comprising anti-ferromagnetically coupled, heterometallic arrays of eight metal ions that are wheel-shaped, is reported.

The compounds were synthesized and provided by Dr. Grigore Timco of The University of Manchester and are formulated by their metal content as Cr_7M, where M = a divalent $3d$ metal. Two families of wheels are the subject of this research, defined 'green' and 'purple' from their physical appearance. Within each family, the compounds are all isostructural.

From simulation using a single Hamiltonian for Cr_7M-purple compounds, where M = Zn, Mn, or Ni, it is shown that with only two exchange parameters, one J_{Cr-Cr} and one J_{Cr-M}, data from bulk magnetization, neutron scattering, Electron Paramagnetic Resonance (EPR) spectroscopy at multiple frequencies and specific heat measurements can be modelled and that there is transferability of parameters. Preliminary attempts to measure electron spin relaxation times for two of the purple wheels have shown values of T_1 and T_2 that are comparable with those of the more extensively studied green wheels and hence further studies in this area are warranted.

Variable temperature Q- and W-band EPR spectra for a series of nine heterodimers comprising one green and one purple wheel, M=Zn, Mn or Ni in each case, are reported. For Cr_7Zn-purple there is no magnetic exchange detected, whereas weak and quantifiable exchange is required to interpret the spectra from the other six dimers.

EPR studies of three trimers of the form purple-green-purple are reported and the presence of magnetic exchange is identified by comparison with the spectra of the component single and double wheel compounds, although this is not quantified because of the numerical size of the simulations that are required.

The process of comparing simulated to experimental spectra is a complex problem and one which is central to the work reported in this thesis. The problem of fitting has been investigated and two novel solutions, one based upon pixel mapping and the other based on wavelet transformation are proposed.

Declaration

No portion of the work submitted in this thesis has been submitted in support of an application for another degree or qualification of this or any other university or other institute of learning.

Copyright statement

i. The author of this thesis (including any appendices and/or schedules to this thesis) owns certain copyright or related rights in it (the "Copyright") and he has given The University of Manchester certain rights to use such Copyright, including for administrative purposes.

ii. Copies of this thesis, either in full or in extracts and whether in hard or electronic copy, may be made **only** in accordance with the Copyright, Designs and Patents Act 1988 (as amended) and regulations issued under it or, where appropriate, in accordance with licensing agreements which the University has from time to time. This page must form part of any such copies made.

iii. The ownership of certain Copyright, patents, designs, trademarks and other intellectual property (the "Intellectual Property") and any reproductions of copyright works in the thesis, for example graphs and tables ("Reproductions"), which may be described in this thesis, may not be owned by the author and may be owned by third parties. Such Intellectual Property and Reproductions cannot and must not be made available for use without the prior written permission of the owner(s) of the relevant Intellectual Property and/or Reproductions.

iv. Further information on the conditions under which disclosure, publication and commercialisation of this thesis, the Copyright and any Intellectual Property and/or Reproductions described in it may take place is available in the University IP Policy (see http://www.campus.manchester.ac.uk/medialibrary/policies/intellectual-property.pdf), in any relevant Thesis restriction declarations deposited in the University Library, The University Library's regulations (see http://www.manchester.ac.uk/library/aboutus/regulations) and in The University's policy on presentation of Theses

Acknowledgements

Chapter I - General Introduction

This chapter introduces the fundamental concepts that underpin this thesis. It begins with a brief overview of the core principles of computing and logic, and how this is implemented in the manipulation of physical systems. This understanding is necessary to introduce the discussion on quantum computing and quantum logic. There are numerous algorithms that exploit quantum logic, and this chapter explores one such algorithm – Grover's algorithm, a method for searching an unsorted database. The requirements for the implementation of quantum computing are described by the DiVincenzo Criteria, and there follows a discussion of these criteria in regards to their relation to this thesis. A particularly famous implementation has been produced by the quantum computing company D-Wave Systems, which offers a quantum solution to a very specific mathematical problem. The implementation that is of interest in this thesis is that of molecular magnetism. By exploring the DiVincenzo Criteria, we can explore molecular systems that exhibit the properties necessary for the physical implementation of quantum computing. A variety of experimental techniques are used to probe molecular magnets, and this chapter introduces the underlying theory behind the techniques that feature in this thesis. The predominant focus in this thesis is Electron Paramagnetic Resonance, a spectroscopic technique for examining materials with unpaired electrons.

Classical Computing

The fundamental unit of information for classical computation is the binary digit, or

bit, a variable that can take one of only two possible values, generally represented as

either **0** or **1**. [1] These 0s and 1s correspond to a state in some physical two-state

system. A *register* is a collection of several bits and a computer is a device that

performs a function f to transform a register of bits into a different register of bits.

$$f : \{a_0, a_1, \ldots, a_n\} \rightarrow \{a'_0, a'_1, \ldots, a'_n\}$$
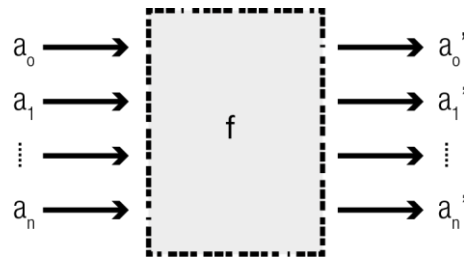
Figure 1 General schematic of classical computer

In Figure 1, we represent the calculation going left to right and the function f

operates on a system of n bits in a binary arithmetic. If we have n bits, we have

$N = 2^n$ states to operate with. For every input, there are 2^n possible outputs so the

total number of possible functions f that can be calculated is $2^{n(2^n)}$. An important

problem concerning f is *universality*. It is possible to identify a universal set of

functions, or gates, that we can use repeatedly and sequentially to simulate the

function f on a set of inputs. Logic gates are implemented using transistors and

diodes and their operation is represented by truth tables that show the effects upon

different combinations of variables. These gates have to be restricted to operating

only on a small number of inputs (usually two, at most three at a time).

 The two-bit gates AND and OR and the one-bit gate NOT are universal for classical

computation. [2]

Table 1 Truth tables for AND, OR and NOT gates

Input		Output	Input		Output	Input	Output
a_0	a_1	a_0 AND a_1	a_0	a_1	a_0 OR a_1	a_0	NOT a_0
0	0	0	0	0	0	0	1
0	1	0	0	1	1	1	0
1	0	0	1	0	1		
1	1	1	1	1	1		

The three gates can be reduced to a single gate, the negated AND or **NAND** gate.

Table 2 Truth table for NAND gate

Input		Output
a_0	a_1	a_0 AND a_1
0	0	1
0	1	1
1	0	1
1	1	0

$$a_0 \text{ NAND } a_1 \equiv \text{NOT } (a_0 \text{AND } a_1)$$

The three gates AND, OR and NOT are represented by

$$a_0 \text{OR } a_1 = (a_0 \text{NAND } a_0) \text{ NAND } (a_1 \text{NAND } a_1)$$

$$a_0 \text{AND } a_1 = (a_0 \text{NAND } a_1) \text{ NAND } (a_0 \text{NAND } a_1)$$

$$\text{NOT } a_0 = a_0 \text{ NAND } a_0$$

A practical concern is also how quickly these calculations can be done, and this may depend on the number of actual components used in the circuitry for *f*. If the number of gates varies polynomially with *n*, the circuit is said to be efficient; if it varies exponentially, it is inefficient. When discussing complexity of calculations, it is more typical to consider an idealised, abstract model of a computer (rather than an actual physical device) called a Turing machine.[3] When studying the complexity of quantum computations, a similarly abstract model is used – called a quantum Turing machine. [4]

Reversibility and Logic

The NAND gate is an important stepping stone towards a quantum computer, because it is building towards a universal set of logic gates. However, one of the requirements for a quantum computer is logic based on reversible principles. The AND and the OR gate are explicitly irreversible, because the original input states cannot be recovered if given the output states. By referring to Table 2 we can see that if the AND gate returns 0, we cannot know what the input was originally − similarly if the output of an OR is 1. The NOT gate is reversible as it is own inverse. From the 1920s through the late 1980s, a philosophical discussion was being had about the nature and connection between physical reversibility and *logical* reversibility.

This connection originates from the Second Law of Thermodynamics, the only fundamental law of Physics that exhibits an intrinsic 'arrow of time' through the concept of entropy. [5,6] Charles Bennet at IBM research reformulated the historical thermodynamic problem of Maxwell's Demon from a computational framework and demonstrated the link between entropy and information. [7] This showed that any irreversible logical process necessarily incurs an entropy increase. [8] The change in entropy associated with one bit of information is $ln(2)$. Thermodynamically, this corresponds to an energy increase known as the *Landauer limit*

$$E_l = kTln(2)$$

If a physical system carries out a logically irreversible process then it must increase the entropy in its surroundings, in the form of this fundamental minimum heat release. This is approximately 3×10^{-21} Joules at room temperature. If a processor has 100,000 gates erasing one bit every cycle at 100 MHz, the Landauer limit predicts it will dissipate at least 28 nanowatts. Current devices are operating far

beyond the Landaur limit, so many – including Feynmann [9] – may argue that this limit may seem unimportant for the time being. However, the importance of this work into computation and thermodynamics was to highlight that there is a fundamental limit on the efficiency of irreversible computations that cannot simply be incrementally improved upon by clever engineering of irreversible architecture. This work by Bennet also showed that a classical computation can be done without this energy dissipation per computational step by use of logically reversible gates. [7] A physical implementation of a logically reversible architecture would also be physically reversible. The NOT gate is the only reversible gate we have experienced so far. A closely related gate that operates on two bits is the XOR gate. In some literature, this is sometimes also called a C-NOT gate but I shall refer to the C-NOT only when discussing quantum logic.

Table 3 Truth table for XOR gate

Input		Output
a_0	a_1	a_0 XOR a_1
0	0	0
0	1	1
1	0	1
1	1	0

This gate performs an exclusive OR operation on the two bits and writes the output. Much as we did before with the NAND gate for irreversible logic, we are still interested in finding a set of universal gates for reversible logic. Reversible logic is different in one respect, however, in if we limit ourselves to gates that operate only on two bits we cannot form a set of universal reversible gates. In 1981, a universal three bit reversible gate was discovered by Tommaso Toffoli which he called the Controlled-Controlled-NOT (CCNOT) gate but subsequently was called the three-bit

Toffoli gate. [10] The Toffoli gate takes three bits as input and applies a NOT gate to the third bit if and only if the first two bits read 1. Otherwise, it does nothing. This gate is universal for reversible Boolean logic because it contains the NAND gate within it. When applied to classical computing, these gates seem like mere academic investigations into the ultimate limitations of computing. But they have found a practical use in recent years due to the investigation of quantum logic, systems that are physically reversible and so require logically reversible gates.

Quantum Computing

A quantum system exists in several states simultaneously until measured. A quantum computer operates on quantum states rather than classical states, a **qu**antum **b**it or qubit. Much as a bit exists in either a state 0 or 1, a qubit has a state of $|0\rangle$ and $|1\rangle$. The fundamental difference is, however, that a qubit can exist in a state $|\psi\rangle$ which is a superposition of states of $|0\rangle$ and $|1\rangle$.

$$|\psi\rangle = \alpha|0\rangle + \beta|1\rangle \qquad\qquad \mathbf{1}$$

where α and β are the probability amplitudes of the states $|0\rangle$ and $|1\rangle$ respectively. If we measure the state $|\psi\rangle$ we will observe $|0\rangle$ with probability $|\alpha|^2$ and $|1\rangle$ with probability $|\beta|^2$.
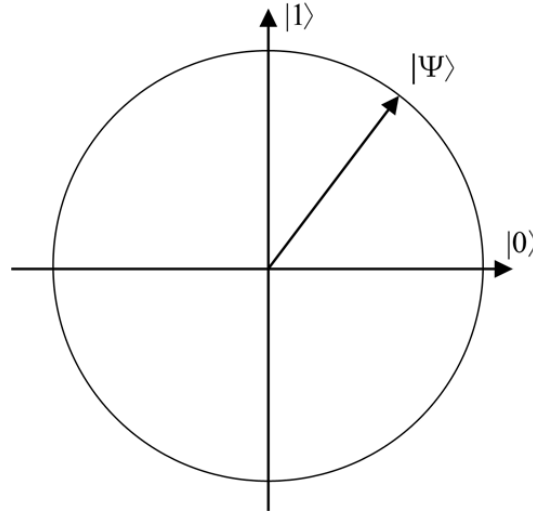
Figure 2 Geometric representation of a qubit [11]

This pure state is represented visually by points upon a Bloch sphere, a cross-section of which is shown in Figure 2. [11]

Since α and β are complex numbers then $|\psi\rangle$ is a vector that exists in a two-dimensional complex vector space where $|0\rangle$ and $|1\rangle$ form an orthonormal basis

$$|0\rangle = \begin{pmatrix} 1 \\ 0 \end{pmatrix} \quad , \qquad |1\rangle = \begin{pmatrix} 0 \\ 1 \end{pmatrix}$$

As $|\alpha|^2$ and $|\beta|^2$ are probabilities of only two possible outcomes, they have the condition

$$|\alpha|^2 + |\beta|^2 = 1 \qquad\qquad \mathbf{2}$$

When the qubit is in the state given by Equation **1**, we can carry out a measurement on $|\psi\rangle$ and collapse it either $|0\rangle$ or $|1\rangle$. This act of measurement cannot tell us the values of α and β. However, we can manipulate the system without carrying out a measurement as long as we satisfy the condition in Equation **2**. The general form of this sort of manipulation is a linear transformation U such that

$$U^\dagger U = UU^\dagger = I \qquad\qquad \mathbf{3}$$

One such linear transformation is a rotation of angle θ

$$|0\rangle \rightarrow \cos(\theta)|0\rangle + \sin(\theta)\,|1\rangle$$

$$|1\rangle \rightarrow -\sin(\theta)|0\rangle + \cos(\theta)|1\rangle$$

To carry out useful computation we need a register of multiple qubits. If we have two qubits, we will have four states and a general superposition of the form

$$|\psi\rangle = \alpha|00\rangle + \beta|01\rangle + \gamma|10\rangle + \delta|11\rangle \qquad\qquad \textbf{4}$$

where α, β, γ and δ are the probability amplitudes with the condition that

$$|\alpha|^2 + |\beta|^2 + |\gamma|^2 + |\delta|^2 = 1$$

In general a state $|\psi\rangle$ of n qubits is in a superposition of

$$|\psi\rangle = \sum_{k=0}^{2^n-1} \alpha_k |k\rangle$$

with amplitudes α_k constrained by

$$\sum_{k=0}^{2^n-1} |\alpha_k|^2 = 1$$

The orthonormal basis $\{|0\rangle, |1\rangle, \dots, |2^n - 1\rangle\}$ is called the *computation basis*. The state of $|\psi\rangle$ is inaccessible unless it is in this computational basis. The act of *measurement* causes it to collapse to one vector of the computational basis.

If we have two qubits, one of them in the state

$$|\phi\rangle = u|0\rangle + v|1\rangle$$

and the second in

$$|\psi\rangle = j|0\rangle + k|1\rangle$$

The state of the pair of qubits is the tensor product

$$|\psi\rangle \otimes |\phi\rangle = uj|00\rangle + uk|01\rangle + vj|10\rangle + vk|11\rangle \qquad \textbf{5}$$

Compare this to the general state of two qubits in equation **4**. It is the same as equation **5** if and only if

$$\alpha = uj \, , \beta = vk \, , \gamma = vj \, , \delta = vk$$

This is significant because it tells us that a general 2 qubit state is not simply a product of two 1 qubit states. The states that are not simply products are *entangled states*, [12] such as

$$|\psi\rangle = \frac{1}{\sqrt{2}}(|00\rangle + |11\rangle) \qquad \textbf{6}$$

On the road from bits to qubits there is a curious half-way house in the form of the classical nat. The nat is the logarithmic unit of information, corresponding to $\frac{1}{\ln(2)}$ bits. [13] The nat is an analogue version of the bit and is used in some continuous classical computations. There are some significant differences between a nat and a qubit. When we perform a measurement, a qubit reduces to a bit. A nat, however, is not changed by an act of measurement. We can use a nat to represent products of a superposition of two states, as in equation **4** – but a nat cannot represent the entangled state in equation **6**.

The remarkable fact about entangled qubits is that a measurement performed on one qubit will affect the other. Entanglement is a quantum correlation between two observables. In a quantum computation, the classical bits are replaced by qubits $|\psi_i\rangle$ and the function f in Figure 1 is replaced by the unitary operator U in Equation **3**.
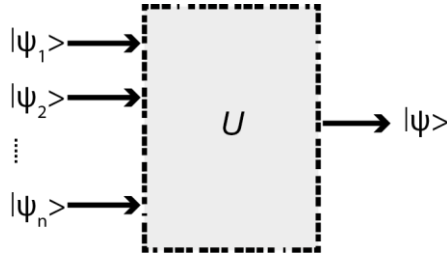
Figure 3 General schematic of a quantum computation

The schematic in Figure 3 is the quantum equivalent of the schematic in Figure 1. In Figure 3, the input on the left is generally a non-entangled state but the output on the right is generally entangled. It is a general description of how a quantum calculation is carried out. After this, a measurement is performed on each qubit.

In classical terms, *f* is written in terms of the logic gates that form a circuit. A similar set of gates exist for the operator *U* to create quantum circuits.

Quantum Logic

To perform quantum calculations, we need quantum logic gates. These gates are represented by unitary operators and the action of the operators is governed by the rule

$$\langle i|j \rangle = \delta_{ij}$$

where δ_{ij} is Kronecker's delta, a function which returns 1 if $i = j$ and zero otherwise. Table 1 shows the truth table for the classical NOT gate. This gate can be written in Dirac notation

$$N = |0\rangle\langle 1| + |1\rangle\langle 0|$$

We can apply this gate to a $|0\rangle$ state and find that this NOT gate transforms $|0\rangle$ to $|1\rangle$.

$$N|0\rangle = (|0\rangle\langle 1| + |1\rangle\langle 0|)|0\rangle = |1\rangle$$

A very important quantum gate is the Hadamard operator, H. This gate takes a register of qubits and transforms them into a superposition state.

$$H|0\rangle = \frac{1}{\sqrt{2}}(|0\rangle + |1\rangle)$$

$$H|1\rangle = \frac{1}{\sqrt{2}}(|0\rangle - |1\rangle)$$

This superposition of states is the necessary starting point for the implementation of quantum algorithms.

Grover's Algorithm

Searching through a database is a very common task required of computers.

The classical method of solving this problem is to systematically examine every possibility until the correct solution is found. If the user is trying to find one particular entry in a database containing N entries then the best case scenario is that the desired entry is the first one in the database. The worst case scenario is that the desired entry is the last one in the database and the algorithm has to go through every single element before it finds it.

The efficiency of algorithms is written in Big O notation, which for this classical search algorithm is $O(N)$. No classical algorithms can operate more efficiently than $O(N)$ and so pursuit for a more efficient searching algorithm has moved into the quantum regime. If N is extraordinarily large, as it is in databases for financial or cryptographic applications, a more efficient search algorithm would yield huge performance increases.

Table 4 Example of a database of phone numbers. The database has N elements, each with an index x. The problem is searching through this list to find one specific phone number.

Index	Element
0	6060842
1	8423089
2	**8675309**
3	8533937
…	
N-1	6345789

We want to search through these N elements, indexed $x \in \{0,1,2,\dots,N-1\}$. We assume that the number of elements is a power of 2 such that $N = 2^n$ and so the index is stored in n bits. We will also assume that there is only one solution, there is

only one particular element we are looking for. The algorithm does work in the case of searching for multiple elements, but we shall limit it to one for the sake of simplicity.

The philosophical difference in Grover's algorithm is that it operates on this index of the list rather than the list itself. We need to have a function that recognises a solution. When presented with an element with index x, this function will flag the solution if this is the element we are searching for. We define this function $f(x)$ where x is the index of the element

$$f(x) = \begin{cases} 0 & \text{if } x \text{ is a solution} \\ 1 & \text{if } x \text{ is not a solution} \end{cases}$$

We need some mechanism that can use this function and tell if a particular index is a solution. This mechanism is called an Oracle.

The Oracle is a quantum logic gate and performs unitary operations on the computational basis. The input for the Oracle is the index register, and if it recognises a solution it signals it via a signalling qubit $|q\rangle$ initialised to $|q\rangle = \frac{1}{\sqrt{2}}(|0\rangle - |1\rangle)$. The action of the Oracle is

$$O|x\rangle|q\rangle = |x\rangle|q + f(x)\rangle$$

This action corresponds to a phase shift of the first register, depending on $f(x)$. The signalling qubit $|q\rangle$ is silent throughout this computation, so we can omit it from the Oracle action.

$$O|x\rangle = (-1)^{f(x)}|x\rangle$$

The Oracle is going to flag the solution based on the output of the function $f(x)$.

The solution to the search problem is now the index marked with a negative sign.

However, when we measure $|x\rangle$ with an experiment we cannot directly observe a change of sign. We need some technique to measure $|x\rangle$ and be reasonably confident that we will get the correct solution. The Grover iteration achieves this. By some simple manipulations on $|\psi\rangle$ and multiple Quantum Fourier Transforms, the Grover iteration maximises the probability that when $|x\rangle$ is measured it will give the correct solution. If there is a single solution, then to obtain a probability near 1 we must apply the Grover iteration $O(\sqrt{N})$ times. If there are M solutions, we must apply the Grover iteration $O\left(\sqrt{\frac{N}{M}}\right)$. [14] This efficiency is the most efficient for any algorithm on a quantum computer. [15] This has vast potential benefits for very large datasets. Grover's algorithm has applications far beyond database searching. It can be used for any problem where finding the answer is difficult but recognising the solution is simple. As long as the Oracle can be constructed, Grover's algorithm can be implemented. Grover's algorithm requires only control over the superposition of states, making it an ideal case for computation with molecular magnets.

DiVincenzo Criteria

In a physical candidate for quantum computation, there are five requirements that must be met. [16] We shall explore those requirements and how they are met by a system of qubits of molecular magnets.

A scalable physical system with well characterised qubits

To begin any quantum computation, we need a system of qubits to manipulate. The requirement for them to be 'well characterised' means several things. The physical parameters of the qubit should be known accurately, including the internal Hamiltonian describing the energy eigenstates of the qubit. This ought to take into consideration couplings to other states, interactions with other qubits and couplings

to external fields that manipulate the states of the qubit. One physical realisation using molecular magnets is achieved by isolating small clusters where the qubits are easily identifiable through their location in space. [16] This comes with the necessary requirement that there is minimal interaction between isolated systems.

Initialisation to a pure state

Even in a classical computation, a register needs to be initialised to a known value before the start of any computation. However, a quantum computation requires this condition for another reason as well. Any sort of error correction requires a continuous supply of qubits in a low-entropy state, for example new qubits in the $|0\rangle$ state. The need for a continuous supply of useful qubits, rather than just a pool of initial qubits, is a stringent condition on any physical proposal for quantum computations.

If the time it takes to set qubits to an initial $|0\rangle$ state, then the quantum computer would have to have some sort of mechanism to bring new qubits in for initialisation into the active computation and draw the used qubits out. There are two main approaches to setting a qubit system into an initialised state. If the ground state of the Hamiltonian is of interest, the system can be naturally cooled. If the standard state is of interest, a measurement can be made which projects the system either into a desired state or a state which can rotate into it. These two approaches are not fundamentally different, since the projection procedure is a sort of cooling. In techniques that use Electron Paramagnetic Resonance, the time scale over which spins align with an applied field is a concern. For magnetic clusters of qubits, this time is heavily dependent on the temperature of the system. This initialisation must be done at temperatures less than the energy gap between the ground state and the

first excited state preventing spin-phonon interactions and thermally assisted resonant tunnelling. [16]

Decoherence times longer than gate operation time

Decoherence times characterise the dynamics of how a qubit interacts with its environment. The simplified description of this decoherence time is the time it takes a generic qubit state

$$|\psi\rangle = a|0\rangle + b|1\rangle$$

to be transformed into a mixture state

$$\rho = |a|^2|0\rangle\langle0| + |b|^2|1\rangle\langle1|$$

More specifically, decoherence time can depend upon the form of the initial state where the amplitudes change as well. Other quantum states of the qubit may be significant too, in a state decay known as leakage in quantum computing. Decoherence is the fundamental quality that describes the boundary between quantum mechanical and classical behavior of a quantum system. Being in control of decoherence is of principal importance for carrying out quantum computations, because if decoherence takes over then the benefits of the quantum mechanical nature of the computation are lost and the system essentially behaves merely as a classical computer. The relevant decoherence times must be long enough so that uniquely quantum features of the calculation are exploited. There may be several different decoherence times corresponding to different degrees of freedom of the system, though many of these are not relevant to the system's behaviour for useful computation. The determination of which coherence time is relevant is determined by the choice of the $|0\rangle$ and $|1\rangle$ states.

Using spin states as qubits, the ability to manipulate them depends strongly on the

magnetic relaxation which in turn is influenced by spin tunnelling. Low temperature

experiments on Mn_{12} clusters have demonstrated the quantum mechanical tunnelling

of the bulk magnetisation and Figure 4 shows a plot of the calculated relaxation time

τ as a function of magnetic field at T=1.9 K.[19] Relaxation time is significant in the

use of molecular magnets for data storage. The magnetic relaxation times measured

are sufficient to store and compute information.
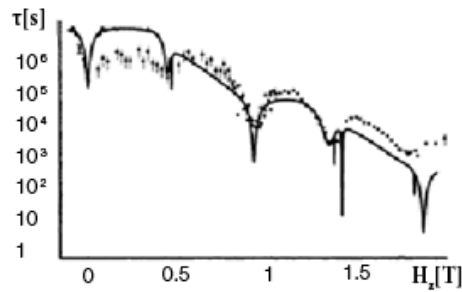
Figure 4 Logarithmic plot of relaxation time τ as a function of magnetic field H_z at
T=1.9 K. Solid lines are calculated, dots and error bars are measurement. [19]

Universal set of Quantum Gates

A quantum algorithm is a sequence of unitary transformations U acting on a small

number of qubits. We can produce a rotation about a particular axis by applying a

resonant pulse. [18] Implementation of two qubit logic gates has been proposed by

manipulating exchange interactions of Mn_4 dimers. [19] The ground state and the three

low lying excited states are chosen as the computational basis. The properties of the

dimer are simplified to label every eigenstate as two quantum numbers with values

$$m = \frac{9}{2}, \frac{7}{2}, \dots, -\frac{7}{2}, -\frac{9}{2}.$$

By applying an oscillating magnetic field and ignoring the phase of each eigenstate,

the resonant frequency ω_m between eigenstates can be tuned to allow specific

transitions. The resonant frequency between the states $\frac{9}{2}$ and m_2 is different from the

frequency between $-\frac{9}{2}$ and m_2. The energy shift due to exchange interactions is [17]

$$\omega_j = \frac{9J_z}{2\hbar}$$

The application of a π pulse in a transverse magnetic field at the resonant frequency

ω_1 can generate a CNOT gate. By labelling the appropriate states as $|0\rangle$ and $|1\rangle$, we

generate a two-qubit gate and associate the evolution of quantum states to a change

in logical states as shown in Table 5.

Table 5 Correspondence between physical quantum states and quantum logic states

Quantum States		Logic States	
$\left(\frac{9}{2},\frac{9}{2}\right)$ $\rightarrow$	$\left(\frac{9}{2},\frac{9}{2}\right)$	$\|00\rangle$ $\rightarrow$	$\|00\rangle$
$\left(\frac{9}{2},\frac{7}{2}\right)$ $\rightarrow$	$\left(\frac{9}{2},\frac{7}{2}\right)$	$\|01\rangle$ $\rightarrow$	$\|01\rangle$
$\left(-\frac{9}{2},\frac{9}{2}\right)$ $\rightarrow$	$\left(\frac{9}{2},\frac{7}{2}\right)$	$\|10\rangle$ $\rightarrow$	$\|11\rangle$
$\left(-\frac{9}{2},\frac{9}{2}\right)$ $\rightarrow$	$\left(-\frac{9}{2},\frac{9}{2}\right)$	$\|11\rangle$ $\rightarrow$	$\|10\rangle$

Qubit-specific measurement

The direct measurement of the spin of a molecular magnet is not yet technically

feasible. The limitations on the sensitivity of microSQUID allow the direct

measurement of spins to the scale of S = 10, 000. [20] Magnetic force microscopy has

been used to detect a single spin $S = \frac{1}{2}$ but the sensitivity cannot determine whether

the state was spin up or down. [17]

D-Wave Systems

Founded in 1999, D-Wave Systems, Inc. is a quantum computing company based in

British Columbia, Canada.

D-Wave Systems has carried out a calculation using 84 qubits on D-Wave One. They have tackled the 'theorem on friends and strangers', a famous problem in Ramsey theory. This is a branch of combinatorics that seeks to find order in chaos.

Consider a party of six people. Some of these people may have met before and already be friends. Some may not have met and will be strangers to each other. There is the most order when all six are all friends, or when all six are strangers. In all other cases, there will be a mix of friends and strangers.
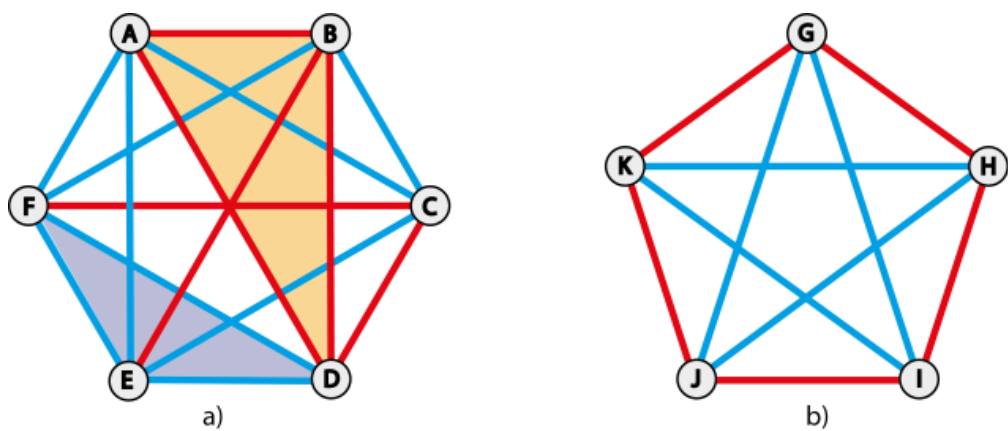
Figure 5 Graph of connections between a party of six (a) and five (b)

This information can be represented by a mathematical *graph*, a set of vertices and connections between them. Lines are drawn between every pair, red representing strangers and blue representing friends. The theorem on friends and strangers asks if this party is big enough such that there will always be a group of at least three mutual strangers or at least three mutual friends. In terms of the graph in Figure 5 a), this corresponds to finding either a red or blue triangle – such as ABD and DEF.

It has been proven that when a party contains six people, then there is guaranteed to be at least three strangers or three friends regardless of whom is invited.[22] This is not the case for a party of five, as it is possible to construct a party of five such that there are no three mutual friends or strangers, as in Figure 5 b).

The Ramsey number *R(n,m)* is the threshold for size of the party *N* necessary for there always to be *n* friends or *m* strangers. In this case, R(3,3) = 6. For there to be four friends or four strangers, their party must contain at least eighteen people – that is R(4,4) = 18. [23] For the case of R(5,5), no precise answer is currently known but it is known to be between 43 and 49. [24] Ramsey numbers grow rapidly and are incredibly difficult to calculate.

To illustrate this complexity, mathematician Paul Erdős wrote:

> *Imagine an alien force, vastly more powerful than us, landing on Earth and demanding the value of R(5,5) or they will destroy our planet. In that case, we should marshal all our computers and our mathematicians and attempt to find the value. Suppose, instead, that they ask for R(6,6). In that case, we should attempt to destroy the aliens.* [25]

The quantum algorithm for solving this problem treats the vertices and lines in Figure 5 as edges and reduces the problem to counting all possible permutations of friends and strangers. A cost function is introduced that is a function of *m* and *n* and the number of possible graphs. The solution is the graph that corresponds to the global minimum of this cost function. To encode this into qubits, the graphs are turned into binary strings which label the computational basis. The computational basis determines whether or not there is an edge on the graph. Solving optimisation problems according to adiabatic quantum evolution is a well-known process. [26]

The algorithm starts by using a probabilistic method to give a lower bound for the Ramsey number. The required number of qubits for a given *N* is

$$n_q = \frac{N(N-1)}{2}$$

The adiabatic algorithm is run until the qubits are in the ground state of the final Hamiltonian. N is increased as is the number of qubits n_q and the algorithm is run

again until there is a difference in energy in the ground state Hamiltonian. The run
that corresponds to this energy difference is the run that corresponds to the correct
value of N. In experimental conditions, this is run multiple times to amplify the
success probability of finding the correct answer.

The D-Wave device implements quantum annealing and can solve quadratic
unconstrained binary optimization (QUBO) problems. This is not a universal
quantum computer, but is ideal for solving problems of Ramsey numbers.   The
physical system uses current-carrying superconducting circuits with qubit states
dictated by the directions of current. [27]

In the experiment, the cost function is given by the local magnetic field and the
coupling between Ising spins. The problem is to find global minima of this cost
function.
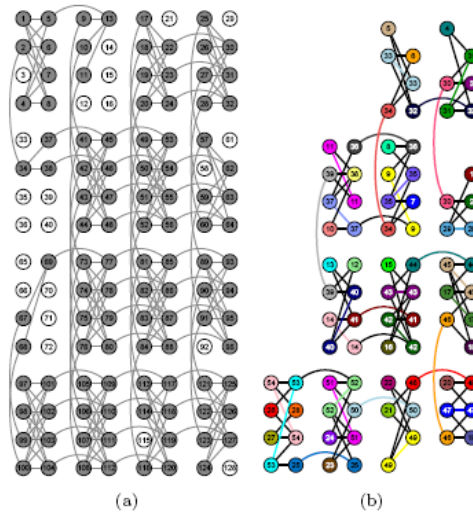
*Figure 6 Layout of qubits and couplers. Grey are useable qubits, while white are
qubits that could not be calibrated (a) and embedding of qubits necessary to
calculate R(8,2) (b)* [27]

The hardware for this calculation involves a 4x4 array of cells of 8 qubits. Within
each cell, each qubit on the left side connects to each qubit on the right side. One
qubit in the cell connects to one other qubit in a neighbouring cell in the

corresponding position, shown in Figure 6 (a). Due to certain defects in the fabrication process, not all qubits were useable resulting in 106 useable qubits out of a possible 128. Calculations of different values of $R(n,m)$ are performed by different combinations of couplings of qubits between cells.

One of the problems encountered is that there can be very many qubit interactions, and the D-Wave machine can only operate 2-qubit interactions. To reduce the problem of many qubit interactions to only 2 qubit interactions, D-Wave implements ancilla qubits. The embedding of the Ramsey problem into the chip for $R(8,2)$ is shown in Figure 6 (b). A problem is encountered if qubit 26 needs to be coupled to qubit 52 as there is no direct interaction between the two. However, there is direct coupling between qubit 53 and 52 and also 26 and 53. The ferromagnetic coupling between these two qubits is increased so they align in the same direction, so when qubit 26 interacts with 53 it also indirectly interacts with 52. These qubits have the same Bloch vector and behave as a single qubit allowing indirect coupling.

Running at 20 mK over 100,000 sweeps with each sweep taking 1 ms, the D-Wave machine found the correct ground state for N=4 92.7% of the time. For N=5, this was 94.1% and N=6 this was 93.3%. The source of error was generally due to the loss of the ferromagnetic coupling across ancilla qubits. The most complex calculation was for $R(8,2)$, involving 28 computational qubits but 84 total qubits. While the results of this calculation are not novel (it is known that $R(2,s) = s$ for all s), it is necessary to implement these quantum algorithms on known problems to determine efficacy. D-Wave claims that this is the largest experimental implementation of a scientifically meaningful quantum algorithm. [28] This is still a long way from performing a quantum computation that is not possible on a classical computer. Even for the smallest unsolved Ramsey number, a minimum of 880

computational qubits are required. The process of calculating how many ancilla qubits are necessary requires calculating the encoding scheme as in Figure 6(b), and that alone is a currently a computation of staggering complexity.

Despite this, it is an important PR result for D-Wave Systems which markets their 128 qubit computer for $10,000,000. [28]

Molecular Magnetism

The ideal molecular magnet must generally satisfy three criteria. It must have: (i) a large total spin, (ii) a weak intermolecular interaction, and (iii) a high magnetic anisotropy.

An ideal example of a system that satisfies these criteria is $Mn_{12}O_{12}(O_2CMe)_{16}(H_2O)_4$ known generally as Mn_{12}. This molecule has a ground spin state $S = 10$ and so a total of 21 available spin eigenstates in which to encode information. These spin eigenstates are shown in Figure 7.
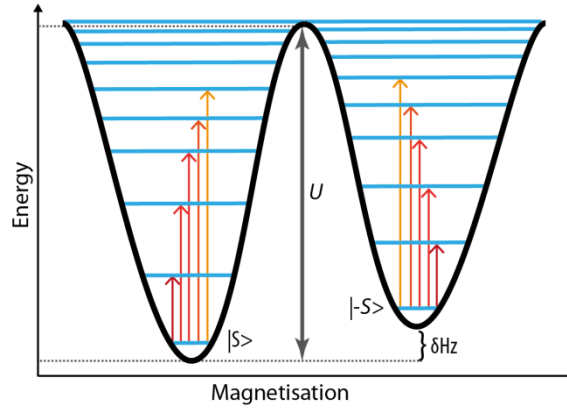
Figure 7 Potential well of spins in Mn$_{12}$. Spin eigenstates are shown by blue horizontal lines and transitions are shown by arrows.

The qubit states are defined by the symmetric and antisymmetric combinations of the degenerate ground state.

$$|0\rangle \equiv |S\rangle + |-S\rangle$$
$$|1\rangle \equiv |S\rangle - |-S\rangle$$

To satisfy the second DiVincenzo criterion, we must initialise the qubits to a ground state of one of the wells in Figure 7. A strong external field H_z aligns the magnetic moment of the molecule with the field. The molecular magnet is described by $H_{spin} = H_a + V$ where $H_a = -AS_z^2 - BS_z^4$ represents the magnetic anisotropy $A \gg B > 0$ and $V = g\mu_B \mathbf{H} \cdot \mathbf{S}$ is the Zeeman term describing coupling between

external field $\mathbf{H}$ and $\mathbf{S}$. We can then reduce this field to a bias field δH_z, so that the offset between the two wells suppresses the tunnelling between equivalent states in the two wells.

The DiVincenzo criteria also require that all states in a system are equally populated. We can do this by inducing transitions between all allowed spin eigenstates. Two different fields are applied

$$\mathbf{H_1}(t) = B_m[\cos(\omega_m t + \phi_m)\,\hat{\boldsymbol{x}} - \sin(\omega_t + \phi_m)\,\hat{\boldsymbol{y}}] \qquad \textbf{7}$$

where B_m is the amplitude of the field, ω_m is the resonant frequency of transition and ϕ_m is the applied phase. This field causes σ transitions, direct transitions where $\Delta m = \pm 1$. This field can only influence the left hand well because it is left circularly polarised. The second field is

$$\mathbf{H_2}(t) = g\mu_B B_o(t)\cos(\omega_0 t)\,\hat{\boldsymbol{z}} \qquad \textbf{8}$$

where $B_0(t)$ is the field amplitude and ω_0 is the frequency that induces transitions in the eigenstate where $\Delta m = 0$. The field in equation **7** controls the reading in of data, as each frequency ω adds a phase 0 or π to the eigenstate $|m>$. This populates all states, and equation **8** ensures equal transition probabilities.
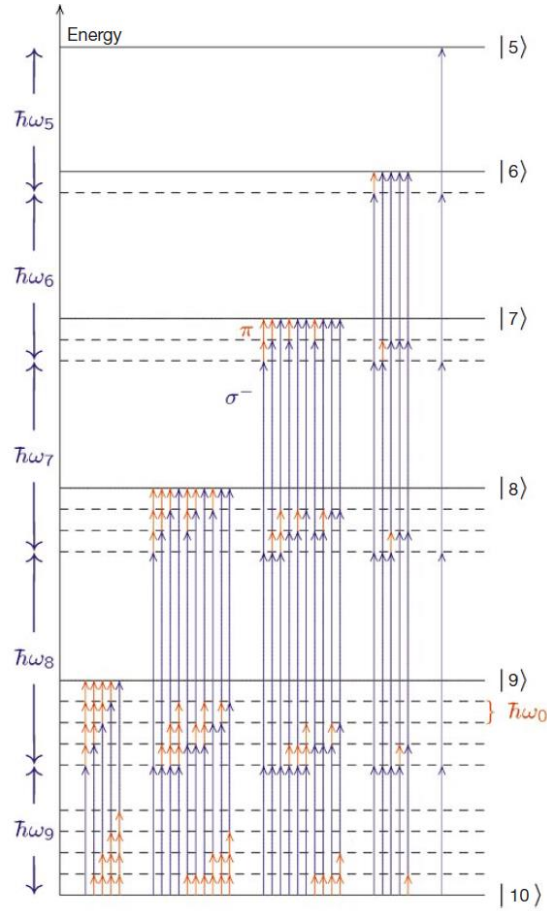
Figure 8 Feynman diagrams that describe transitions in the left well of Figure 7. Solid arrows show σ^- transitions and dotted arrows show π transitions. [19]

In Figure 8, transitions between spin eigenstates are governed by fine and hyperfine structure of atomic energy levels. [19]

Table 6 Binary value corresponding to specific states

State m	9	8	7	n
Binary value	2^0	2^1	2^2	2^{9-n}

We can encode a binary number by setting phase ϕ_m in equation **8** by reference to Figure 8. The value of each phase is determined by the number of ρ photons required to reach a given eigenstate. We read data out again by applying the same pulse as in equations **7** and **8**. The phase of each state is modified by $-\nu$, which suppresses any

state with positive amplitude and amplifies those with a negative amplitude. The 'marked' states are read out by Electron Paramagnetic Resonance Spectroscopy.

Each well in Figure 7 can store $N = 2^{S-1}$ states. For the Mn_{12} molecule with $S = 10$ this is 262,144 states. As a comparison, this is roughly equivalent to the computing power of the NSSC-1 (NASA Standard Spacecraft Computer 1) developed in 1974 for use on the Solar Maximum Mission satellite investigating solar flare activity. [26] The access times for this encoded data are constrained by the magnetic pulse lengths T for reading and writing, ultimately giving a clock speed of 10 GHz. [19]

The key advantage for molecular magnets is that each molecule is identical to every other molecule, making manipulation and measurement of the system much easier than systems with larger qubits. The key disadvantage is that to address these spin states we need to operate at very low temperatures so that we can control decoherence.

Anti-ferromagnetically coupled heterometallic wheels

When magnetic centres are close to each other, the unpaired electrons may interact and produce a coupling between them. A *ferromagnetic* interaction is a mutually parallel coupling that increases the overall magnetic dipole. An *anti-ferromagnetic* interaction is a mutually anti-parallel coupling and cancels out the overall dipole interaction. A *ferrimagnetic* interaction is an anti-ferromagnetic coupling with different magnitudes resulting in an overall magnetic moment. This coupling can also occur in clusters of wheels with unpaired electrons. The homometallic wheel $[Cr_8F_8(O_2CCMe_3)_{16}]$ with an octagonal arrangement of Cr^{III} metal centres with an anti-ferromagnetic coupling between them. [42] This gives the wheel an overall ground state spin of zero. Substituting one of the anti-ferromagnetically coupled Cr^{III} ions

$(S = {}^{3}/_{2})$ for a divalent metal produces a heterometallic wheel with a non-zero resultant spin ground state as shown in Figure 9.
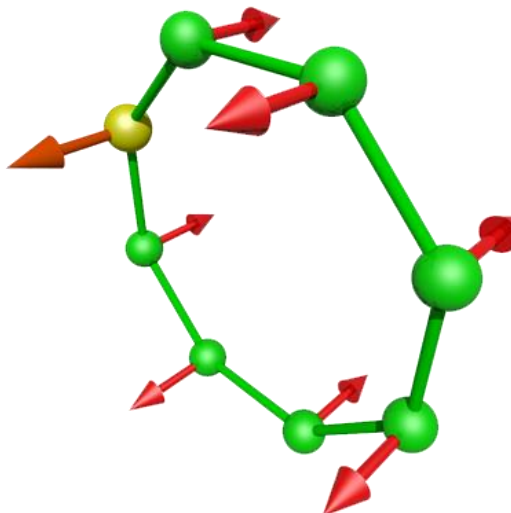
Figure 9 Schematic of an anti-ferromagnetically coupled Cr$_7$M wheel

The heterometallic variant Cr$_7$Ni wheel has a spin ground state of ½ and has been proposed as a candidate for a qubit. [43]

To satisfy the Divincenzo Criteria to form a two-qubit quantum gate, two wheels must be linked together with a controllable interaction between the magnetic components. The schematic of this coupling is shown in Figure 10. The quantum gate must have both an 'on' and an 'off' state, corresponding to the strength of the communication between these wheels.
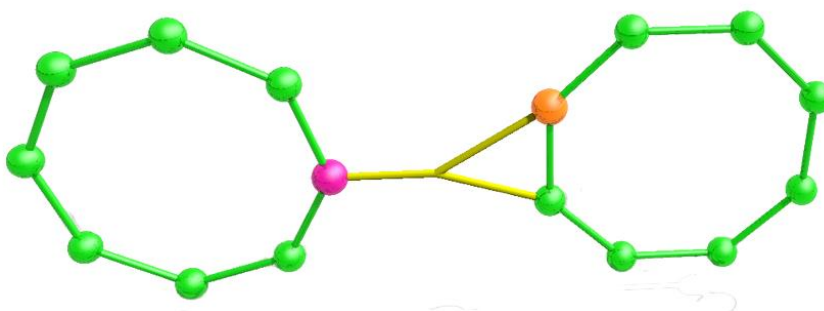
Figure 10 Schematic of coupling between two Cr$_7$M heterometallic wheels

This is the motivation for the study of the electronic properties of such linked wheel systems.

Experimental Techniques

Magnetisation

Magnetism has been a source of fascination since antiquity. The first understanding of magnetic attraction comes from the philosopher Guiguzi, writing in the 4th century that lodestone – naturally occurring magnetic oxide – can attract iron. Later in the Song Dynasty, lodestone is fashioned into a 'south pointing fish' – an early implementation of a compass. [31] Meanwhile, Greek scholars Pliny and Potelmy were asserting that lodestone loses its magnetic properties when rubbed with garlic or onions, or in the presence of diamond [32] and the herbalist Matthiolus reports that Muhammed's coffin in Medina was suspended in the air by an arched roof of magnets. [33] In 1616, the English physician William Gilbert was the first to ruthlessly refute ancient theories unquestioned since Aristotle and to carry out the first rigorous scientific investigation into magnetism. [33]

In 1778, Dutch botanist Sebald Brugmans first discovered *diamagnetism* in bismuth and antinomy. [34] *Diamagnetism* is an opposing response to an applied magnetic field, and is a feature of all materials but generally is very weak. *Paramagnetism* is a response in the direction of the applied field proportional to the magnitude of the field. A paramagnetic response is not present in all materials, but when it does arise it is much stronger than the diamagnetic response. *Ferromagnetism* is stronger still, and is a result of long-range ordering of spins within a substance. Ferromagnets will remain magnetised for some duration even after the applied field is switched off.

A material in an applied magnetic field **H** acquires a *magnetisation* **M**. The relationship between this magnetisation and the applied field is given by the susceptibility χ.

$$\mathbf{M} = \chi\mathbf{H}$$

As stated by Curie's Law, this magnetisation is also approximately inversely proportional to temperature

$$\mathbf{M} = C\,\frac{\mathbf{H}}{T - T_C}$$

where T_C is a critical temperature above which the ferromagnetic material becomes paramagnetic and C is a constant.

Magnetisation and magnetic susceptibility is measured by a Superconducting Quantum Interference Device (SQUID). A SQUID is a magnetometer capable of measuring very small magnetic fields. A sample is magnetised by a superconducting magnet and is moved through a detection coil such that the magnetic moment of the sample induces a current. This variation in magnetic flux causes a resultant change in voltage proportional to the magnetic moment of the sample.

For more information about SQUID instruments and applications, the reader is directed to the following literature:

- Principles and Applications of Superconducting Quantum Interference Devices by Antonio Barone, *World Scientific Publishing Co* **1992**

- The SQUID Handbook Vol. I Fundamentals and Technology of SQUIDs and SQUID Systems by John Clarke and Alex I. Braginski, *Wiley VCH* **2004**

Electron Paramagnetic Resonance

During World War II, the development of radar required reliable and tuneable microwave sources. By the end of the war, microwave research had advanced and components become cheap enough that basic spectrometers could be constructed with good sensitivity. [35] Building upon work on paramagnetic relaxation, Yevgeny Zavoisky developed these spectrometers and in 1944 discovered Electron Paramagnetic Resonance (EPR). [36]

EPR spectroscopy is a technique for studying samples with unpaired electrons. An unpaired electron in a constant magnetic field will align either parallel or anti-parallel to the field. The anti-parallel arrangement is more energetically favourable; hence an energy gap opens between the two states.
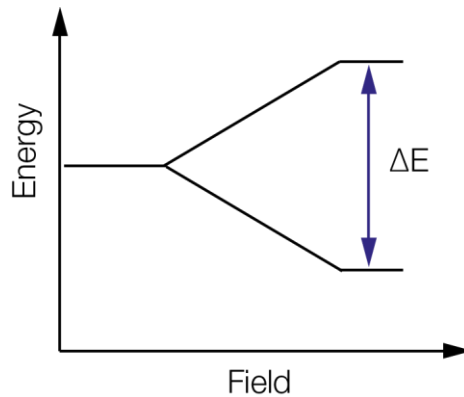
Figure 11 Energy level diagram of an electron in an applied magnetic field

This is described by the spin Hamiltonian

$$H_S = g\mu_B B \, \hat{S}_z \qquad\qquad \mathbf{9}$$

where

- g is the Landé g-factor, a particular type of g factor. For a free electron, g_e = 2.00232.

- B is the magnetic field strength

- $\hat{S}_z$ is the z component of spin angular momentum operator.

This gap is known as a Zeeman splitting. Electrons can be flipped between the two states by a second applied alternating magnetic field oscillating a frequency generally in the 'microwave' range of the EM spectrum. Charles Poole describes EPR succinctly as '*the study of direct transitions between electronic Zeeman levels'*. [35]

The difference between two energy levels in Figure 11 is

$$\Delta E = E_+ - E_- = g\mu_B B = h\nu$$

The energy $h\nu$ corresponds to the photon energy required to cause transitions between E_+ and E_-. The frequency of an EPR experiment is denoted by one of several 'bands'. In subsequent chapters, spectra of Q Band ($\nu \approx 35$ GHz) and W Band ($\nu \approx 95$ GHz) will be shown. The g value is related to frequency and field by the resonant condition

$$g = \frac{h\nu}{\mu_B B}$$

Referring to g by a single numeric parameter applies only to systems that behave isotropically as in Figure 12, where

$$g_x = g_y = g_z$$
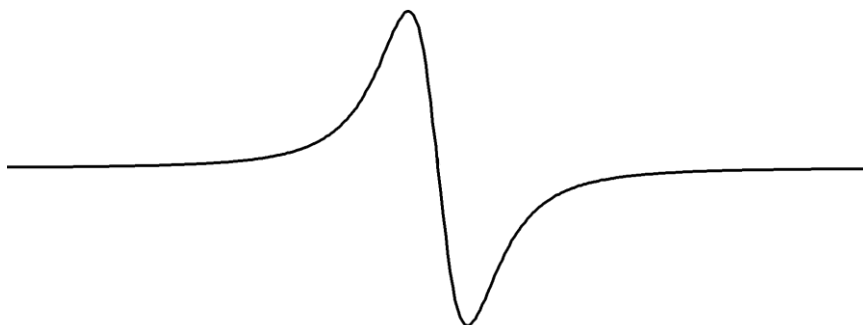
Figure 12 EPR spectrum of S=1/2 spectrum with isotropic g

For S>1 systems, there can be splitting of degenerate states even at zero applied field. This Zero Field Splitting (ZFS) causes the preferred orientation even without an external field. This is described by two parameters, the axial and rhombic ZFS constants. This introduces an additional term in equation **9**.

$$H = \mu_B(\mathbf{g} \cdot \mathbf{B})\hat{S} + D\left[\hat{S}_z^2 - \frac{S(S+1)}{3}\right] + E\left[\hat{S}_x^2 - \hat{S}_y^2\right]$$

10

D is a second rank traceless tensor

$$D_{xx} + D_{yy} + D_{zz} = 0$$

The axial term D is defined

$$D = D_{zz} - \frac{D_{xx} + D_{yy}}{2}$$

while the rhombic term E

$$E = \frac{D_{xx} - D_{yy}}{2}$$
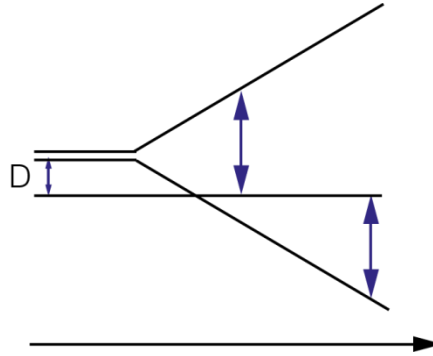
Figure 13 Energy level diagram for spin triplet state

In a spin triplet S=1, the m_s states are split by D as shown in *Figure 13*.
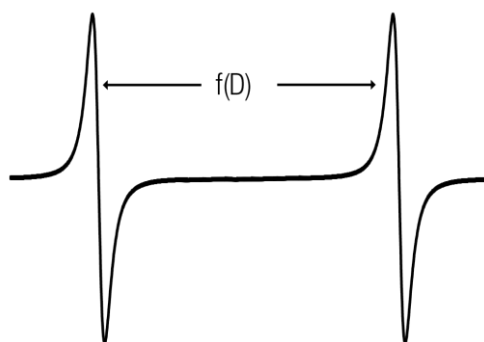
Figure 14 EPR spectrum of an S=1 spin triplet system for a single orientation

The peaks in the resultant EPR spectrum in Figure 14 are split by a function of D and

centred on a specific g value.

For a more detailed understanding of the principles and instrumentation of continuous wave EPR the reader is invited to read the following textbooks:

- Electron Spin Resonance: A Comprehensive Treatise on Experimental

  Techniques by Charles Patton Poole, *John Wiley & Sons Australia, Limited*

  1983

- Electron Paramagnetic Resonance by John A. Weil and James R. Bolton,

  John Wiley & Sons, **2007**

- Electron Paramagnetic Resonance: A Practitioners Toolkit by Marina

  Brustolon and Elio Giamello *Wiley-Blackwell* **2009**

Pulsed EPR

The difference between CW and pulsed EPR can be illustrated by a musical analogy. [37] Consider the spectrometer as a piano and the sample as some unknown chord. In a cw-EPR EPR experiment, each key on the piano is played and we test for any resonances between the frequency from the piano and our sample chord. In a pulsed EPR experiment, every single key on the piano is pressed simultaneously. The resulting cacophony is Fourier transformed to obtain a frequency spectrum. The Fourier transform is discussed in more detail in Chapter 6. The advantage of this is that it only requires one short experiment to obtain all of the signals from the sample.

In a pulsed EPR experiment, a short microwave pulse is applied and the signals from the sample are Fourier transformed to obtain the spectrum in the frequency domain. Immediately after this pulse, there will be an interaction between the magnetisation of the sample and its surroundings before returning to an equilibrium.

A *frame of reference* is the co-ordinate system used to display and measure quantities. To intuitively understand complex motion, it is often simpler to move to a non-inertial frame of reference that is rotating relative to some inertial frame of reference.
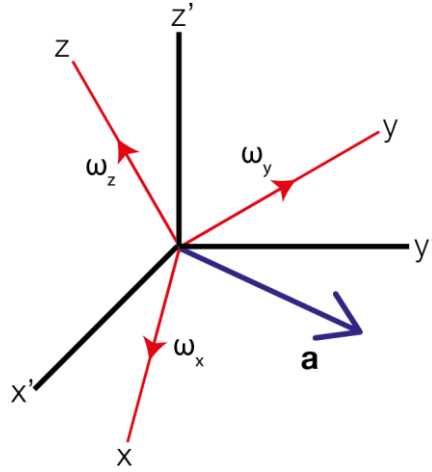
*Figure 15 Cartesian frame of reference (black) and rotating frame of reference (red)
with angular velocity ω and arbitrary vector a*

Figure 15 shows a Cartesian frame of reference with coordinates

$$\mathbf{r}' = \begin{pmatrix} x' \\ y' \\ z' \end{pmatrix}$$

and rotating frame of reference with coordinates

$$\mathbf{r} = \begin{pmatrix} x \\ y \\ z \end{pmatrix}$$

rotating with an angular velocity **ω** with respect to the Cartesian frame. The time

derivative of some arbitrary vector a is

$$\left(\frac{d\mathbf{a}}{dt}\right)_{fixed} = \left(\frac{d\mathbf{a}}{dt}\right)_{rotating} + (\boldsymbol{\omega} \times \boldsymbol{a})$$

An interesting result of switching to a rotating frame of reference is the emergence of fictitious forces. The centrifugal force and the Coriolis force are both fictitious forces that emerge not from any real physical interactions, but purely from the acceleration of a non-inertial reference frame.

The laboratory frame for EPR is usually defined with the magnetic field $\mathbf{B_0}$ parallel to the z' axis and $\mathbf{B_1}$ parallel to the x' axis, as in Figure 16.
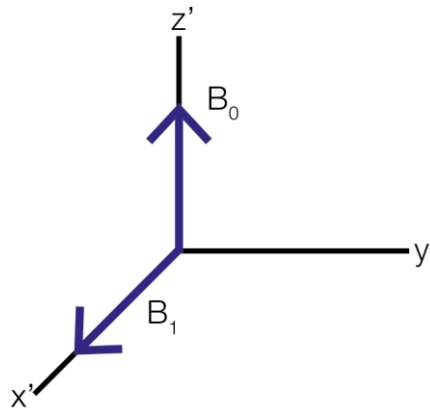
Figure 16 Frame of reference for EPR laboratory frame

An electron in a field experiences a torque and the magnetic moment will begin to precess about the axis of the field at an angular frequency called the *Larmor frequency*.

$$\omega_L = -\gamma B_0$$

Electrons spins can be either parallel to B_0 or antiparallel. The parallel state is energetically more favourable and so there will be a net magnetisation along the z' axis. However, there is no preference for the x' or y' axis so the electron spins will be randomly orientated in the plane. The components of the magnetic moment in this plane will cancel each other out and produce a stationary magnetisation $\mathbf{M_0}$ along $\mathbf{B_0}$, as in Figure 17.
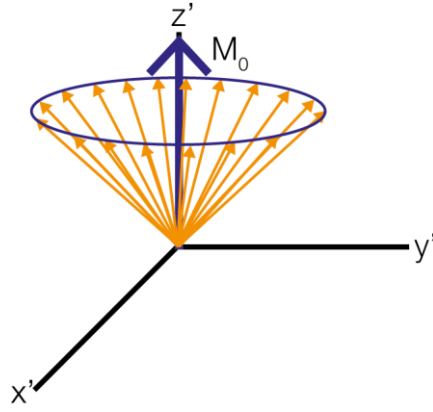
Figure 17 Stationary magnetisation from Larmor precession

An EPR resonator produces linearly polarised microwaves. Assuming that this microwave frequency ω_0 is equal to the Larmor frequency ω_L, we can shift the frame of reference to a rotating reference frame with this same angular frequency. The magnetisation precesses about $\mathbf{B_1}$ at a frequency ω_1 known as the *Rabi frequency*. If $\mathbf{B_1}$ is parallel to the x axis, the field will rotate the magnetisation about the +x axis, as in Figure 18.
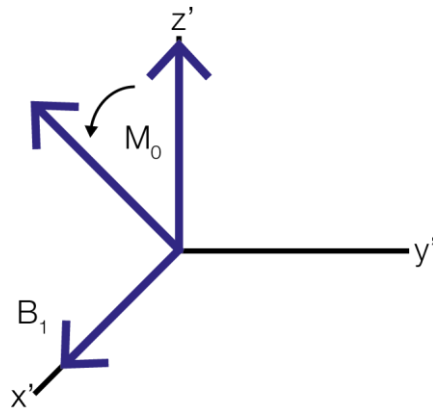
Figure 18 Rotation of magnetisation

The angle of rotation of M_0 is known as the *tip angle*

$$\alpha = -\gamma |B_1| t_p$$

Where t_p is the pulse length. These pulses are labelled by the tip angle, such that a π pulse corresponds to rotation of M_0 by 180 degrees. Pulses are also labelled by the axis parallel to B_1, +x, +y, or +z.

Immediately after the microwave pulse, a sample tends to emit microwaves back again. A stationary magnetisation becomes a rotating magnetisation and generates a current within the resonator. This signal generated is a *Free Induction Decay* (FID).

Magnetic moments can align either parallel or anti-parallel to an applied field. The parallel arrangement is more energetically favourable and so at thermal equilibrium there will be more moments aligned parallel.

However, after applying a $\frac{\pi}{2}$ pulse, the system is not in thermal equilibrium. Through interactions with its surroundings, the system will eventually return to equilibrium. This is *spin-lattice relaxation*. The rate at which magnetization returns to equilibrium is T_1

$$M_z(t) = M_0 \cdot \left[1 - e^{-\left(\frac{t}{T_1}\right)} \right]$$
    11

The magnetisation will also decay in the x-y plane, fanning out around a particular axis. This is the *spin-spin relaxation*, and the time constant is T_2.

$$M_y(t) = e^{-\left(\frac{t}{T_2}\right)}$$
    12

Inelastic Neutron Scattering

Inelastic Neutron Scattering (INS) is a technique to study molecular motion and crystal field excitations by directing a neutron beam at a sample. Elastic neutron scattering conserves momentum from the neutron to the sample, not affecting the

internal state of the sample. Inelastic neutron scattering does not conserve momentum and either creates or annihilates excitations within the sample. When a neutron beam is fired at a sample, the beam interacts with electrons via a magnetic dipole interaction.

When generated in a reactor, a neutron beam is composed of a wide range of wavelengths and energies. A neutron chopper is a rotating mechanical device that blocks the neutron beam as it rotates. This produces a neutron beam with a very precise initial wavelength k_i and energy E_i. This beam is scattered from the sample and directed towards a series of detectors. These detectors calculate the final energy E_f and wavelength k_f and a change in that energy will be due to a transition in the sample. The dependence of the scattering vector $Q = k_i - k_f$ provides information about magnetic properties of the sample.

Specific Heat

Few discoveries have been as profoundly significant, and as profoundly misunderstood, as the phenomenon of *heat*. Seeking to explain oxidation, Johann Joachim Becher proposed in 1667 that heat was a material called *phlogiston* which escaped from an object when burnt.[38] The accomplished French chemist Antoine-Laurent de Lavoisier discovered oxygen, demonstrated its role in oxidation, and promptly debunked Becher's phlogiston theory. Lavoisier instead stated that heat is a weightless, self-repellent, invisible fluid called *the caloric* that flows from a hot body to a cool one through microscopic pores in solids. [39] A body was thought to contain a certain amount, or capacity, of the caloric.

Despite heat now considered a transfer of energy, the term 'heat capacity' is still in use to describe the amount of heat needed to raise the temperature of a body a specific amount – a remnant from Lavoisier's obsolete caloric theory.

The heat capacity C is the ratio of the heat energy transferred to an object and the increase in temperature that results from it, measured in J/K.

$$C = \frac{\Delta Q}{\Delta T}$$

This property C scales with the size of the sample, but it is more meaningful to measure the intrinsic property of a sample. This can be done by reporting the heat capacity per mole of substance - the *molar heat capacity* - or the heat capacity per unit mass – the *specific heat capacity.*

The law of Dulong-Petit states that the molar heat capacity of a substance is *3R.* Hence, the specific heat capacity c is

$$c = \frac{3R}{M}$$

where R is the gas constant, and M is the molar mass. Significantly, this model predicts that the specific heat capacity of solids is independent of temperature. This law is accurate for simple structures at high temperatures, but breaks down in a regime where the quantum mechanical nature overcomes the classical regime. [40]

While the Dulong-Petit model assumed Maxwell-Boltzmann statistics, the Einstein model applied Einstein-Bose statistics. Einstein saw that at low temperatures, heat capacity is indeed temperature-dependent reaching zero at absolute zero. The Einstein model treats every atom in a lattice as a quantum harmonic oscillator oscillating at the same frequency ω.

$$E_n = \hbar\omega\left(n + \frac{1}{2}\right) \qquad 13$$

This harmonic oscillator in equation **13** has equally spaced energy levels at quanta of $\epsilon = \hbar\omega$. Calculating the multiplicity of this system is equivalent to distributing

pebbles into N boxes. This leads to the determination of the thermal energy of this set of N oscillators

$$U = \frac{N\hbar\omega}{e^{\frac{\hbar\omega}{k_b T}} - 1}$$

Differentiating with respect to T gives the heat capacity

$$C = 3Nk \left(\frac{\epsilon}{kT}\right)^2 \cdot \frac{e^{\frac{\epsilon}{kT}}}{\left(e^{\frac{\epsilon}{kT}} - 1\right)^2}$$

The Einstein model is important because it introduces a quantum mechanical description of the phenomenon of heat. However, the primary assumption that all the harmonic oscillators oscillate at the same frequency is an oversimplification and does not predict behaviour at very low temperatures.

The Debye model extends this work, and instead treats atoms as vibrating phonons in a box. The derivation of energy levels in the Debye model involves solving the 'particle in a box' problem and results in the heat capacity.

$$C \approx \frac{12\pi^4 Nk}{5} \left(\frac{T}{T_D}\right)^3$$

Where T_D is the Debye temperature, the temperature at which all modes are excited. The Debye model accurately describes behaviour at very low temperatures, and also tends towards the law of Dulong-Petit at high temperatures. However, it is not accurate at intermediate temperatures between the two.

Project Aims

The aims of this project are to investigate the physics of transition metal clusters of anti-ferromagnetically coupled heterometallic wheels. The Cr_7Ni wheel has been well studied previously, [42] and a family of related wheels with a different divalent metal has been made subsequently. [44] The first aim of this project is to determine the microscopic spin Hamiltonian parameters of this latter family of wheels by simultaneous simulations of the results from different experimental techniques. This project also seeks to use pulsed EPR techniques to probe the relaxation times of these single wheels.

The single wheels can be linked together to form large supramolecular structures.[45] The second aim of this project is to use the understanding of the single wheels to simulate the EPR spectra of the linked wheels and to estimate the magnitude of the communication between the wheels. Of particular interest is the relative magnitude of this inter-ring communication with the variation of the divalent metal within two-wheel structures.

These wheels can be linked together into even larger structures still, composed of three wheels linked together. While the complexity of these structures is currently beyond the computational limits of simulation software, a third aim of the project is to gain some understanding of the electronic structures by comparison with the EPR spectra of the related dimer two-wheel structures.

A fourth aim is to study the general problem of algorithmically comparing experimental spectra to simulated spectra. This is a problem repeatedly encountered when investigating the electronic structure of complex systems, [46] and any proposed routine for solving this problem would be greatly beneficial.

References

[1] Shannon, C. E., *Mob. Comput. Commun. Rev.* **2001**, 5, 3.

[2] Morris, M., Kime, C. *Logic and Computer Design Fundamentals*; Prentice Hall, University of Michigan, **2004**.

[3] Ralston, A., *Encyclopedia of Computer Science*; John Wiley and Sons Ltd., p 260, New York, **1971**.

[4] Barenco, A., Bennett, C. H., Cleve, R., DiVincenzo, D. P., Margolus, N., Shor, P., Sleator, T., Smolin, J. A., Weinfurter, H. *Phys. Rev. A.,* **1995**, 52, 3457.

[5] Szilard, L. Z. *Physik* **1929**, 53, 840.

[6] Bejan, A. *Int. Commun. Heat Mass.,* **1988**, 15, 571.

[7] Bennett, C., *Int. J. Theor. Phys.,* **1982**, 21, 905.

[8] Landauer, R,. *IBM J. Res. Dev*., **1961**, 5, 183.

[9] Feynman, *R., Found. Phys.,* **1986**, 16, 507.

[10] Toffoli, T., *Lecture Notes in Computer Science*, **1980**, 85, 632

[11] Nielsen, M. A.; Chuang, I. L. *Quantum Computation and Quantum Information: 10th Anniversary Edition*; Cambridge University Press, **2010**.

[12] Bohr, N. *Phys. Rev.,* **1935**, 48, 696

[13] Reza, F. M. *An Introduction to Information Theory*; Dover, New York, **1994**.

[14] Zalka, C. *Phys. Rev. A.,* **1999**, 60, 2746.

[15] Grover, L. K. *In Proceedings of the Twenty-Eighth Annual ACM Symposium on Theory of Computing*; ACM: Philadelphia, Pennsylvania, USA, **1996**, p 212.

[16] DiVincenzo, D. P. *Fortschr. Phys.,* **2000**, 48, 771-783

[17] Cerletti V., Gywat O., Loss D., *Nanotechnology* **2005**, 16.

[18] Wernsdorfer, W. *Comptes Rendus Chimie* **2008**, 11, 1086.

[19] Leuenberger, M. N.; Meier, F.; Loss, D. *Monatsh. Chem.,* **2003**, 134, 217.

[20] Tejada, J., Chudnovsky, E. M., Barco, E. d., Hernandez, J. M., Spiller, T. P. *Nanotechnology* **2001**, 12, 181.

[21] Hou, J. M, Tian, L.-J, Ge, M.-L. *Chin. Phys. Lett.,* **2005**, 22, 2147.

[22] Ramsey, F. *Proc. London Math. Soc* **1929**, 30, 264.

[23] Greenwood, R. E.; Gleason, A. M. *Canad. J. Math* **1955**, 7, 7.

[24] McKay, B. D.; Radziszowski, S. P. *J. Graph Theory* **1995**, 19, 309.

[25] Spencer, J. *Ten Lectures on the Probabilistic Method*; SIAM, **1994**.

[26] Farhi, E., Goldstone, J., Gutmann, S., Sipser, M. *arXiv:quant-ph/0001106* **2000**.

[27] Bian, Z., Chudak, F., Macready, W. G, Clark, L, Gaitan, F. *Phys. Rev. Lett*, **2012**, 111, 130505.

[28] O'Brien, T. 'D-Wave One claims mantle of first commercial quantum computer', *Engadget* **2011**

[29] Leuenberger, M. N., Loss, D., *Nature* **2001**, 410, 789.

[30] Trevathan, C. E.; Taylor, T. D.; Hartenstein, R. G.; Merwarth, A. C.; Stewart, W. N. *Commun. ACM* **1984**, 27, 902.

[31] Fu, C.; Yang, L.; Editorial, A.; Han, Y. N. *Origins of Chinese Science and Technology*; Asiapac, **2004**.

[32] Mourino, M. R. *Radiology* **1991**, 180, 593.

[33] Gilbert, W. *De Magnete*; Dover Publications, New York, **1958**.

[34] Band, Y. B. *Light and Matter: Electromagnetism, Optics, Spectroscopy and Lasers*; John Wiley & Sons, Chichester **2006**.

[35] Poole, C. P. Electron Spin Resonance: *A Comprehensive Treatise on Experimental Techniques*; Dover Publications, New York, **1996**.

[36] Eaton, G. R.; Eaton, S. S.; Salikhov, K. M.; Salikhov, K. M. *Foundations of Modern EPR*; World Scientific, Singapore, **1998**.

[37] Schweiger, A.; Jeschke, G. *Principles of Pulse Electron Paramagnetic Resonance*; Oxford University Press, **2001**.

[38] Conant, J. B. *The Overthrow of the Phlogiston Theory : the Chemical Revolution of 1775-1789*; Harvard University Press: Cambridge, Mass., **1964**.

[39] Mendoza, E. *Physics Today* **1961**, 14, 32.

[40] Landau, L. D.; Lifshitz, E. M. *Statistical Physics*; Elsevier Science, Oxford, **1996**.

[41] Arzhang, A., Rival O., Morton J., Blundell S. *Phys. Rev. Lett.,* **2007** 98 5

[42] Slageren J. van, Sessoli R., Gatteschi D., Smith A. A., Helliwell M., Winpenny R. E. P., Cornia A., Barra A-L., Jansen A. G. M., Rentschler E., Timco G. A., *Chem. Eur. J.*, **2002**, *8*, 1, 277

[43] Larsen F. K., McInnes E. J. L., Mkami H. El, Overgaard J., Piligkos S., Rajaraman G., Rentschler E., Smith A. A., Smith G. M., Boote V., M. Jennings, Timco G. A., Winpenny R. E. P., *Angew. Chem. Int. Ed.*, **2003**, *42*, 1, 101

[44] Timco G. A., McInnes E. J. L., Pritchard R G., Tuna F., Winpenny R. E. P., *Angew. Chem. Int. Ed.*, **2008**, *47*, 9681

[45] Timco G. A., Carretta S., Troiani F., Tuna F., Pritchard R. J., Muryn C. A., McInnes E. J. L., Ghirri A., Candini A., Santini P., Amoretti G., Affronte M., Winpenny R. E. P., *Nature Nano.* **2009**, *4*, 173

[46] Kirste B., *Anal. Chim. Acta,* **1992**, 265, 191-200

Chapter II - Materials and Methods

In this thesis, a variety of compounds has been studied using a selection of different techniques. This chapter details compounds that have been studied and the technical details of the apparatus used to probe them.

Heterometallic Wheels

In 1985, the homometallic wheel $[Cr_8F_8(O_2CCMe_3)_{16}]$ was first synthesised.[1] Every Cr^{III} is bridged to its neighbouring Cr^{III} ions through one fluoride and two pivalate anions and experiences a somewhat distorted octahedral geometry. The Cr^{III} ions have been shown to be anti-ferromagnetically coupled, resulting in an overall ground state spin of zero. [2]

This compound is the basis for the family of heterometallic variants that have been reported in this thesis. The heterometallic wheels have eight metal centres, seven of which are Cr^{III} ions and one divalent metal, producing a wheel with a non-zero overall ground state spin.

The first family, referred to as 'green wheels' due to their appearance, have the general formula $[NH_2R_2][Cr_7MF_8(O_2C^tBu)_{16}]$ where R is a linear alkyl and M is a divalent ion. These wheels consist of an octagon of metal ions and every edge is bridged by one fluoride and two pivalates. In single crystal X-ray diffraction studies, the Cr^{3+} and M sites are disordered around the ring. [9] The cases of interest in subsequent chapters are where M = Zn **1**, Mn **2**, and Ni **3**. These compounds are isostructural and their structure is shown in Figure 19.
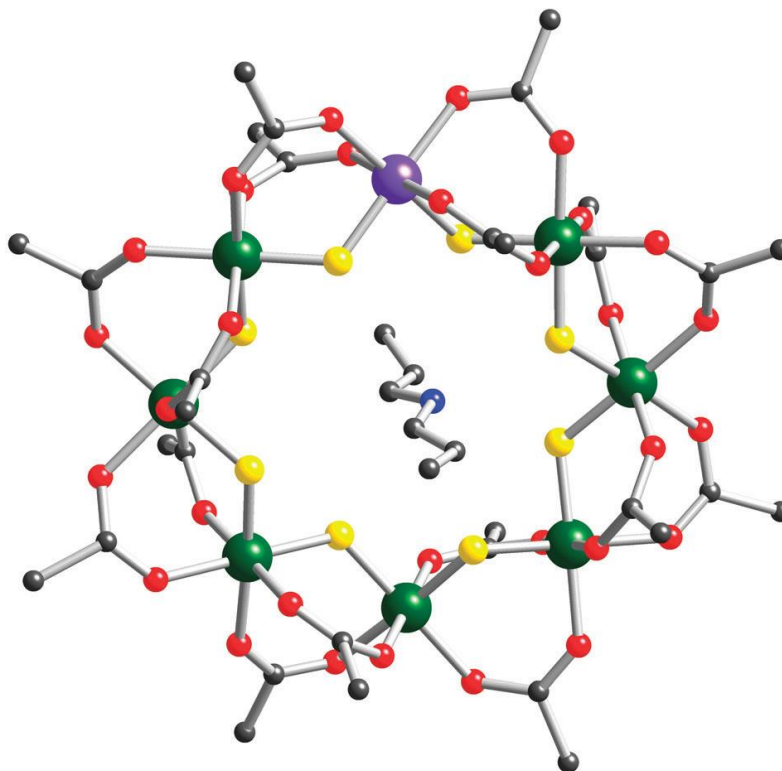
Figure 19 Structure of green wheels. Colours are :- Cr: green, M*: purple, O: red, F: yellow, N: blue, C: black.* [3]

The second family, referred to as 'purple wheels', have the general formula $[Cr_7MF_3(Etglu)(O_2C^tBu)_{15}(Phpy)]$ where Etglu is *N*-ethyl-D-glucamine ($C_8H_{19}NO_5$) and Phpy is 4-phenylpyridine ($C_6H_5-C_5H_4N$). These wheels form an irregular octagon and there are five bridging alkoxides and only three bridging fluorides. Seven edges have two bridging pivalates attached, while the remaining edge has one pivalate and a bridging fluoride. We will be reporting analysis of measurements of the cases where M = Zn, **4**; Mn, **5** and Ni, **6**. These compounds are isostructural, and their structure is shown in Figure 20 and the Cr and *M* sites are localised. These compounds were synthesised by Dr. Grigore Timco of The University of Manchester according to literature methods. [6]
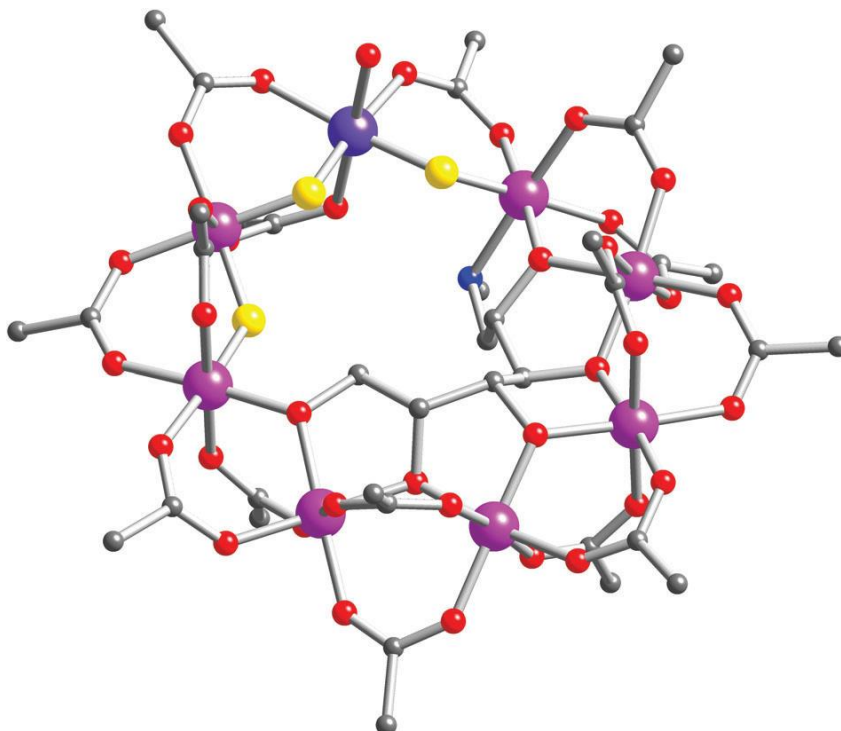
Figure 20 Structure of purple wheels. Colours are :- Cr: purple, M*: dark blue, O: red, F: yellow, N: blue, C: black.* [3]

A new series of mixed-wheel systems has been synthesised, linking the green and purple wheels together through an iso-nicotinic linker. The green Cr_7M wheels are synthesised with 16 pivalate ligands, and have a hydrocarbon exterior that can be functionalised to introduce a linker. The ring is reacted with iso-nicotinic acid (NC_5-H_4CO_2H) in boiling *n*-propanol. Following a chromatographic separation this produces a functionalised compound. The iso-nicotinate ligand provides a pyridine nitrogen atom that can be used to bind to other metal centres. The substitution is selective as the Cr^{III} ions are relatively inert, and so the iso-nicotinate is introduced on the divalent metal site and one of the adjacent Cr^{III} ions. Figure 21 shows the structure of the substituted wheels. [4]
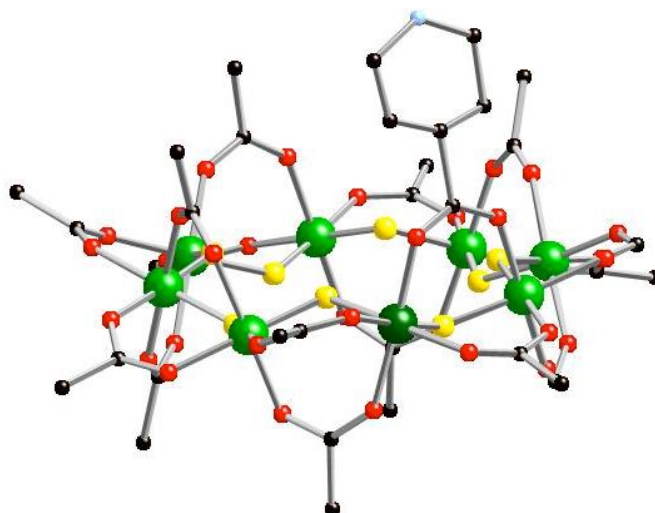
Figure 21 A mono-substituted wheel with iso-nicotinic acid.[4]

The purple Cr_7M wheels can be linked directly to the green wheel without requiring any additional magnetic ions in the linker. The coupling between the rings arises from the pyridyl groups that link directly to the metal ions. [8]

Pairs of these wheels are coupled to each other through these metallic links. The linker is attached to the purple wheel through the divalent metal only, while the green wheel is attached through the divalent metal and one adjacent Cr^{III} site.

These dimers have the general formula $[Cr_7M''F_3(C_8H_{14}NO_5)(O_2C^tBu)_{15}](NC_5H_4CO_2)[\{Cr_7M'F_8(O_2C^tBu)_{15}\}\{(C_3H_7)_2NH_2\}]$.

Table 7 Compound numbers for the purple-green dimers studied

M'' \ M'	Zn^{II}	Mn^{II}	Ni^{II}
Zn^{II}	7	8	9
Mn^{II}	10	11	12
Ni^{II}	13	14	15

A total of nine different compounds with different combinations of M' and M'' have been studied, as shown in Table 7. These compounds are isostructural and their

structure is shown in Figure 22. All compounds were synthesised by Dr. Grigore Timco of the University of Manchester, following literature methods. [4]
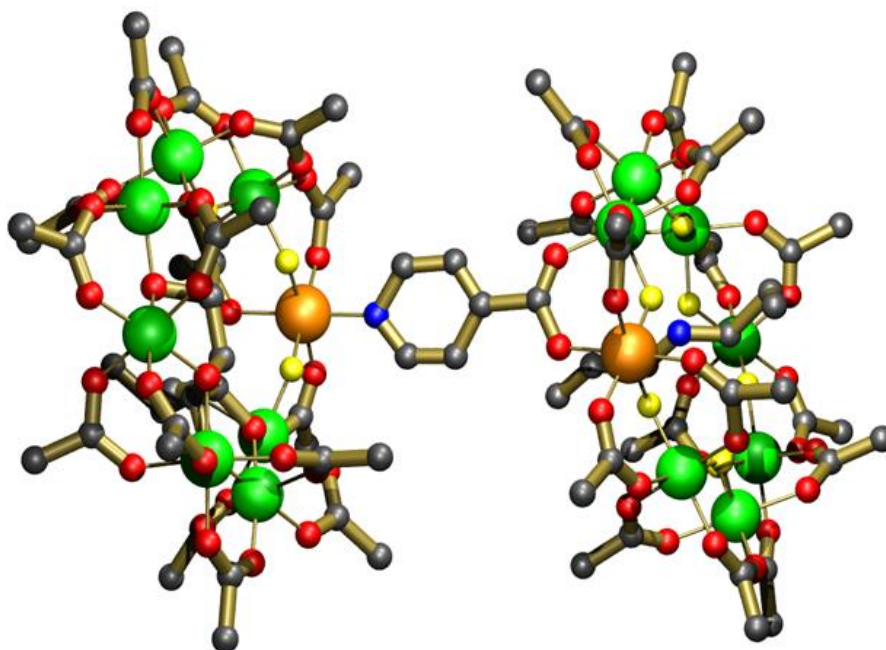
Figure 22 Structure of [Cr$_7$M''F$_3$(C$_8$H$_{14}$NO$_5$)(O$_2$C^{t}Bu)$_{15}$] (NC$_5$H$_4$CO$_2$) [{Cr$_7$M'F$_8$(O$_2$C^{t}Bu)$_{15}$}{(C$_3$H$_7$)$_2$NH$_2$ }] [4]

The series of dimers has been even further extended by introducing a third wheel. Another isonicotinate linker is attached to the opposite side of the green wheel, resulting in a purple-green-purple arrangement of wheels. These compounds have the general formula

[{(C$_3$H$_7$)$_2$NH$_2$Cr$_7$M' F$_8$(O$_2$CCMe$_3$)$_{14}$ }] (O$_2$CC$_5$H$_4$N)$_2$ [Cr$_7$M'' F$_3$(O$_2$CCMe$_3$)$_{15}$(C$_8$H$_{14}$NO$_5$)]$_2$

A small selection of these trimers with different divalent metals *M'* and *M''* have been studied, as shown in Table 8.

Table 8 Compound numbers for purple-green-purple trimers studied

M'' \ M'	Mn^{II}	Zn^{II}
Ni^{II}	16	17
Zn^{II}	18	
Mn^{II}		19

These compounds are isostructural and the structure is shown in Figure 23.

All compounds were synthesised by Dr. Grigore Timco of the University of Manchester.
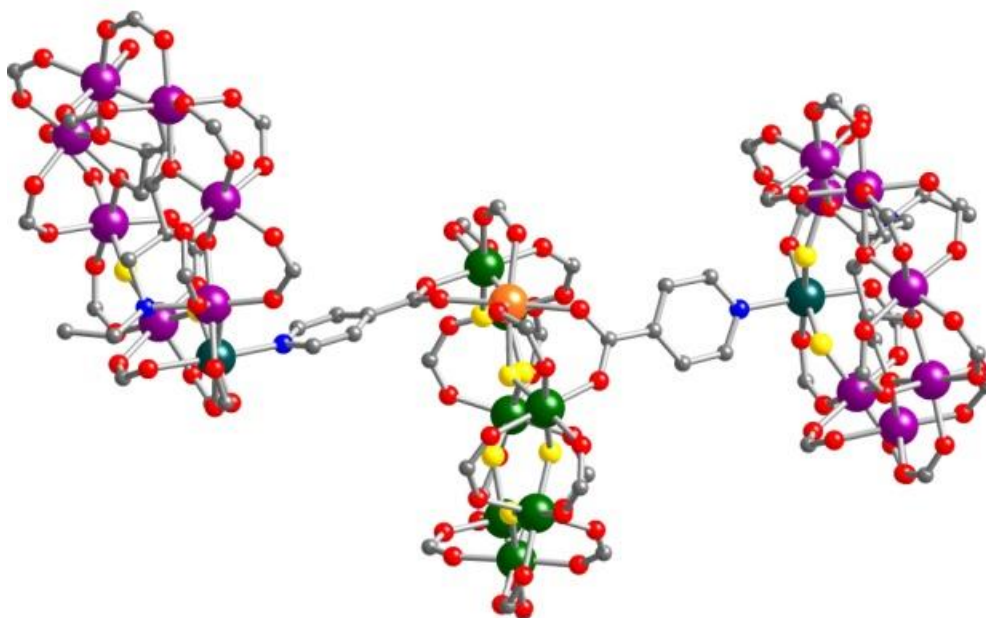
Figure 23 Structure of $(C_3H_7)_2NH_2Cr_7M'F_8(O_2CCMe_3)_{14}(O_2CC_5H_4N)_2$ $[Cr_7M''F_3(O_2CCMe_3)_{15}C_8H_{14}NO_5]_2$

Electron Paramagnetic Resonance Measurements

The Q-Band *cw*-EPR spectra were recorded on a Bruker Elexsys E500 spectrometer with a 2 T electromagnet and an Oxford Instruments CF 935 continuous flow cryostat. The W-Band *cw*-EPR spectra were recorded on a Bruker Elexsys E600 spectrometer with a 6 T superconducting magnet. With both frequencies,

measurements were collected at temperatures down to 5 K and also at higher temperatures at regular intervals.

Where necessary, baseline corrections were applied using the WinEPR CW-EPR Acquisition & Processing software. For cw-EPR spectra, all samples were lightly crushed and polycrystalline. In order to obtain accurate g-values, the magnetic field was calibrated according to the 'strong pitch' calibration sample with a known g = 2.0028. [5]

Pulsed EPR spectra were recorded using a Bruker E580 spectrometer and an Oxford Instruments cryostat. Samples were dissolved in toluene at a concentration of 0.1 mg ml^{-1} and then frozen in liquid nitrogen prior to mounting. This concentration was chosen such that the dipolar coupling between clusters would be negligible.

For all cw and pulsed EPR experiments, samples were contained in quartz EPR tubes inserted into a sample holder which was screwed into a sample rod.

Superconducting Quantum Interference Device Measurements

Magnetisation measurements were recorded on a Quantum Design MPMS-XL SQUID magnetometer with a 7 T superconducting helium-cooled magnet. All samples were polycrystalline and lightly crushed, and fixed with eicosane. The samples were contained in a gelatin capsule held inside a plastic straw with minimal magnetic susceptibility. The straw was attached to a sample rod with a plastic stopper preventing the sample from unmounting.

The diamagnetic contribution of the gelatine capsule and the eicosane and sample holder was corrected for afterwards, using calibration measurements of the capsule and the eicosane.

Inelastic Neutron Scattering Measurements

Inelastic neutron scattering measurements were performed using the IRIS spectrometer at the ISIS pulsed Neutron and Muon Source at the Rutherford Appleton Laboratory. IRIS is a time-of-flight inverted-geometry crystal analyser capable of high resolution spectroscopy and consists of two parts, a *primary* and *secondary* spectrometer.

In the *primary* spectrometer, the neutron beam transports from the moderator to the sample position along a neutron guide – consisting of carefully aligned nickel-plated glass tubes. At the end of the neutron guide, a nickel-titanium supermirror focuses the beam at the sample. The neutrons pass through two choppers, which control the wavelength range of the neutrons.

In the *secondary* spectrometer there are two large single crystal arrays of pyrolytic graphite and muscovite mica and two ZnS scintillator detector banks containing ^{3}He gas tubes. The analyser bank is cooled to 10 K to reduce background noise.

The polycrystalline powder sample is mounted in a flat plate aluminium can and sealed with a tight indium seal. The cans incorporate holes for heaters and temperature sensors for fine control over temperature. The sample can is oriented at $\pm 45°$ relative to the incident neutron beam, and is loaded into the IRIS beam line from the intermediate shutter control system in the sample environment enclosure. [7]

References

[1] Gerbeleu N. V, Batasnov A. S., Timco G. A., Struchkov Yu. T., Indricham K. M., Popovich G. A., *Patent* 1299116, **1985**

[2] Slageren J. van, Sessoli R., Gatteschi D., Smith A. A., Helliwell M., Winpenny R. E. P., Cornia A., Barra A-L., Jansen A. G. M., Rentschler E., Timco G. A., *Chem. Eur. J.*, **2002**, *8*, 1, 277

[3] Timco G., Faust T., Tuna F.,Winpenny R. E. P., *Chem. Soc. Rev*., **2011**, 40, 3067–3075

[4] Timco G., Carretta S., Troiani F., Tuna F.,Pritchard R. J., Muryn C. A., McInnes E. J. L., Ghirri A., Candini A., Santini P., Amoretti G., Affronte M., Winpenny R. E. P., *Nature Nano*. **2009**, 4, 173

[5] Weil J., Bolton J., *Electron Paramagnetic Resonance: Elementary Theory and Practical Applications*, John Wiley & Sons, Hoboken New Jersey, **2007**, 559

[6] Timco G. A., McInnes E. J. L., Pritchard R G., Tuna F., Winpenny R. E. P., *Angew. Chem. Int. Ed.*, **2008**, *47*, 9681

[7] Adams M. A., Howells W. S., Telling M. T. F., *The IRIS User Guide, 2nd edition* ISIS Facility, Rutherford Appleton Laboratory, **2001**.

[8] Candini A., Lorusso G., Troiani F., Ghirri A., Carretta S., Santini P., Amoretti G., Muryn C., Tuna F., Timco G., et al. *Phys. Rev. Lett.,* **2010**, *104*, 037203

[9] Larsen, F. K.; McInnes, E. J.; El Mkami, H.; Overgaard, J.; Piligkos, S.; Rajaraman, G.; Rentschler, E.; Smith, A. A.; Smith, G. M.; Boote, V.; Jennings, M.;

Timco, G. A.; Winpenny, R. E. *Angewandte Chemie (International ed. in English)* **2003**, *42*, 101.

Chapter III - Electronic Structure of Cr$_7$M Purple Wheels

This chapter covers investigations into the electronic structure of Cr$_7$M purple wheels. The structure of these wheels is presented, as well the theoretical approach used to model the experimental data measured of these wheels. The results from magnetisation, specific heat, INS and EPR studies are shown and the simulations of these experimental data are used to model the exchange interactions within the wheel.

Introduction

Molecular magnets have been proposed to be promising components for probing quantum phenomena at a macroscopic scale.[1,2] These systems are some of the best examples of ensembles of non-interacting quantum objects embedded in a solid state environment.[3] This has led to proposals that molecular magnets could be used in quantum information processing (QIP)[4,5] and in esoteric devices such as quantum simulators.[6] For such applications a full understanding of the low temperature physics of these materials is needed, and such an understanding invariably involves a mathematical description based on a spin Hamiltonian.

Such models are dependent on the symmetry and nuclearity of the system studied. Early work in molecular magnetism often focused on di-metallic complexes where only one parameter − the isotropic exchange interaction, J − was significant in the spin Hamiltonian. This allowed derivation of magneto-structural correlations[7,8] between J and structural parameters, typically an angle at a bridging ligand involved in the super-exchange path. Such correlations contain an implicit assumption that

spin Hamiltonian parameters are transferable between structures, i.e. if the same structural feature is found in two different structures we can use the same magnetic parameter in the two cases.

As molecular magnetism has developed larger less symmetric structures have been studied, and the number of parameters needed in spin Hamiltonians has increased. This brings a new set of problems. Firstly, it creates a conflict between the number of parameters required by an X-ray crystal structure, where often multiple metal centres will lead to multiple exchange paths and single ion coordination environments, and the number of parameters needed to model magnetic data adequately. Often the magnetic data can be modeled with many fewer parameters than could be justified by X-ray structures. Secondly, where there are many parameters there is a much greater chance of correlation between parameters when fitting. Thirdly, the computational resources required increase as more and more parameters are introduced.

We have been studying anti-ferromagnetically coupled heterometallic rings as possible components for QIP [9-11] and because of the interesting physics they display. In the first family of such rings, of general formula [NH$_2$R$_2$][Cr$_7$$MF_8$(O$_2$C^{t}Bu)$_{16}$] (R = a linear alkyl, typically ethyl; M = a divalent ion, e.g. Ni^{II}, Mn^{II}, Zn^{II}, Co^{II}, Cu^{II}), which are green in colour, a regular octagon of metal sites is found with the divalent metal site disordered about the eight sites of the octagon.[12] The specific cases where M = Zn, **1;** Mn, **2;** and Ni, **3** will be of interest as a point of comparison in this chapter, and will form a component of set of dimer systems in a subsequent chapter. Each edge of the octagon is bridged by one fluoride and two pivalates and we can find crystallographic symmetry as high as D$_{4d}$. In such a system we need only consider two isotropic exchange interactions, J_{CrCr} and $J_{Cr M}$ and two sets of single ion

parameters, d_{Cr}, d_M, e_M, and e_{Cr} where d is the axial zero-field splitting and e is the rhombic zero-field splitting. In practice we find that data can require introduction of anisotropic exchange parameters and/or higher order zero-field splitting parameters.[13]

In this chapter I discuss a second series of rings, which are purple in solution and in the solid state. The formula of these rings is $[Cr_7MF_3(Etglu)(O_2C^tBu)_{15}(Phpy)]$, ($H_5Etglu$ = N-ethyl-D-glucamine, Phpy = 4-phenylpyridine). Here we restrict ourselves to the cases where M = Zn, **4**; Mn, **5** and Ni, **6**. Etglu^{5-} is chiral and this chirality is maintained in the metal rings.

Therefore, these rings have eight different edges and are a good test case for examining transferability of parameters between different molecular magnets. To understand these complex systems we have used four distinct experimental techniques: magnetic susceptibility measurements, heat capacity measurements, inelastic neutron scattering (INS) and electron paramagnetic resonance (EPR) spectroscopy. We then describe these systems with a full microscopic spin Hamiltonian.

Results

Structure

*Figure 24 Structure of [Cr$_7$ZnF$_3$(Etglu)(O$_2$C^{t}Bu)$_{15}$(Phpy)] (**4**), where Etglu is N-ethyl-D-glucamine, methyl and phenyl groups have been removed for clarity* [22]

Compounds **4**, **5** and **6** are isostructural (Figure 24). The eight metals are arranged at the corners of an irregular octagon. The internal edges of the octagon are bridged by three fluorides and five alkoxides derived from Etglu[5-]. The divalent site is ordered and bound to two bridging fluorides, three bridging pivalate ligands and a terminal phenylpyridine ligand. The seven Cr[III] sites vary. One site adjacent to the divalent site has an N-donor from Etglu[5-] coordinated to it, one bridging fluoride, one bridging alkoxide and three bridging pivalates. The other site adjacent to the M[II] sites is bound to two fluorides and four oxygens from pivalate. Four of the remaining Cr[III] sites are bound to two alkoxides and four pivalates, while the final site is bound to a single fluoride, a single alkoxide and four pivalates.

Five Cr…Cr edges of the ring are bridged by a single alkoxide and two pivalates, the Cr1-Cr2 edge is bridged by a single fluoride while the two Cr…M edges vary – one bridged by one fluoride and one pivalate the second bridged by one fluoride and two pivalates.

The octagon is therefore irregular. In all three structures the five alkoxide bridged Cr…Cr contacts fall in the range 3.32 to 3.40 Å. The two edges bridged by a fluoride and two pivalates fall in the range 3.40 – 3.44 Å. The Cr-M edge bridged by one fluoride and one pivalate is longer in every case, falling in the range 3.55 to 3.58 Å. Most of the M…M…M angles within the octagon are close to that expected for a regular octagon (135°); the two exceptions are the Cr1-M1-Cr7 angle, which is near 120° in each structure, and the Cr4-Cr5=Cr6 angle, which is around 127° in all compounds. The octametallic ring is not perfectly planar, with a mean deviation from planarity of near 0.3 Å. In each structure Cr7 is the metal furthest out of plane (0.7 Å).

Metal-ligand lengths show expected trends. The bonds to the divalent metal sites fall in the ranges: **4**(Zn) 2.05 – 2.13; **5** (Mn) 2.03 – 2.13; **6** (Ni) 2.00-2.09 Å. The bonds to Cr(III) are generally normal with a few exceptions. The bonds to fluorides bridging to the divalent centre (F1 and F2) are shorter than other Cr-X bonds, falling in the range 1.88 to 1.90 Å. The bonds to the N-donor from Etglu^{5-} are longer, in the range of 2.08 to 2.12 Å. The remaining bonds, to O-donors or F3, average 1.96 ± 0.04 Å.

Bond angles are again normal. Looking at potential super-exchange pathways, the bond angles at the μ-fluorides and μ-alkoxides were examined. All Cr-O-Cr angles fall in a narrow range from 118 to 122°. The single Cr-F-Cr angle is around 124° in each structure. The two M-F-Cr angles in the structure are quite different; the angle

at the fluoride bridging to Cr7 (F1 in Figure 1) is around 131° in all three structures, while the angle at the F bridging to Cr1 (F2 in Figure 1) is around 122° in each case.

The variation in structural parameters between structures is therefore quite small. The Cr…Cr contacts are all quite similar, and there is little change between the Cr-X-Cr bridging angle for fluoride and alkoxide.

Theory

The simulations below use a microscopic Hamiltonian operator:

$$H = \sum_{i=1}^{8} J_{i,i+1}\, s_i \cdot s_{i+1} + \sum_{i=1}^{8} d_i \left[s_{i,z}^2 - \frac{1}{3} s_i(s_i + 1) \right] + \sum_{i=1}^{8} e_i \left(s_{i,x}^2 - s_{i,y}^2 \right)$$

$$+ \sum_{i>j=1}^{N} D_{ij}\left[2 s_{i,z} s_{j,z} - s_{i,x} s_{j,x} - s_{i,y} s_{j,y} \right] + \mu_B \sum_{i=1}^{8} \mathbf{B} \cdot \mathbf{g_i} \cdot \mathbf{s_i}$$

1

where $s_9 \equiv s_1$.

The first term in this equation describes the nearest-neighbour anti-ferromagnetic Heisenberg-Dirac Van Vleck exchange interaction. In our model we use only two exchange interactions: J_{CrCr} describes the exchange interactions between pairs of Cr^{3+} ions and J_{Cr-M} describes the interaction between Cr^{3+} ions and the divalent metal.

The second term describes local crystal-field (zero-field splitting) interactions and the z-axis is chosen to be perpendicular to the mean plane of the ring. This crystal field interaction can be expressed as a sum of an axial term d_i and a rhombic term e_i

We chose as a first model to include only a single d_i and e_i for the Cr^{III} sites and a single d_i and e_i for the divalent site if paramagnetic.

The third term describes the anisotropic exchange, which is largely due to the dipole-dipole intra-cluster interaction D_{ij} evaluated within the point-dipole approximation using the crystallographically derived distances but does not take into account the non-planarity of the rings.

Long range inter-ring interactions are negligible because there are no available paths for super-exchange and also because the inter-cluster dipolar interaction is small due to the small total spin of the cluster in the lowest energy states.

The fourth term is the Zeeman term. Throughout the simulations discussed below we used $g_{Cr} = 1.98$ and $g_{Mn} = 2.00$. For compound **6** we allowed the parameter g_{Ni} to vary to obtain the best simulations. Simulations using this Hamiltonian also include the mixing between different total spin multiplets (S-mixing).

Specific heat measurements have been simulated using the eigenvalues of the Hamiltonian in equation **1**.

$$\frac{C_m}{R} = \frac{\sum_i E_i^2 e^{-\beta E_i} \sum_i e^{-\beta E_i} - \left(\sum_i E_i e^{-\beta E_i}\right)^2}{(\sum_i e^{-\beta E_i})^2}$$

The simulations taken into account the vibrational contribution

$$\frac{C_{vib}}{R} = \frac{243 r T^3}{[\theta_D + \varepsilon T^2]^3}$$

where r is the number of atoms per molecule fitting the Debye temperature with Debye parameters θ_D and ε.

Cr$_7$Zn purple (4)

As Zn^{2+} is diamagnetic this compound is the best starting point as it allows us to determine the Cr^{3+} parameters in the Hamiltonian in equation **1**.
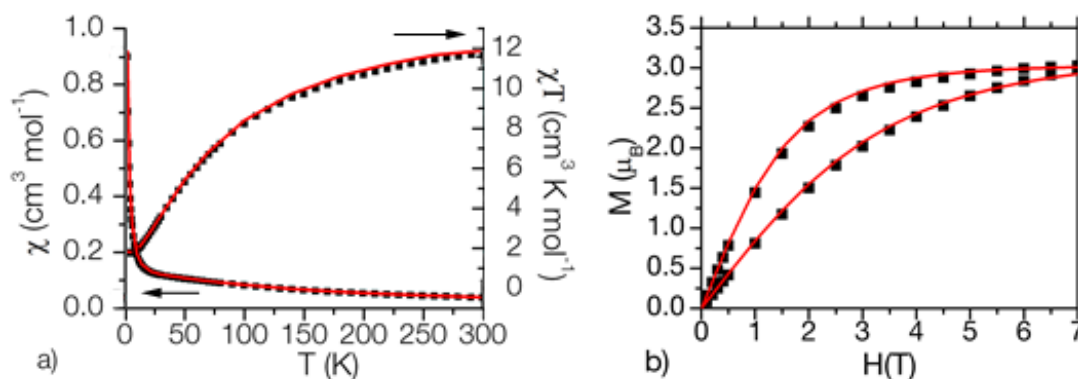
Figure 25 Susceptibility χ and χT (a) of 4 measured at 100 mT from 2 K to 300 K and DC magnetisation (b) of 4 measured at 2 K and 4 K. Black squares are experimental data points and red lines are simulations using parameters in Table 9.

The magnetic susceptibility χ (Figure 25a) increases slowly with decreasing temperature until approximately 23 K, below which χ_m rises rapidly. This is evidence of a non-zero spin ground state. $\chi_m T$ falls smoothly with temperature, showing the predominant interaction between spins is anti-ferromagnetic, and plateaus at 11.66 cm^3 K mol^{-1}. The saturation value of magnetisation at 2 K is 3.0 μ_B, consistent with a ground state spin $|S = 3/2\rangle$.

Simulations of susceptibility and magnetization were performed using the MAGPACK package. Both curves can be reproduced using a single $J_{CrCr} = 20.4$ K (solid red in Figure 25). It is conceivable that the magnetism of compound **4** may be more adequately described by several non-identical Cr-Cr exchange interactions, which might be consistent with the crystal structure, but the data do not justify the inclusion of additional free parameters.
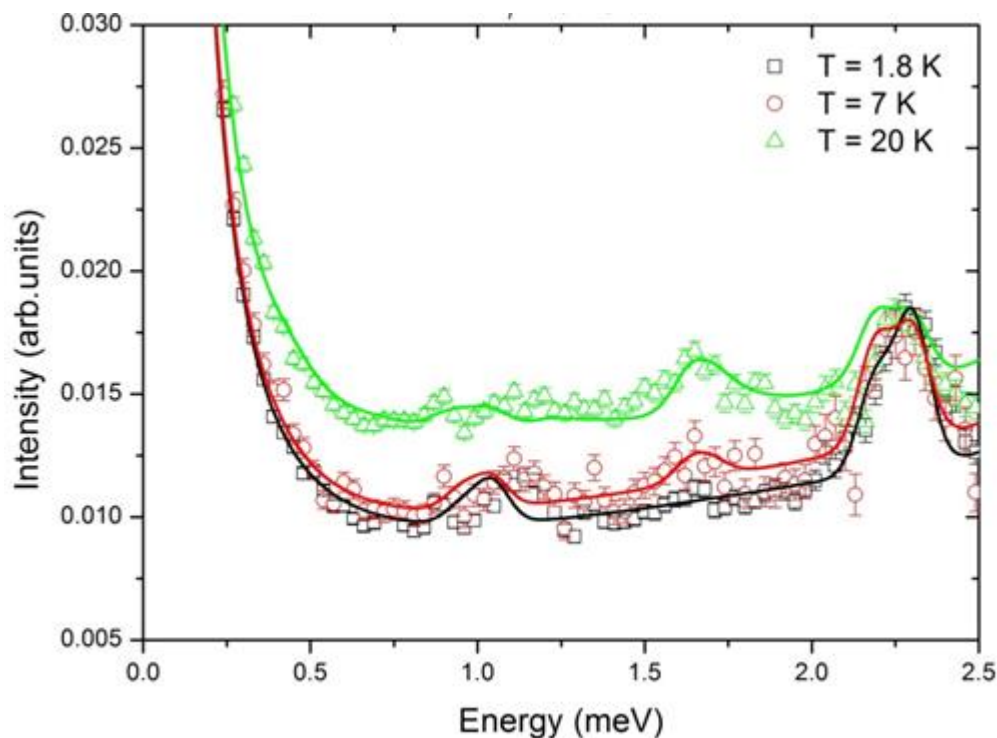
*Figure 26 INS energy spectra for **4** from 0 to 2.5 meV at 1.8 K (black squares), 7 K (red circles) and 20 K (green triangles). Solid lines below show simulations using parameters in Table 9.*

INS spectra provide important information on low lying spin states and a direct determination of the J_{CrCr} exchange interaction. The energy spectra at 1.8 K, 7 K and 20 K contain four transitions (Figure 26).

The simulation of the INS spectra of a powder sample of **4** provides a good determination of the Cr-Cr exchange interaction, and fixes this parameter at J_{CrCr} = 20.4 K, in agreement with the magnetisation and susceptibility data (Figure 25). However it is noticeable that the peaks are broader than in INS studies of the green family of {Cr$_7$M} rings. [13]
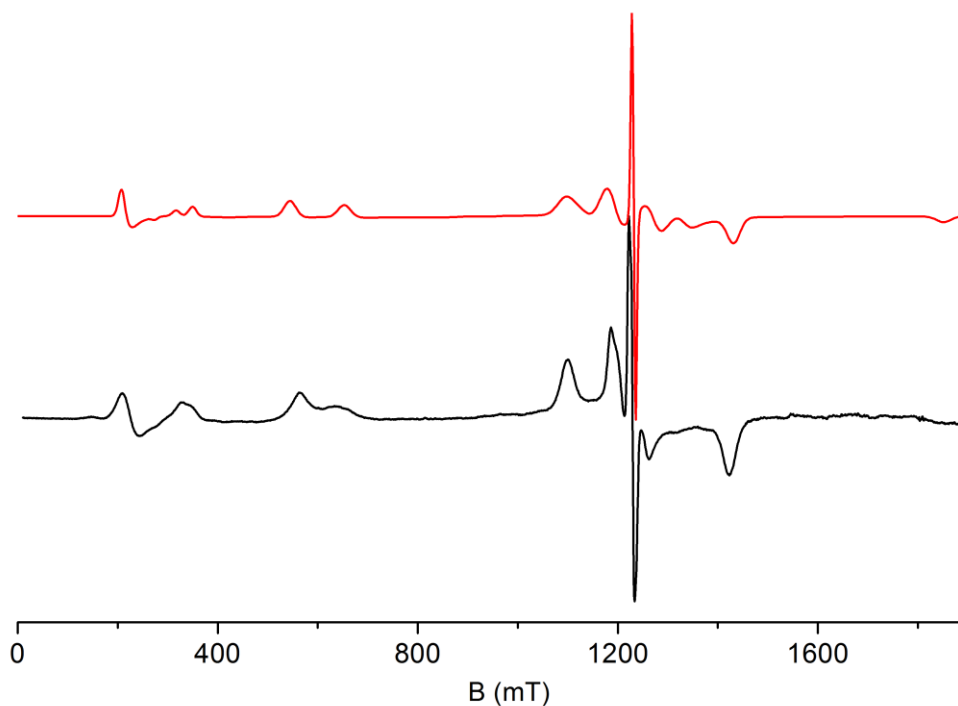
*Figure 27 Q-band (34.1212 GHz) EPR spectrum (black) and simulation using parameters in Table 9 (red) for a powder sample of **4** measured at 5 K.*

EPR spectra of a powder sample of **4** at Q- and W-band at 5 K are shown in Figure 27 and Figure 28. The spectra contain a large number of features, showing contributions from two total spin multiplets. At Q-band there is a clear and sharp resonance at 1243 mT, close to g = 2.00, and broader features through the field range from 200 to 1700 mT are from the $|S = 3/2\rangle$ ground state.
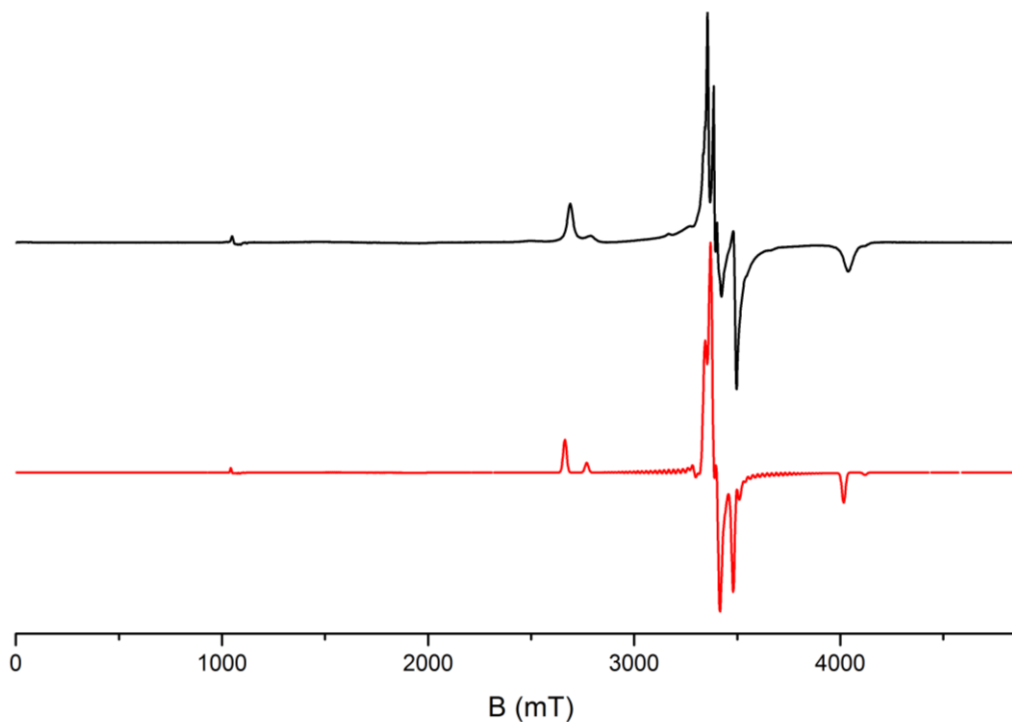
*Figure 28 W-band (94.96804 GHz) EPR spectrum (black) with simulation using parameters in Table 9 (red) for a powder sample of **4** measured at 5 K.*

At W-band, there are sharp features around 3450 mT, smaller features at 4000 mT and 2650 mT and a small peak at 1000 mT from the $|S = 3/2>$ ground state.

Running multiple simulations including progressively higher excited states show that the sharp feature at $g = 2.00$ is due to the $|S = 1/2>$ excited state, with the broader features due to the $|S = 3/2>$ ground state. No resonances from higher excited states are seen. Using J_{CrCr} from INS and magnetic measurements allows determination of $d_{Cr} = -0.27$, $e_{Cr} = -0.09$ K. Repeated simulations have fixed both the sign and magnitude of these parameters.
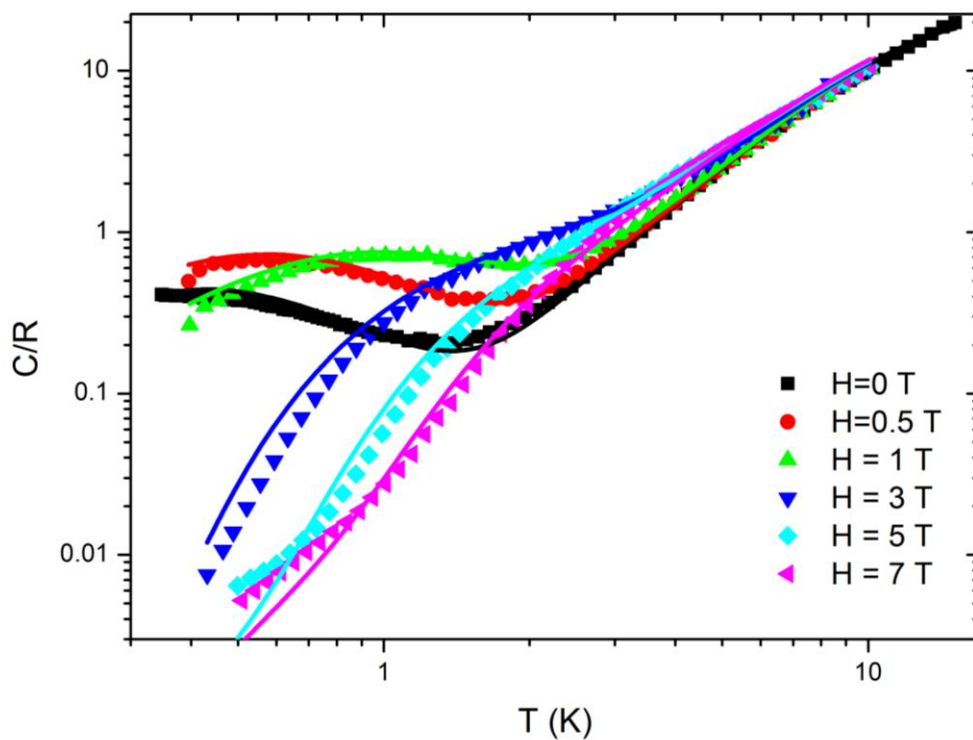
*Figure 29 Specific heat data for **4** where points are experimental data points and solid lines are simulations using parameters in Table 9*

To complete the characterization, the three parameters (J_{CrCr}, d_{Cr} and e_{Cr}) were used to simulate specific heat data. An accurate fit is found (Figure 29), fitting the Debye temperature with $\theta = 145$ K and $\varepsilon = 0.55$ K^{-1}. This is a good confirmation of the parameters found in the fits of the magnetization, the INS and EPR data. These parameters will then be used to model data obtained for compounds **5** and **6**.

Cr$_7$Mn purple (5)

To model the data for **5**, we used the parameters from compound **4** as a starting

point, with additional parameters to account for the paramagnetic manganese site.
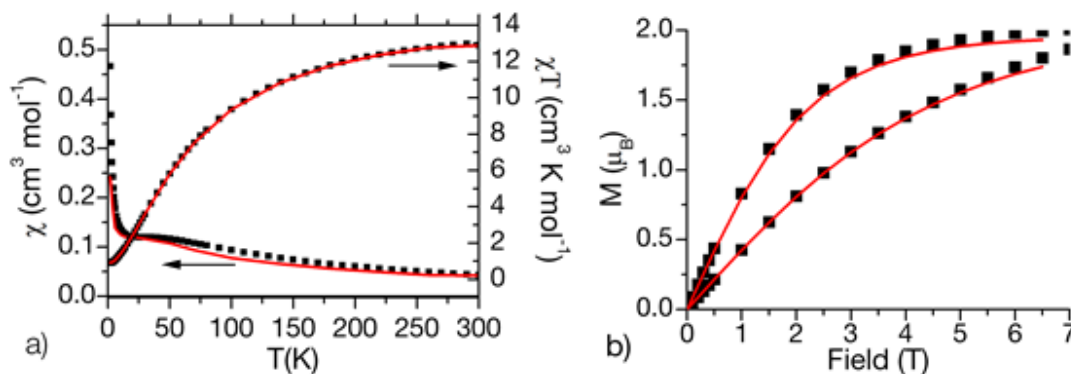
*Figure 30 Susceptibility χ and χT (a) of **5** measured at 100 mT from 2 K to 300 K and DC magnetisation (b) measured at 2 K and 4 K. Black squares are experimental data points and red lines are simulation using parameters in Table 9.*

As with **4**, the magnetic susceptibility χ (Figure 30a) of **5** increases slowly with

decreasing temperature, with a broad maximum around 50 K, until 12 K, below

which χ_m rises rapidly. $\chi_m T$ falls with temperature, showing the interaction between

spins is anti-ferromagnetic. The saturation vaue of magnetisation (Figure 30b) is 2.0

μB, showing there is a ground state spin |$S = 1$>.
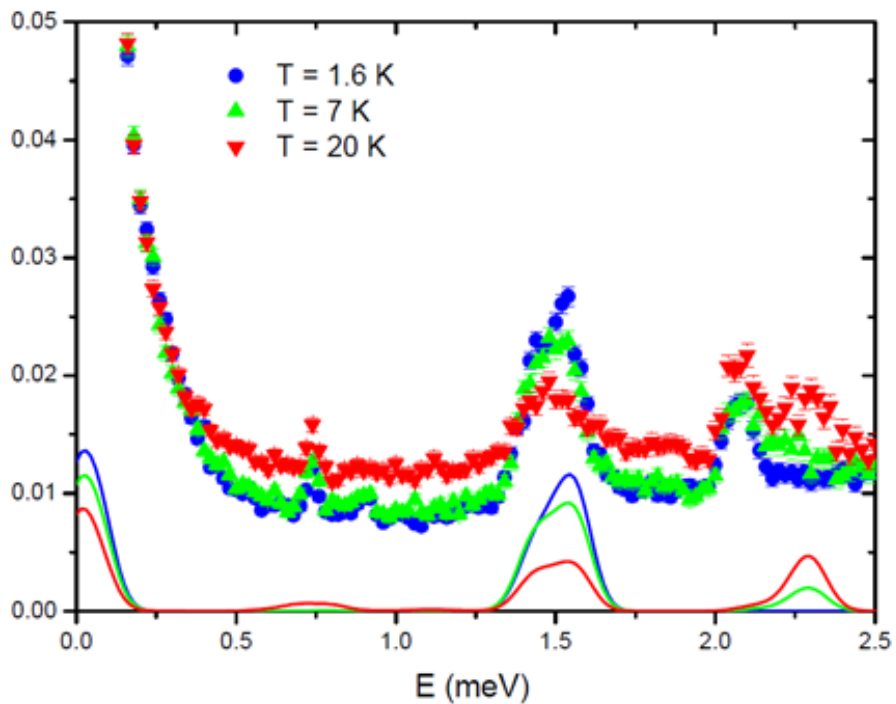
*Figure 31 INS data for **5** from 0 to 2.5 meV at 1.6 K (blue circles), 7 K (green upward-pointing triangles) and 20 K (red downward-pointing triangles). Solid lines below show simulation using parameters in Table 9.*
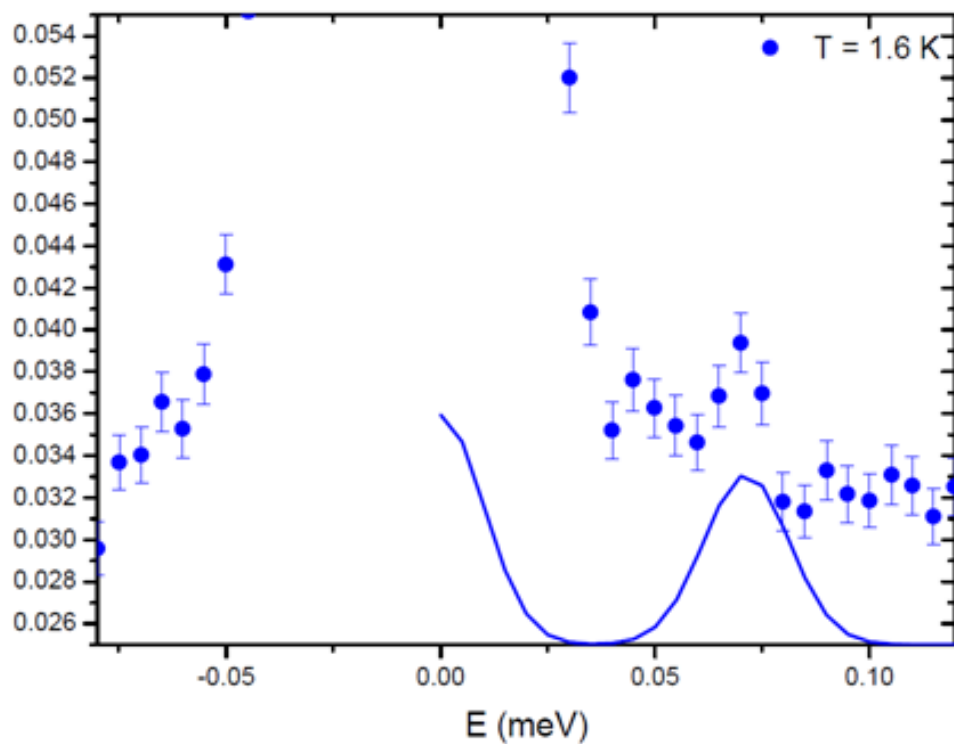
*Figure 32 INS data for **5** from -0.075 to 0.125 meV at 1.6 K. Solid line shows simulation using parameters in Table 9.*

The INS spectra were measured at 1.6, 7.0 and 20 K (Figure 31 and Figure 32).

Four transitions are observed, hot transitions at 2.25 meV and 0.75 meV and cold

transitions at 1.50 meV and 0.075 meV. The simulation began with the same values

as for **4**, and a second exchange parameter J_{Cr-Mn}= 12 K was determined from fitting

the INS and magnetic data.
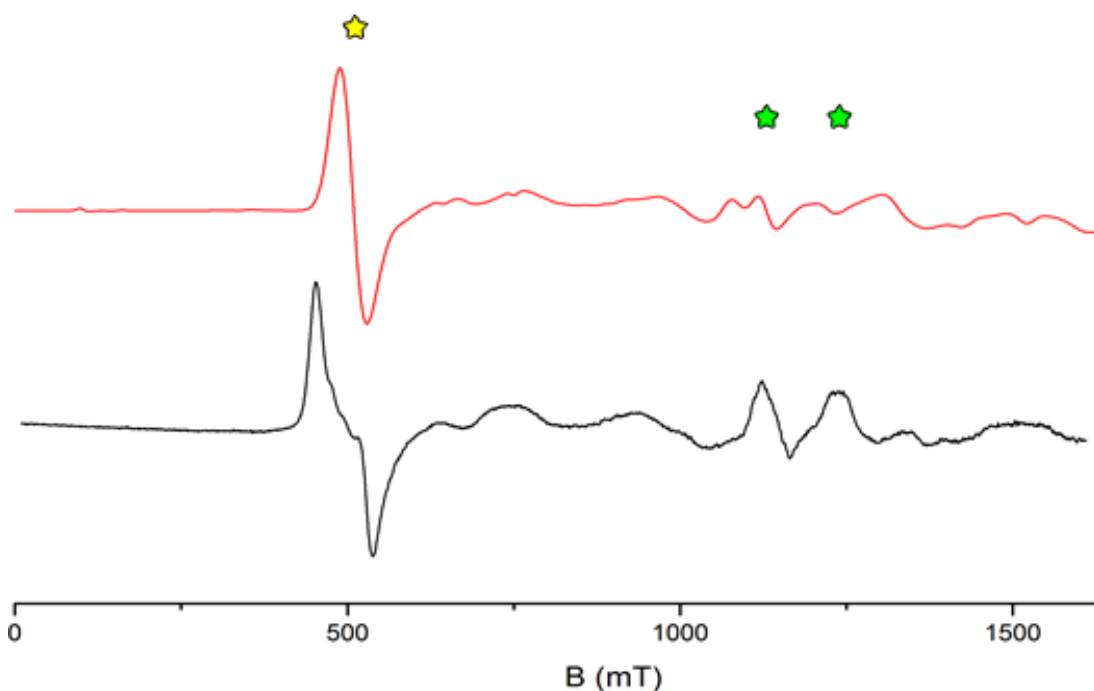
*Figure 33 Q Band EPR spectrum of **5** recorded at 5 K (black) with simulation using parameters in Table 9 (red) with yellow star highlighting contribution from ground state and green stars showing contribution from excited states*

For the determination of the zero-field splitting parameters it is necessary to

investigate the EPR spectra. Polycrystalline measurements were made on **5** at Q- and

W-band measured at 5 K (Figure 33 and Figure 34). These are particularly detailed

spectra with contributions from two different spin multiplets. The Q-band spectrum

(Figure 33) shows features from the $|S = 1\rangle$ ground state (yellow star) and the $|S = 2\rangle$ excited state (green stars).
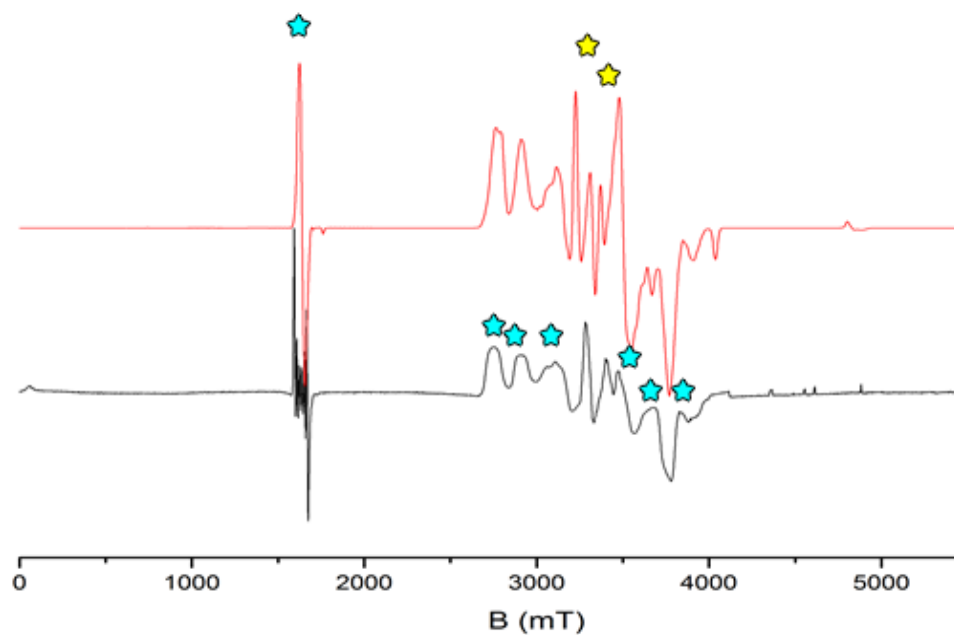
*Figure 34 11 W Band EPR spectrum of **5** recorded at 5 K (black) with simulation using parameters in Table 9 (red) with blue stars highlighting contribution from ground state and yellow stars showing contribution from excited states*

The W-Band spectrum of **5** resolves a hyperfine interaction at 1633 mT and shows features from excited states centered at 3250 mT. This hyperfine splitting has been modelled previously with $A_{iso} = 0.0146$ cm^{-1}. [21]

The simulations of the EPR spectra of **5** use the exchange parameters found from the INS and the Cr zero-field splitting parameters determined from simulations of **4**. Simultaneous simulation of Q- and W-band spectra give $d_{\text{Mn}} = 0.01$ and $e_{\text{Mn}} = 0$ K using an isotropic g-factor g$_{\text{Mn}}$=2.00.
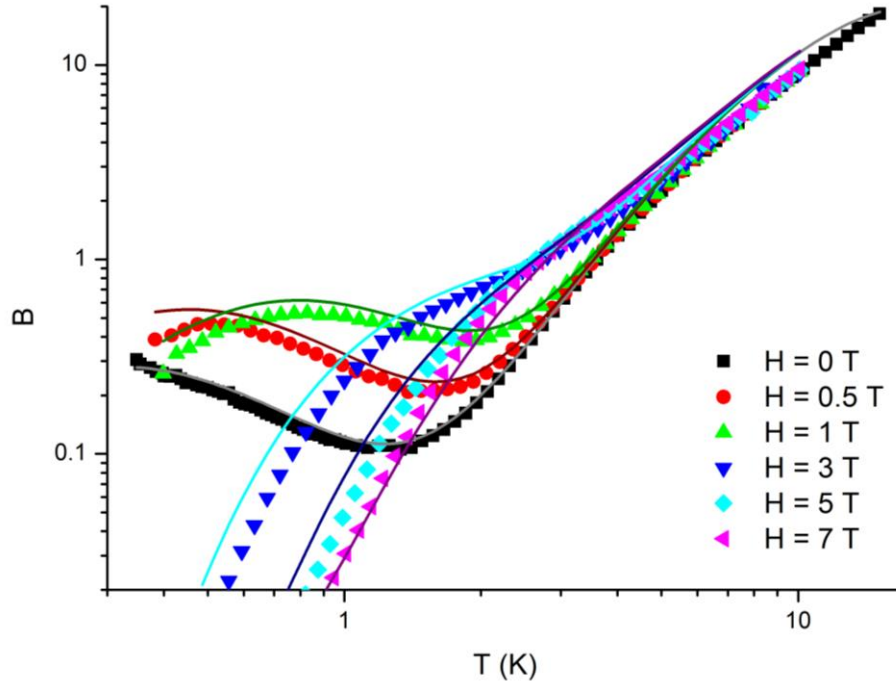
*Figure 35 Specific heat data and fit for **5**, where points represent experimental data
points and solid lines show simulation using parameters in Table 9.*

The exchange interaction parameters and the zero-field parameters have also been
used to simulate specific heat data (Figure 35) with Debye parameters $\theta = 145$ K^3
and $\varepsilon = 0.55$ K. An accurate fit is found using all of the parameters assembled from
the different techniques. This is a good confirmation of the parameters found in the
fits of the magnetization, the INS and EPR data: $J_{CrCr} = 20.4$ K, $J_{CrMn} = 12.0$ K, $d_{Cr} =$
-0.27 K, $e_{Cr} =$ -0.09 K, $d_{Mn} = 0.01$ K, $e_{Mn} = 0$ K.

Cr$_7$Ni purple (6)

As with **5**, to model **6** we begin with the parameters found from **4** as a starting point

and will introduce additional parameters for the nickel site.
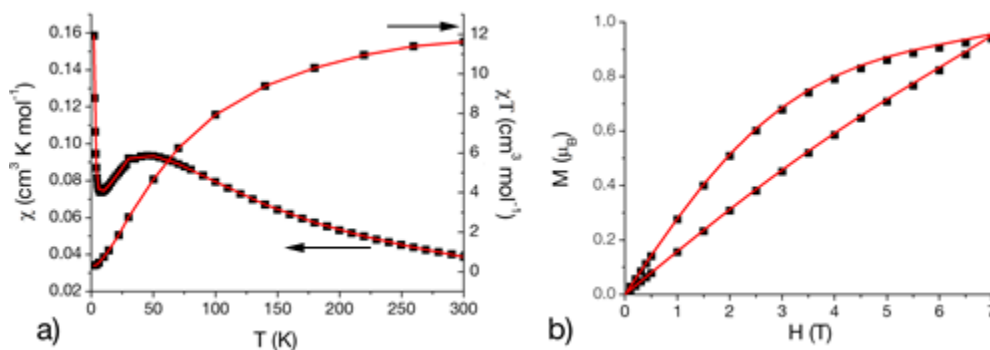
*Figure 36 Susceptibility χ and χT (a) of **6** measured at 100 mT from 2 K to 300 K and DC magnetisation (b) of **6** measured at 2 K and 4 K. Black lines are experimental data and red circles are simulation.*

The magnetic susceptibility χ (Figure 36a) of **6** increases slowly with decreasing

temperature with a well defined maximum at 40 K, then reaching a minimum value

of 12 K before rising rapidly.

The interaction between spins is shown to be anti-ferromagnetic because χT falls

with temperature. The saturation value of magnetization at 2K (Figure 36b) is 1.0 μB

showing the ground state spin |S = ½>. Using the J_{Cr-Cr} found by fitting **4,** the

magnetization data have been fitted using J_{Cr-Ni} = 12.4 K.

The INS spectra were measured at 2.2 and 6 K (Figure 37) showing the cold

transitions at 1.56 and 1.44 meV.
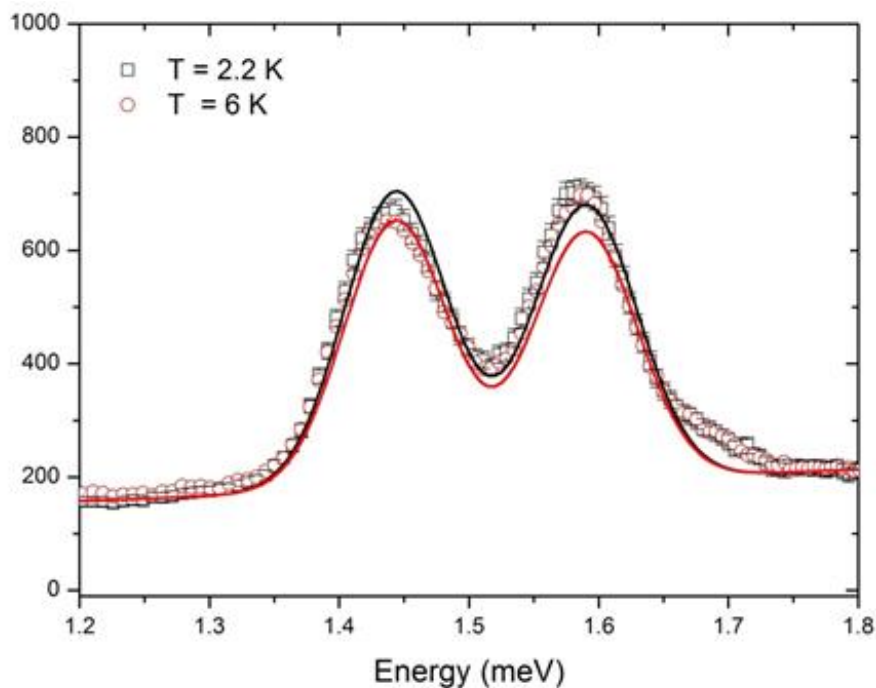
*Figure 37 INS data for **6** from 1.2 meV to 1.8 meV at 2.2 K (black), 6 K (red). Solid
lines below show simulations using parameters from Table 9.*

The cold peaks at 1.56 and 1.44 meV correspond to the $|S = \frac{1}{2}>$ to $|S = 3/2>$
transition. The J_{Cr-Cr} was taken from the fit of **4** and the J_{Cr-Ni} exchange parameter
was found to be $J_{Cr-Ni} = 30$ K.

Polycrystalline measurements of **6** were measured by EPR spectroscopy at Q-band
(Figure 38). The Q-band spectrum is comparatively simple, showing a sharp $|S = \frac{1}{2}>$
feature centered at 1320 mT. The simulation of the spectrum in Figure 38 is sensitive
to the parameter g_{Ni} and was used to precisely fit the anisotropic values $g_x = g_y =$
$2.16, g_z = 2.22$.
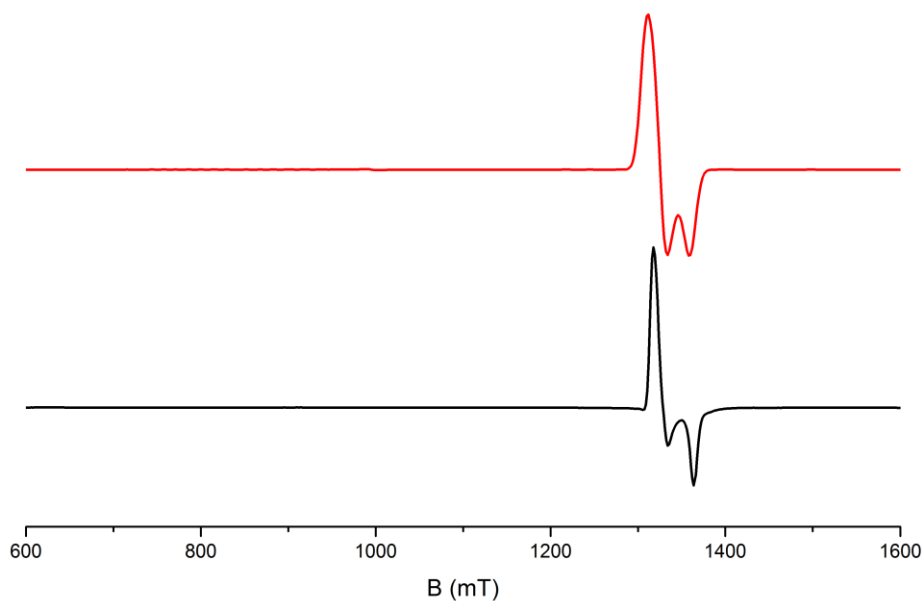
Figure 38   Q-band (34.1587 GHz) EPR spectrum of 6 recorded at 5 K (black) with simulation (red) using parameters in Table 9

The W-band spectrum of **6** in Figure 39 shows a large, sharp peak at 3650 mT and another at 3775 mT with a smaller feature between the two at 3700 mT. Using parameters found in simulations of 4, simultaneous fitting of Q- and W-band spectra give d_{Ni}=-6 K and e_{Ni} = 0 K. The signs of these parameters are determined unambiguously by fitting of the EPR data. The values above are consistent with those determined by means of inelastic neutron scattering and thermodynamic data.[3,14]
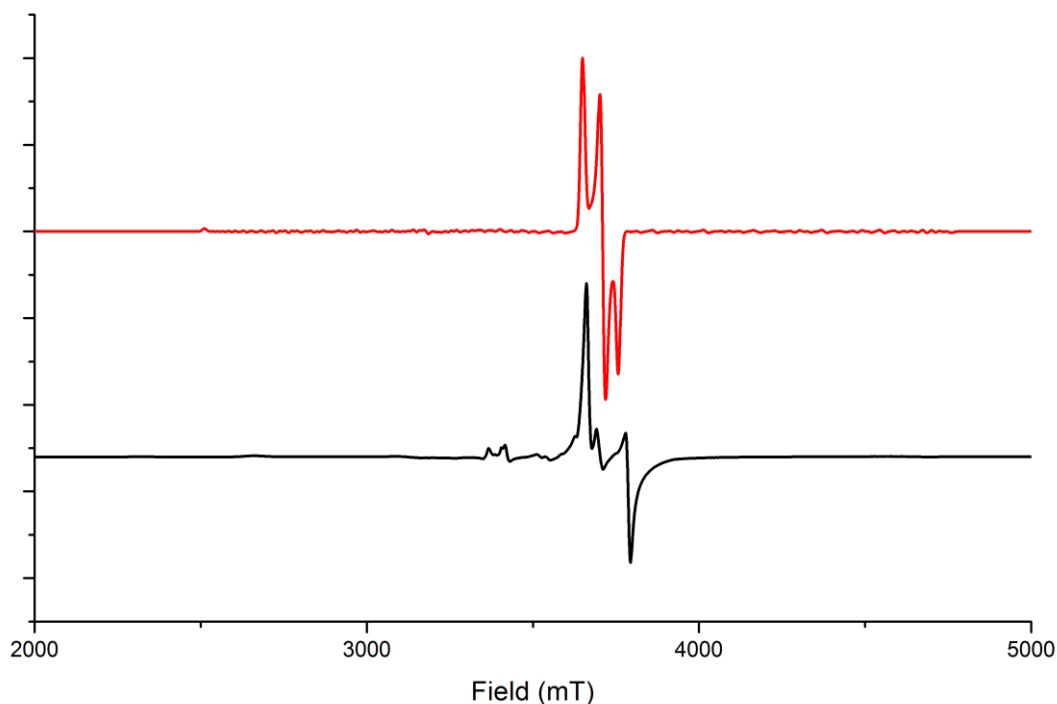
*Figure 39 W-Band (93.90816 GHz) EPR spectrum of **6** recorded at 5 K (black) with simulation (red) using parameters in Table 9*

Analysis

We have probed this series of compounds by a large array of experimental techniques, and have performed a systematic and rigorous process to use all of these techniques to understand the series of compounds within the framework of a microscopic Hamiltonian. The set of parameters is given in Table 9. The J_{Cr-Cr} and J_{Cr-M} exchange parameters are not uniquely determined by fitting of EPR alone, a wide variety of combinations of J_{Cr-Cr} and J_{Cr-M} produce qualitatively accurate simulations. This wide solution space is reduced by simultaneously fitting Q and W Band spectra, but a unique determination of exchange parameters is only found by the inclusion of simulations of INS. By adopting those exchange parameters, precise determination d_{Cr} and e_{Cr} is found by EPR simulations. The simulations of the EPR

spectra also involve broadening parameters to describe the lineshapes. At every point of the field, the EPR energy absorption is described by the absorptive part of susceptibility χ, δ(ω-ΔE). The response is a broadening in energy due to resolution of the instrument. As the convolution of the Dirac delta function is Gaussian, the EPR absorption line is described by a Gaussian lineshape as well. The broadening is described by a variation in this Gaussian. In every spectrum, the excited states may have a different lineshape. For this reason, there is an additional parameter MFσ which is a constant multiplicative factor applied to the sigma for all excited states above the ground state. It is possible that there ought to be several d_{Cr} parameters for the different crystal field environments throughout the wheel. Some information may be obscured due to an averaging over several d_{Cr} parameters and some information about variation in d_{Cr} parameters may be hidden within these broadening parameters. Determination of this requires better resolution of experimental data, and so attribution of physical meaning to the current broadening parameters is merely speculative.

We have found that for **5**, the Cr-Cr exchange interaction is significantly larger than the Cr-Mn exchange interaction. However, for **6** the Cr-Ni exchange interaction is significantly larger than Cr-Cr exchange interaction. The Cr-Cr exchange interaction is assumed a priori to be the same across **4**, **5** and **6**. This assumption proves to reproduce the INS specra. There is clearly a much stronger communication along the J_{Cr-Ni} pathway than the J_{Cr-Mn}. For compound **5**, the zero-field splitting on the Mn site is significantly weaker than the Cr sites, but in compound **6** the Ni site makes the dominant contribution. This detailed understanding of these single wheels is essential for the understanding of the dimers of these wheels and their 'green' counterparts, which will be discussed in the upcoming chapter.

Table 9 Simulation parameters for Cr$_7$M purple wheels

	4	5	6
$J_{Cr\text{-}Cr}$ (K)	20.4	20.4	20.4
$J_{Cr\text{-}M}$ (K)	0	12.0	30.0
d_{Cr} (K)	-0.27	-0.27	-0.27
e_{Cr} (K)	-0.09	-0.09	-0.09
d_M (K)	0	+0.01	-6.0
e_M (K)	0	0	0
g_{Cr}	1.98	1.98	1.98
g_{xx}^M	0	2.00	2.16
g_{yy}^M	0	2.00	2.16
g_{zz}^M	0	2.00	2.22
σ	0.019	0.04	0.008
MFσ	0.23	0.4	2.0

The calculated energy manifolds of compounds **4**, **5** and **6** are shown in Figure 40. These manifolds show that for all three compounds there is a large gap (ca. 15 K) between the ground state and the first excited state, and a gap of a similar magnitude above this. One of the requirements of the physical realization of quantum information processing is a quantum system with two well-separated levels.[15] This separation shows the suitability of these systems as qubits.
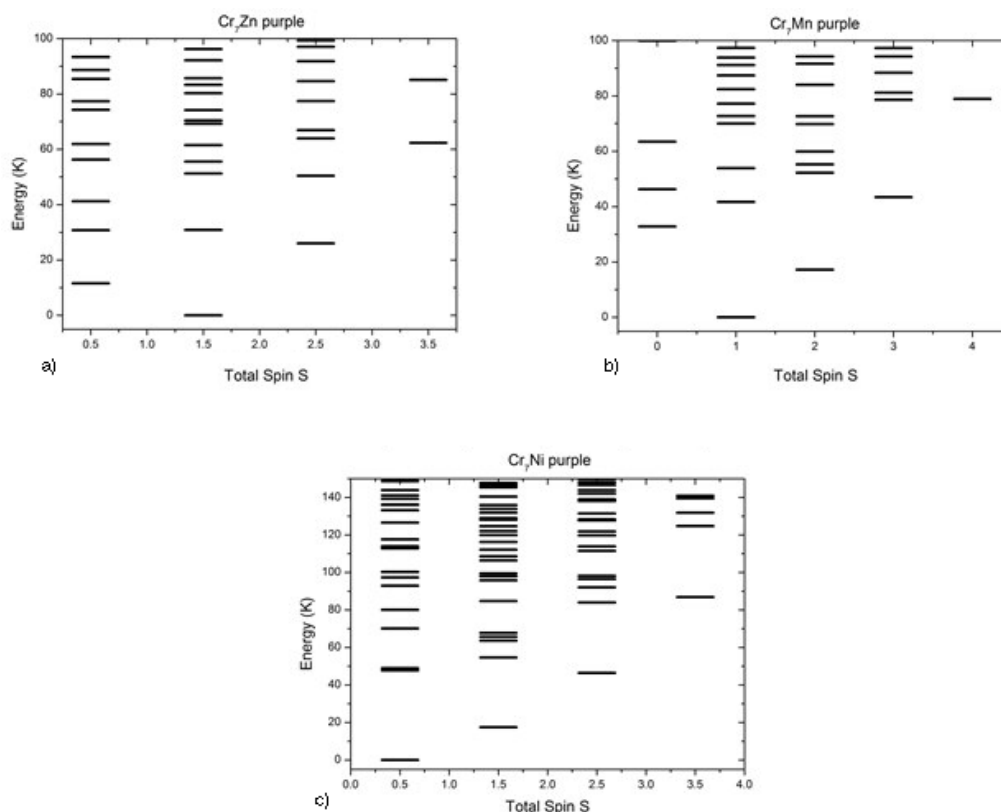
Figure 40 Energy of the lowest spin eigenstates at zero field calculated for Cr$_7M$ purple wheels (a) M = Zn, (b) M = Mn, (c) M = Ni

Comparison with green wheels

A different family of isostructural heterometallic wheels [H$_2$NMe$_2$][Cr$_7M$F$_8$(O$_2$C^{t}Bu)$_{16}$] has been synthesized previously. [12] There is a bridging fluoride ion and two pivalate groups between every metal centre and eight of those pivalate groups occupy an equatorial position in the plane of the wheel. At the centre of the wheel there is a dimethylammonium templating cation. This wheel forms compounds of a green crystalline appearance. For comparison with the purple family, we consider the cases where *M* = Zn **1**, Mn **2**, Ni **3**. These compounds form a nearly perfect planar octagon. As with the purple family, there is an anti-ferromagnetic coupling between metal centres and a non-zero net spin ground state. The green wheels have the same spin states as the lowest spin eigenstates of the purple wheels, though there is a larger gap between the ground and first excited states in the purple rings.

I have modelled this green family using the same microscopic Hamiltonian and the same software as the purple wheels, running numerous simulations over the solution space. The parameters found, shown in Table 10, are consistent with the literature.

Table 10 Simulation parameters for Cr$_7$M green wheels

	1	2	3
$J_{\text{Cr-Cr}}$ (K)	16.9	16.9	16.9
$J_{\text{Cr-M}}$ (K)	0	16.6	19.6
d_{Cr} (K)	-0.35	-0.35	-0.35
e_{Cr} (K)	-0.09	-0.09	-0.09
d_{M} (K)	0	-0.2	-4
e_{M} (K)	0	-0.01	0
g_{Cr}	1.98	1.98	1.98
g_{xx}^{M}	0	2.00	2.27
g_{yy}^{M}	0	2.00	2.27
g_{zz}^{M}	0	2.00	2.25
σ	0.005	0.04	0.013
$MF\sigma$	0.4	0.4	2

The $J_{\text{Cr-Cr}}$ values are larger for the purple wheels than the green wheels, suggesting there is a stronger exchange pathway through bridging alkoxide groups as compared with bridging fluorine ions.

The crystal field splitting for the purple wheels (**4, 5, 6**) is smaller than that of the green wheels (**1, 2, 3**). This is consistent with interpretation of the structure. In the purple compounds **4, 5, 6** there are five bridging alkoxide groups replacing the bridging fluoride ligands in the green compounds **1, 2,** and **3**.

Additionally, in the purple compounds there is a large number of different coordination environments at the metal centres as compared to the green compounds.

Comparison with related clusters

The series of heterometallic Cr$_7$*M* rings is only a part of a larger series of Cr^{3+} based clusters.

The homometallic analogue is the purple variant of the Cr$_8$ wheel, [Cr$_8$F$_4$(Etglu)(O$_2$C^{t}Bu)$_{15}$]. This consists of an octagonal arrangement of Cr^{3+} centres. [23] There is a penta-deprotonated chiral glutamine molecule bound to the metal centre and three bridging flourides with one terminal fluoride at one of the metal centres. This terminal fluoride is in the equivalent position to the terminal 4-phenylpyridine ligand in the heterometallic purple Cr$_7$M. The spin Hamiltonian parameters of this wheel are shown in Table 11. The purple Cr$_8$ wheel has a d_{Cr} value ~30% smaller than in the green Cr$_8$, presumably due to the presence of alkoxide donors in place of fluoride ions. The percentage decrease in d_{Cr} in the purple Cr$_7$*M* wheels is also ~30%. [19]

There also exists a family of finite molecular chains of chromium centres, forming a 'horseshoe' structure. These linear chains of ions are of particular interest for applications as molecular quantum spin wires.

The synthesis begins from the same approach that produces the homometallic [(CrF(O$_2$CCMe$_3$)$_2$)$_8$] wheel and results in a class of open rings. [16,17] Bridging Cr^{3+} ions with carboxylate and fluoride ligands results in AF coupling between spins.

The dimer chain [Et$_2$NH$_2$]$_3$[Cr$_6$F$_{11}$(O$_2$CCMe$_3$)$_{10}$]$_2$ is composed of magnetically isolated facing horseshoes linked by hydrogen-bonding. [16] These horseshoes were structurally isolated by capping the ends with either hexafluoroacetylacetonate (hfac) or acetylacetonate (acac), producing two different isolated chains [(Et$_2$NH$_2$)(Cr$_6$F$_7$)O$_2$C^{t}Bu)$_{10}$(hfac)$_2$] and [(Et$_2$NH$_2$)(Cr$_6$F$_7$(O$_2$C^{t}Bu)$_{10}$ (acac)$_2$)]. [17]

The spin Hamiltonian model for these horseshoe compounds contains two nearest neighbour exchange coupling constants, J_a for ions at the ends of the chain and J_b for ions within the body. The exchange coupling within the body of the horseshoe is almost identical to the J_{CrCr} coupling in the green rings **1**, **2** and **3**, though the coupling at the ends of the horseshoe is much weaker.

Table 11 Spin Hamiltonian parameters of selected Cr^{3+} clusters

	{Cr$_6$}$_2$ [18]	{Cr$_6$}(hfac)[17]	{Cr$_6$}(acac)[17]	{Cr$_8$} [19]
J_a (K)	12.6	17.3	16.3	17.0
J_b (K)	17.0	17.0	17.0	17.0
d_{Cr} (K)	-0.33	-0.52	-0.52	-0.45
e_{Cr} (K)	-0.059	-0.082	-0.082	-0.046

The d_{Cr} parameter for the Cr$_6$ horseshoes includes anisotropic dipolar interactions and may also be an average of two different axial anisotropy parameters with differing principal directions. For this reason the Cr$_6$ have much greater d_{Cr} in comparison to the **1**, **2** and **3**.

Two homometallic Cr$_9$ rings have been synthesized both showing strong antiferromagnetic interaction. [20]

The first of these rings [^{i}Pr$_2$NH$_2$][Cr$_9$F$_{10}$(O$_2$C^{t}Bu)$_{18}$] has a S = 3/2 spin ground state and a calculated d_{Cr} = -0.34 K. This is almost identical to the d_{cr} found for the series of Cr$_7$M green wheels **1, 2,** and **3**. This compound has been studied with a spin Hamiltonian using three different exchange coupling constants, one for the coupling between chromium ions not in the unique edge, one for the coupling on the edge bridged by a pivalate and a fluoride and one for the coupling between the chromium ions on the unique edge and its nearest neighbour. This model is based on studies on the Cr$_7$ horseshoe. [17] The exchange constants reported are significantly smaller than

those found for the either the series of green wheels **1**, **2**, **3** or the purple wheels **4**, **5**, **6**.

The second of these rings [^{i}Pr$_2$NH$_2$][Cr$_9$F$_{11}$(O$_2$C^{t}Bu)$_{17}$] has a S=1/2 ground state and S = 3/2 excited state with a calculated d_{Cr} = -0.44 K. This is much greater than the d_{Cr} found in either green series.

The heterometallic (NiCr$_6$)$_2$Zn segment has also been created by the inclusion of Ni^{2+} at the end of Cr$_6$ chain attached through Zn^{2+}. These S-shaped clusters are collections of identical spin segments. Cr$_8M$, where M = Ni,Cd, are also heterometicallic open rings composed of an even number of spins. [19]

This comparison of spin Hamiltonian parameters contextualises the results of the investigations into the purple Cr$_7M$ wheels in the wider context of related Cr-based clusters.

Conclusion

Previous work [21] on the green and purple heterometallic rings has operated under the strong exchange limit. This model assumes effective total spin states are isolated with no mixing between states and the resultant Hilbert space is tiny and rapidly diagonalisable. This model is most appropriate for systems where the magnetic properties are dominated by one large spin ground state and effects of higher states can be considered as small perturbations. For the simulation of EPR spectra for this series of purple wheel compounds, the strong exchange limit is decidedly inappropriate because of the contribution of several spin states and the effects of s-mixing. The microscopic spin Hamiltonian is the essential method to characterize these systems, although it may appear that these systems are under-parameterised in order to accommodate this microscopic approach.

From the structural information of the Cr_7M compound (Figure 24) it could be inferred that there ought to be eight non-equal exchange parameters J, one for each pathway between metal centres. To be consistent, this model also would assume there to be eight zero-field splitting parameters each with a rhombic component. Simulating any experimental data under this sophisticated model would be extremely computationally expensive due to the number of exchange parameters involved and the resulting size of the Hilbert space.

A more nuanced model would be to attribute exchange parameters to the bridging arrangement: one J_{Cr-Cr} corresponding to the bridge involving a fluoride and two carboxylates, another J_{Cr-Cr} for the alkoxide and two carboxylates, a J_{Cr-M} corresponding to the bridge for one fluoride and two carboxylates and a another J_{Cr-M} for the fluoride and one carboxylate. This is model is computationally feasible, but still involves the fitting of a large number of free parameters. However, this model operates on the underlying assumption that structural information is sufficient for the deduction of exchange parameters for modeling magnetic data.

A significant result from our work is that this assumption is not necessary. Our model begins with the experimental data and uses only the fewest number of parameters required to model these experimental data. This process does not require the assumption that there is a necessary link between structural and magnetic information, although nor does it preclude it as a possibility. The same conclusion is found in the discussion of the correlation of structure and magnetic behavior of Cr_6 and Cr_7 horseshoes. [18]

We have shown that with only two exchange parameters, one J_{Cr-Cr} and one J_{Cr-M}, we can accurately model bulk magnetization, neutron scattering, EPR at multiple frequencies and specific heat of highly asymmetric systems.

Further refinements to the model could possibly be made with the introduction of another non-equal J$_{Cr-Cr}$ parameter. The INS spectrum of **(4)** in Figure 26 contains one peak that is not precisely simulated with our current model. The relative intensity of peaks in the Q-Band simulation of **6** in Figure 38 is not accurate and the averaging out of the small sharp feature in the W-Band spectrum of **6** in Figure 39 may also be due to the averaging of J$_{Cr-Cr}$ parameters.

However, accurate determination of an additional exchange parameter must be justified by greater resolution of spectroscopic data. We have shown that it is not necessary to build theoretical models of Cr$_7M$ wheels from arguments of magneto-structural correlation alone and that spin Hamiltonian parameters need only be introduced when experimental data require it.

This same approach will be used to model the dimer systems of Cr$_7M$ purple − Cr$_7M$ green dimers in Chapter V. The model for the dimers uses all of the parameters found for the single wheels, in Table 9 and Table 10, and also introduces a single additional exchange parameter to describe the interaction between the wheels.

References

[1] Gatteschi, D.; Sessoli, R.; Villain, J. *Molecular Nanomagnets*; OUP Oxford, 2006

[2] Leuenberger, M. N.; Loss, D. *Nature* **2001**, *410*, 789

[3] Carretta, S.; Santini, P.; Amoretti, G.; Affronte, M.; Ghirri, A.; Sheikin, I.; Piligkos, S.; Timco, G. A.; Winpenny, R. E. P. *Phys. Rev. B* **2005**, *72*, 060403.

[4] Winpenny, R. E. P. *Angew. Chem. Int. Ed.* **2008**, *47*, 7992.

[5] Meier, F.; Levy, J.; Loss, D. *Phys. Rev. Lett.* **2003**, *90*, 047901.

[6] Santini, P.; Carretta, S.; Troiani, F.; Amoretti, G. *Phys. Rev. Lett.* **2011**, *107*, 230502.

[7] Bleaney, B. *Rev. Mod. Phys.* **1953**, *25*, 161.

[8] van Niekerk, J. N.; Schoening, F. R. L.; Talbot, J. H. *Acta Crystallogr.* **1953**, *6*, 720.

[9] Timco, G. A.; McInnes, E. J. L.; Winpenny, R. E. P. *Chem. Soc. Rev.* **2013**, *42*, 1796.

[10] Wedge, C. J.; Timco, G. A.; Spielberg, E. T.; George, R. E.; Tuna, F.; Rigby, S.; McInnes, E. J. L.; Winpenny, R. E. P.; Blundell, S. J.; Ardavan, A. *Phys. Rev. Lett.* **2012**, *108*, 107204.

[11] Amiri, H.; Lascialfari, A.; Furukawa, Y.; Borsa, F.; Timco, G. A.; Winpenny, R. E. P. *Phys. Rev. B* **2010**, *82*, 144421.

[12] Larsen, F. K.; McInnes, E. J. L.; El Mkami, H.; Overgaard, J.; Piligkos, S.; Rajaraman, G.; Rentschler, E.; Smith, A. A.; Smith, G. M.; Boote, V.; Jennings, M.; Timco, G. A.; Winpenny, R. E. P. *Angew. Chem. Int. Ed.* **2003**, *42*, 101.

[13] Caciuffo, R.; Guidi, T.; Amoretti, G.; Carretta, S.; Liviotti, E.; Santini, P.; Mondelli, C.; Timco, G. A.; Muryn, C. A.; Winpenny, R. E. P. *Phys. Rev. B* **2005**, *71*, 174407.

[14] Carretta, S.; Santini, P.; Amoretti, G.; Guidi, T.; Copley, J. R. D.; Qiu, Y.; Caciuffo, R.; Timco, G. A.; Winpenny, R. E. P. *Phys. Rev. Lett.* **2007**, *98*, 167401.

[15] DiVincenzo, D. P. *Fortschr. Phys.* **2000**, *48*, 771.

[16] Larsen, F. K.; Overgaard, J.; Parsons, S.; Rentschler, E.; Smith, A. A.; Timco, G. A.; Winpenny, R. E. P. *Angew. Chem. Int. Ed.* **2003**, *42*, 5978.

[17] Baker, M. L.; Bianchi, A.; Carretta, S.; Collison, D.; Docherty, R. J.; McInnes, E. J. L.; McRobbie, A.; Muryn, C. A.; Mutka, H.; Piligkos, S.; Rancan, M.; Santini, P.; Timco, G. A.; Tregenna-Piggott, P. L. W.; Tuna, F.; Gudel, H. U.; Winpenny, R. E. P. *Dalton Trans.* **2011**, *40*, 2725.

[18] Ochsenbein, S. T.; Tuna, F.; Rancan, M.; Davies, R. S. G.; Muryn, C. A.; Waldmann, O.; Bircher, R.; Sieber, A.; Carver, G.; Mutka, H.; Fernandez-Alonso, F.; Podlesnyak, A.; Engelhardt, L. P.; Timco, G. A.; Güdel, H. U.; Winpenny, R. E. P. *Chem. Eur. J.* **2008**, *14*, 5144.

[19] Carretta, S.; van Slageren, J.; Guidi, T.; Liviotti, E.; Mondelli, C.; Rovai, D.; Cornia, A.; Dearden, A. L.; Carsughi, F.; Affronte, M.; Frost, C. D.; Winpenny, R. E. P.; Gatteschi, D.; Amoretti, G.; Caciuffo, R. *Phys. Rev. B.* **2003**, *67*, 094405.

[20] Baker, M. L.; Timco, G. A.; Piligkos, S.; Mathieson, J. S.; Mutka, H.; Tuna, F.; Kozłowski, P.; Antkowiak, M.; Guidi, T.; Gupta, T.; Rath, H.; Woolfson, R. J.; Kamieniarz, G.; Pritchard, R. G.; Weihe, H.; Cronin, L.; Rajaraman, G.; Collison, D.; McInnes, E. J. L.; Winpenny, R. E. P. *Proc. Natl. Acad. Sci.* **2012**, *109*, 19113.

[21] Docherty, R, J.; *EPR Spectroscopy of Antiferromagnetically-Coupled Cr^{3+} Molecular Wheels*, Thesis submitted to University of Manchester, 2011

[22] Timco, G. A.; McInnes, E. J. L.; Pritchard, R G.; Tuna, F.; Winpenny, R. E. P. *Angew. Chem. Int. Ed.*, **2008**, *47*, 9681

[23] Gerbeleu, N. V.; Batasnov, A. S.; Timco, G. A.; Struchkov, Yu. T.; Indricham, K. M.; Popovich, G. A.; *Pat. SU*, 1299116, **1985**

Chapter IV – Pulsed EPR of Purple Cr$_7$M rings

In this chapter, the relaxation times of Cr$_7$Zn (**4**) and Cr$_7$Ni (**6**) were measured from pulsed EPR experiments. The purpose behind the work presented in this chapter was to ascertain whether the purple Cr$_7$M rings might have unexpectedly lengthy electron spin relaxation times as found previously for their green counterparts. This is a preliminary study. This chapter outlines the pulse sequences used, the measurements taken and the fits to exponential functions to obtain values for the relaxation times T_1 and T_2. These quantities are important for determining the viability of these compounds for quantum information processing.

Introduction

The DiVicenzo criteria for the physical implementation of Quantum Information Processing require that we have long enough coherence times to exploit uniquely quantum properties of the system. [1] However, the coherence time cannot be too long or else the system will behave just like a classical system. It is for this reason that the behaviour of the magnetisation of the system is important for understanding its applicability for quantum information processing.

The net magnetisation of the spins of a sample can be affected by the application of certain oscillating microwave pulses. Over time, the magnetisation will return to its thermal equilibrium state and this process is known as *relaxation*. There are two mechanisms via which relaxation occurs, characterised by two relaxation times T_1 and T_2. The components of the magnetisation decay exponentially with these relaxation times. [2]

$$\frac{dM_{x,y}}{dt} = -\frac{M_{x,y}}{T_2} \qquad\qquad \textbf{1}$$

$$\frac{dM_z}{dt} = \frac{M_0 - M_z}{T_1} \qquad\qquad \textbf{2}$$

where M_0 is the equilibrium value of the magnetisation, M_z is the longitudinal component and $M_{x,y}$ is the transverse component of the magnetisation.

The two relaxation times are fundamental properties for the encoding of quantum information. The *spin-lattice* relaxation time T_1 measures the rate of energy transfer from the spin system to its neighbouring molecules and corresponds to the lifetime of a classical bit. The *spin-spin* relaxation (or *phase memory*) time T_2 measures the rate at which the ensemble of spins dephase from one another and corresponds to the time over which a qubit can reliably store information. [2]

The concepts of relaxation and decoherence are not only central to quantum information processing, but also our conceptual understanding of quantum mechanics and proposed fundamental models of physics that extend beyond it. [3]

The relaxation times are determined by pulsed EPR, the application of short microwave pulses that manipulate the magnetisation of a sample and then the resulting behaviour of the spins generates a response.

Spin echo

When an electron spin is in a magnetic field, it experiences a torque and causes the magnetic moment to precesses about the magnetic field vector with a specific angular frequency. This angular frequency is the *Larmor frequency* ω_L, related to field by

$$\omega_L = -\gamma B_0 \qquad\qquad \textbf{3}$$

where γ is the gyromagnetic ratio and B_0 is the magnitude of the external magnetic field. With a large assembly of spins, each spin will align either parallel or antiparallel to the field. The parallel state is energetically favourable and so there will be a net magnetisation vector in the direction of the magnetic field.

An additional magnetic field B_1 is required to perform a pulsed EPR experiment. The detection coils are in the x-y plane, so only transverse magnetisation produces a signal. A pulsed EPR experiment manipulates the magnetisation by B$_1$ with specific *tip angles*.
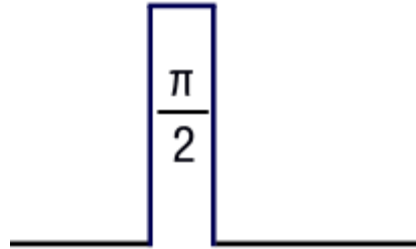
Figure 40 $\pi/2$ pulse that rotates the magnetisation about 90 degrees.

A $\frac{\pi}{2}$ pulse, shown in Figure 40, tips the magnetisation by 90 degrees into the x-y plane. This reduces the population difference the antiparallel and parallel states to zero, and is known as a saturating pulse. After tipping, the spins will establish phase coherence but due to interactions between the spins and their surroundings, the traverse magnetisation decays away and returns to equilibrium. The magnetisation rotates at the Larmor frequency, in equation **3**, which generates a signal. This signal is known as a *Free Induction Decay.* [2]
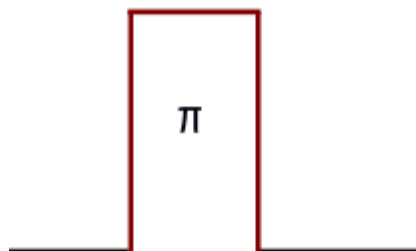
Figure 41 A π pulse that rotates the magnetisation about 180 degrees.

A π pulse, shown in Figure 41, tips the magnetisation by 180 degrees. This swaps the populations of the parallel and antiparallel states.

Due to variations in the local field strength at different parts of the sample, the precession of some spins will slow in comparison to other spins. As a result, the total magnetisation vector will decay away. By applying a π pulse, the slower spins move ahead and the faster spins move behind.

Eventually the faster precessing spins will catch up as the slower spins drift backwards, and as the spins refocus then a *spin echo* is observed.

The spin echo was discovered by Erwin Hahn working at the University of Illinois in 1950 [1] and has since become one of the most powerful building blocks of pulsed EPR. The spin echo experiment begins with applying a $\frac{\pi}{2}$ pulse and waiting for the magnetisation to decay away, and then applying a π pulse and waiting for a further period of time for an echo. These two periods of time are designated as τ and the full pulse sequence for the spin echo experiment is shown in Figure 42.
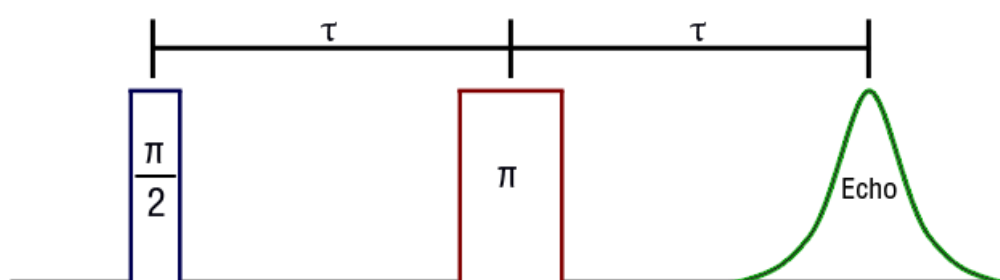
Figure 42 Pulse sequence for a spin echo experiment

The spin echo experiment is used to measure the spin-spin relaxation times, varying this time τ and recording the size of the echo. This shows the decoherence that is not refocused by the π pulse, and results in an exponential decay which is characterised

by the T_2 time. This is known as the *spin-spin* relaxation time, or *transverse* relaxation time.
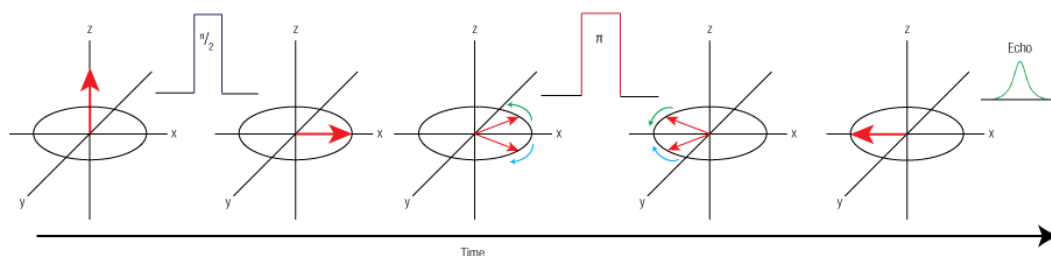
Figure 43 The motion of spins during a spin echo experiment, illustrated in a rotating frame of reference. The red arrows represent the magnetisation, the blue and green arrows represent the different rates of precession.

This phenomenon is called spin-spin relaxation because it involves an exchange of energy between the spins, the process by which the spins become out of step with each other and cause irreversible loss of magnetisation that cannot be recovered by the spin echo experiment. It is also called transverse relaxation because it leads to a decay of that transverse magnetisation precessing in the spin echo experiment. The motion of these spins is shown in Figure 43.

The decay of the magnetisation via this process is given in equation **1** and integrating with respect to *t* gives us

$$M_{x,y} = M_0 e^{-\frac{t}{T_2}}$$ **4**

where M_0 is the equilibrium value of the magnetisation. Fitting the measurement of the echo to an exponential decay function allows us to determine a value for T_2.

Inversion Recovery

There is a separate mechanism for relaxation, and this is the *spin-lattice* relaxation time quantified by T_1. This measures the rate of energy transfer from the spin system to its neighbouring molecules. [2]

The T_1 relaxation is known as the *spin-lattice* relaxation time, or *longitudinal* relaxation. This is the process where nuclei come to thermal equilibrium in a magnetic field and the direction of the magnetisation is along the longitudinal component of the magnetic field. T_1 is an exponential process that restores the Boltzmann equilibrium.

The standard method for measuring T_1 is by *inversion recovery*. A π pulse inverts the magnetisation along the z axis, and the spin-lattice relaxation causes M_z to vary from $-M_0$ through to M_0 over a time period τ. After a $\frac{\pi}{2}$ pulse, the Free Induction Decay is recorded. By varying this value of τ, we can calculate T_1.
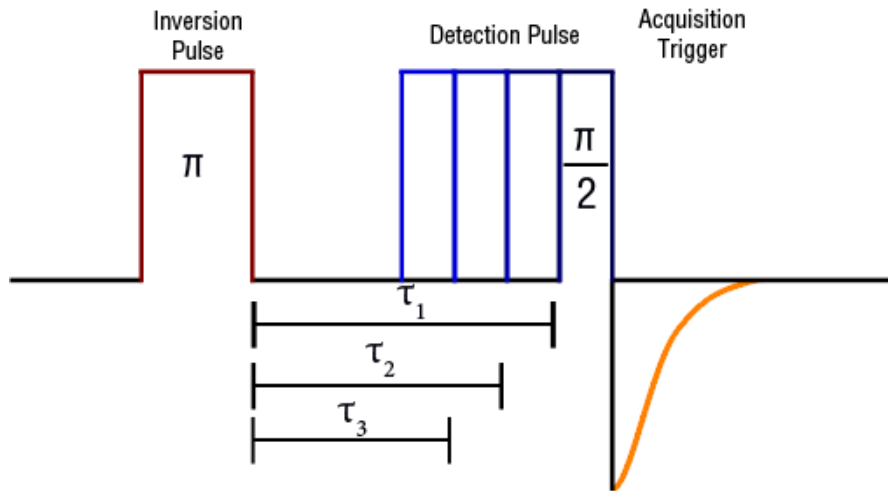
Figure 44 Pulse sequence of inversion recovery experiments, with varying time constants τ_1, τ_2 and τ_3 between the inversion pulse and detection pulse

The decay of the magnetisation is given by equation **2** and integrating this equation with respect to *t* gives the longitudinal component of the magnetisation

$$M_z = M_0 \left[1 - 2\, e^{-\frac{t}{T_1}} \right]$$

5

where M_0 is the equilibrium value of the magnetisation. The spin-lattice relaxation time T_1 can be found by fitting the magnetisation curve to equation **5**.

The motion of spins during an inversion recovery experiment is in Figure 45, showing the effect of varying the amount of time between the inversion pulse and the detection pulse.
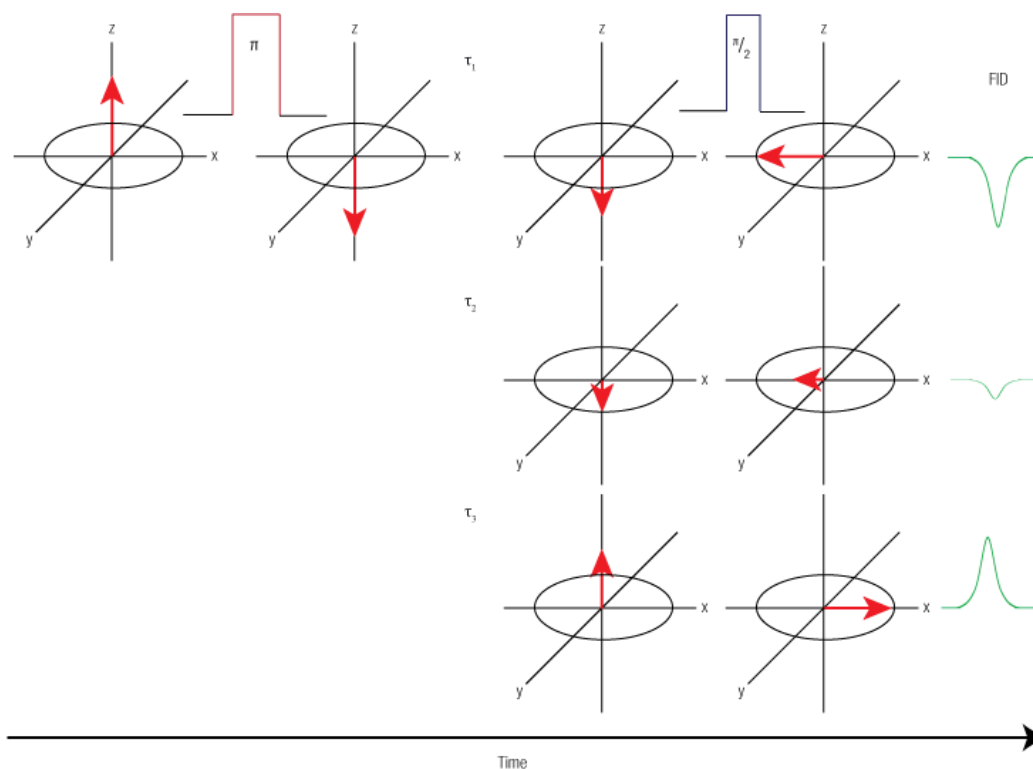
Figure 45 The motion of spins during an inversion recovery experiment, for different values of the time constant τ where $\tau_1 < \tau_2 < \tau_3$. The red arrow represents the average magnetic moment of a group of spins. This arrow is flipped 180 degrees by a π pulse, and then some amount of time τ passes before a $\frac{\pi}{2}$ pulse flips the arrow 90 degrees and an FID is recorded.

Experimental considerations

All samples were diluted in toluene to a concentration such that the dipolar interactions between individual molecules did not contribute to dephasing, the concentration chosen from literature studies on similar compounds. [4]

Cr$_7$Zn purple (4)

Compound **4** was measured on a pulsed Q Band (33.6161 GHz) spectrometer at 20 mW. The sample was dissolved in toluene at a concentration of 0.1 mg ml^{-1}.
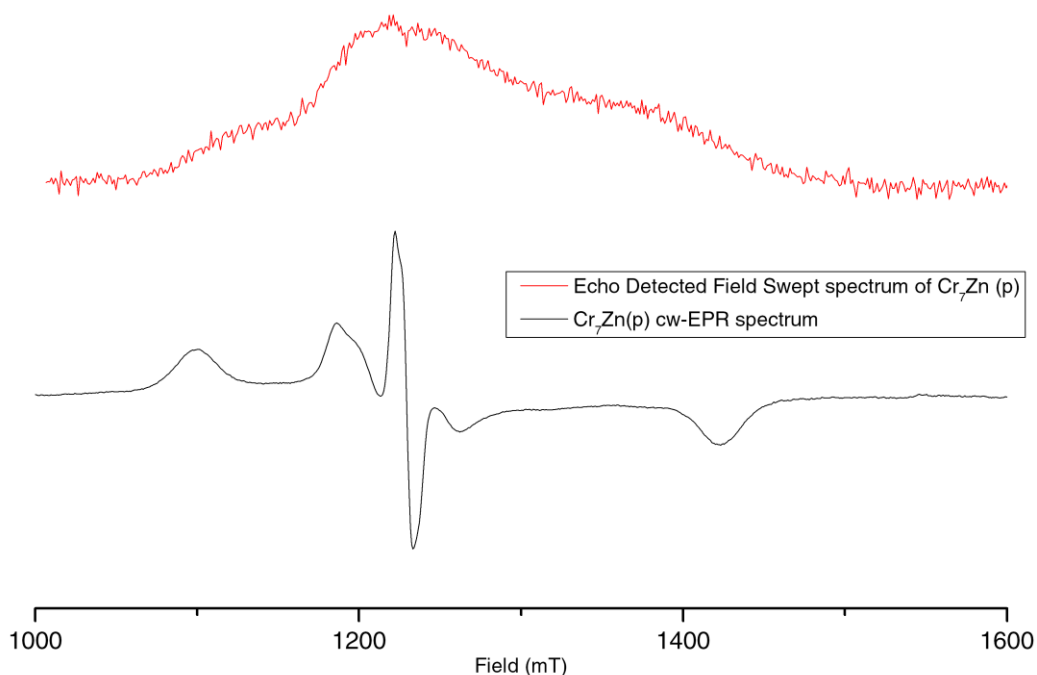
*Figure 46 Q-Band echo detected field sweep spectrum of **4** recorded at 5 K (red) and Q-Band cw-EPR spectrum of **4** at 5 K (black)*

The echo detected field swept spectrum of **4** recorded at Q-Band at 5 K is shown in Figure 46, along with the Q-Band cw-EPR spectrum at 5 K. The peak of the echo detected field swept spectrum is at 1223 mT, corresponding to the central sharp peak in the cw spectrum originating from the S = 3/2 spin ground state. The field swept echo detected spectrum is used to determine the field value at which to perform the spin echo and inversion recovery experiments.

The population of spins follows a Boltzmann distribution inversely proportional to temperature, and so measurement of T_1 requires low temperature measurements. The T_1 is obtained from the recovery of the magnetisation after an inversion pulse $(\pi \rightarrow \tau \rightarrow \frac{\pi}{2} \rightarrow FID)$ with a 40 ns π pulse and a 20 ns $\frac{\pi}{2}$ pulse. The time constant τ is initially set to 40 ns, increasing in increments of 4 ns.

Model	ExpDec1		
Equation	y = A1*exp(-x/t1) + y0		
Reduced Chi-Sqr	5.05916E6		
Adj. R-Square	0.9969		
		Value	Standard Error
T1 4.5K	y0	-202769.71976	112.20213
T1 4.5K	A1	284855.78142	1026.02979
T1 4.5K	t1	4.36507	0.02171
T1 4.5K	k	0.22909	0.00114
T1 4.5K	tau	3.02563	0.01505
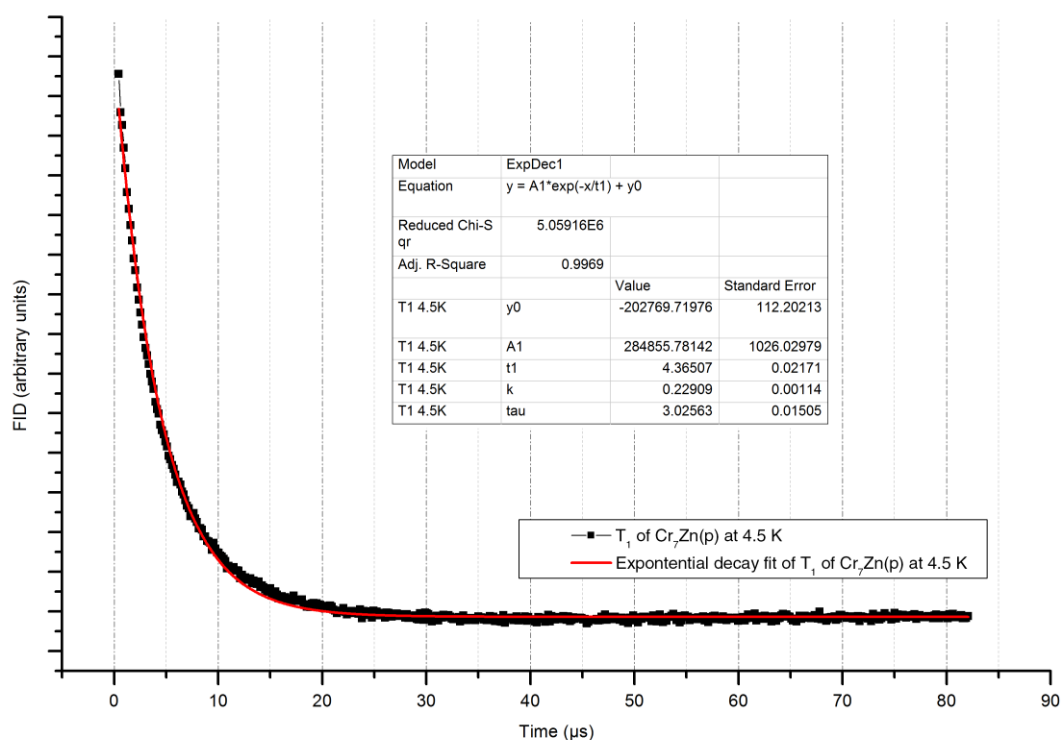
*Figure 47 T_1 decay measurement of **4** at 4.5 K over 181 scans, fitted with an exponential decay function*

The fit of the exponential decay function to the 4.5 K spectrum finds a T_1 of 4.36 $\pm$ 0.02 μs.

The measurements of T_1 were carried out at a variety of temperatures. Measurements on compound **4** were performed with pulsed Q Band at 4.5 K, 6 K, 6.5 K and 7 K. The signal to noise ratio for measurements above 8 K was too poor to obtain results.

The T_2 was observed by the decay of the echo from the two pulse echo sequence $\left(\frac{\pi}{2} \rightarrow \tau \rightarrow \pi \rightarrow \tau \rightarrow echo\right)$ with a 20 ns $\frac{\pi}{2}$ pulse and a 40 ns π pulse with a time constant τ of 400 ns separating them and in increment of 4 ns. Spectra were averaged over 250 scans.

Model	ExpDec1		
Equation	y = A1*exp(-x/t1) + y0		
Reduced Chi-Sqr	3.38361E7		
Adj. R-Square	0.98373		
		Value	Standard Error
Cr7Zn(p) T2 4.5	y0	8404.1611	393.83351
Cr7Zn(p) T2 4.5	A1	724565.58099	15263.95427
Cr7Zn(p) T2 4.5	t1	0.37815	0.00612
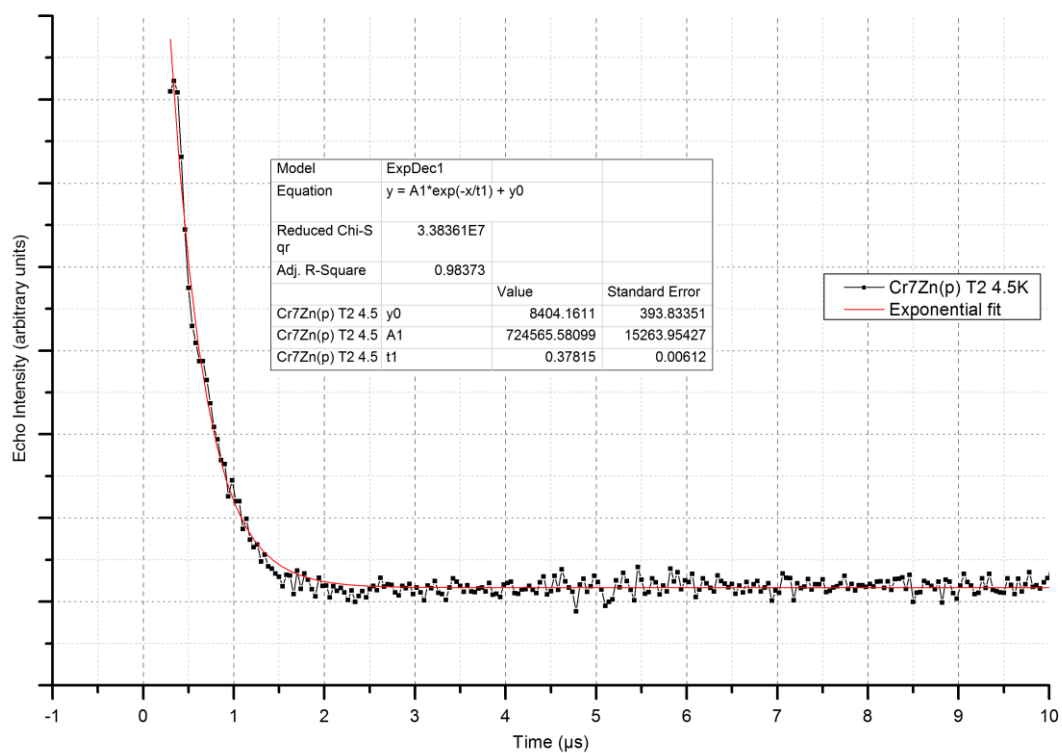
*Figure 48 T$_2$ measurement of **4** at 4.5 K (black) and exponential fit (red) finding T$_2$ = 0.378 μs*

The fit of an exponential decay function to the spectrum finds T$_2$ = 0.378 $\pm$ 0.006 μs.
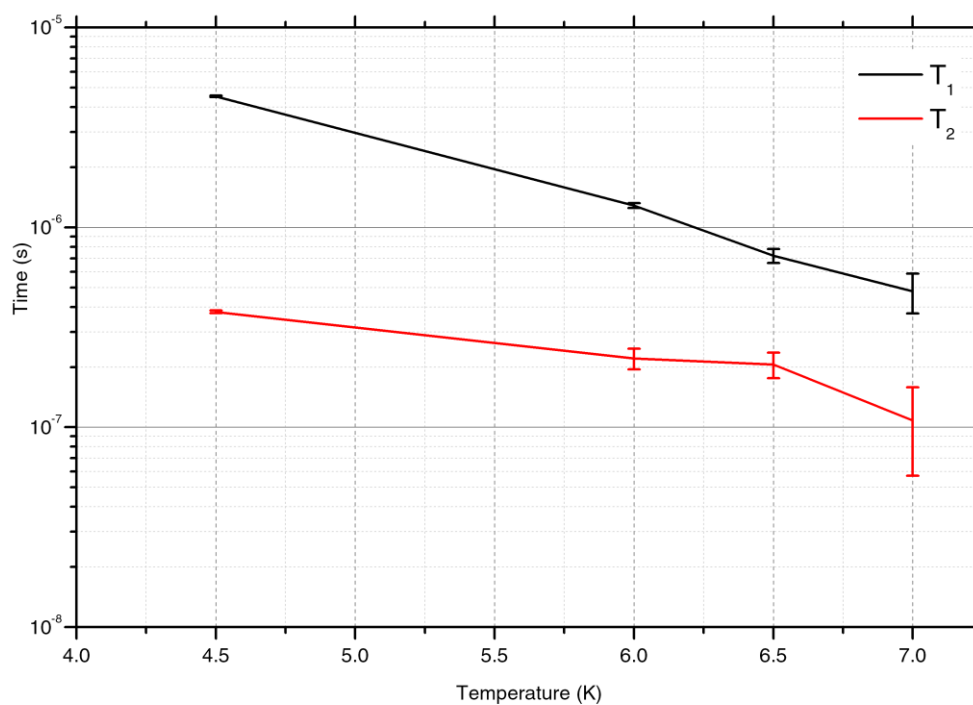
Figure 49 Logarithmic plot of temperature dependence of relaxation times T$_1$ (black triangles) and T$_2$ (red squares) of 4.

The logarithmic plot in in Figure 49 shows the temperature dependence of T_1 and T_2 for **4.** The lowest temperature measurements were at 4.5 K, for which T_1 and T_2 are 4522 ± 32 ns and 378 ± 6 ns respectively. At 6 K, both T_1 and T_2 have reduced to 1285 ± 35 ns and 221 ± 26 ns respectively. At 6.5 K, the T_1 has dropped to 722 ± 57 ns while the T_2 remains fairly stable at 206 ± 51 ns. At 7 K, T_1 and T_2 have both fallen to 480 ± 108 ns and 108 ± 51 ns respectively. The errors on the 7 K measurements are considerable, and so higher temperatures do not provide meaningful data.

Equation	y = a + b*x		
Weight	Instrumental		
Residual Sum of Squares	3.25777	0.65998	
Pearson's r	0.99934	0.99084	
Adj. R-Square	0.99802	0.97265	
		Value	Standard Error
1/T1	Intercept	3.67669	0.04414
	Slope	0.37063	0.00953
1/T2	Intercept	5.76325	0.0643
	Slope	0.14651	0.01412
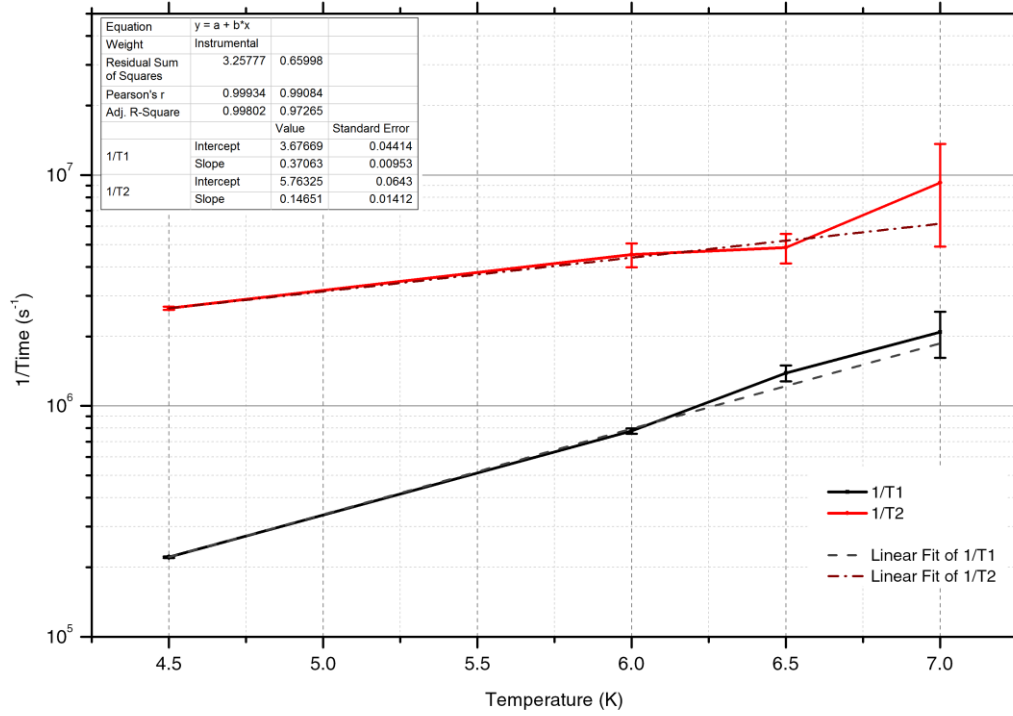
*Figure 50 Logarithmic plot of temperature dependence on relaxation rates T_1^{-1} (black) and T_2^{-1} (red) for **4**, with linear fits of both (dotted lines)*

The quantity $1/T_2$ is the spin-spin relaxation rate, the rate that spins transfer energy between each other, and $1/T_1$ is the spin-lattice relaxation rate, the rate at which spins transfer energy to the lattice. The temperature-dependence of these quantities can be modelled with a linear fit, as shown in the dotted lines in Figure 50. These linear fits show that the spin-lattice relaxation rate has a stronger temperature-dependence (0.371 ± 0.009 s^{-1} K^{-1}) than the spin-spin relaxation rate (0.147 ± 0.014 s^{-1} K^{-1}).

Cr$_7$Ni purple (6)

Compound **6** was measured on a pulsed X-Band (9.615 GHz) spectrometer at 0.4743 mW. The sample was dissolved in toluene at a concentration of 0.1 mg ml^{-1}.
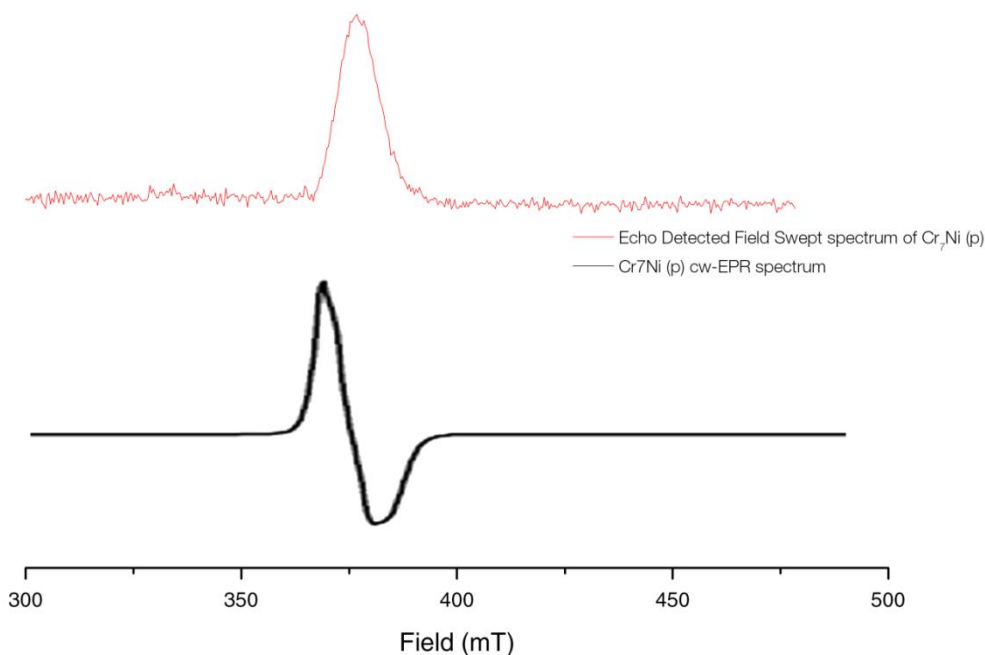
*Figure 51 X-Band echo detected field sweep spectrum of **6** recorded at 5 K (red) and X-Band cw-EPR spectrum of **6** at 5 K (black)* [5]

The X-Band echo detected field sweep spectrum of **6** recorded at 5 K is shown in Figure 51, together with the cw-EPR X-Band spectrum **6** from literature. [5] The field swept spectrum has a peak at 376 mT, corresponding to the centre of the single feature in the cw-EPR spectrum of **6**. The echo detected field swept spectrum is used to determine the field at which T_1 and T_2 measurements are made.

Spin echo measurements were taken at 3.5 K, 7.5 K and 7.9 K and inversion recovery measurements were taken at 3 K, 4 K, 5 K, 6 K.

The T_1 is obtained from the recovery of the magnetisation after an inversion pulse

$(\pi \to \tau \to \frac{\pi}{2} \to FID)$ with a 32 ns π pulse and a 16 ns $\frac{\pi}{2}$ pulse. The time constant τ is

initially set to 40 ns, increasing in increments of 4 ns.
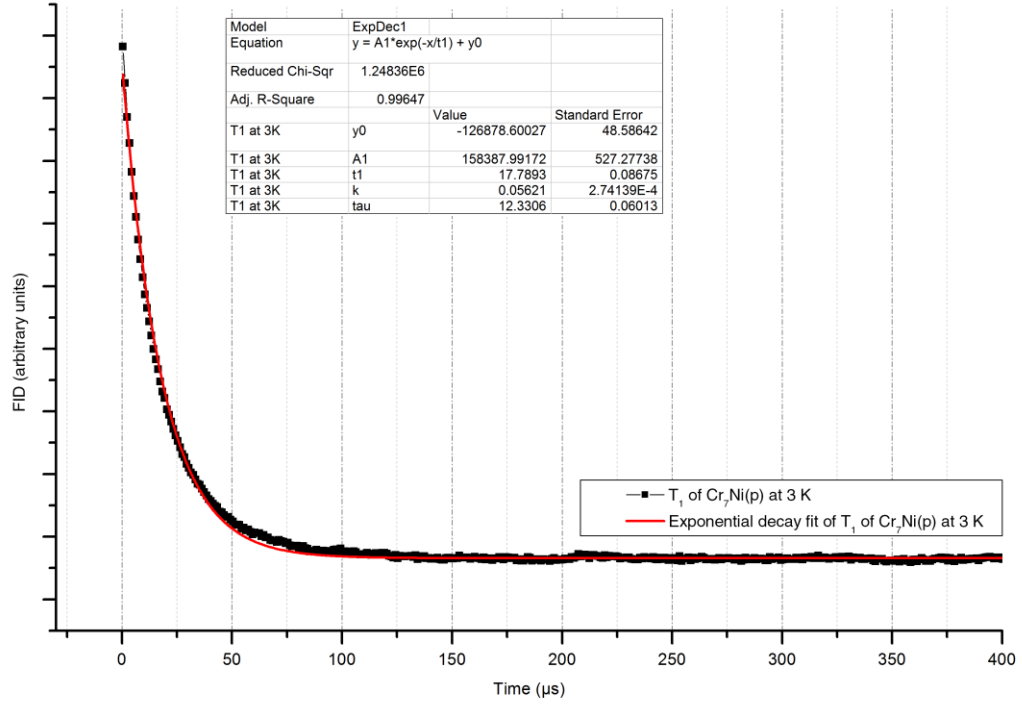
*Figure 52 T₁ decay measurement of **6** at 3 K (black) and fit to an exponential decay*
function (red)

The T_1 decay of **6** at 3 K is shown in Figure 52, and with the exponential decay fit

finds $T_1 = 17.79 \pm 0.09$ μs.

The T_2 was observed by the decay of the echo from the two pulse echo sequence

$\left(\frac{\pi}{2} \to \tau \to \pi \to \tau \to echo\right)$ with a 16 ns $\frac{\pi}{2}$ pulse and a 32 ns π pulse with a time

constant τ of 400 ns separating them and a time increment of 4 ns.

Model	ExpDec1		
Equation	y = A1*exp(-x/t1) + y0		
Reduced Chi-Sqr	1.24104E6		
Adj. R-Square	0.99819		
		Value	Standard Error
T2 at 3.5 K	y0	16086.53886	82.00085
T2 at 3.5 K	A1	372662.77333	2850.65455
T2 at 3.5 K	t1	0.4285	0.00232
T2 at 3.5 K	k	2.33371	0.01263
T2 at 3.5 K	tau	0.29702	0.00161
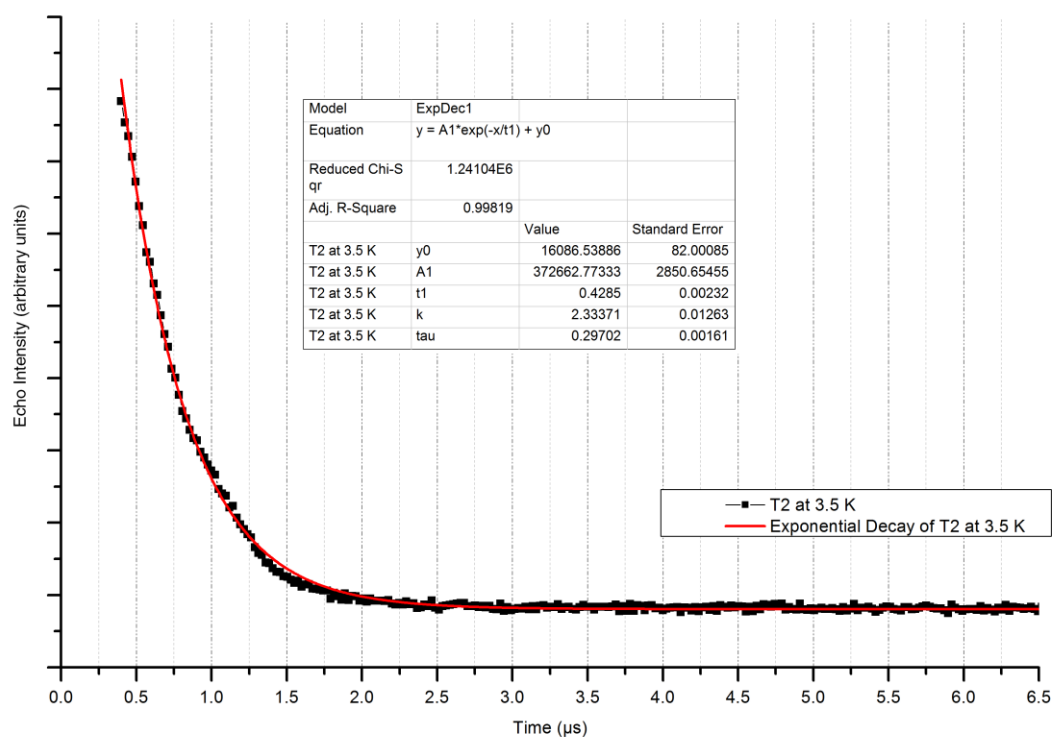
*Figure 53 T$_2$ measurement of **6** at 3.5 K (black) and fit of exponential decay function (red)*

The T_2 decay of **6** at 3.5 K is shown in Figure 53 and the exponential fit finds T_2 = 428.5 $\pm$ 0.23 ns.
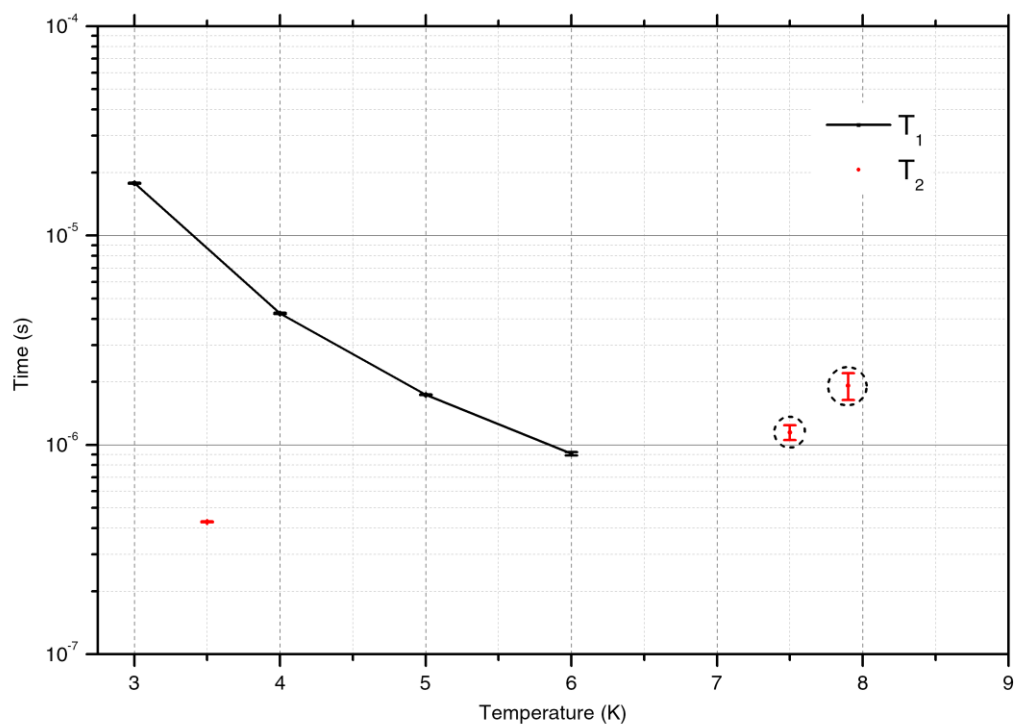
Figure 54 Logarithmic plot of temperature dependence of relaxation time T$_1$, and T$_2$, with possibly unreliable T$_2$ data points circled

The temperature-dependence of T_1 and T_2 of **6** are shown in Figure 54. Measurements of T_2 on compound **6** were also taken at 7.5 K and 7.9 K, but due to technical issues with the spectrometer these data are possibly unreliable (circled in Figure 54) and it is not possible to deduce a temperature-dependent trend for T$_2$.
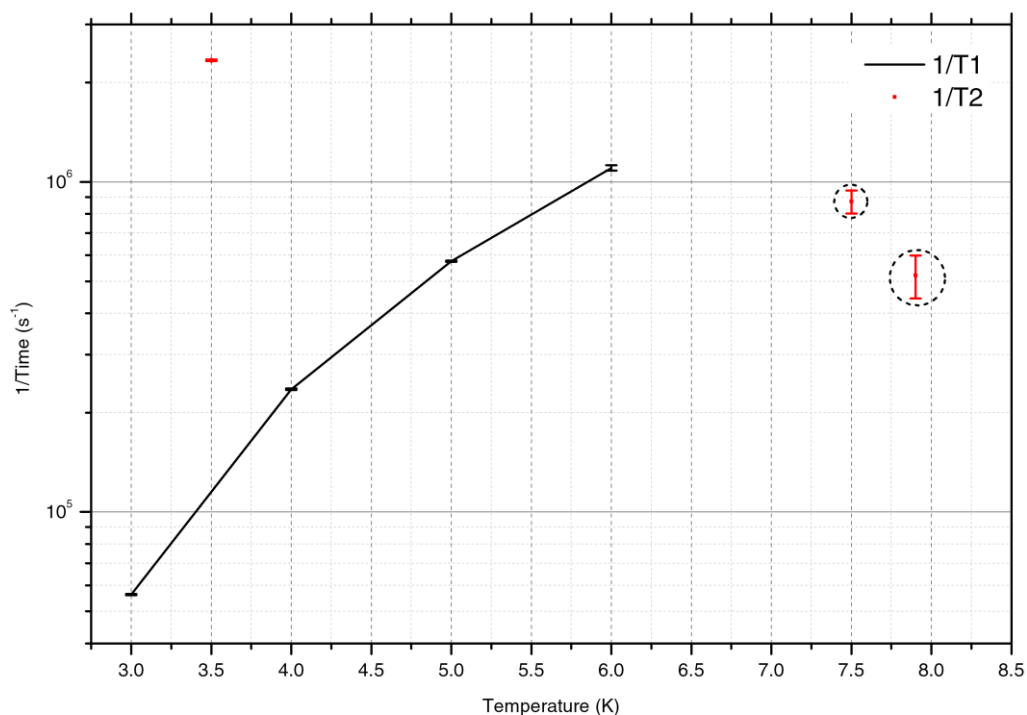
*Figure 55 Logarithmic plot of temperature dependence on relaxation rates T_1^{-1} (black) and T_2^{-1} (red) for **6***

The quantity $1/T_2$ is the spin-spin relaxation rate, the rate that spins transfer energy between each other, and $1/T_1$ is the spin-lattice relaxation rate, the rate at which spins transfer energy to the lattice. The plots of $1/T_2$ and $1/T_1$ for **6** are shown in Figure 54. As noted above, the two data points at 7.5 K and 7.9 K are possibly unreliable, and so it is not possible to plot a temperature-dependence of $1/T_2$.

Conclusions

In order to ascertain whether these antiferromagnetically coupled wheels can be reasonable candidates as qubits, we ought to compare our results with other qubit candidates. The green variants of Cr$_7$Mn (**2**) and Cr$_7$Ni (**3**) have been studied at X-Band frequency, and it was found for Cr$_7$Ni that T_2 = 379 ns at 4.5 K. [12] From *Figure 3* in reference 12, the T_1 and T_2 for Cr$_7$Ni at 3.7 K were found to be 7.50 μs and 392 ns respectively. For the purple variant of Cr$_7$Ni (**6**), T_1 is found to be 17.79 μs at 3 K and T_2 is 428.5 ns at 3.5 K.

The relaxation times of other variants of Cr$_7$Ni have been studied, with different bridging ligands and templating cation and replacing ^{1}H by ^{2}H. [6]

Table 12 Overview of T_2 values of green Cr$_7$Ni variants [6]

Label in reference	Carboxylate bridging ligand	Central templating cation	T_2 at 3.5 K (ns)
1	Piv	$Et_2NH_2^+$	1000
2	*d*-Piv	*d*-$Et_2NH_2^+$	2688
3	Ad1CO$_2$	$^nPr_2NH_2^+$	1813

Table 12 shows the T_2 values at 3.5 K for the green Cr$_7$Ni variants from Figure 2 in the literature reference. [6] Measurements on the purple Cr$_7$Ni find a T_2 of 428.5 ns, significantly less than any of the variants in Table 12. This time T_2 is the time over which a quantum bit could reliably store quantum information, and while it is shorter than the other variants this T_2 is still much greater than the length of the spin

manipulation pulse. This result suggests that compound **6** could still be a viable candidate for quantum information processing.

For green Cr$_7$Mn, the values of T_1 and T_2 are 4.870 µs and 453 ns respectively. [12] This is a slightly longer T$_2$ than the purple Cr$_7$Ni.

Long decoherence times have been observed in other molecular magnets at low temperatures, such as Fe$_8$ single crystals, [7] V$_{15}$ clusters, [8] Mn$_4$ dimers. [9]

V$_{15}$ is a large cluster that has also been proposed as a qubit system. [10] The V$_{15}$ cluster consists of 15 V^{IV} ions $\left(S = \frac{1}{2}\right)$ in a quasi-spherical layered structure of large triangles held between two smaller hexagons. Every hexagon has three pairs of coupled spins, and every spin at a corner of the inner triangle is coupled to two of those pairs. At low temperatures, this system forms an $S = \frac{1}{2}$ ground state with an $S = \frac{3}{2}$ excited state, well separated from other levels. [10] At 4 K, a decoherence time $T_2 = 340$ ns is reported. The spin ladder at low temperature is similar to that of **6**, making it an interesting comparison to the results reported in this chapter.

Semiconductors such as Cu^{II} phthalocyanine have also been studied, and report much longer relaxation times. [11]
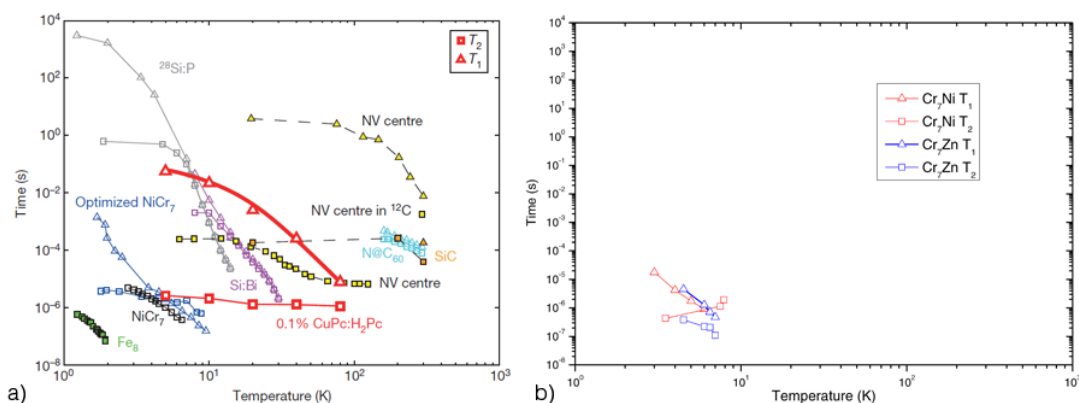
Figure 56 Temperature dependence of relaxation times for common spin qubit systems [11] (a), and results of relaxation times for compounds 4 and 6 plotted on the same scale for more direct comparison (b).

The plot in Figure 56 shows the comparison between relaxation times in the literature (a), and the results found from the purple compounds **4** and **6**. The plot shows that the measured compounds exhibit relaxation times in the same region as comparable spin qubits, but do not noticeably outperform in comparison to other candidates. The relaxation time T_2 is slightly longer for the purple Cr_7Ni than the green variant in reference 6, though it should be noted that there are slight differences in the temperatures at which measurements have been taken. The closest possible temperature values from the literature have been chosen, and are shown in Table 13.

Table 13 Overview of relaxation times for spin qubit candidates from the literature and measured compounds (grey). Some numbers have been interpreted from the figures in literature.

	Ref	Temperature (K)	T_1 (s)	T_2 (s)	Frequency
CuPc	11	5	5.90×10^{-2}	2.60×10^{-6}	Q-Band
CuPc	11	80	1.00×10^{-5}	1.00×10^{-6}	Q-Band
Fe$_8$	7	1.3		7.12×10^{-7}	240 GHz
green Cr$_7$Mn	12 (fig 3)	3.7	4.87×10^{-6}	4.53×10^{-7}	X-Band
purple Cr$_7$Ni		3.5	1.78×10^{-5}	4.28×10^{-7}	X-Band
green Cr$_7$Ni	12 (fig 3)	3.7	7.50×10^{-6}	3.92×10^{-7}	X-Band
purple Cr$_7$Zn		4.5	4.52×10^{-6}	3.78×10^{-7}	Q-Band
V$_{15}$	8	4	Not reported	3.40×10^{-7}	X-Band

Future work

As seen in Figure 54, measurements of T_2 of **6** had some issues at 7.5 K and 7.9 K. It would be necessary to obtain reliable measurements at these temperatures, and intermediate temperatures, to ascertain the temperature-dependence of T_2 of **6**.

Measurements of **4** were taken at Q-Band frequency, and measurements of **6** were taken at X-Band. It would be interesting to measure both at different frequencies, to ascertain any frequency-dependence of T_1 and T_2 for these systems. These measurements could also be taken at different field positions in order to ascertain any anisotropy in relaxation times.

It would also be interesting to investigate the purple Cr$_7$Mn (**5**), to see how the T_2 compares with the green variant.

References

[1] DiVincenzo, D. P.; *Fortschr. Phys.,* **2000**, 48, 771-783

[2] Schweiger, A.; Jeschke, G.; *Principles of Pulse Electron Paramagnetic Resonance*, Oxford University Press, **2001**

[3] Legget, A. J, *J. Phys. Condens. Matter*, **2002**, 14, R415-R451

[4] Schleger, C.; Slageren, J. van; Timco, G.; Winpenny, R. E. P; Dressel, M; *Phys. Rev. B*, **2011**, 134407, 83

[5] Timco, G. A.; McInnes, E. J. L.; Pritchard, R. G.; Tuna, F.; Winpenny, R. E. P.; *Angew. Chem*, **2008**, 47, 9681-9684

[6] Wedge, C. J.; Timco, G. A.; Spielberg, E. T.; George, R. E.; Tuna, F.; Rigby, S.; McInnes, E. J. L.; Winpenny, R. E. P.; Blundell, S. J.; Ardavan, A.; *Phys. Rev. Lett* **2012**, *108*, 107204

[7]. Takahashi, S.; Tupitsyn, I. S.; Tol, J. van; Beedle, C. C.; Hendrickson, D. N.; Stamp, P. C. E, *Nature*, **2011**, *476*, 76

[8] Bertaina, S.; Gambarelli, S.; Mitra, T.; Tsukerblat, B.; Müller, A., Barbara, B.; *Nature Letters*, **2008**, *453*, 203-206

[9] Hill, S.; Edwards, R. S.; Aliaga-Alcalde, N.; Christou, G.; *Science*, **2003**, *302*, 1015

[10] Barbara, B.; *J. Mol. Struct.*, **2003,** *656*, 135-140

[11] Warner, M.; Din, S.; Tupitsyn, I. S.; Morley, G. W.; Stoneham, A. M.; Gardener, J. A.; Wu, Z.; Fisher, A. J.; Heutz, S.; Kay, C. W. M.; Aeppli, G., *Nature*, **2013**, *503*, 504

[12] Ardavan, A.; Rival, O.; Morton, J. J. L.; Blundell, S. J., *Phys. Rev. Lett*, **2007**, *98*, 057201

Chapter V –Electronic Structure of [Cr$_7$M]-{Cr$_7$M} Heterometallic dimers

This chapter presents the results of the investigations into the [Cr$_7$$M$]-{Cr$_7$$M$} heterometallic dimers of the purple and green wheels. The primary purpose of this investigation is to determine whether there is an exchange interaction between these wheels of a significant magnitude. Nine compounds have been measured and analysed, with EPR spectra collected at Q Band and W Band frequencies. The lowest attainable temperature was 5 K, and all compounds have been measured at variable temperatures across both frequencies. The same microscopic Hamiltonian for the single wheels is used to simulate the spectra of these dimers with the introduction of a single additional exchange interaction. The simulations estimate the magnitude of this exchange interaction between the wheels.

Introduction

For qubits to be used appropriately in a functional computing system, it is necessary to form a quantum gate. In 1985, Deutsch compared a conventional logic gate to a quantum logic gate and suggested that for such a gate to be formed it needed two $S = ½$ qubits linked together by a molecule allowing some degree of electronic coupling between these qubits. [1] This coupling is a necessary step towards entanglement, such that the qubits can be considered only as one system. The entanglement of n qubits allows for 2^n obtainable states.

In Chapter III, we have modelled the magnetic data, heat capacity, INS and EPR spectra of two families of anti-ferromagnetically coupled heterometallic rings. The family of 'green' rings have the general formula [NH$_2$R$_2$][Cr$_7$$MF_8$(O$_2$C^{t}Bu)$_{16}$] (where

R is a linear alkyl, typically ethyl, and M is a divalent ion. The EPR spectra of the cases where the divalent metal M is Zn^{II} (**1**), Mn^{II}, (**2**) and Ni^{II}, (**3**) have been modelled with the microscopic Hamiltonian in Chapter 3.

The second family of 'purple' (or 'sugared') rings has the general formula [Cr$_7$MF$_3$(Etglu)(O$_2$C^{t}Bu)$_{15}$(Phpy)], (where H$_5$Etglu is N-ethyl-D-glucamine and Phpy = 4-phenylpyridine). We modelled the cases where the divalent metal M is Zn^{II} (**4**), Mn^{II} (**5**), and Ni^{II} (**6**).

We have modelled both families of individual ring systems using two isotropic exchange interactions $J_{Cr\text{-}Cr}$ and $J_{Cr\text{-}M}$ and the single ion zero-field splitting parameters d_{Cr}, e_{Cr}, d_M, e_M.

A new series of mixed-wheel dimer systems has been synthesised by reacting mono-substituted green wheels with purple wheels. The Cr$_7$Ni-Cr$_7$Ni dimer with a variety of linkers of different lengths has been studied previously, showing that the strongest interaction occurs with an isonicotinate linker. [2]

These dimers, with the general formula [Cr$_7$M'F$_3$(C$_8$H$_{14}$NO$_5$)(O$_2$C^{t}Bu)$_{15}$](NC$_5$H$_4$CO$_2$) [{Cr$_7$M''F$_8$(O$_2$C^{t}Bu)$_{15}$}{(C$_3$H$_7$)$_2$NH$_2$ }] (where M', $M'' =$ Zn^{II} , Mn^{II} and Ni^{II}), are the focus of this discussion. The structure is shown in Figure 57. We have been studying the effect of the variation of the divalent metal in each Cr$_7$M individual wheel and the effect that this has upon the communication between the rings. Nine compounds have been studied as shown in Table 14.

Figure 57 Structure of $[Cr_7M'F_3(C_8H_{14}NO_5)(O_2C^tBu)_{15}]$ $(NC_5H_4CO_2)$
$[\{Cr_7M''F_8(O_2C^tBu)_{15}\}\{(C_3H_7)_2NH_2\}]$

Theory

The simulations of the individual rings use a microscopic Hamiltonian operator. The full set of microscopic parameters to describe the individual purple and green rings have been found previously, and those parameters will be used to model the dimers.

Figure 58 Schematic of model for dimer simulations

The dimer systems are modelled by introducing an additional exchange parameter J' for the communication between the rings, as shown in Figure 58. The dimers are described by a sum of Hamiltonians, in equation 1

$$H = H_p + H_g + H_{pg} \qquad\qquad 1$$

where H_p and H_g are the Hamiltonians describing the individual purple and green wheels respectively, see Table 15 for the spin-Hamiltonian parameters, and H_{pg} describes the interaction between the wheel in equation 2.

$$H_{pg} = J's_8^p \cdot \left(s_7^g + s_8^g\right) \qquad\qquad 2$$
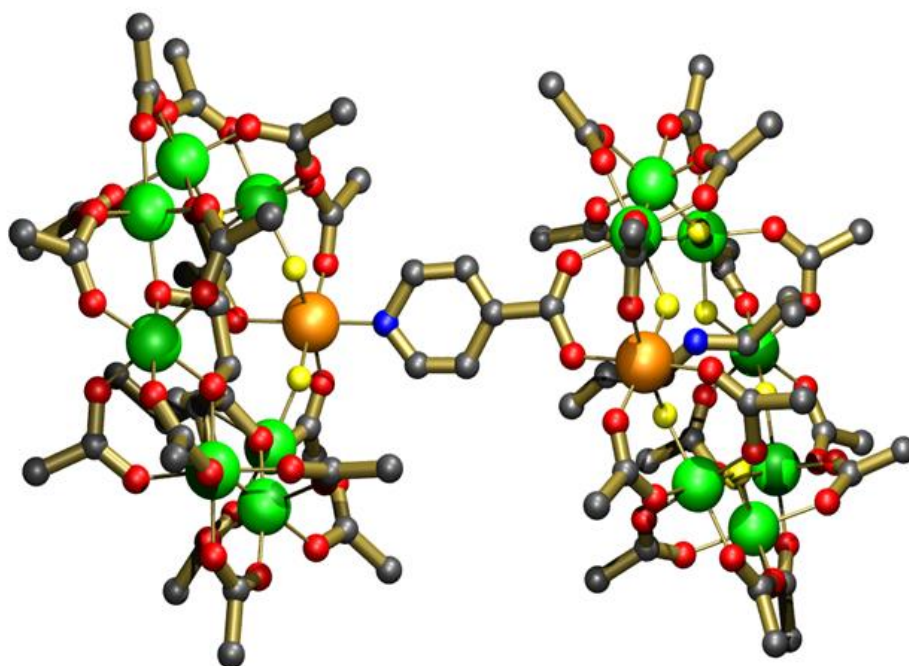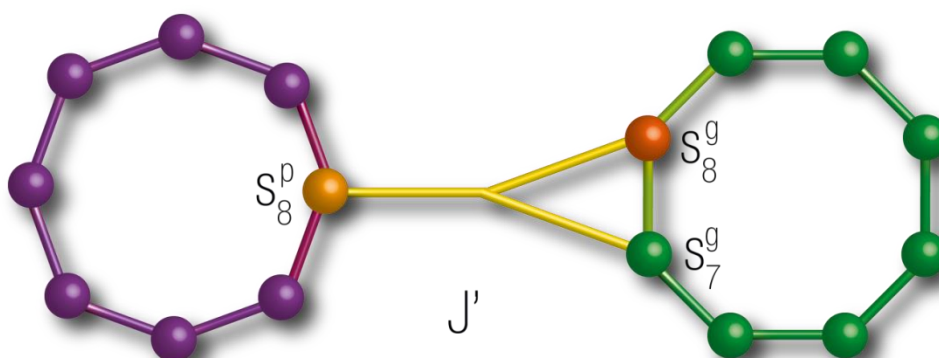
Table 14 Compound numbers for purple-green dimers

Green Purple	Cr₇Zn **1**	Cr₇Mn **2**	Cr₇Ni **3**
Cr₇Zn **4**	7	8	9
Cr₇Mn **5**	10	11	12
Cr₇Ni **6**	13	14	15

This chapter discusses only the EPR spectra of the compounds in Table 14, at Q Band and W Band, as the magnitude of J' in equation 2 may be very small and not revealed by bulk magnetisation measurements.

Table 15 Overview of parameters for single wheels

	Green			Purple		
	1	**2**	**3**	**4**	**5**	**6**
$J_{Cr\text{-}Cr}$ (K)	16.9	16.9	16.9	20.4	20.4	20.4
$J_{Cr\text{-}M}$ (K)	0	16.6	19.6	0	12.0	30.0
d_{Cr} (K)	-0.35	-0.35	-0.35	-0.27	-0.27	-0.27
e_{Cr} (K)	-0.09	-0.09	-0.09	-0.09	-0.09	-0.09
d_M (K)	0	-0.2	-4	0	+0.01	-6.0
e_M (K)	0	-0.01	0	0	0	0
g_{Cr}	1.98	1.98	1.98	1.98	1.98	1.98
g_{xx}^{M}	0	2.00	2.27	0	2.00	2.16
g_{yy}^{M}	0	2.00	2.27	0	2.00	2.16
g_{zz}^{M}	0	2.00	2.25	0	2.00	2.22
σ	0.005	0.04	0.013	0.019	0.04	0.008
MF_{σ}	0.4	0.4	2.0	0.23	0.4	2.0

[Cr₇Zn purple] – {Cr₇Zn green} dimer   7

For the dimers involving purple Cr₇Zn (**4**), there can be no communication between the wheels through the linker as the linker on the purple side is connected only through the diamagnetic Zn^{II}. The EPR spectra of compounds **7**, **8** and **9** should therefore be able to be modeled by a linear summation of the spectra of the respective individual rings.
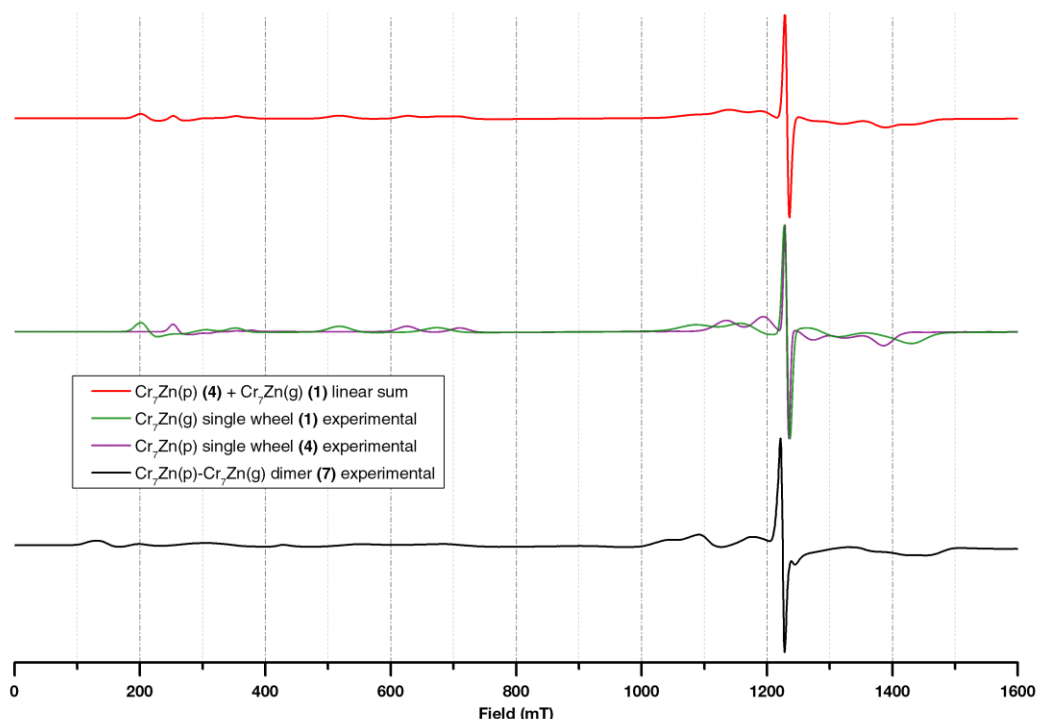
*Figure 59 Q Band spectrum at 5 K of **7** (black), **4** (purple), **1** (green) and linear sum of spectra of **4** and **1** (red)*

Polycrystalline measurements of **7** were made at Q-band (Figure 3) at 5 K, showing contributions from several spin multiplets. There is a sharp resonance at 1243 mT close to g = 2 and broader features from 200 to 1700 mT.

The spectra of **1** and **4** are fairly similar. The spectrum of **4** has two very distinct features at 1197 mT and 1132 mT, which appear broadened and slightly shifted in **1**. Similarly, the feature at 1392 mT in the spectrum of **4** appears slightly broadened and shifted to 1430 mT in the spectrum **1**. In the spectrum of **4**, there are two small

features at 712 mT and 631 mT, which are moved to 669 mT and 511 mT in the spectrum of **1**. The slightly more intense feature at 250 mT in the spectrum of **4** appears with more intensity at 203 mT in the spectrum of **1.** These same features appear in the spectrum of the dimer **7**.

The red line in Figure 59 shows the linear sum of the spectrum of **4** and the spectrum of **1** with equal contributions from both. This linear sum fairly accurately reproduces the experimental spectrum of **7**. The low field features of the comparison spectra appear at different positions and so the linear sum further broadens them. These features also appear similarly broadened in the experimental dimer spectrum. The exception is the feature at 132 mT in the spectrum of **7**, which appears at a much lower field than any features in either **4** or **1**. This suggests that while this model may be broadly accurate, it is not complete in its description of the spectrum.
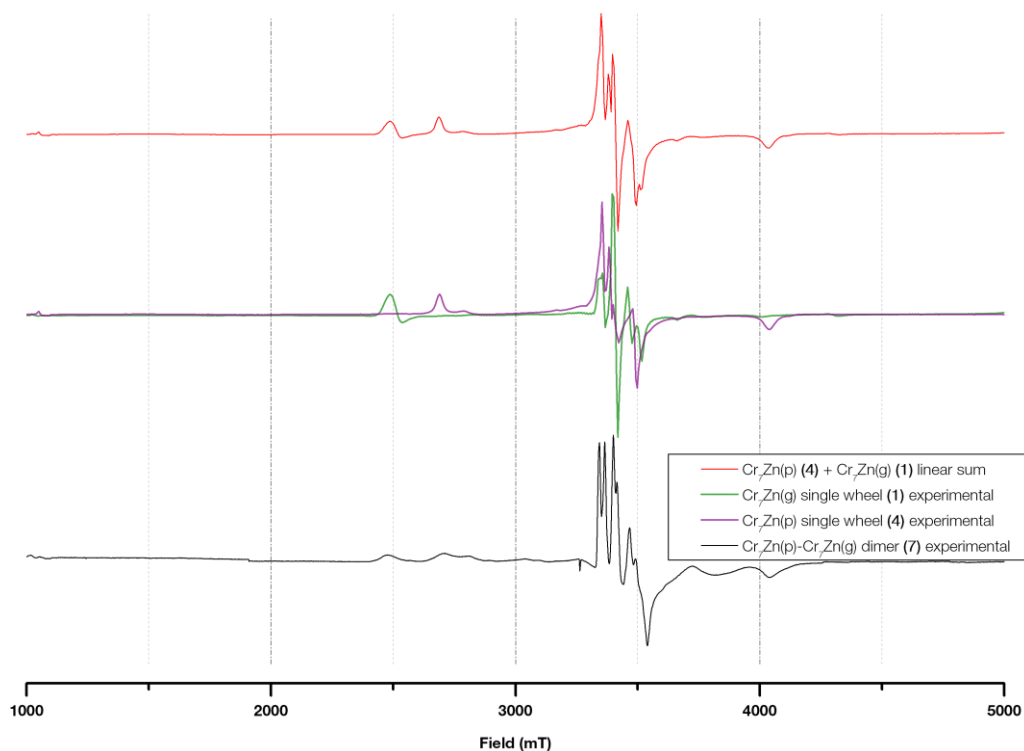
Figure 60 W Band spectrum at 5 K of 7 (black), 4 (purple), 1 (green) and linear sum of spectra of 4 and 1 (red)

The W-Band spectra of the single green and purple Cr$_7$Zn wheels (**1** and **4** respectively) are compared to the Cr$_7$Zn-Cr$_7$Zn (**7**) dimer spectrum in Figure 60. In the dimer spectrum, there are three low field features at 2470 mT, 2702 mT, and 2807 mT. The first of these features is present in the spectrum of **1** and the other two are present in the spectrum of **4**, and the linear sum of the two spectra reproduces these features quite accurately.

The high field features in the region of 3337 mT to 3634 mT are more complex. There are six clearly identifiable peaks in the spectrum of **7** while in the linear sum of **1** and **4** there are only five. In the spectrum of **1**, there are two very close peaks at 3353 mT that overlap with a much larger peak at the same position in the spectrum of **4**. There is a shallow feature in the shoulder of the linear sum. The relative intensity of the peaks in the linear sum do not correspond to the spectrum of **7**, suggesting that there may be a non-identical contribution from the two wheels.
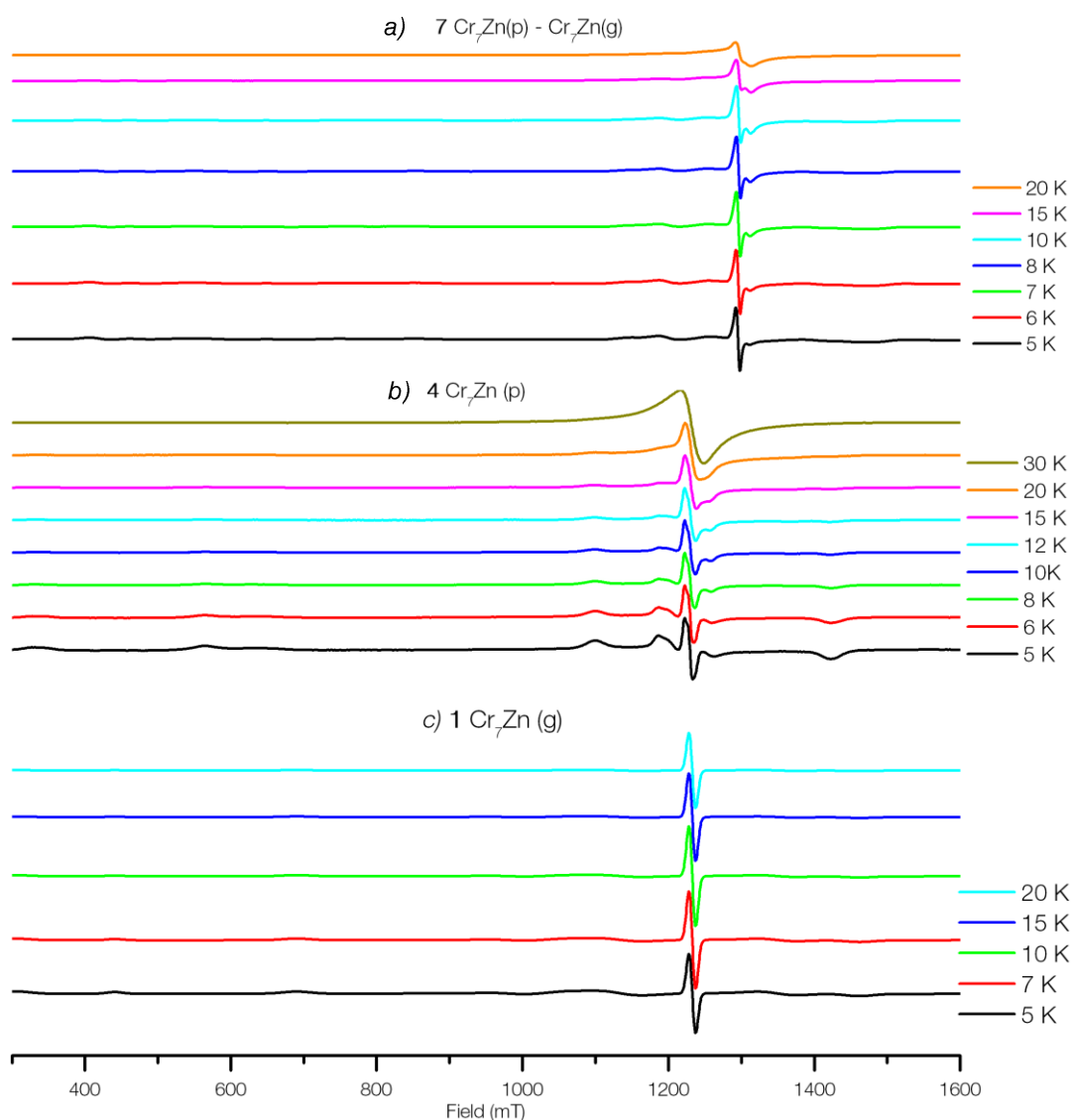
*Figure 61 Variable temperature Q Band EPR spectra of **7** measured at 34.0616 GHz (a), variable temperature Q Band EPR spectra of **4** measured at 34.1587 GHz (b), and variable temperature Q Band EPR spectra of **1** measured at 34.1238 GHz (c)*

The variable temperature Q Band spectra of **7** are shown in Figure 61 (a), and the comparisons with the single wheels **4** and **1** are shown in Figure 61 (b) and Figure 61 (c) respectively. Figure 61 (a) shows the dominance of the sharp feature at 1225 mT and suppression of features at 1081 mT and 141 mT at higher temperatures. Figure 61 (b) shows a similar trend with the spectra of **4**, with the prominent features at 215 mT, 324 mT, 566 mT, 1106 mT, and 1181 mT at 5 K broadening and disappearing by 15 K. Above 20 K, only the central feature at 1225 mT remains. The Q-Band

spectra of **1** also have the same temperature-dependent behaviour in Figure 61 (c), with features at 155 mT, 313 mT, 696 mT, 1099 mT appearing at low temperatures but broadening and disappearing at higher temperatures leaving only the central feature at 1225 mT. The temperature-dependence of the features of the Q-Band spectrum of **7** are represented in the temperature-dependence of the features of the Q-Band spectra of **4** and **1**, further reinforcing the interpretation of the dimer as a linear sum of the two components.

*Figure 62 Variable temperature W Band EPR spectra of **7** measured at 97.99198 GHz (a), variable temperature W Band EPR spectra of **4** measured at 93.96804 GHz (b), and variable temperature W Band EPR spectra of **1** measured at 93.72122 GHz (c)*

The variable temperature W Band spectra of **7** are shown in Figure 62 (a), and the comparisons with the single wheels **4** and **1** are shown in Figure 62 (b) and Figure 62 (c) respectively. The sharp blip at 3262 mT in the 5 K of **7** spectrum is due to a correction in frequency due to a drift during the experiment. The spectrum of **7** in Figure 62 (a) has two broad features at 2484 mT and 2726 mT which disappear above 8 K. These two features appear in the spectra of **1** and **4** respectively with the same temperature-dependent behaviour.

The feature at 3401 mT in the spectrum of **7** in Figure 62 (a) grows with increasing temperature, and this is seen in the spectrum of **4** in Figure 62 (b) as well. The spectrum of **7** has two features at 3342 mT and 3365 mT that broaden and merge with increasing temperature, which also occur in the spectrum of **4**. The small feature at 3408 mT in the spectrum of **7** corresponds to the feature at the same position in the spectrum of **1** in Figure 62 (c), and the intensity decreases with increasing temperature in both spectra. The temperature-dependence of the features of the W-Band spectrum of **7** are represented in the temperature-dependence of the features of the W-Band spectra of **4** and **1**, further reinforcing the interpretation of the dimer as a linear sum of the two components.

[Cr$_7$Zn purple] – {Cr$_7$Mn green} dimer   8
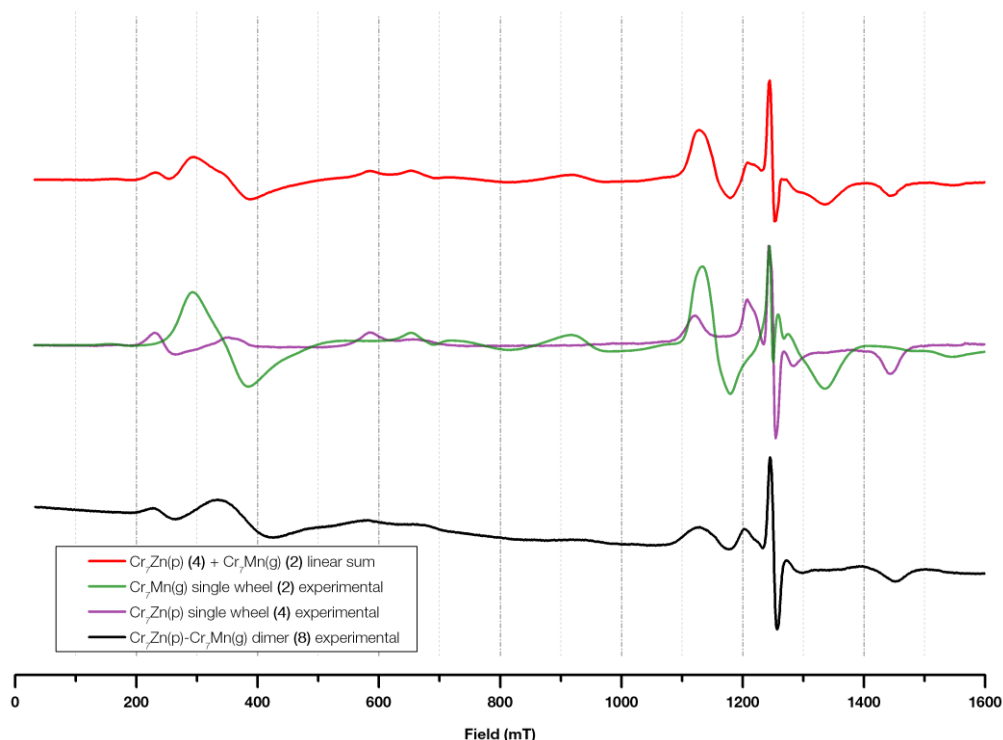
Figure 63 Q Band spectrum at 5 K of 8 (black), 4 (purple), 2 (green) and linear sum of spectra of 4 and 2 (red)

Polycrystalline measurements were taken of **8** at Q Band at 5 K at 33.9908 GHz, shown in Figure 63 together with the linear sum the 5 K Q Band spectra of the single wheels **4** and **2**. The spectrum of **8** has a sharp central feature at 1250 mT, which corresponds to both sharp features at the same location in the spectra of **4** and **2**. The dimer spectrum **8** also has two features at slightly lower field, at 1124 mT and 1200 mT, which correspond to features in the spectrum of **2** and **4** respectively. The two features at much lower field, at 221 mT and 339 mT, both appear in the spectra of **4** and **2** respectively also. The small feature at 1453 mT in the spectrum of **8** appears in the spectrum of **4**. The linear sum of **4** and **2** almost exactly reproduces the spectrum of the dimer **8**, indicating that there is no communication between the two wheels in the dimer.
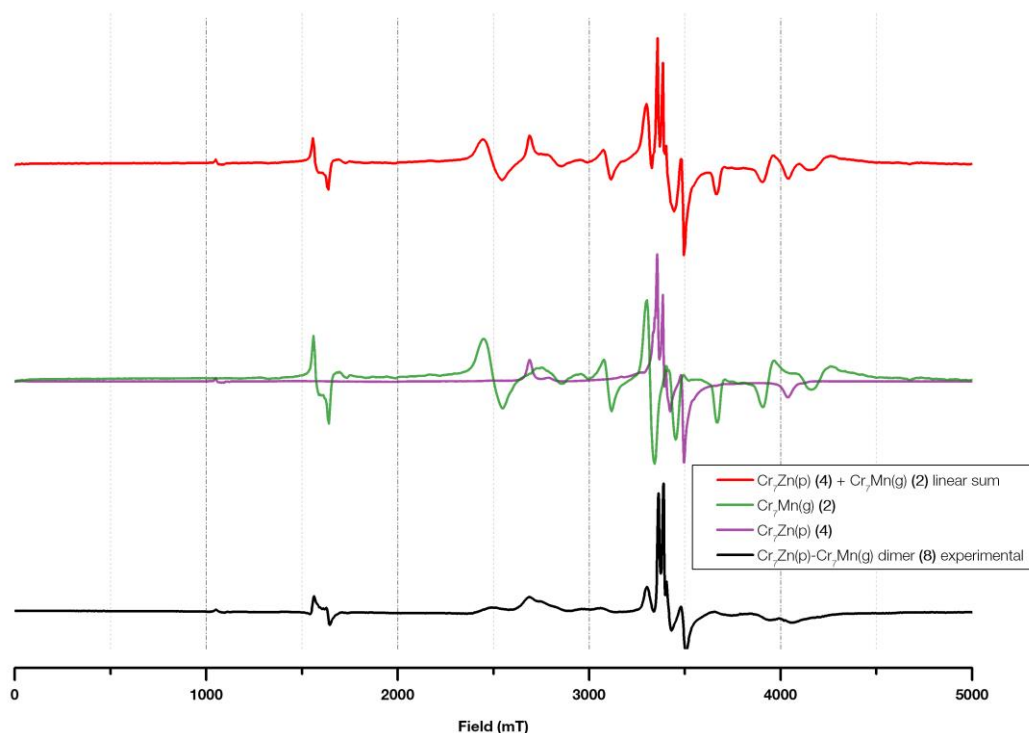
*Figure 64 W Band spectrum of **8** (black), **4** (purple), **2** (green) and linear sum of spectra of **4** and **2** (red)*

The 5 K spectrum of the dimer **8** at W-Band is compared to that of the single wheels **4** and **2** and their linear sum in Figure 64. The dimer spectrum has low field features at 1054 mT and 1557 mT that appear in the purple and green Cr_7Mn spectra respectively. The 2470 mT peak in the dimer spectrum appears in the green Cr_7Mn spectrum but with greater relative intensity as compared to the features near 2669 mT. The sharp central peaks at 3354 mT and 3384 mT appear in the purple Cr_7Zn spectrum. All the features in the dimer spectrum of **8** are represented by the linear sum of **2** and **4**, but with a slight variation in the relative intensity of peaks.
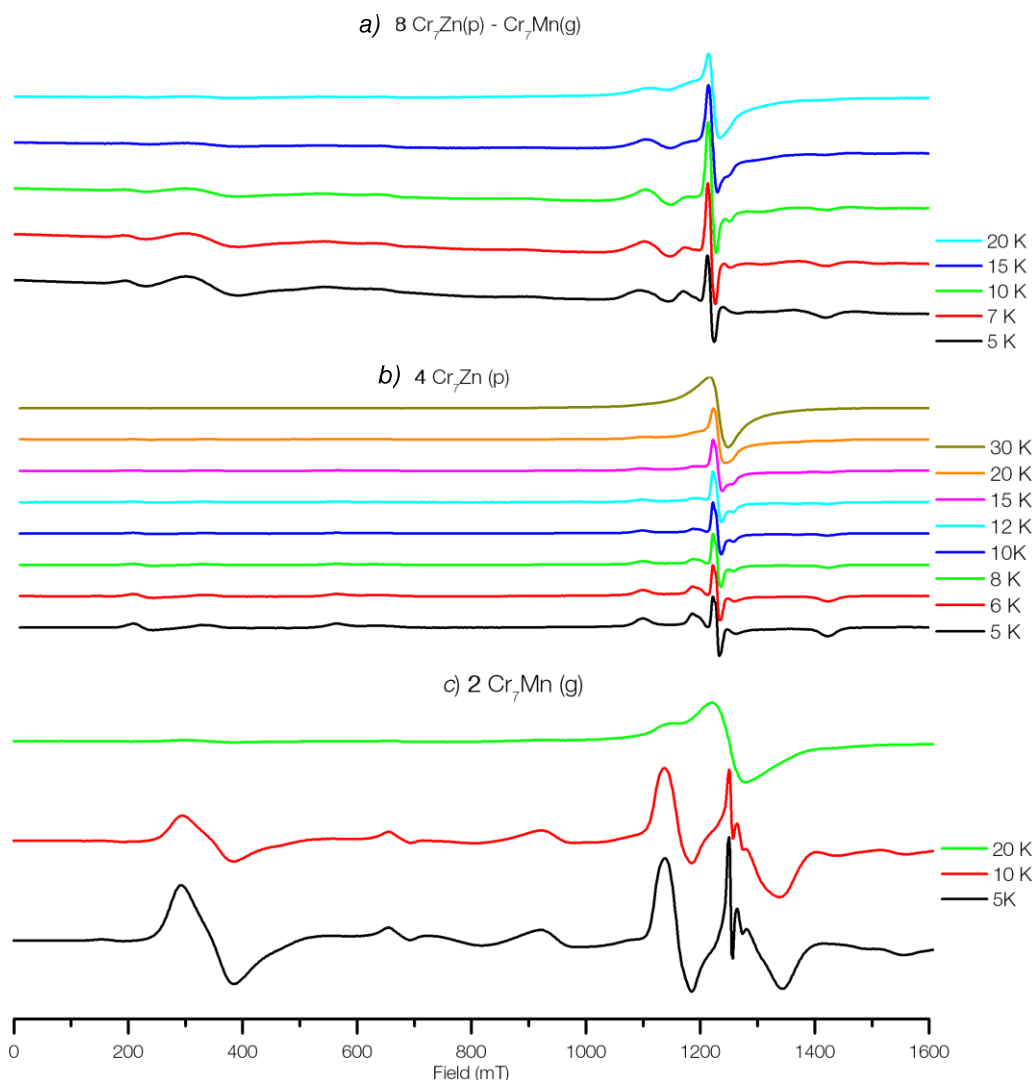
*Figure 65 Variable temperature Q Band EPR spectra of **8** measured at 33.990 GHz (a), variable temperature Q Band EPR spectra of **4** measured at 34.1587 GHz (b), and variable temperature Q Band EPR spectra of **2** measured at 34.0978 GHz (c)*

The variable temperature Q Band spectra of **8** are shown in Figure 65 (a), and the comparisons with the single wheels **4** and **2** are shown in Figure 65 (b) and Figure 65 (c) respectively. The spectrum of **8** has features at 221 mT and 339 mT which are broadened with increasing temperature and are not visible above 15 K. These correspond to features in the spectra of **4** and **2** respectively, which display the same temperature-dependent behaviour. At higher temperatures, only a single central feature in the spectrum of **8** remains. Both spectra of **4** and **2** also display a similar temperature-dependent behaviour, with a single feature at 1250 mT in both spectra remaining at temperatures above 20 K. The temperature-dependence of the features

146

of the Q-Band spectrum of **8** are represented in the temperature-dependence of the features of the Q-Band spectra of **4** and **2**, further reinforcing the interpretation of the dimer as a linear sum of the two components.
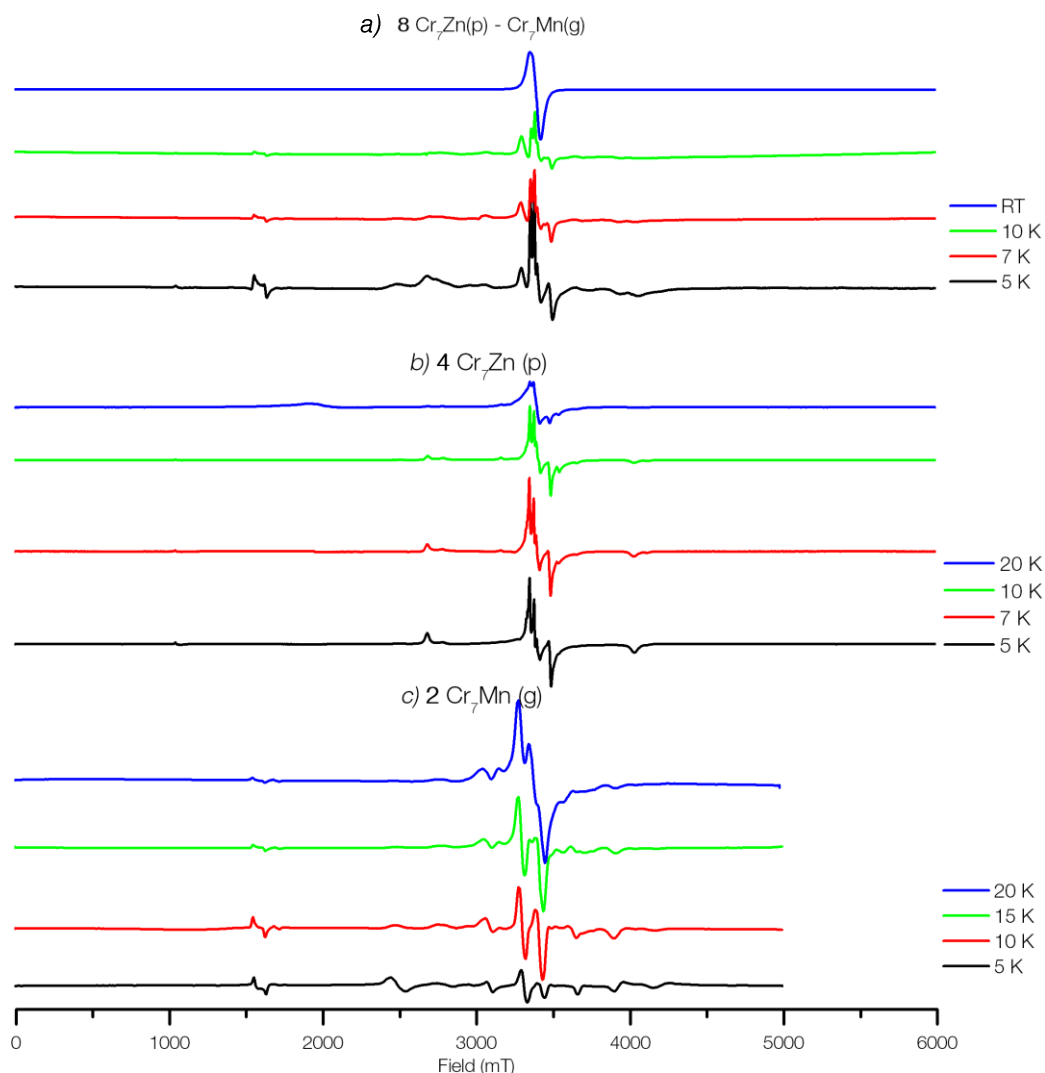
*Figure 66 Variable temperature W Band EPR spectra of **8** measured at 95.8224 GHz (a), variable temperature W Band EPR spectra of **4** measured at 93.96804 GHz (b), and variable temperature W Band EPR spectra of **2** measured at 93.1243 GHz (c)*

The variable temperature W Band spectra of **8** are shown in Figure 66 (a), and the comparisons with the single wheels **4** and **2** are shown in Figure 66 (b) and Figure 66 (c) respectively. The spectrum of **8** has a feature at 1557 mT that also appears in the spectrum of **2** and in both spectra this feature diminishes at higher temperatures. The features in the spectrum of **8** at 2470 mT and 2669 mT appear in the spectra of **2** and **4** respectively, and in both cases they disappear at higher temperatures. At higher temperatures, the W-Band spectrum of **8** is dominated by a single feature at 3389

mT, which matches the trend in the W-Band spectrum of **2** where the feature at 3301 mT increases intensity at higher temperatures as compared to the other features in the spectrum. The temperature-dependence of the features of the W-Band spectrum of **8** are represented in the temperature-dependence of the features of the W-Band spectra of **4** and **2**, further reinforcing the interpretation of the dimer as a linear sum of the two components.

[Cr₇Zn purple] – {Cr₇Ni green} dimer   9

Legend:
- Cr$_7$Zn(p) (4) + Cr$_7$Ni (g) (3) linear sum
- Cr$_7$Ni(g) (3)
- Cr$_7$Zn(p) (4)
- Cr$_7$Zn(p)-Cr$_7$Ni(g) dimer (9)

Field (mT)

*Figure 67 Q Band spectrum at 5 K of **9** (black), **4** (purple), **3** (green) and linear sum of spectra of **4** and **3** (red)*

The Q Band spectrum of **9** shows two very distinct features at 1219 mT and 1347 mT, and a broader feature at 228 mT. The feature at 1219 mT, and the smaller features in its vicinity, is clearly a contribution from **4**. There is clearly a discrepancy in position, which is due to a slight variation in the frequency at which experiments were taken. The feature at at 1347 mT is a contribution due to **3**. The linear sum of **4** and **3** reproduces all of the features in **9**, though the relative intensity is not correct and could be reproduced by favouring the contributions from **3**.
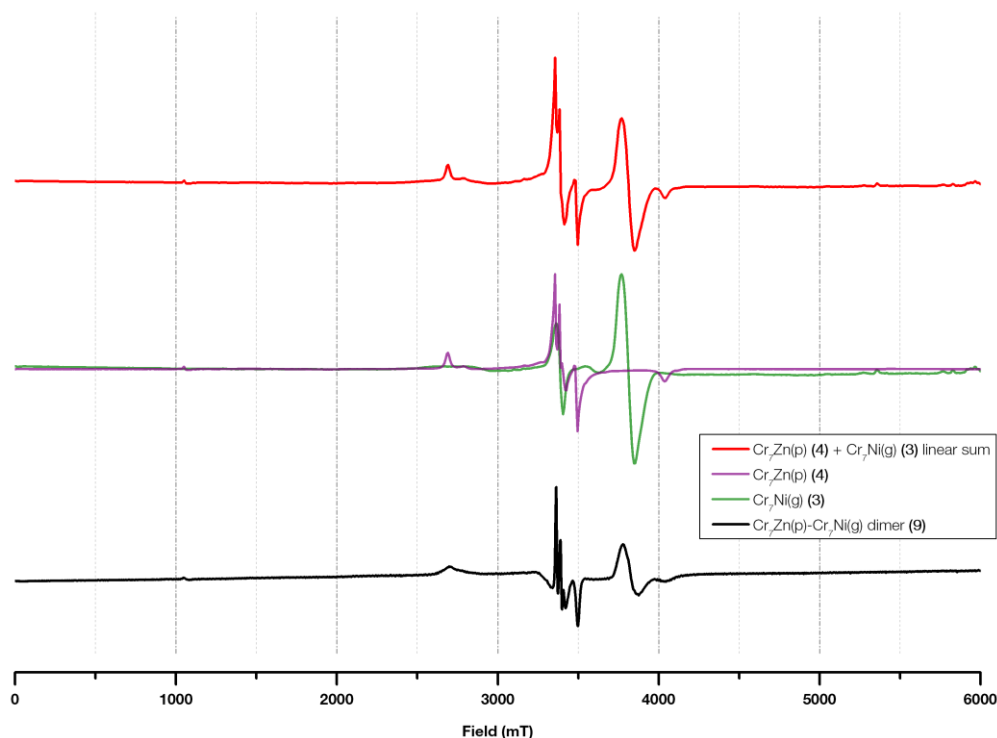
*Figure 68 W Band spectrum at 5 K of **9** (black) measured at 95.4321 GHz, **4** (purple), **3** (green) and linear sum of spectra of **4** and **3** (red)*

The W-Band spectrum of **9** is shown in Figure 68, together with the W-Band spectra of the single wheels **4** and **3**. The spectrum of the dimer is well reproduced by the linear sum of the individual wheels. The dimer spectrum has a peak at 2705 mT, which occurs in the purple Cr_7Zn spectrum. The sharp central features at 3364 mT, 3383 mT and 3462 mT also occur in the purple Cr_7Zn spectrum while the feature at 3803 mT occurs in the green Cr_7Ni spectrum.
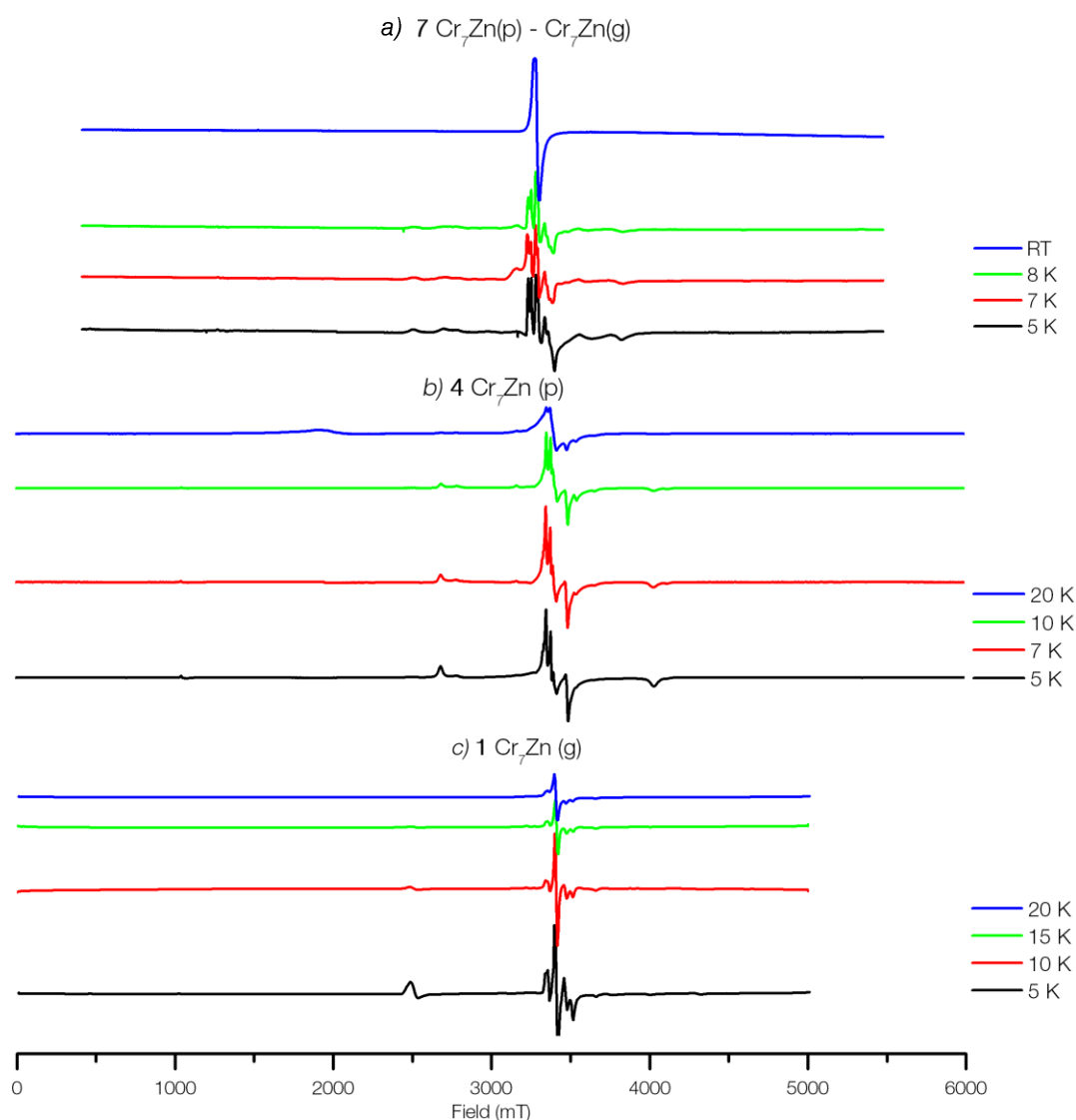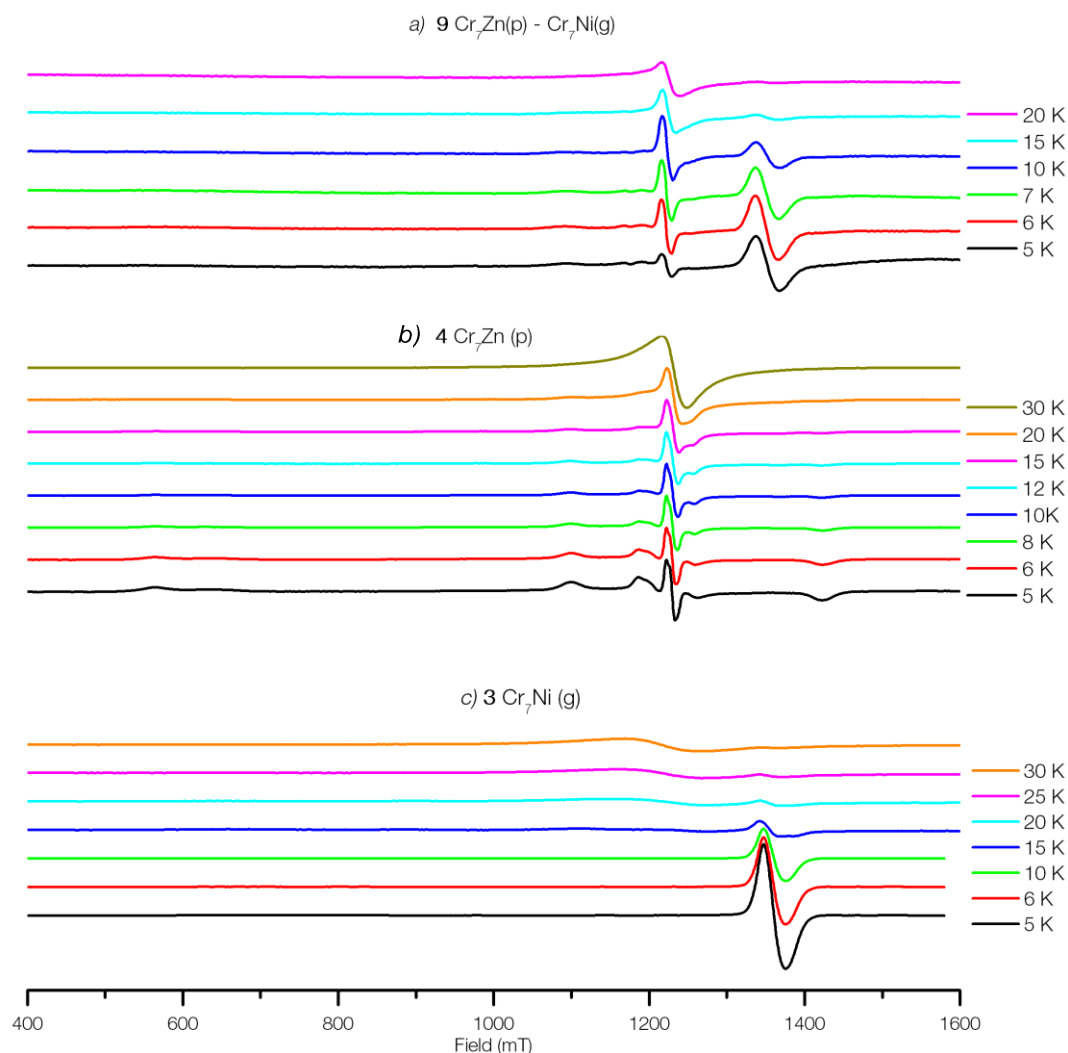
*Figure 69 Variable temperature Q Band EPR spectra of **9** measured at 34.1419 GHz (a), variable temperature Q Band EPR spectra of **4** measured at 34.1587 GHz (b), and variable temperature Q Band EPR spectra of **3** measured at 33.2238 GHz (c)*

The variable temperature Q Band spectra of **9** are shown in Figure 69 (a), and the comparisons with the single wheels **4** and **3** are shown in Figure 69 (b) and Figure 69 (c) respectively. The spectrum of **9** shows the dominance of the feature at 1219 mT at higher temperatures, which is mirrored in the spectrum of **4**. The feature at 1347 mT in the spectrum of **9** is prominent at low temperatures, but rapidly diminishes at 15 K and above, which is also seen in the spectrum of **3**. The temperature-

dependence of the features of the Q-Band spectrum of **9** are represented in the temperature-dependence of the features of the Q-Band spectra of **4** and **3**, further reinforcing the interpretation of the dimer as a linear sum of the two components.
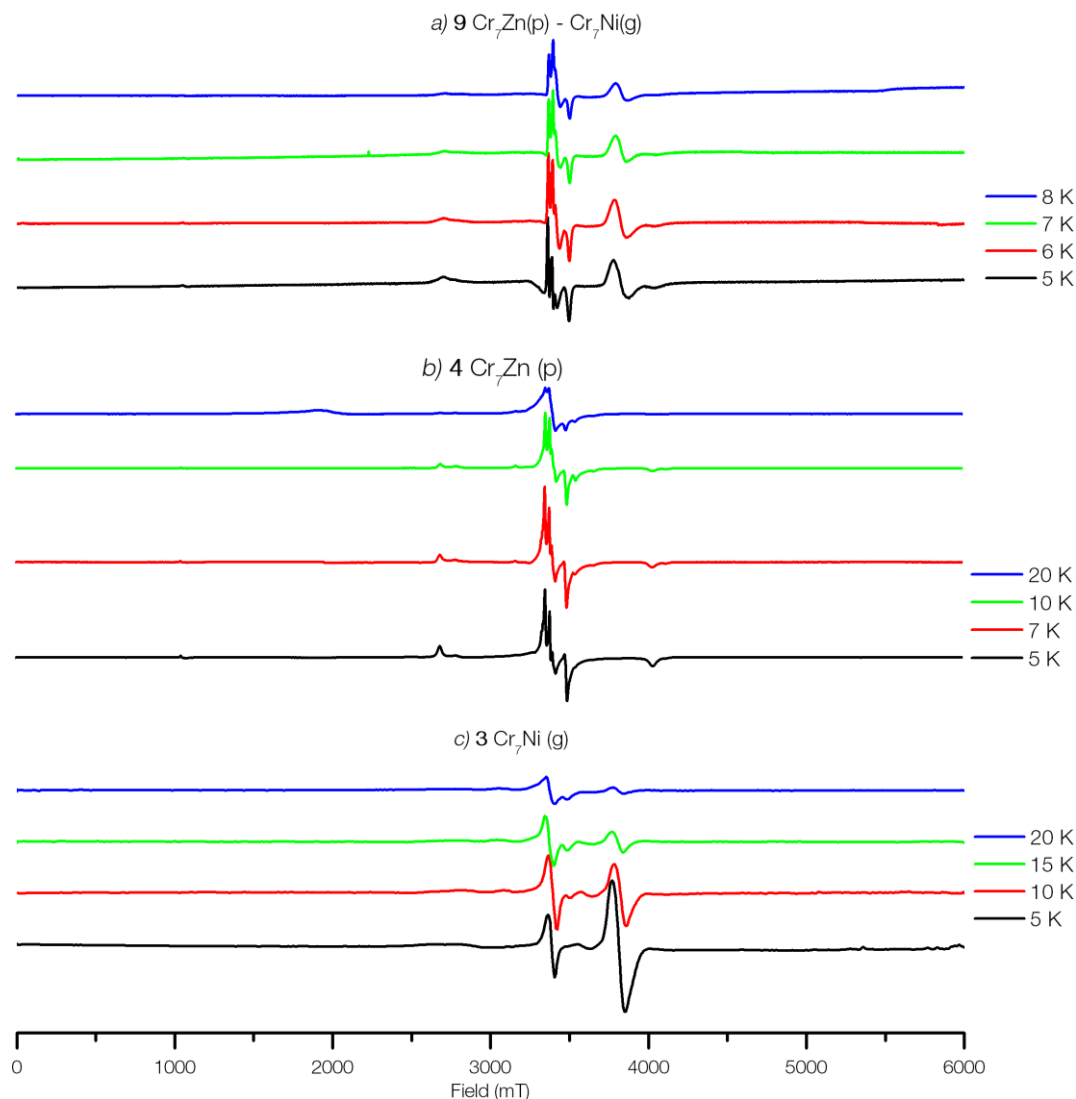

*Figure 70 Variable temperature W Band EPR spectra of **9** measured at 95.4321 GHz (a), variable temperature W Band EPR spectra of **4** measured at 93.96804 GHz (b), and variable temperature W Band EPR spectra of **3** measured at 94.321 GHz (c)*

The variable temperature W Band spectra of **9** are shown in Figure 70 (a), and the comparisons with the single wheels **4** and **3** are shown in Figure 70 (b) and Figure 70 (c) respectively. The W Band spectrum of **9** has a feature at 3803 mT which is prominent at low temperatures but decreases in intensity as temperature increases, which is mirrored in the W Band spectra of **3**. The sharp features at 3364 mT, 3383

153

mT and 3462 mT in the W Band spectrum of **9** begin to merge into each other at higher temperatures, and similar behaviour is also seen in those features in the W Band spectra of **4**. The intensity of the small feature at 2705 mT in the W Band spectrum of **9** decreases with increasing temperature, which also occurs to that feature in the W Band spectrum of **4**. The temperature-dependence of the features of the W-Band spectrum of **9** are represented in the temperature-dependence of the features of the W-Band spectra of **4** and **3**, further reinforcing the interpretation of the dimer as a linear sum of the two components.

[Cr₇Mn purple] – {Cr₇Zn green} dimer   10

For the remaining compounds in the series, there can in principle be expected to be some communication between the rings. Simulations with non-zero *J'* are going to be required to model these systems.
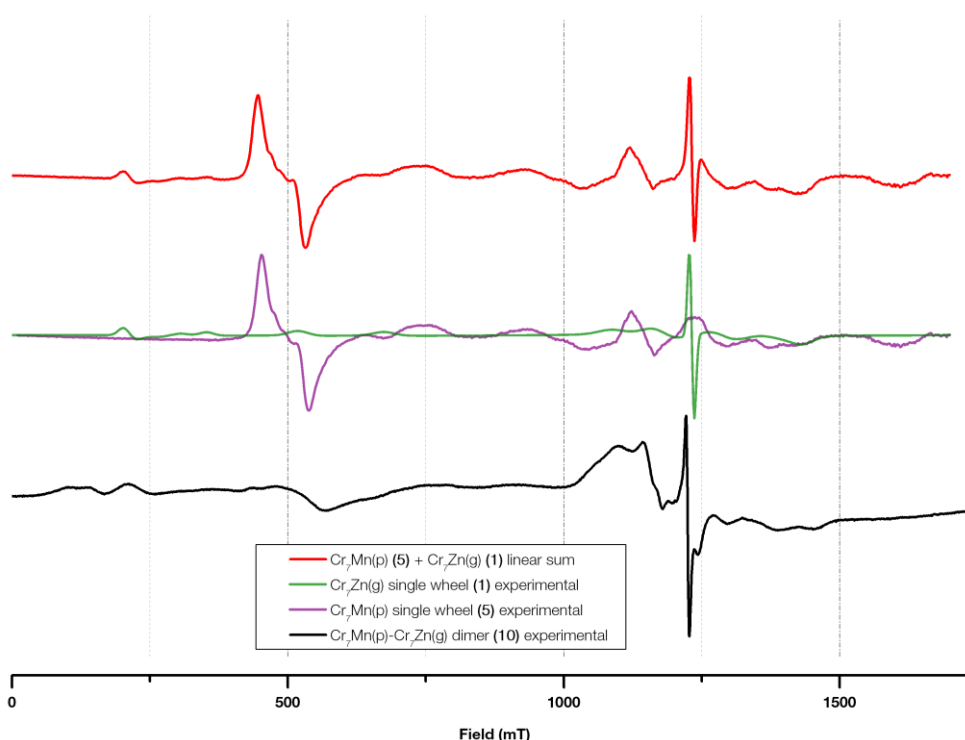

*Figure 71 Q Band spectrum at 5 K of **10** (black), **5** (purple), **1** (green) and linear sum of spectra of **5** and **1** (red)*

The Q band spectrum of the dimer **10** is compared to that of the single wheels and their linear sum in Figure 71. The dimer spectrum has a sharp central feature at 1224 mT, which occurs in the spectrum of the green Cr_7Zn **1.** The dimer spectrum has two peaks at 1150 mT and 1097 mT, while the linear sum only has one peak in that approximate region from the spectrum of **5**. The spectrum of **5** also has a prominent feature at 490 mT, which does appear – albeit very much broadened.

Unlike dimers containing the purple Cr_7Zn (**4**), the spectrum of **10** is not well reproduced by the linear sum of the single wheels. This indicates that there is some

communication between the wheels, a non-zero exchange interaction that affects the

5 K Q-Band spectrum of **10**.
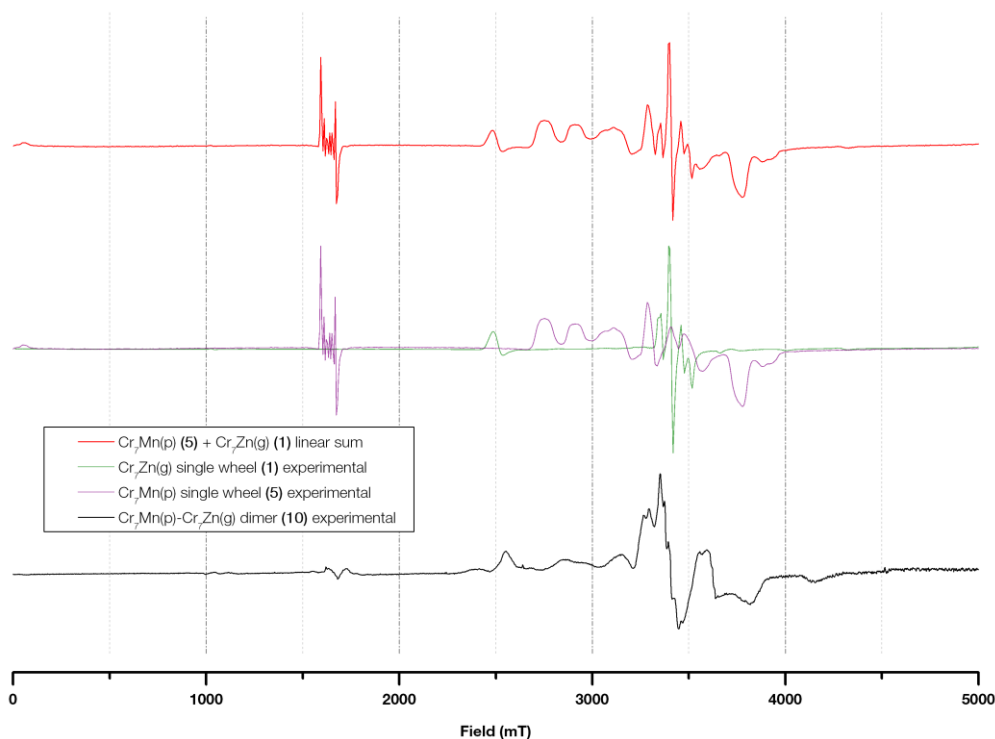
Figure 72 W Band spectrum of 10 (black), 5 (purple), 1 (green) and linear sum of spectra of 5 and 1 (red)

The comparison of the W Band spectrum of the dimer **10** and the single wheels **1** and

5 is shown in Figure 72. In the central region of the dimer spectrum, there are nine

peaks in the region of 3269 mT to 3603 mT. The linear sum has only seven peaks,

and they appear much sharper than in the dimer spectrum. The features in the dimer

spectrum are much broader than the linear sum. The Cr$_7$Mn purple (**5**) spectrum

shows the Mn^{2+} hyperfine splitting at the half-field resonance. This does not appear

in the dimer spectrum at all. The broadening of the dimer spectrum in comparison

with the linear sum of the individual wheels suggests that there is a non-zero

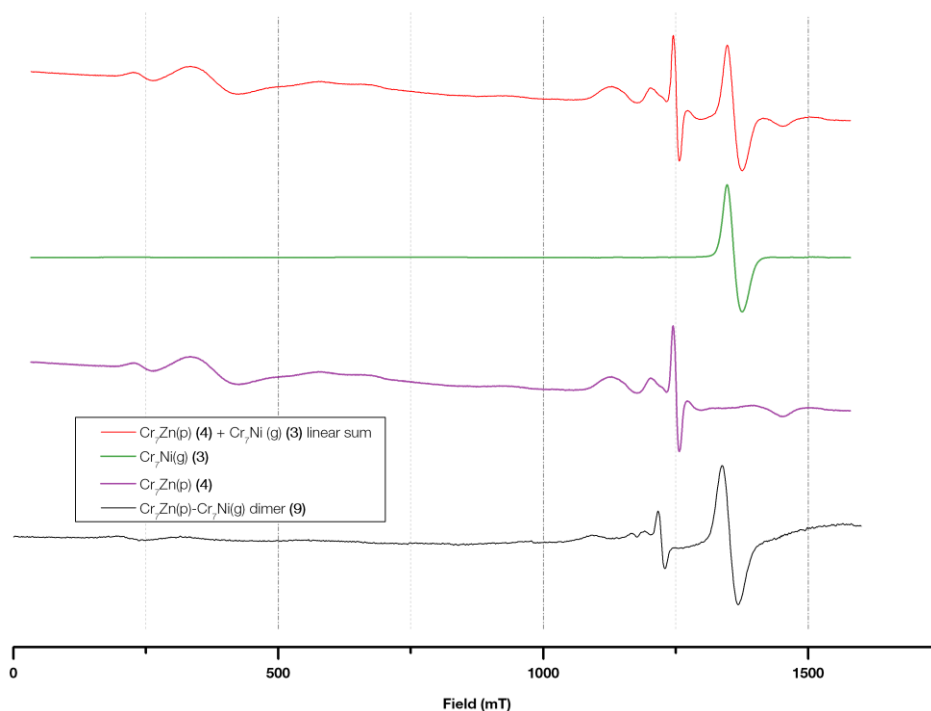exchange interaction between the wheels that affects the W-Band spectrum.

*Figure 73 Variable temperature Q Band EPR spectra of **10** measured at 34.1076 GHz (a), variable temperature Q Band EPR spectra of **5** measured at 34.1697 GHz (b), and variable temperature Q Band EPR spectra of **1** measured at 34.1238 GHz (c)*

The variable temperature Q Band spectra of **10** are shown in Figure 73 (a), and the comparisons with the single wheels **5** and **1** are shown in Figure 73 (b) and Figure 73 (c) respectively. The Q Band spectra of **10** have a sharp central feature at 1224 mT, which increases in intensity and merges with adjacent, broader features at higher temperatures. While the position of this feature corresponds precisely with the spectra of **1**, the temperature-dependent behaviour of the feature is somewhat different. This may in part be due to the contribution of the large broad feature in the spectra of **5**, which increases in intensity at higher temperatures. The spectra of **5**

have a feature at 490 mT which is prominent at low temperatures and diminishes with increasing temperature. While there does appear to be a broadened feature at that position in the spectra of **10**, this feature is already greatly diminished at 5 K and does not resemble the feature in the spectra of **5**.

The temperature-dependence of the features of the Q-Band spectrum of **10** are not all represented in the temperature-dependence of the features of the Q-Band spectra of **5** and **1**, further indicating that there is a non-zero exchange interaction between the wheels.

*Figure 74 W Band EPR spectra of **10** measured at 95.7853 GHz (a), variable temperature W Band EPR spectra of **5** measured at 94.8821 GHz (b), and variable temperature W Band EPR spectra of **1** measured at 93.72122 GHz (c)*

The variable temperature W Band spectra of **10** are shown in Figure 74 (a), and the comparisons with the single wheels **5** and **1** are shown in Figure 74 (b) and Figure 74 (c) respectively. The W Band spectrum of **10** at 5 K has many sharp features in the range of 3269 mT to 3603 mT, which broaden and merge at higher temperatures. Although these features do not appear to map directly on to any specific features in the spectra of **5** or **1**, the features in **5** do all diminish with increasing temperature except for a single feature at 3290 mT.

The temperature-dependence of the features of the W-Band spectrum of **10** are not all represented in the temperature-dependence of the features of the W-Band spectra of **5** and **1**, further indicating that there is a non-zero exchange interaction between the wheels.
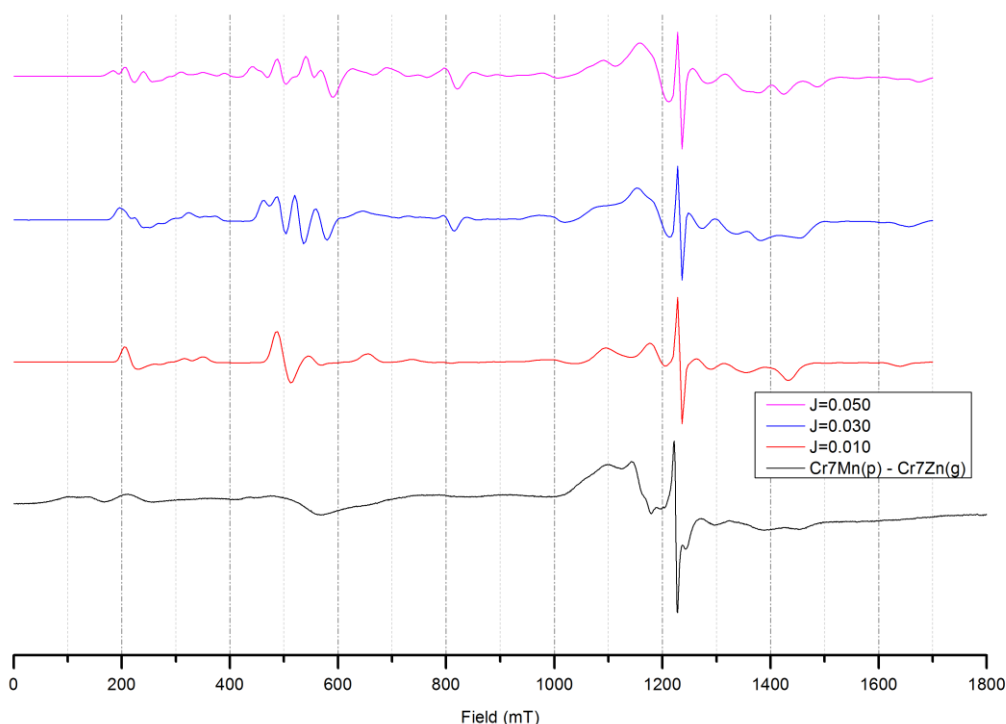
*Figure 75 Q Band spectrum at 5 K (black) and simulation of **10** with J' = 0.01 K (red), J' = 0.03 K, J' = 0.05 K*

Simulations of **10** focusing on small positive values of *J'* are shown in Figure 75, showing the effects of *J'* on the spectrum. The difficulty in these simulations comes at balancing the presence of the features at 1140 mT and 1087 mT with the low field features at 541 mT and 163 mT. Of these simulations, the 1140 mT and 1087 mT features are most accurately reproduced with *J'* = 0.03 mT, but the 498 mT feature is split into multiple features. In the experimental spectrum, there is a broad feature that spans this field range but does not at all appear as in the simulation. This discrepancy cannot be resolved simply by increasing the magnitude of broadening parameters as

this affects the 1140 mT and 1087 mT features as well. At values of *J'* greater than 0.05 K, the 1140 mT and 1087 mT features merge into one large feature with an intensity greater than that of the sharp 1219 mT feature.
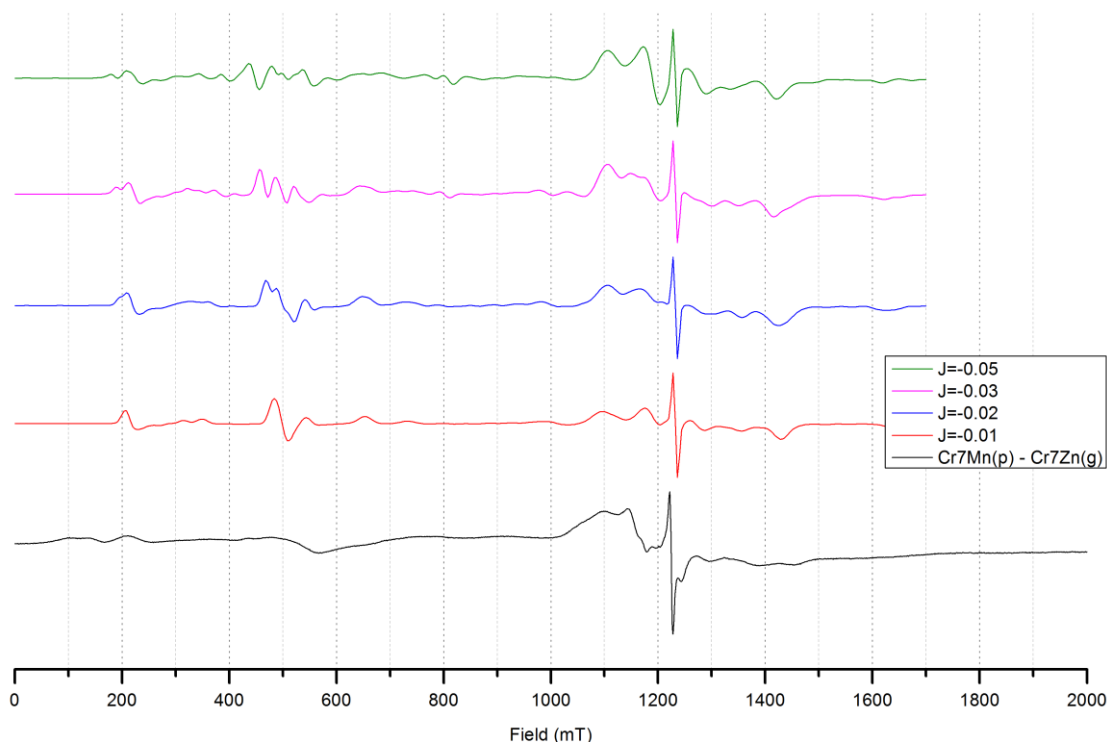
*Figure 76 Q Band spectrum at 5 K (black) and simulation of **10** with J' = -0.01 K (red), J' = -0.02 K (blue), J' = -0.03 K (pink), J' = -0.05 K (green)*

Simulations of **10** with small negative values of *J'* are shown in Figure 76. These simulations have the same problem with the low field feature as the positive *J'* simulations in Figure 75. The behaviour of the 1140 mT and 1087 mT features is different, remaining distinct even at *J'* = -0.05 K. The 1140 mT and 1087 mT features are most accurately reproduced with *J'* = -0.02 K, but the 498 mT is once again split into multiple features that do not correspond to the experimental spectrum. Below *J'* = -0.05 K, the intensity of the two 1140 mT and 1087 mT features overcomes the sharp 1219 mT feature.

While no single simulation reproduces the experimental spectrum precisely, these simulations do set boundaries on possible values of J' within this model: $(0.01 < |J'| < 0.05)$ K

[Cr$_7$Mn purple] – {Cr$_7$Mn green} dimer   11
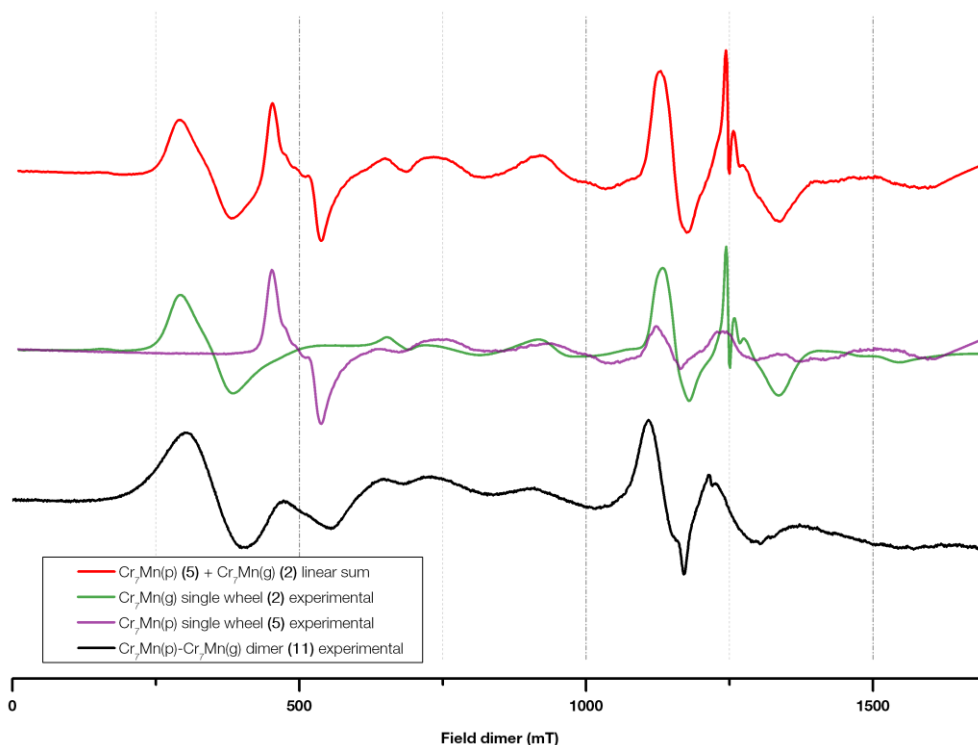
Figure 77 Q Band spectrum at 5 K of 11 (black), 5 (purple), 2 (green) and linear sum of spectra of 5 and 2 (red)

The comparison of the Q Band spectrum of the dimer **11** to the spectra of the single wheels **5** and **2** is shown in Figure 77. The dimer spectrum has a peak at 1105 mT, which corresponds to peaks in the spectrum of both single wheels and is well reproduced in the linear sum of the single wheels. The spectrum of the green wheel **2** has a sharp feature at 1243 mT, which does appear in the dimer spectrum, but with much less intensity relative to the peak at 1105 mT.

The spectrum of the green wheel **2** has a broad low-field feature at 287 mT, and an almost identical feature appears in the spectrum of the dimer **11**. The purple wheel spectrum has a low-field feature at 482 mT, and while the dimer spectrum does have a feature at this position it is again with much less intensity. The linear sum of the individual wheels does not reproduce the dimer spectrum, suggesting that there may

be a non-zero exchange interaction between the wheels that is broadening certain features.


*Figure 78 W Band spectrum at 5 K of **11** (black), **5** (purple), **2** (green) and linear sum of spectra of **5** and **2** (red)*

The W Band spectrum of **11** at 5 K is compared to the W Band spectra of the single wheels **5** and **2** in Figure 78. As with the W Band spectrum of **10**, the Mn^{2+} hyperfine splitting at the half-field resonance of the spectrum of **5** does not appear clearly resolved in the dimer spectrum **11**. There does appear a much smaller, broadened feature at that position in the dimer spectrum. The high field features, in the range of 2515 mT to 3835 mT, in the dimer spectrum are somewhat reproduced in the linear sum spectrum but with significant broadening – with the possible exception of the feature at 4182 mT from the spectrum of the green wheel **2**, which does not seem to appear in the dimer spectrum at all. The linear sum of the W Band spectra of **5** and **2** do not reproduce the dimer spectrum, suggesting a non-zero exchange interaction is necessary to model the spectrum.
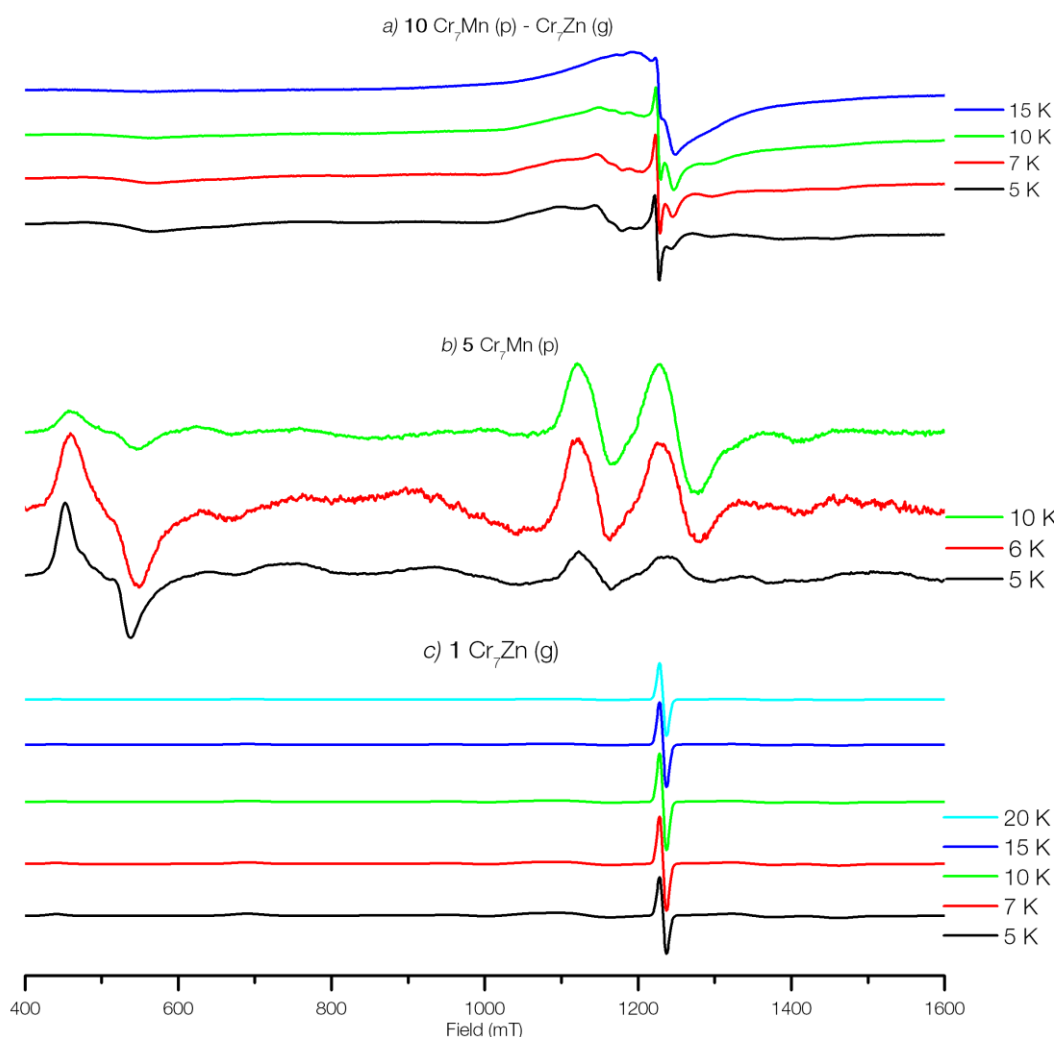
*Figure 79 Variable temperature Q Band EPR spectra of **11** measured at 33.9295 GHz (a), variable temperature Q Band EPR spectra of **5** measured at 34.1697 GHz (b), and variable temperature Q Band EPR spectra of **2** measured at 34.0978 GHz (c)*

The variable temperature Q Band spectra of **11** are shown in Figure 79 (a), and the comparisons with the single wheels **5** and **2** are shown in Figure 79 (b) and Figure 79 (c) respectively. The spectra of **11** have a feature at 1105 mT which grows in intensity with increasing temperature, and corresponds to the similar behaviour of that feature in the spectra of **5**. The 5 K spectrum of **2** has a prominent, sharp feature at 1243 mT which quickly diminishes at higher temperatures, and the spectra of **11** have a small blip in that position that behaves similarly, disappearing at 15 K. The

spectra of **11** have a feature at 1105 mT that grows in intensity with increasing temperature. Both the spectra of **5** and **2** have a feature in this position, but the feature in the spectra of **2** decreases in intensity with increasing temperature while in **5** it grows with increasing temperature.

The temperature-dependence of the features of the Q-Band spectrum of **11** are not all represented in the temperature-dependence of the features of the Q-Band spectra of **5** and **2**, further indicating that there is a non-zero exchange interaction between the wheels.
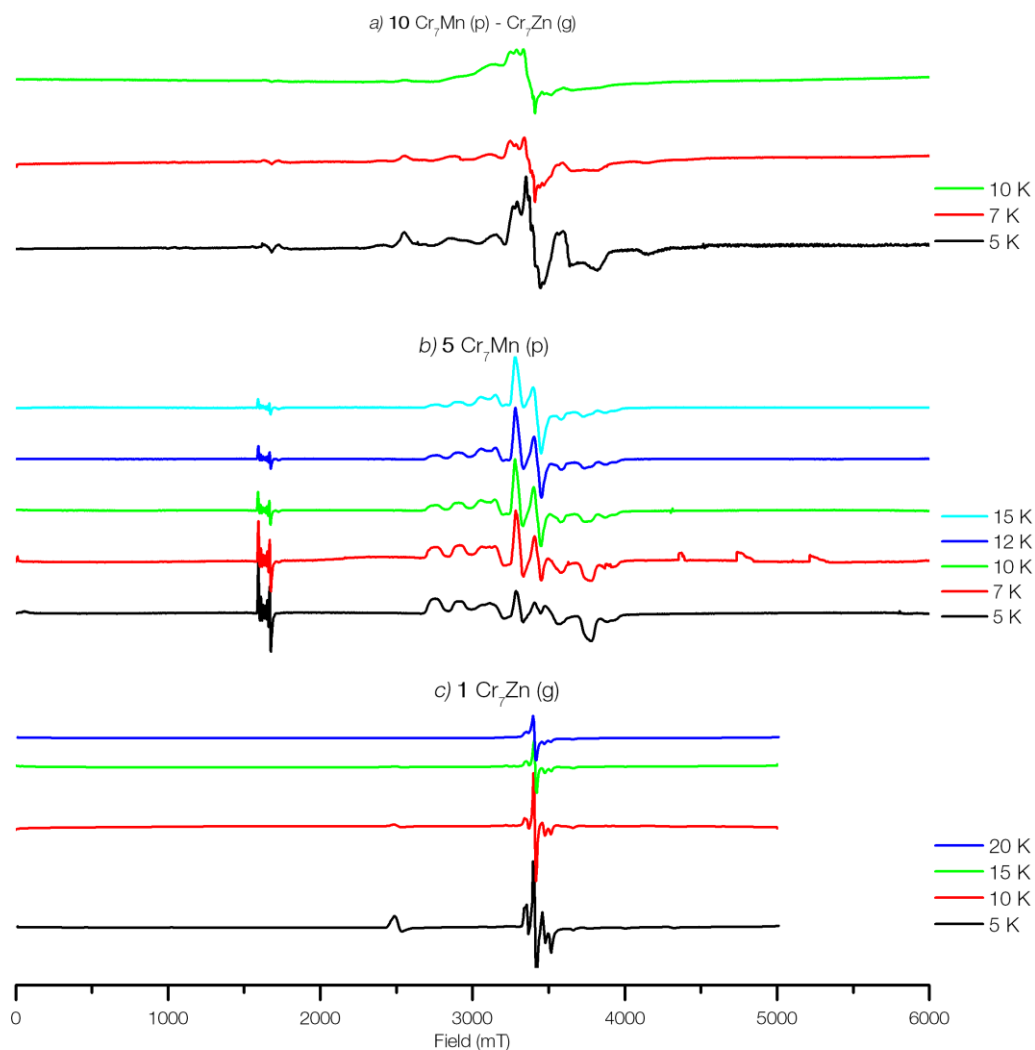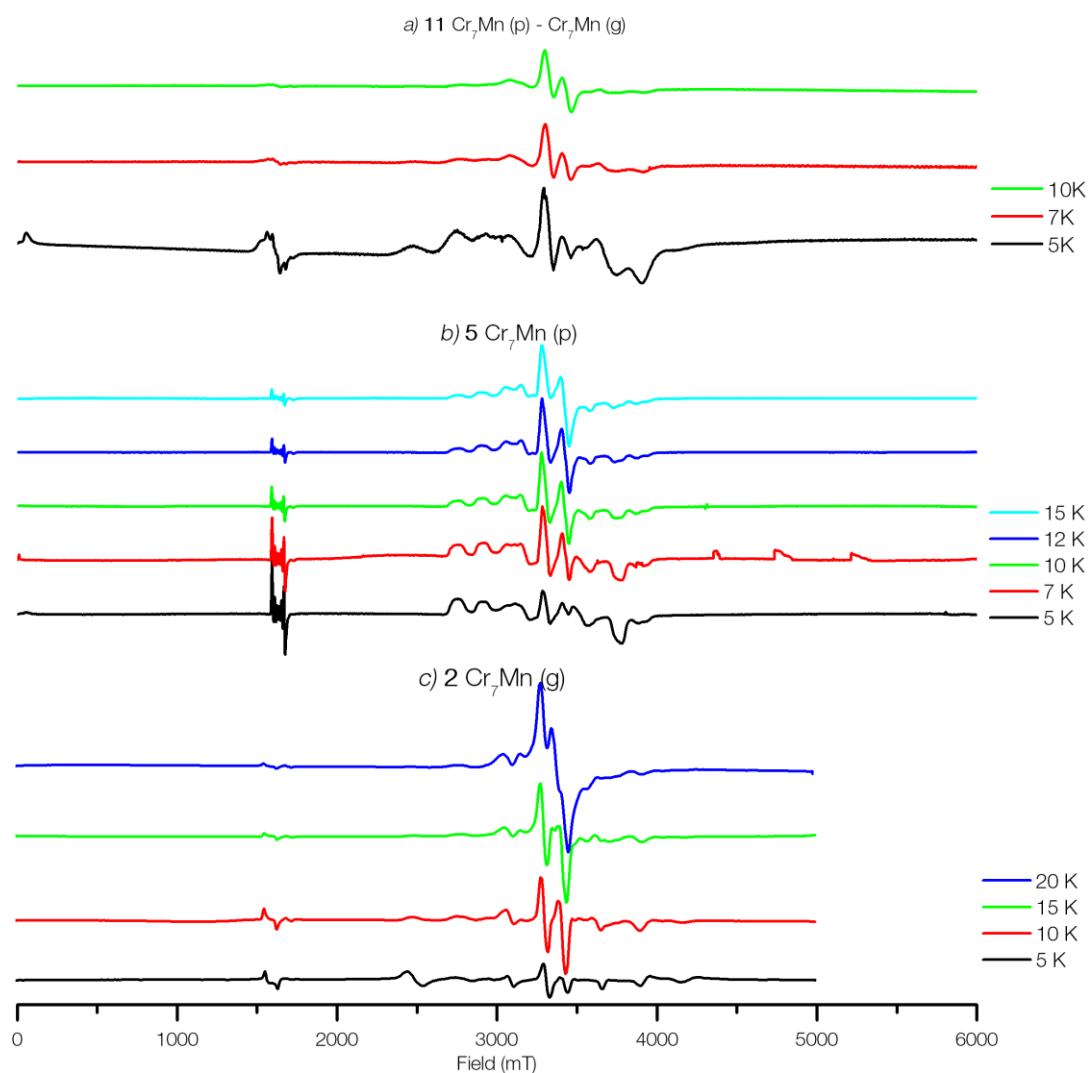
*Figure 80 Variable temperature W Band EPR spectra of **11** measured at 94.1712 GHz (a), variable temperature W Band EPR spectra of **5** measured at 94.8821 GHz (b), and variable temperature W Band EPR spectra of **2** measured at 93.1243 GHz (c)*

The variable temperature W Band spectra of **11** are shown in Figure 80 (a), and the comparisons with the single wheels **5** and **2** are shown in Figure 80 (b) and Figure 80 (c) respectively. The small sharp blips at 3039 mT in the 5 K spectrum of **11** and 3960 mT in the 7 K spectrum of **11** are due to corrections to the frequency during the experiment. The feature at 67 mT in the 5 K spectrum of **11** is unlikely to be a feature from the sample, and is a common blip from the W Band instrument. The spectra of **11** have a feature at 3396 mT which grows slightly in intensity with

increasing temperature, which approximately corresponds to a similar feature in the spectra of **2**. The features at 1579 mT in the spectra of **11** diminish with increasing temperature. Both the spectra of **5** and **2** have features in this position with the same temperature-dependence, but the feature in **11** does not match the detail or shape of either.

The temperature-dependence of the features of the W-Band spectrum of **11** are not all represented in the temperature-dependence of the features of the W-Band spectra of **5** and **2**, further indicating that there is a non-zero exchange interaction between the wheels.


*Figure 81 Simulations of Q Band 5K spectrum of **11** with J' = 0.2 K, J' = 0.3 K, J' = 0.4 K, J' = 0.5 K, J' = 0.6 K, J' = 0.7 K, J' = 0.8 K, J' = 0.9 K*

Figure 81 shows attempts at fitting the Q Band 5 K spectrum of **11** using positive values of *J'*. It is clear that *J'* has a complex effect upon the spectrum, most

prominently in the position of low field features. With J' = 0.3 K, those low field features are far off from the experimental spectrum though the 1121 mT and 1190 mT features appear to be reproduced fairly correctly. Increasing J' moves the low field feature into position, but appears to suppress the 1190 mT feature. At J' = 0.6 K, the 1190 mT feature emerges again. A fairly good compromise is made with J' = 0.7 K.
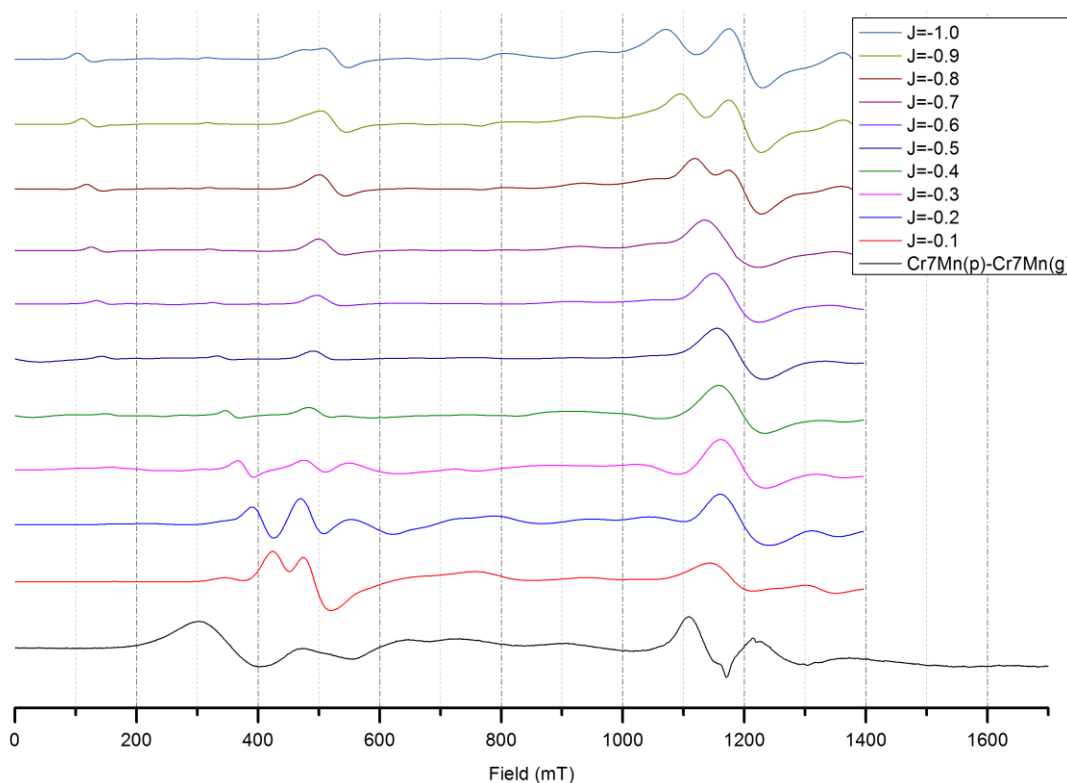
*Figure 82 Simulations of Q Band 5 K spectrum of **11** with J' = -0.2 K, J' = -0.3 K, J' = -0.4 K, J' = -0.5 K, J' = -0.6 K, J' = -0.7 K, J' = -0.8 K, J' = -0.9 K*

The effect of negative values of J' is shown in Figure 82. As J' increases in magnitude, the low field feature at 307 mT is entirely absent and the 1121 mT and 1190 mT features are increasingly split apart, and no negative value of J' will reproduce the experimental spectrum.

Within this model, the best fit is found within the range $(0.6 < J' < 0.8)$ K.

[Cr₇Mn purple] – {Cr₇Ni green} dimer   12
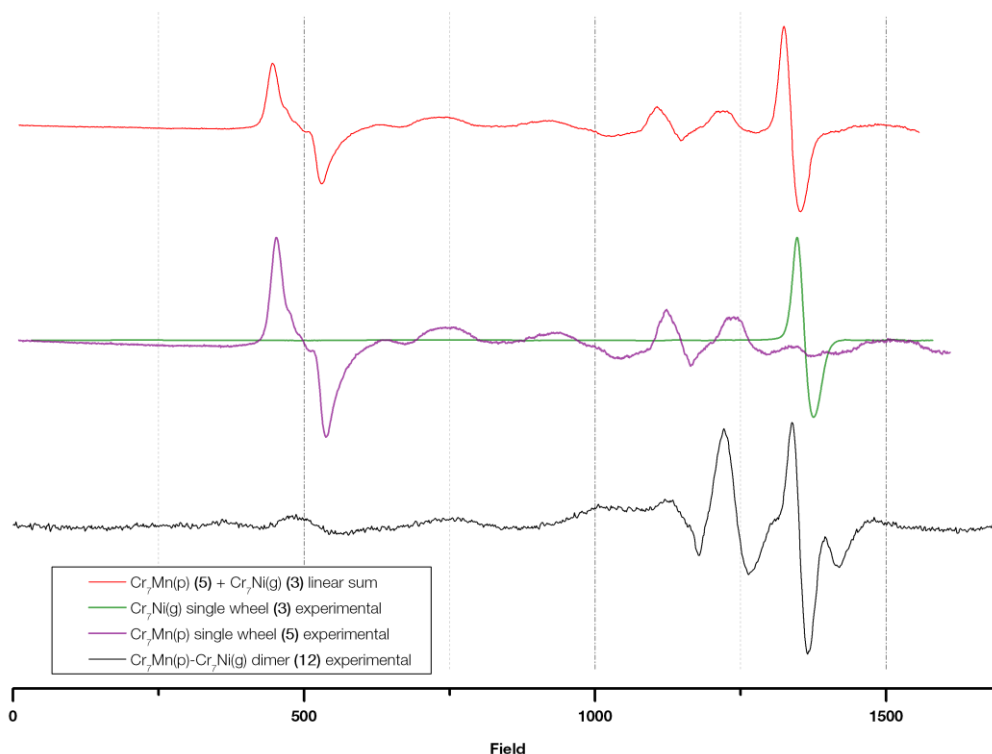
*Figure 83 Q Band spectrum at 5 K of **12** (black), **5** (purple), **3** (green) and linear sum of spectra of **5** and **3** (red)*

The comparison between the Q Band spectrum of the dimer **12** and the single wheels **5** and **3** is shown in Figure 83. The green wheel spectrum **3** features a single feature at 1356 mT, which also appears in the dimer spectrum. The dimer spectrum shows two peaks at 1214 mT and 1131 mT, which correspond to two peaks in the spectrum of **5** but with differing relative intensities. The spectrum of **5** has a large low-field feature at 508 mT, and the dimer spectrum does appear to have a feature at this position although it occurs with much less intensity. This broadening, in comparison to the linear sum of **5** and **3**, suggests that there should be an exchange interaction that affects the spectrum.
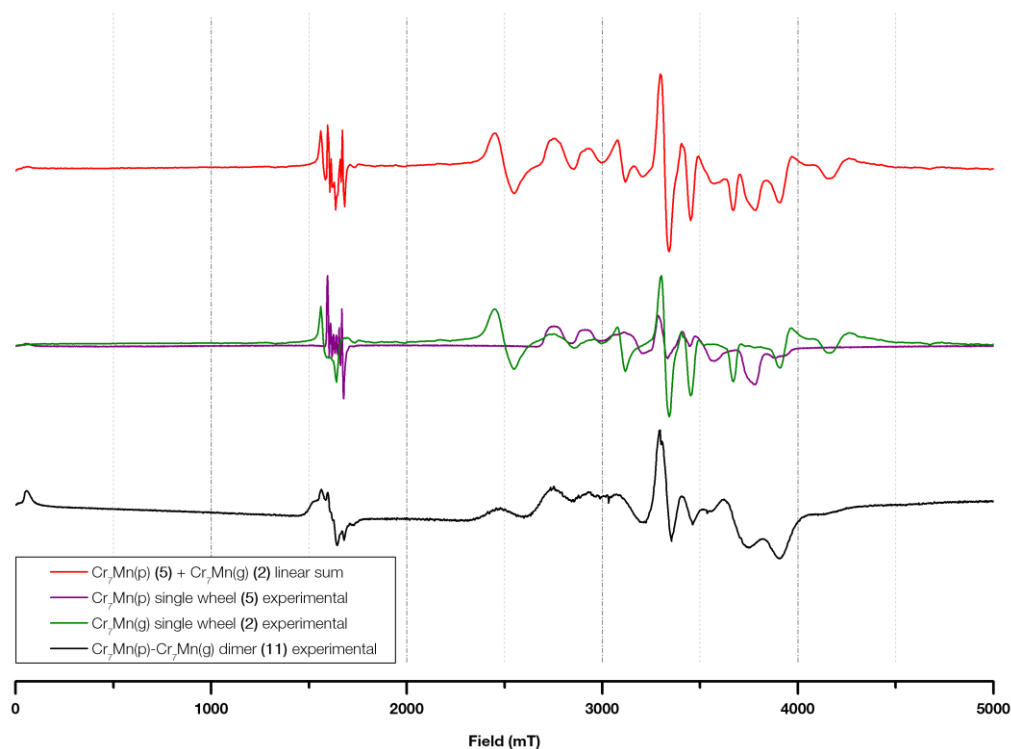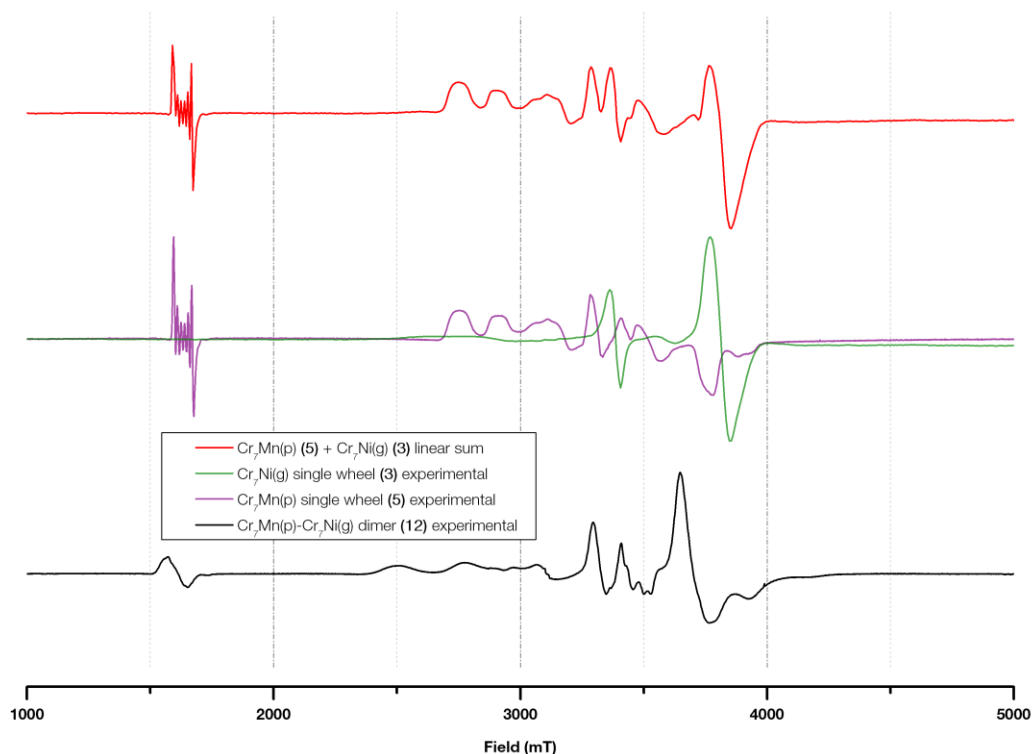
*Figure 84 W Band spectrum at 5 K of **12** (black), **5** (purple), **3** (green) and linear sum of spectra of **5** and **3** (red)*

The comparison of the W Band spectrum of **12** to the single wheels **5** and **3** is shown

in Figure 84. The green single wheel **3** spectrum has two features, at 3367 mT and

3772 mT and these two features appear in the dimer spectrum as well, though at

slightly offset field positions. The purple wheel **5** spectrum has a feature at 3283 mT,

which also appears in the dimer spectrum. The features at 2729 mT, 2897 mT and

3102 mT also appear in the dimer spectrum but much more broadened. As with the

W Band spectra of **10** and **11**, the Mn^{2+} hyperfine splitting at the half-field resonance

of the spectrum of **5** does not appear resolved in the dimer spectrum of **12**. The

differences between the dimer spectrum and the linear sum of **5** and **3** indicate that

there is a non-zero exchange interaction that affects the spectrum.
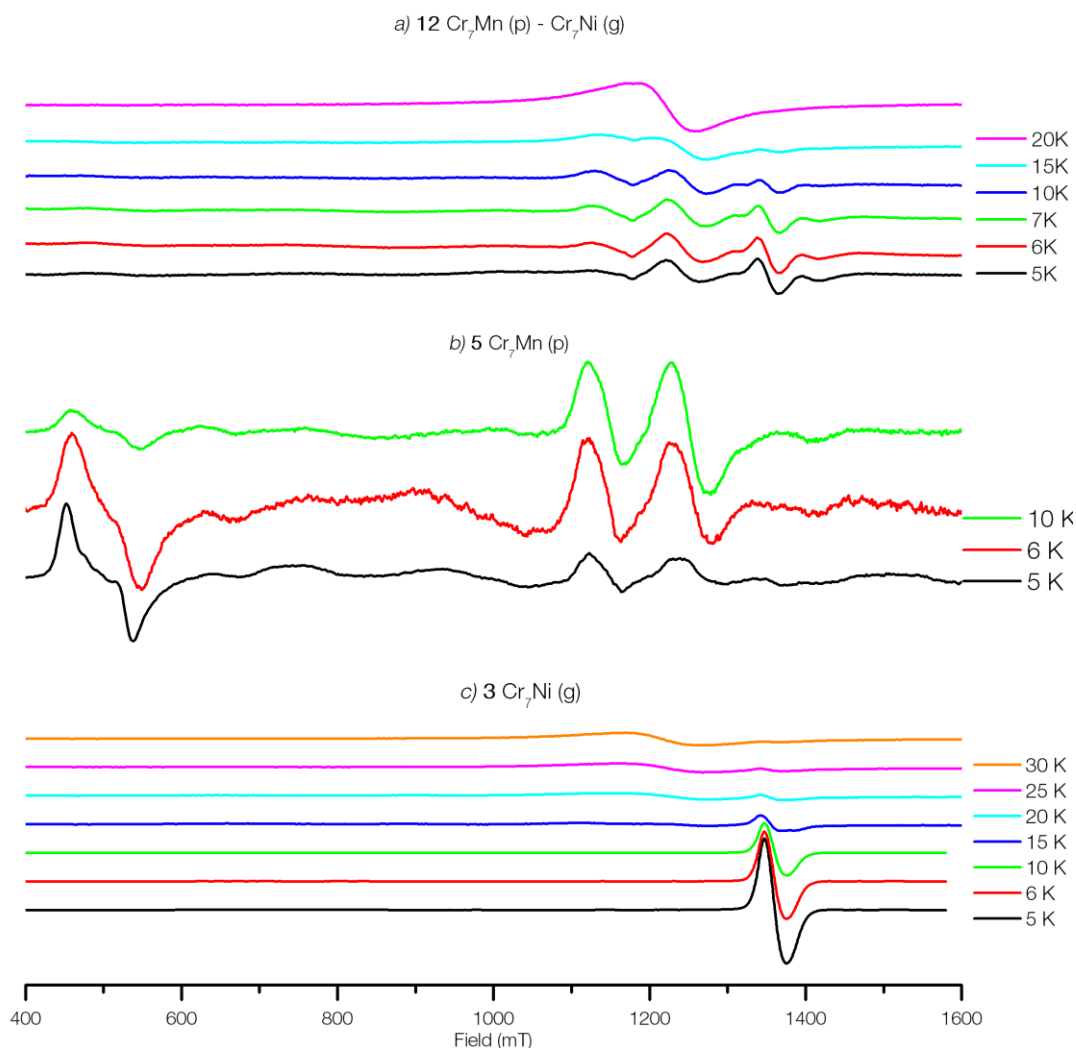
*Figure 85 Variable temperature Q Band EPR spectra of **12** measured at 34.1286 GHz (a), variable temperature Q Band EPR spectra of **5** measured at 34.1697 GHz (b), and variable temperature Q Band EPR spectra of **3** measured at 33.2238 GHz (c)*

The variable temperature Q Band spectra of **12** are shown in Figure 85 (a), and the comparisons with the single wheels **5** and **3** are shown in Figure 85 (b) and Figure 85 (c) respectively. The feature at 1356 mT in the spectra of **12** diminishes with temperature and almost entirely disappears by 15 K, which matches the behaviour of that feature in the spectra of **3**. The features at 1131 mT and 1214 mT in the spectra of **12** broaden into one large feature at 20 K. This does not match the behaviour of the features in the spectra of **5**, although a similar feature does appear in the 30 K spectrum of **3**.

The temperature-dependence of the features of the Q-Band spectrum of **12** are not all represented in the temperature-dependence of the features of the Q-Band spectra of **5** and **3**, further indicating that there is a non-zero exchange interaction between the wheels.
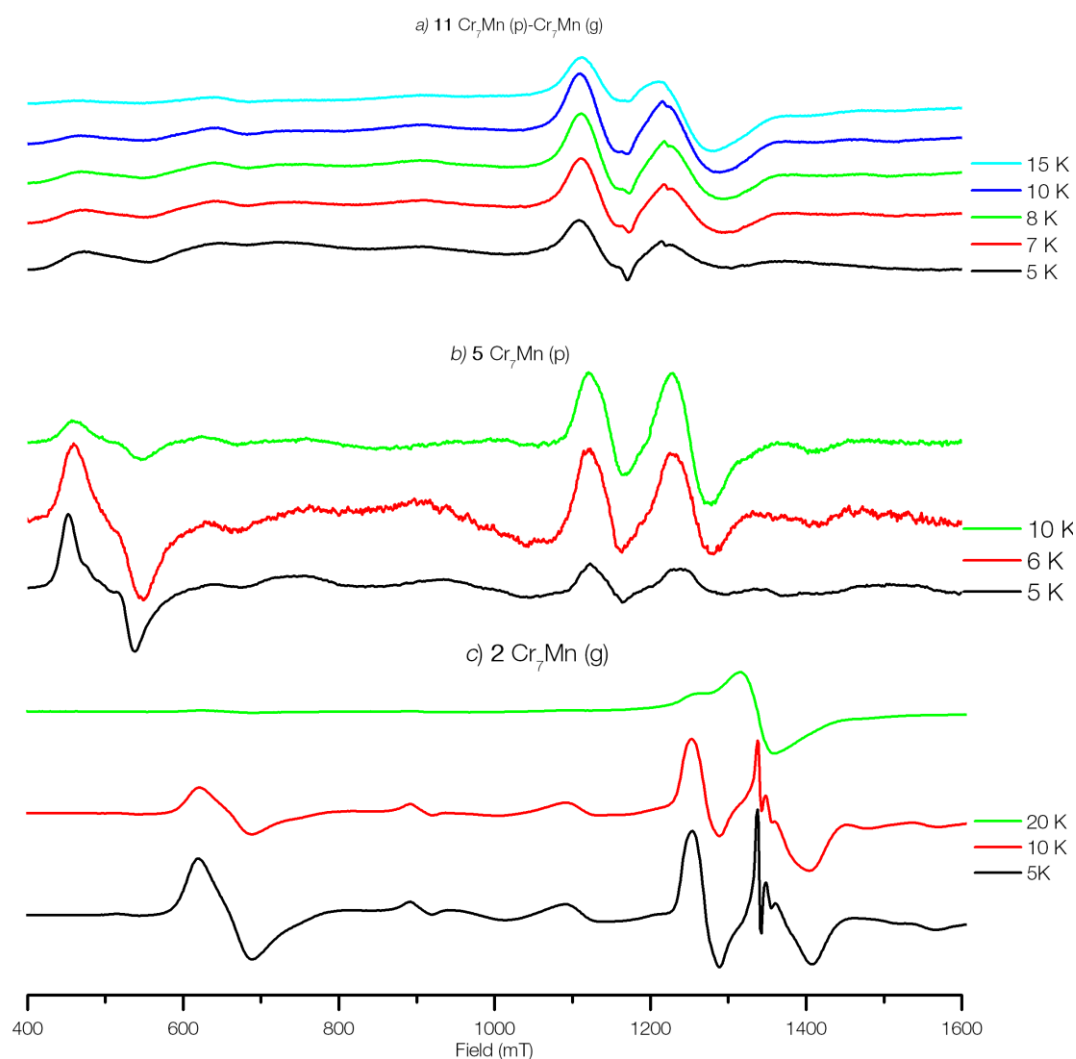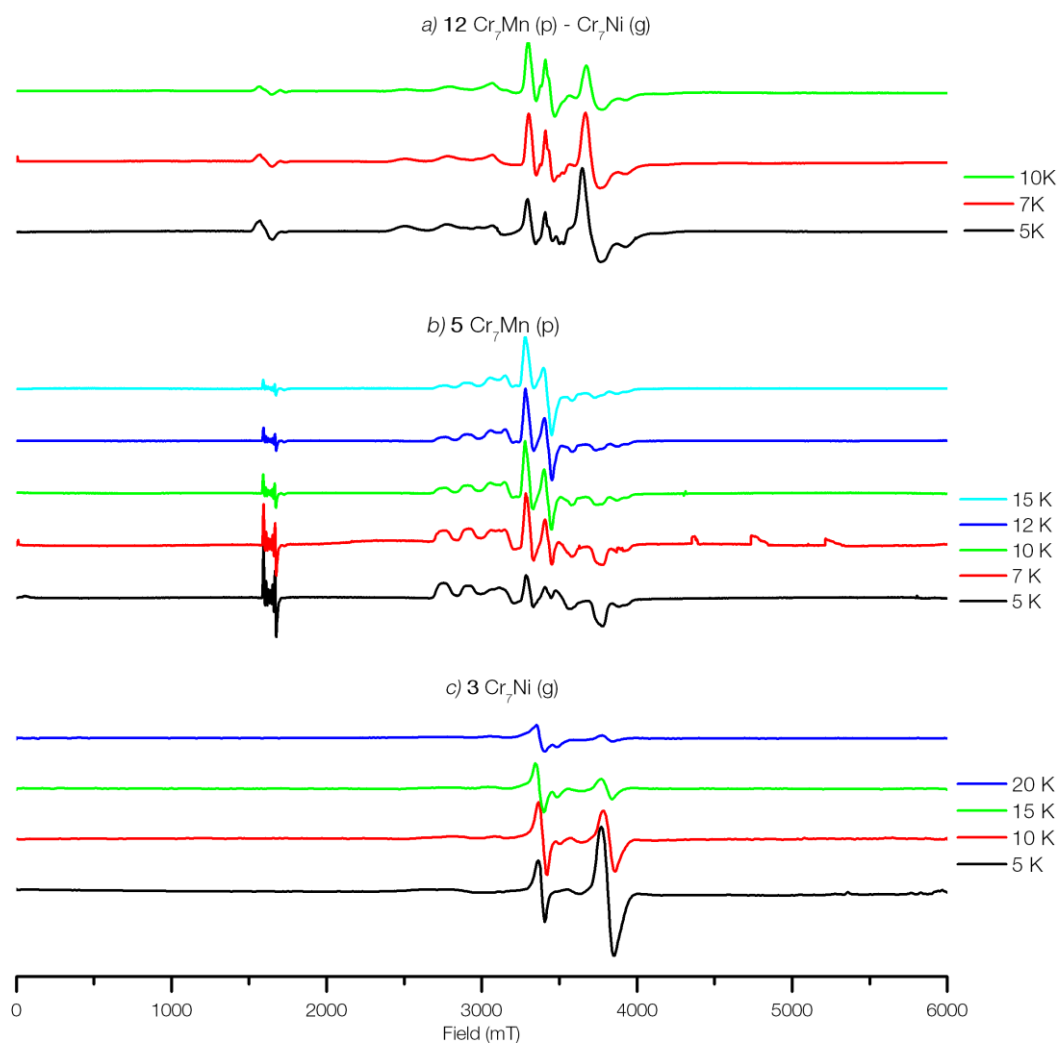

Figure 86 Variable temperature W Band EPR spectra of 12 measured at 95.7959 GHz (a), variable temperature W Band EPR spectra of 5 measured at 94.8821 GHz (b), and variable temperature W Band EPR spectra of 3 measured at 94.321 GHz (c)

The variable temperature W Band spectra of **12** are shown in Figure 86 (a), and the comparisons with the single wheels **5** and **3** are shown in Figure 86 (b) and Figure 86 (c) respectively. The spectra of **12** have features at 3367 mT and 3772 mT, which

correspond to the features in the spectra of **3**. The first feature grows while the second decreases with increasing temperature, in both **12** and **3**. The spectra of **5** has features at 2729 mT, 2897 mT and 3102 mT which persist up until 15 K, while the corresponding features in **12** are significantly broadened even at 5 K.

The temperature-dependence of the features of the W-Band spectrum of **12** are not all represented in the temperature-dependence of the features of the W-Band spectra of **5** and **3**, further indicating that there is a non-zero exchange interaction between the wheels.
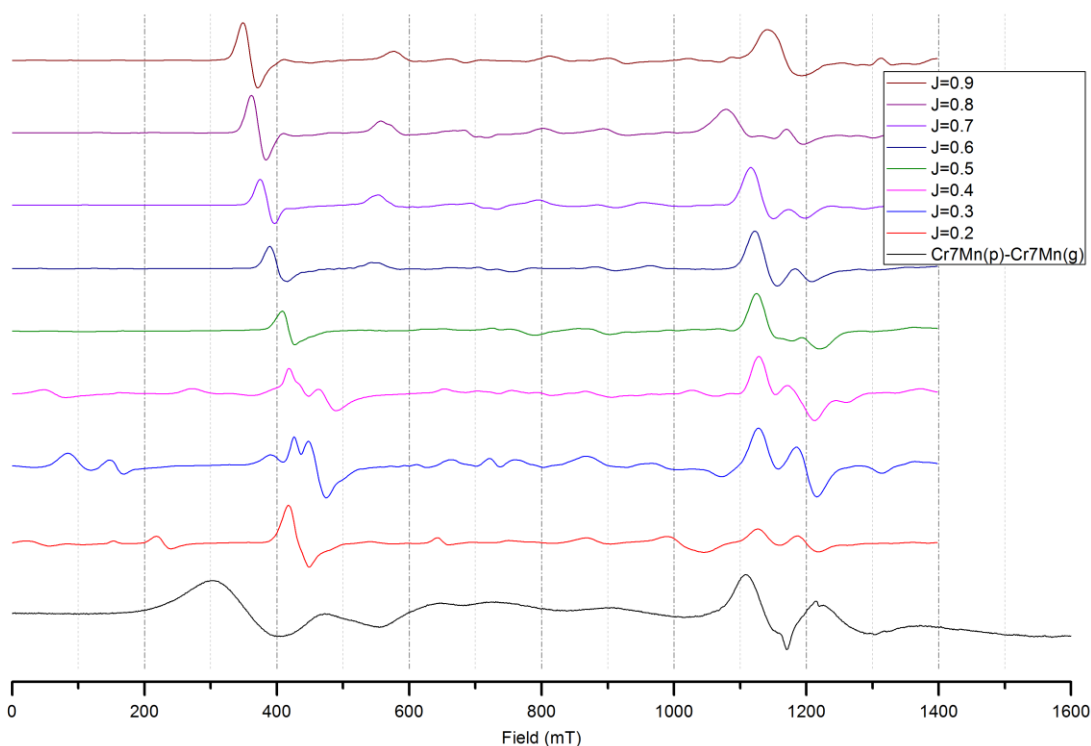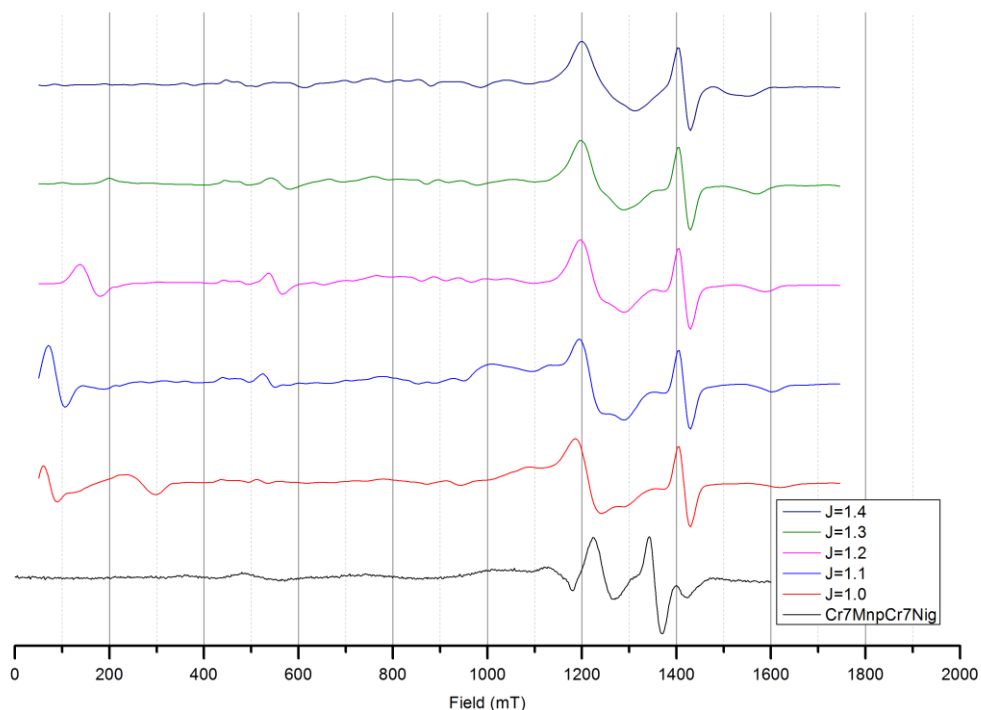

*Figure 87 Simulations of Q Band 5 K spectrum of **12** (black) with J' = 1.0 K, 1.1 K, 1.2 K, 1.3 K, 1.4 K*

The simulations of **12** in Figure 87 show some discrepancy of the positions of the 1222 mT features and 1337 mT features. This discrepancy is not improved by increasing the value of *J'*. The lineshape of the feature between the two at 1308 mT is broadened with increasing *J'*, and there is significant shifting of low field features.

In the experimental spectrum, there is a weak and broad feature at 472 mT. This feature is best reproduced with simulations in the range $(1.4 < J' < 1.5)\ K$.
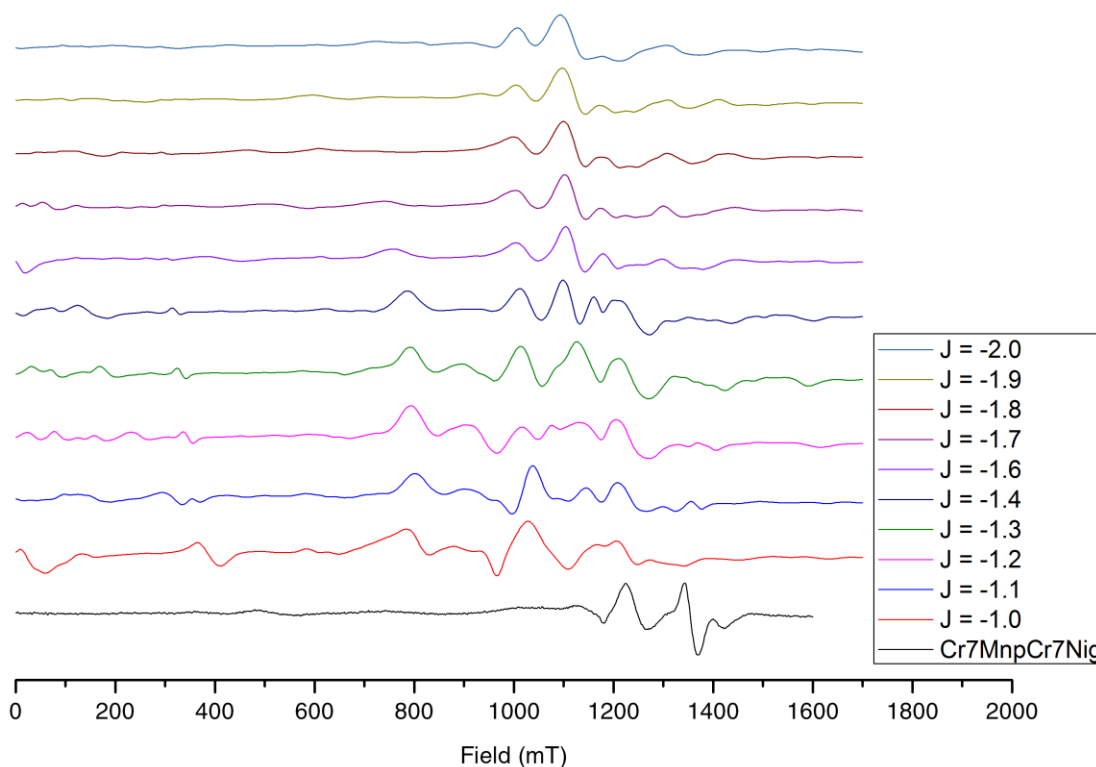
*Figure 88 Simulations of Q Band 5 K spectrum of **12** (black) with J' = - 1.0 K, -1.1 K, -1.2 K, -1.3 K, -1.4 K, -1.6 K, -1.7 K,-1.8 K, -1.9 K, -2.0 K*

Simulations of the Q Band spectrum of **12** have also been run with negative values of *J'*, shown in Figure 88. No negative values of *J'* reproduce the experimental spectrum, confirming that the exchange interaction in this dimer is described by a positive *J'*.

[Cr$_7$Ni purple] – {Cr$_7$Zn green} dimer   13
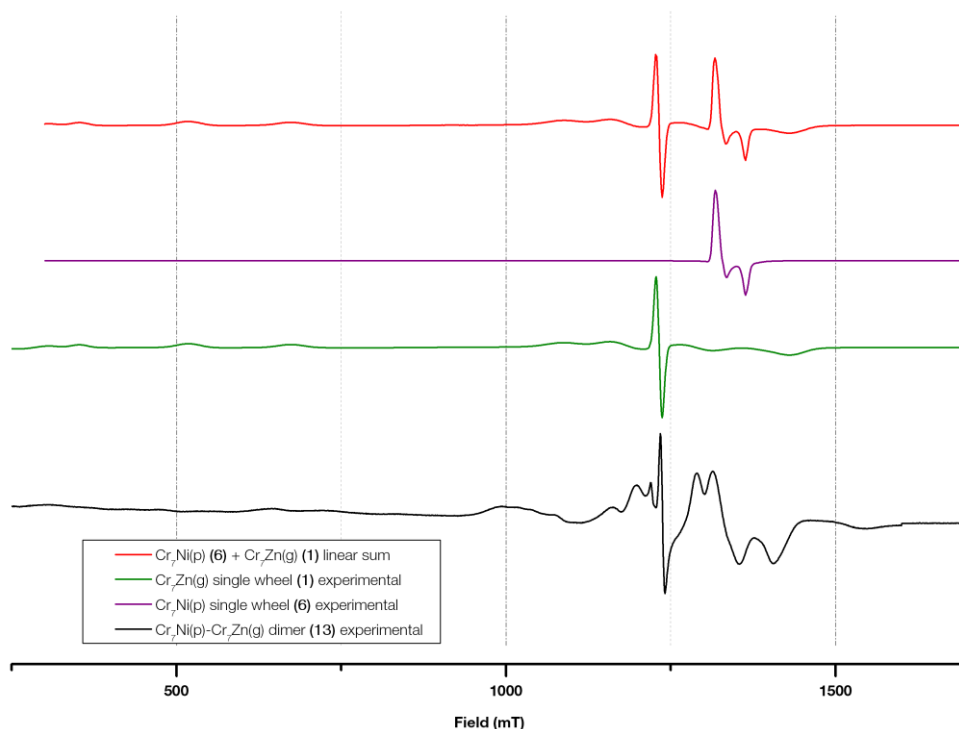
*Figure 89 Q Band spectrum at 5 K of **13** (black), **6** (purple), **1** (green) and linear sum of spectra of **6** and **1** (red)*

The comparison of the Q Band spectrum of **13** with the single wheels **6** and **1** is shown in Figure 89. The sharp feature at 1228 mT from the green wheel **1** spectrum is clearly present in the dimer spectrum **13**, as are the two features from the purple wheel **6** spectrum. The dimer spectrum, however, does have features at 1295 mT, 1219 mT and 1199 mT that do not appear in either single wheel spectrum. This indicates some exchange interaction between the wheels produces these features in the dimer spectrum.
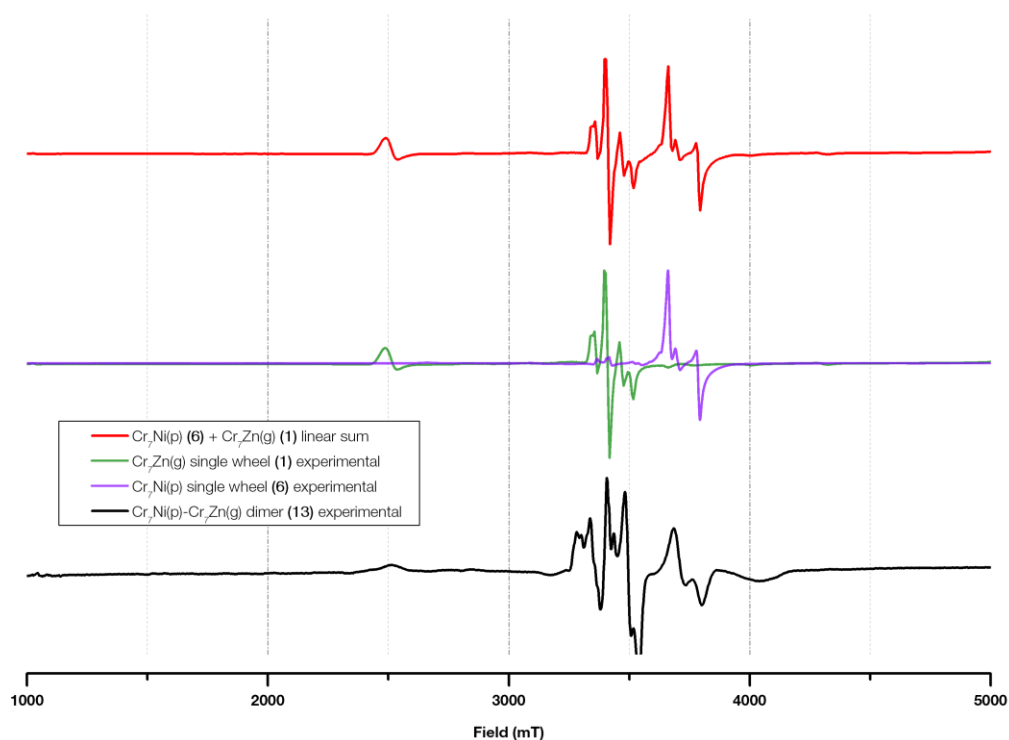
*Figure 90 W Band spectrum at 5 K of **13** (black), **6** (purple), **1** (green) and linear sum of spectra of **6** and **1** (red)*

The comparison of the W Band spectrum of **13** with the spectra of the single wheels **6** and **1** is shown in Figure 90. The spectrum of the purple wheel **6** has sharp features at 3659 mT, 3688 mT and 3784 mT. These features appear in the dimer spectrum of **13**, but broadened slightly. The peaks in the spectrum of the green wheel **1** also appear in the dimer spectrum, but with differing relative intensities and there do also appear to be additional features in the dimer spectrum that are not present in either spectrum of **1** or **6**.

These differences between the spectrum of **13** and the linear sum of **1** and **6** suggest that there is a non-zero exchange interaction between the wheels that affects the spectrum.
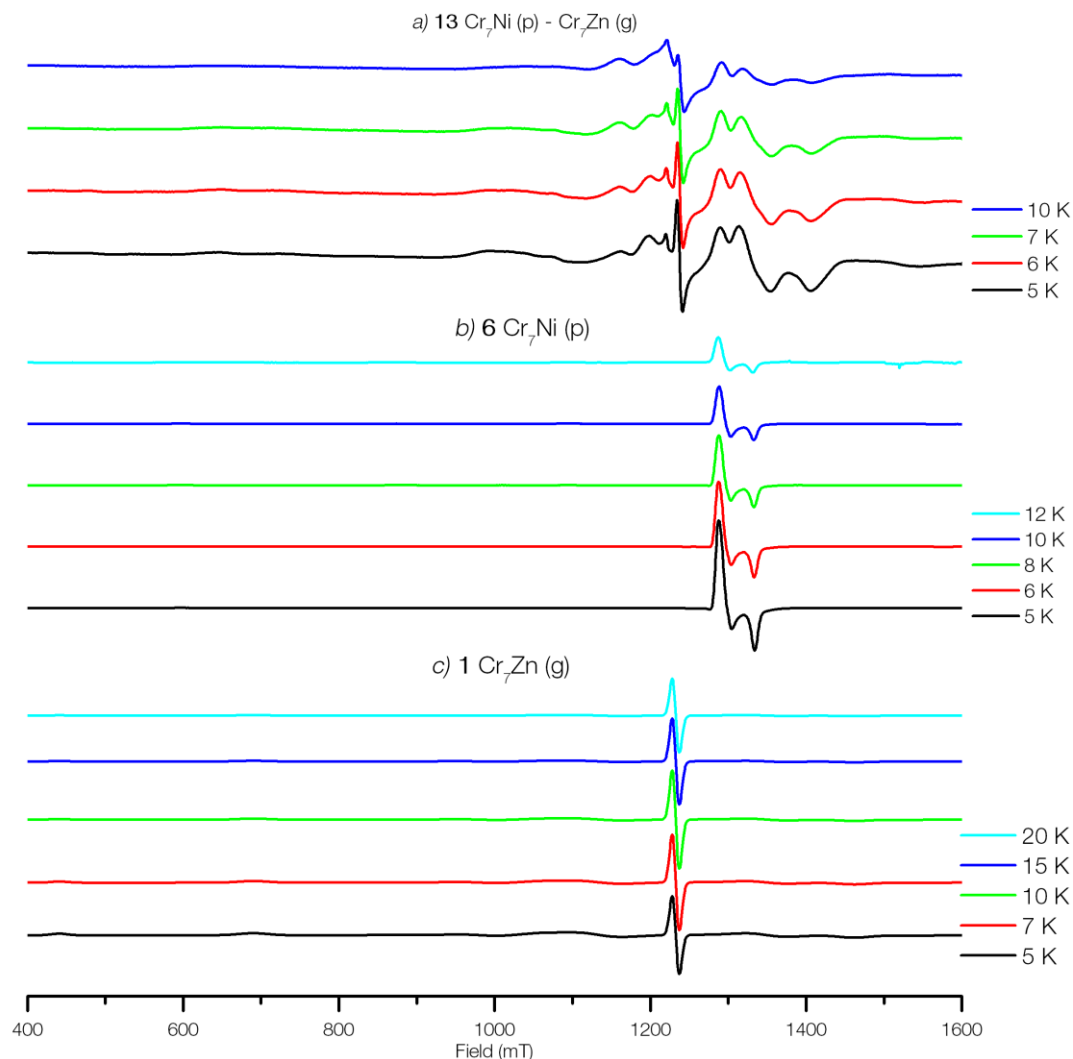
*Figure 91 Variable temperature Q Band EPR spectra of **13** measured at 34.09104 GHz (a), variable temperature Q Band EPR spectra of **6** measured at 34.3187 GHz (b), and variable temperature Q Band EPR spectra of **1** measured at 34.1238 GHz (c)*

The variable temperature Q Band spectra of **13** are shown in Figure 91 (a), and the comparisons with the single wheels **6** and **1** are shown in Figure 91 (b) and Figure 91 (c) respectively. The sharp feature at 1228 mT in the spectra of **13** matches the spectra of **1**, and decreases in intensity with increasing temperature. The two features in the spectra of **6** diminish with increasing temperature, and the same behavior is seen in the spectra of **13**.

The temperature-dependence of the features of the Q-Band spectrum of **13** are not all represented in the temperature-dependence of the features of the Q-Band spectra of **6** and **1**, further indicating that there is a non-zero exchange interaction between the wheels.
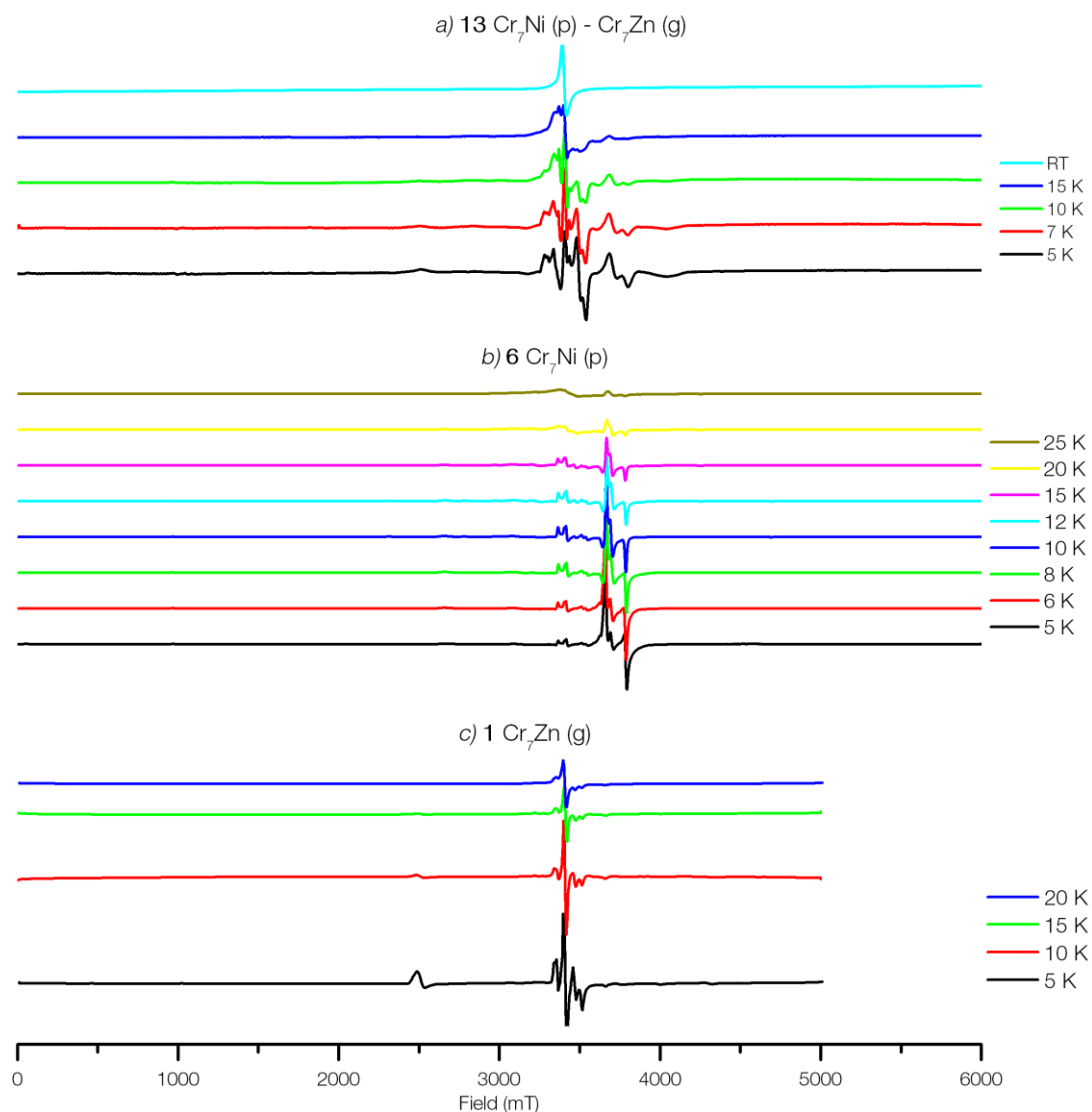
Figure 92 Variable temperature W Band EPR spectra of 13 measured at 95.27767 GHz (a), variable temperature W Band EPR spectra of 6 measured at 95.5777 GHz (b), and variable temperature W Band EPR spectra of 1 measured at 93.72122 GHz (c)

The variable temperature W Band spectra of **13** are shown in Figure 92 (a), and the comparisons with the single wheels **6** and **1** are shown in Figure 92 (b) and Figure 92

(c) respectively. The features in the spectra of **6** at 3659 mT, 3688 mT and 3784 mT decrease in intensity with temperature, and the corresponding features in the spectra of **13** behave similarly although significantly broadened in comparison. The features from the spectra of **1** also appear in the spectra of **13**, with the same temperature-dependence.

The temperature-dependence of the features of the W-Band spectrum of **13** are not all represented in the temperature-dependence of the features of the W-Band spectra of **6** and **1**, further indicating that there is a non-zero exchange interaction between the wheels.
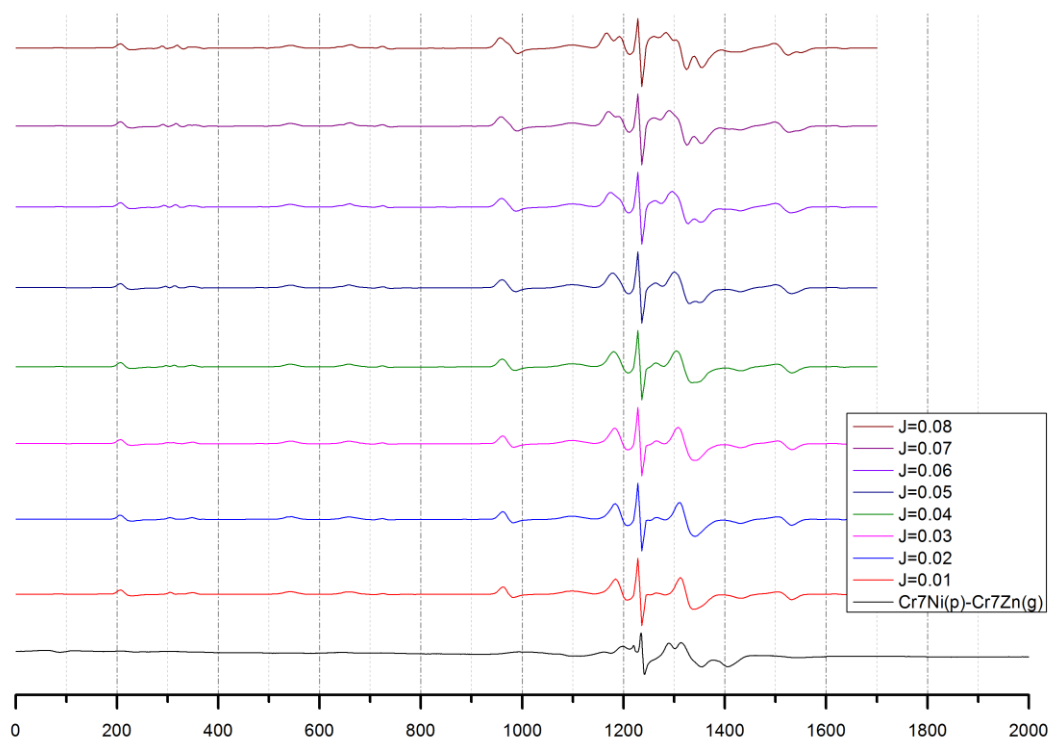
*Figure 93 Q Band spectrum of **13** at 5 K (black) and simulation with positive J' = 0.01 K, J' = 0.02 K, J' = 0.03 K, J' = 0.04 K, J' = 0.05 K, J' = 0.06 K, J' = 0.07 K, J' = 0.08 K*

The powder measurements of **13** at Q Band show a complex spectrum with many features across the field range. The effect of *J'* is complex and so a wide range of simulations is shown in Figure 93.

The experimental spectrum in Figure 93 has a notable set of two peaks at 1287 and 1315 mT and two dips at 1355 and 1408 mT. These are features that are difficult to reproduce in the simulation, but begin to appear at *J'* = 0.05 K. At *J'* = 0.08 K, the peaks have shifted and that part of the spectrum is not well reproduced.
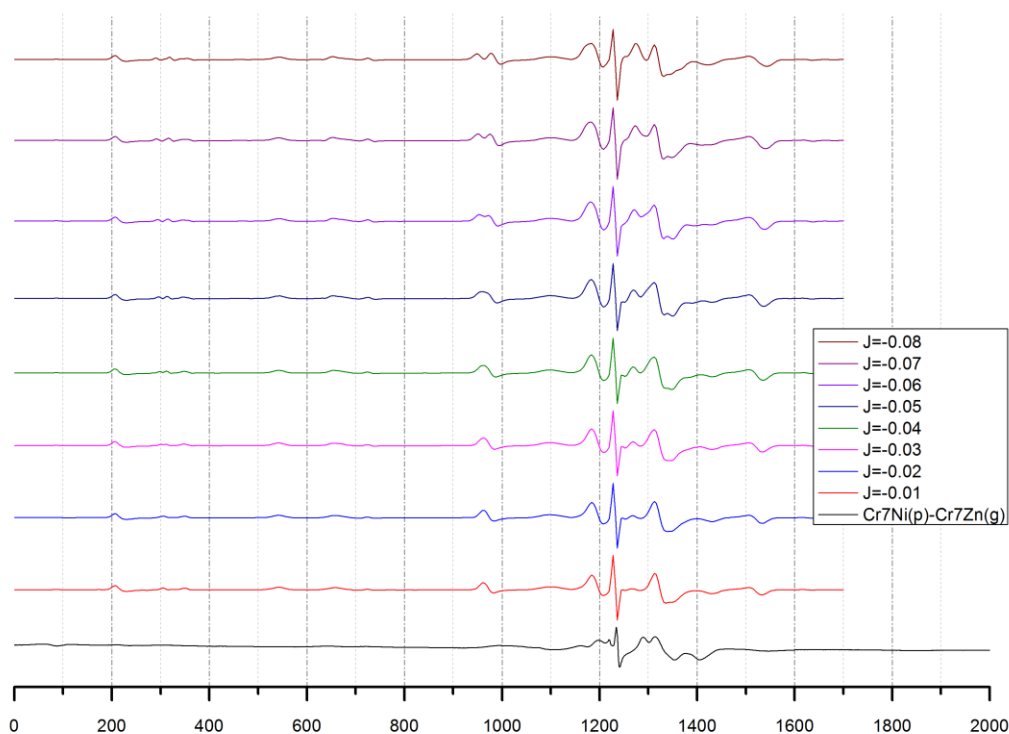
*Figure 94 Q Band spectrum of **13** at 5 K (black) and simulation with negative J' = -0.01 K, J' = -0.02 K, J' = -0.03 K, J' = -0.04 K, J' = -0.05 K, J' = -0.06 K, J' = -0.07 K, J' = -0.08 K*

Figure 94 shows the simulations of 13 with a negative *J'*. The two peaks at 1287 mT and 1315 mT emerge at *J'* = -0.03 K, but the two dips do not appear with the correct relative intensity until approximately *J'* = -0.06 K. However, at this point the 960 mT feature begins to split in two.

For this reason, a positive *J'* is taken as the best simulation in this model. The closest fit is with J' in the range $(0.05 < J' < 0.09)\ K$.
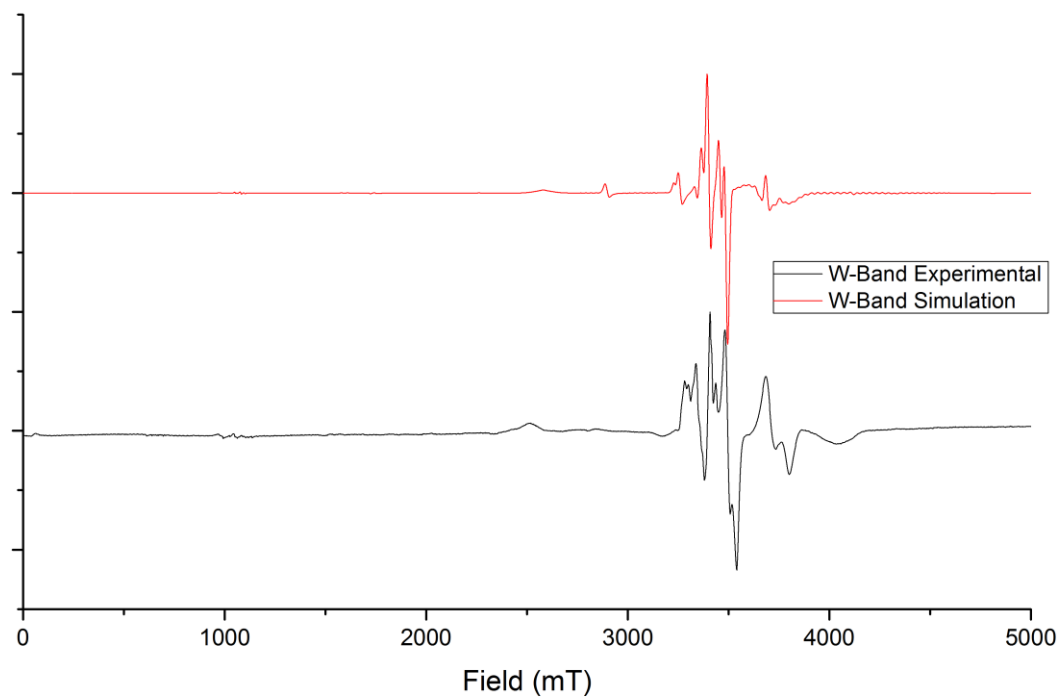
*Figure 95 W Band spectrum (black) and simulation (red) of **13** at 5 K*

The W-Band spectrum has sharp features centred around 3389 mT, with much broader features at 2590 mT and 1034 mT. The positions of these features are fit fairly well with $J' = 0.075$ K, consistent with the Q Band simulations.

[Cr$_7$Ni purple] – {Cr$_7$Mn green} dimer   14
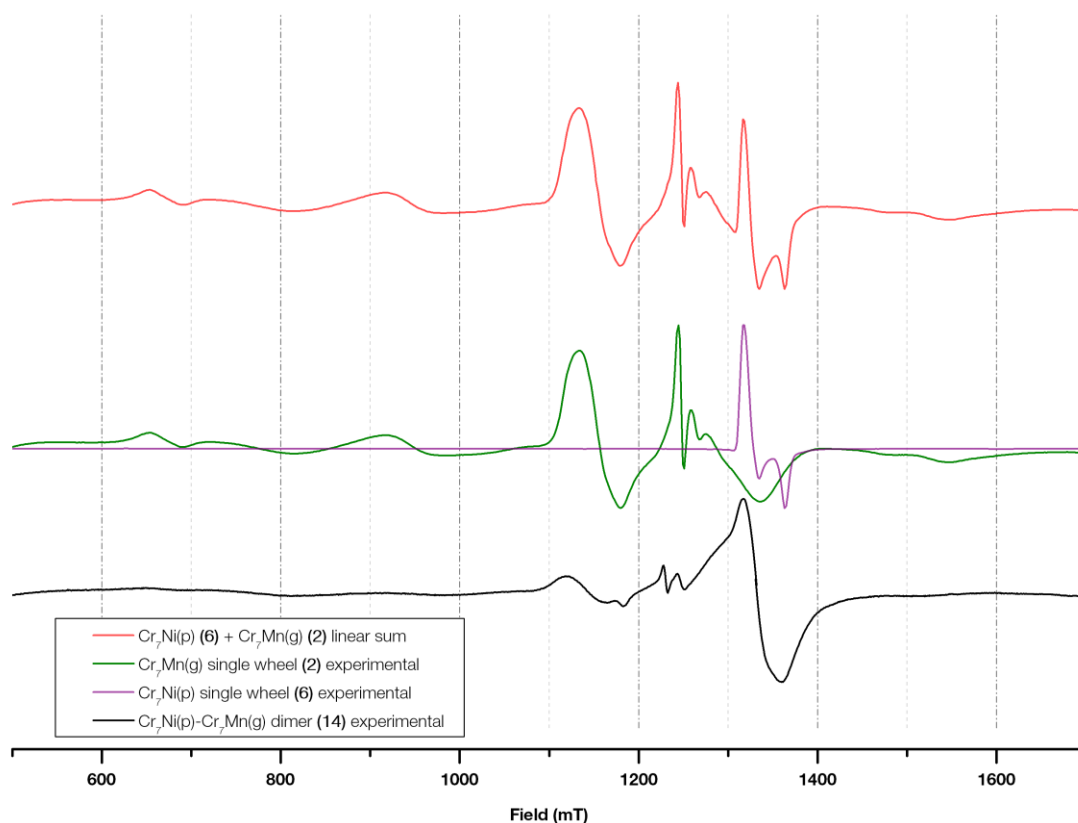
*Figure 96 Q Band spectrum at 5 K of **14** (black), **6** (purple), **2** (green) and linear sum of spectra of **6** and **2** (red)*

The comparisons of the Q band spectrum of **14** to the single wheels **6** and **2** are shown in Figure 96. The features from the spectrum of the green wheel **2** appear in the dimer spectrum, but with much less intensity compared to the feature at 1333 mT. This broad feature in the dimer spectrum spans the region of the purple wheel **6** spectrum, but is clearly significantly broadened. This broadening is the significant difference between the dimer spectrum and the linear sum of **2** and **6**.
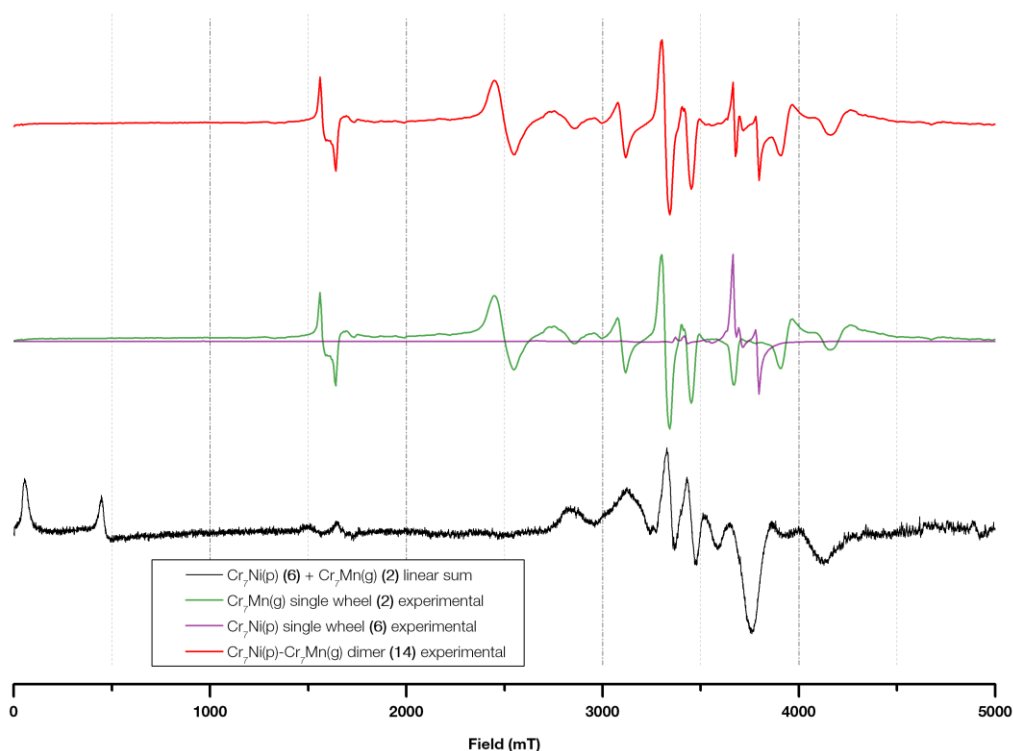
*Figure 97 W Band spectrum at 5 K of **14** (black), **6** (purple), **2** (green) and linear sum of spectra of **6** and **2** (red)*

The comparison of the W Band spectrum of the dimer **14** at 5 K and the single wheels **6** and **2** is shown in Figure 97. The dimer spectrum shows many of the features of both the green and purple wheel spectra, but significantly broadened. The three features from the purple wheel **6** spectrum at 3666 mT, 3692 mT and 3774 mT as well as overlapping features from the green wheel **2** spectrum appear all to have been broadened into one large single feature in the dimer spectrum. The four features at 2839 mT, 3131 mT, 3332 mT and 3435 mT in the dimer spectrum are from the green wheel spectrum. The spectrum of the green wheel has a feature at 2459 mT which does not appear in the dimer spectrum at all. The green wheel spectrum has a feature at 1565 mT which appears although broadened and with less intensity in the spectrum of **14**. There are significant differences between the dimer **14** spectrum and the linear sum of the spectra of **6** and **2.**
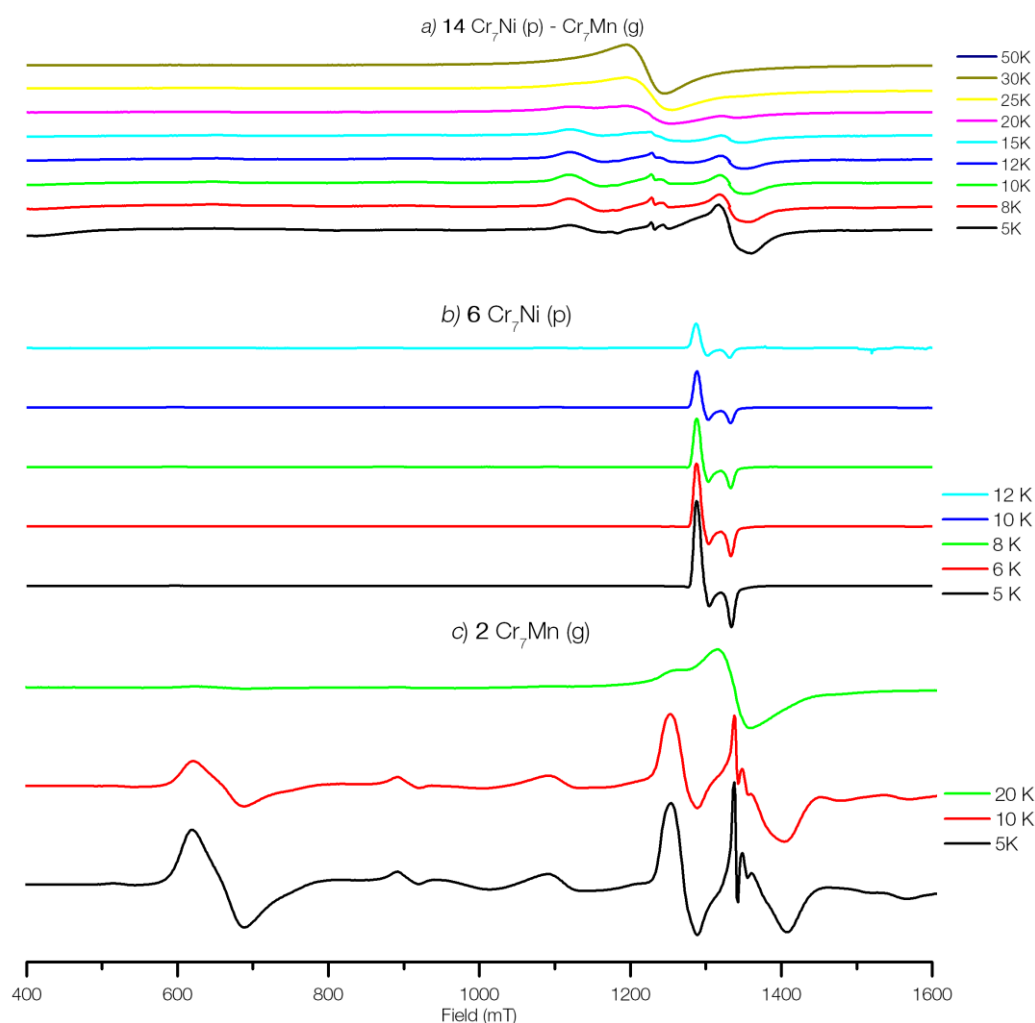
*Figure 98 Variable temperature Q Band EPR spectra of **14** measured at 34.1437 GHz (a), variable temperature Q Band EPR spectra of **6** measured at 34.3187 GHz (b), and variable temperature Q Band EPR spectra of **2** measured at 34.0978 GHz (c)*

The variable temperature Q Band spectra of **14** are shown in Figure 98 (a), and the comparisons with the single wheels **6** and **2** are shown in Figure 98 (b) and Figure 98 (c) respectively. The features from the spectra in **6** diminish with temperature, and the broad features in **14** that span that region also behave similarly with temperature. The sharp features from the spectra of **2** broaden into one large feature at high temperatures, and the same behaviour is seen in the high temperature spectra of **14**.

The temperature-dependence of the features of the Q-Band spectrum of **14** are not all represented in the temperature-dependence of the features of the Q-Band spectra of **6**

and **2**, further indicating that there is a non-zero exchange interaction between the wheels.
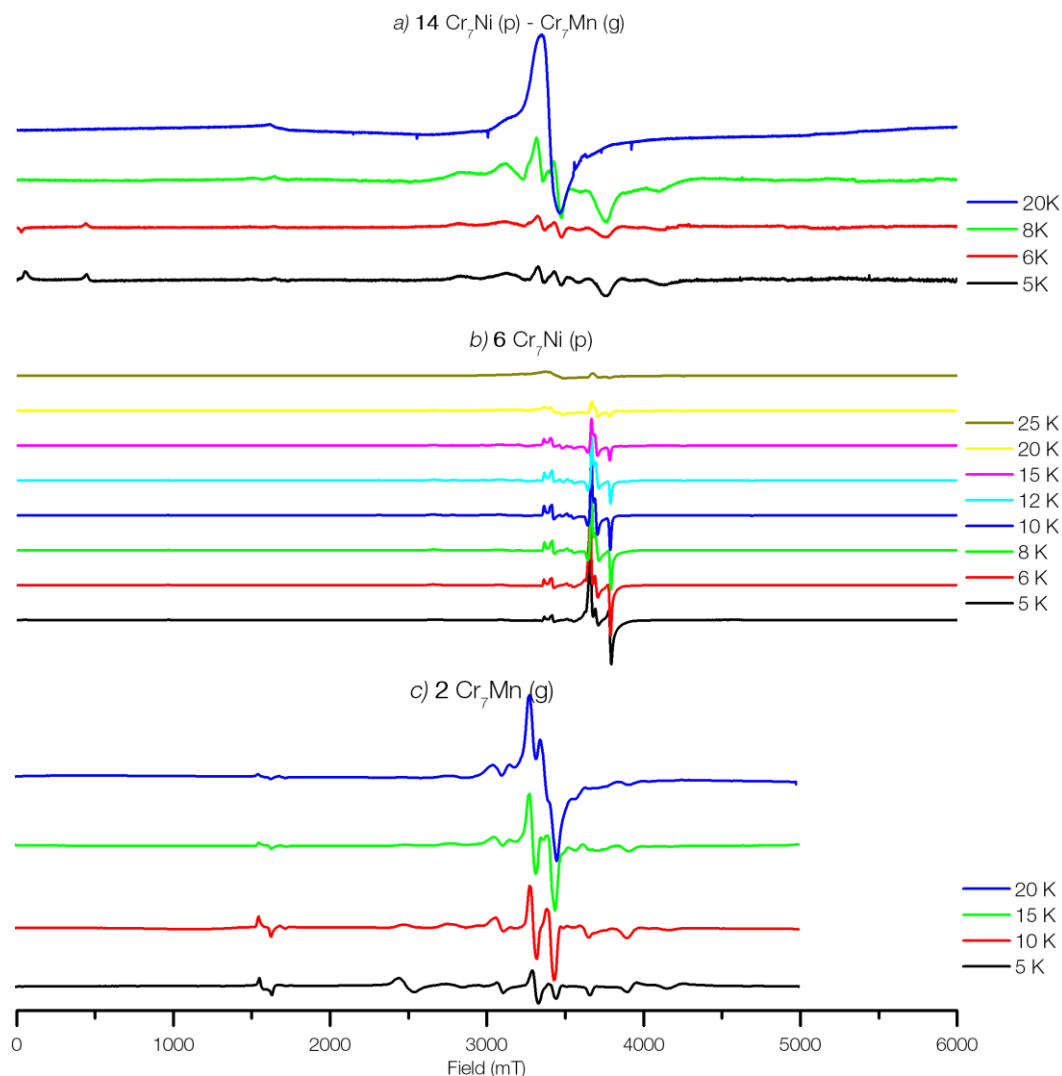
*Figure 99 Variable temperature W Band EPR spectra of **14** measured at 95.0518 GHz (a), variable temperature W Band EPR spectra of **6** measured at 95.5777 GHz (b), and variable temperature W Band EPR spectra of **2** measured at 93.1243 GHz (c)*

The variable temperature W Band spectra of **14** are shown in Figure 99 (a), and the comparisons with the single wheels **6** and **2** are shown in Figure 99 (b) and Figure 99 (c) respectively. The three features in the spectra of **6** at 3666 mT, 3692 mT and 3774 mT decrease in intensity with temperature. In the spectra of **14**, this region is spanned by a single broad feature. The two features at 3291 mT and 3428 mT in the

spectra of **2** grow in intensity with temperature, merging in together at higher temperatures. The corresponding features in the spectra of **14** behave similarly.

The temperature-dependence of the features of the W-Band spectrum of **14** are not all represented in the temperature-dependence of the features of the W-Band spectra of **6** and **2**, further indicating that there is a non-zero exchange interaction between the wheels.
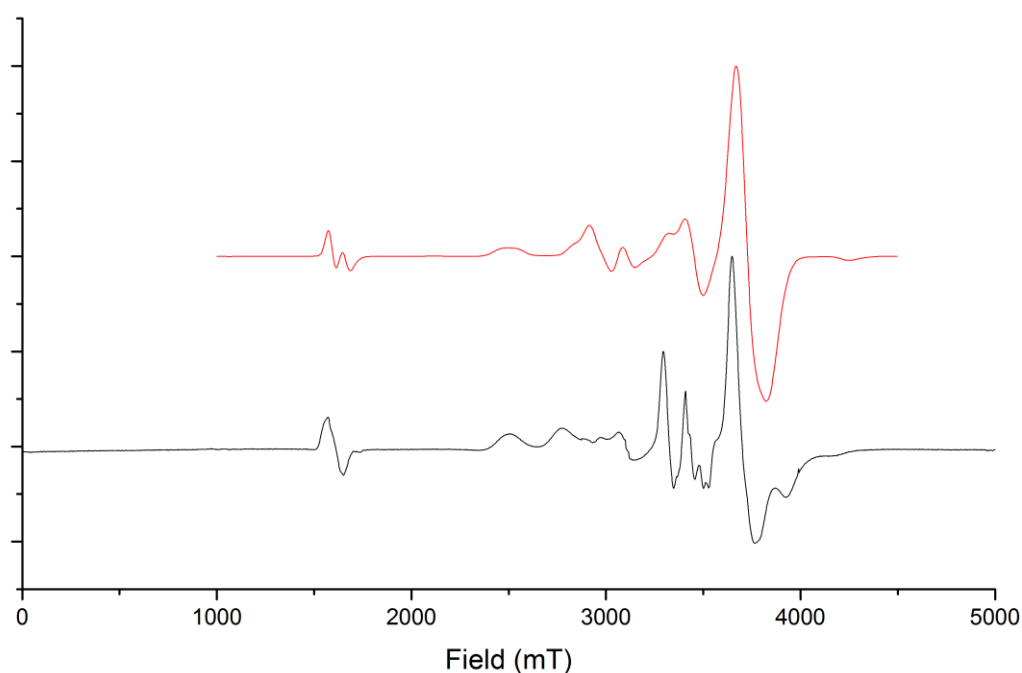

*Figure 100 W Band spectrum (black) and simulation (red) of **14***

It was not possible to simulate the Q-Band spectrum of **14**, although the best attempt at simulating the W Band spectrum is shown in Figure 100.

W Band powder measurements of **14** show a sharp peaks at 3631 mT, 3401 mT, and 3297 mT. The spectrum has been simulated with J = 0.2 K.

[Cr$_7$Ni purple] – {Cr$_7$Ni green} dimer   15
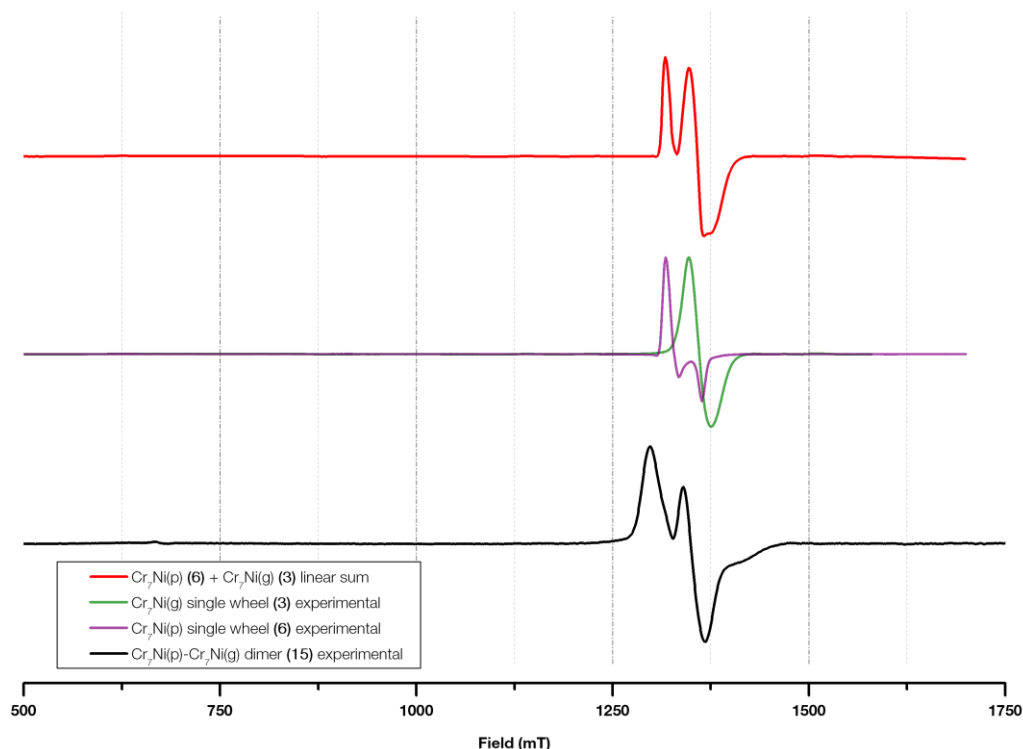
*Figure 101 Q Band spectrum at 5 K of **15** (black), **6** (purple), **3** (green) and linear sum of spectra of **6** and **3** (red)*

The comparison between the Q band spectrum of the dimer **15** and the single wheels **3** and **6** is shown in Figure 101. The dimer spectrum has two peaks, at 1294 mT and 1342 mT, and the linear sum has the two peaks. However, the position of the broadened shoulder is different – in the linear sum it appears at the very bottom of the main feature, but in the dimer spectrum it is shifted significantly up field. The position of the second peak is also shifted slightly. This indicates that there ought to be a small non-zero exchange interaction that subtly affects the spectrum.
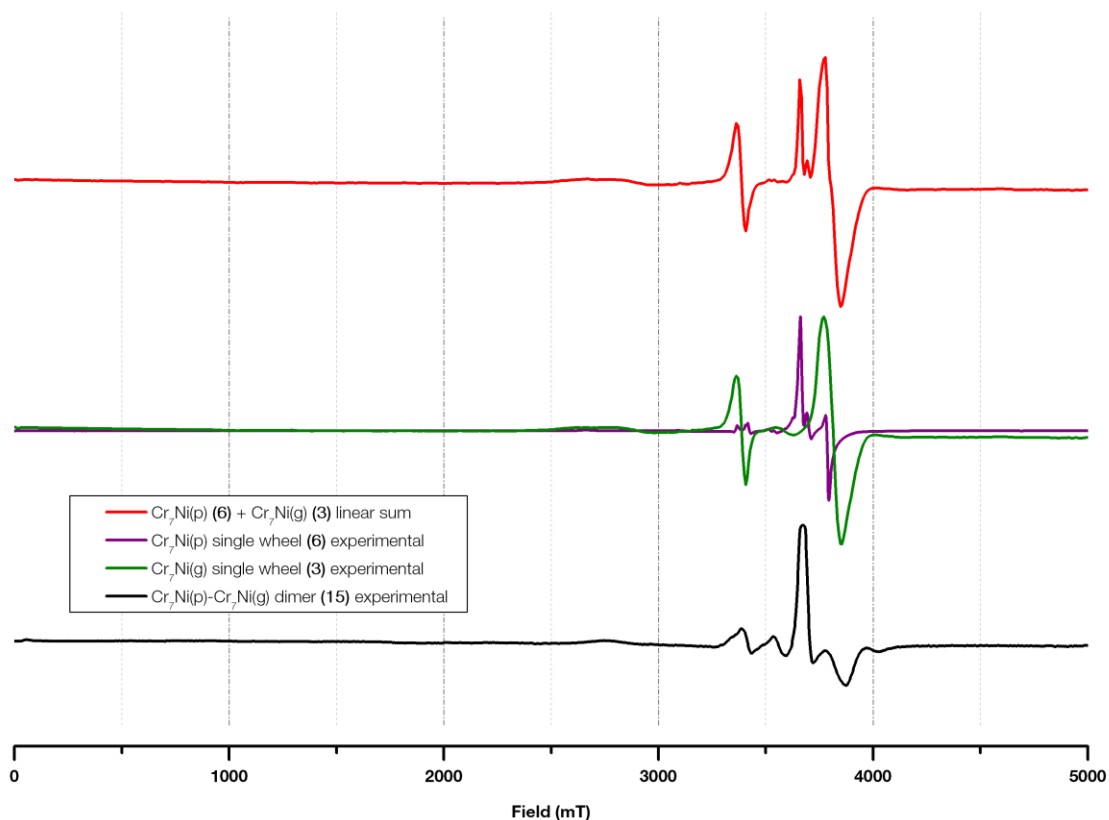
Figure 102 W Band spectrum at 5 K of 15 (black), 6 (purple), 3 (green) and linear sum of spectra of 6 and 3 (red)

The comparison between the W-Band dimer **15** spectrum and the single wheels **6** and **3** is shown in Figure 102. The single wheels **6** and **3** have peaks at 3663 mT and 3754 mT respectively, which appear in the dimer spectrum to be broadened into one single peak at 3674 mT. The feature in the green wheel spectrum at 3368 mT appears in the dimer spectrum, but with less intensity. These are significant differences between the dimer spectrum **15** and the linear sum of **6** and **3**, indicating a non-zero exchange interaction between the wheels in the dimer affecting the 5 K W-Band spectrum.
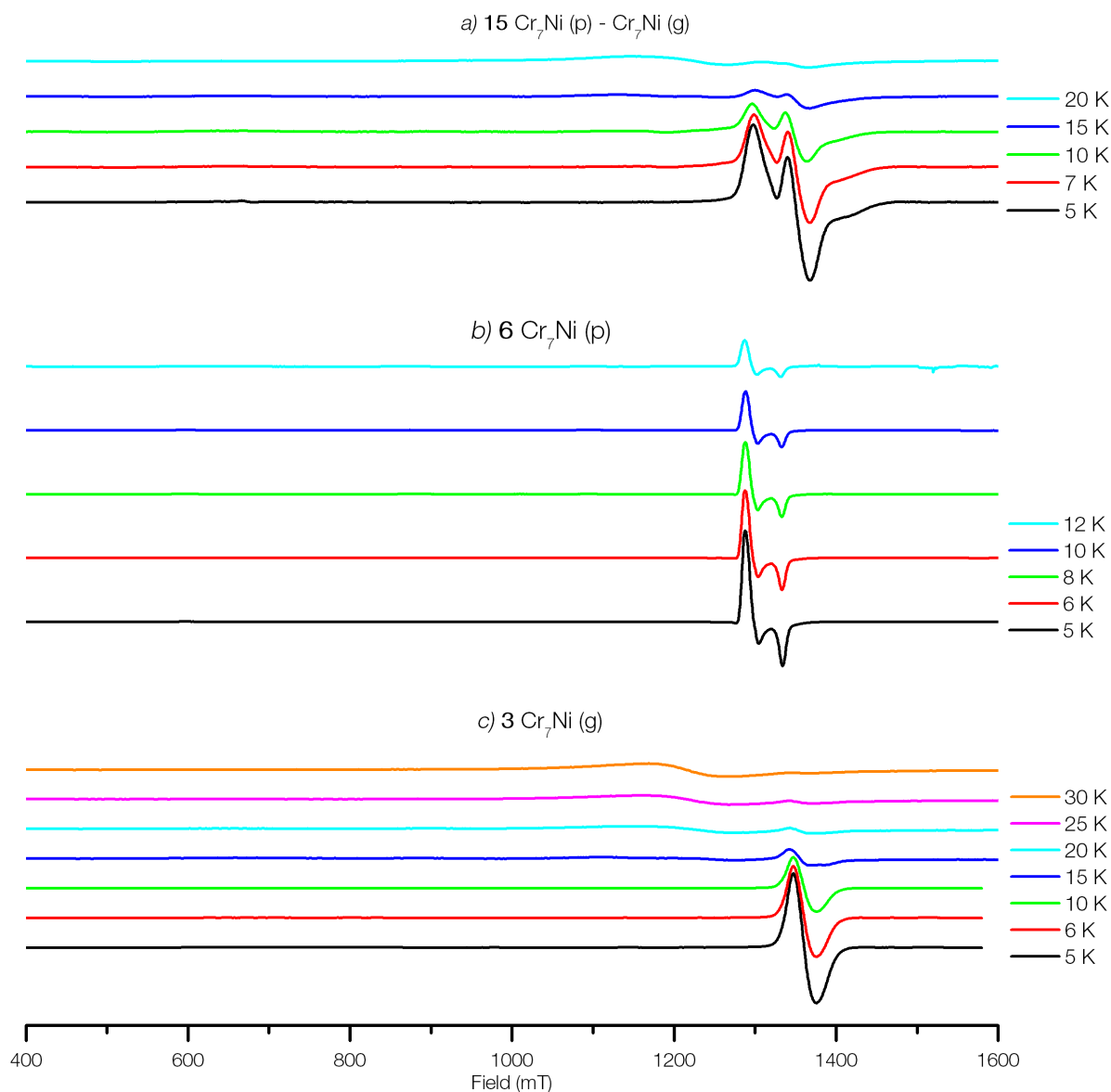
Figure 103 Variable temperature Q Band EPR spectra of 15 measured at 34.1587 GHz (a), variable temperature Q Band EPR spectra of 6 measured at 34.3187 GHz (b), and variable temperature Q Band EPR spectra of 3 measured at 33.2238 GHz (c)

The variable temperature Q Band spectra of **15** are shown in Figure 103 (a), and the comparisons with the single wheels **6** and **3** are shown in Figure 103 (b) and Figure 103 (c) respectively. The spectra of **15** have features at 1294 mT and 1342 mT which diminish with increasing temperature. The spectra of **6** and **3** also have the same temperature-dependence.

The temperature-dependence of the features of the Q-Band spectrum of **15** are subtly different from the temperature-dependence of the features of the Q-Band spectra of **6** and **3**, suggesting that there is a non-zero exchange interaction between the wheels.
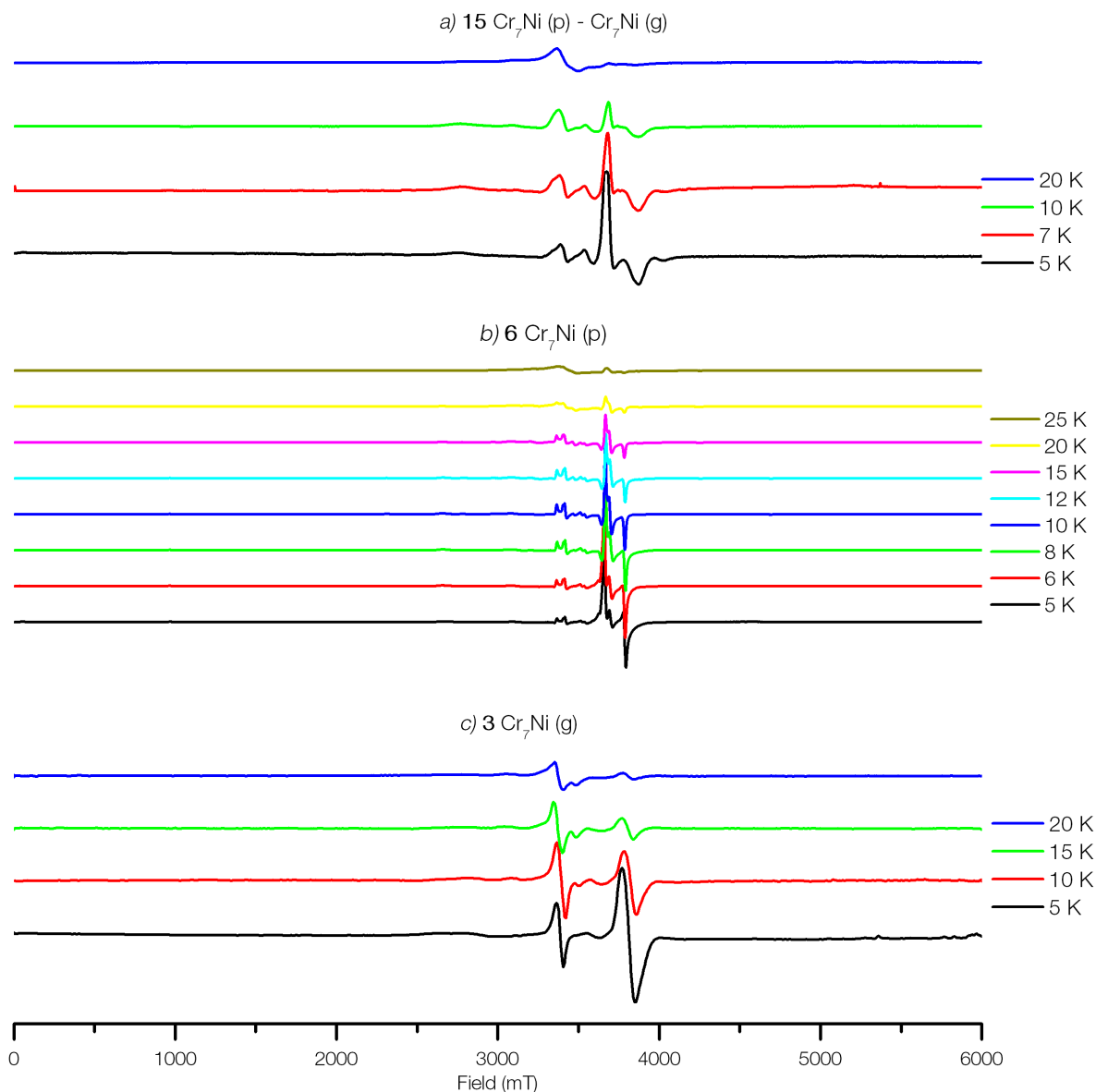
*Figure 104 Variable temperature W Band EPR spectra of **15** measured at 97.3033 GHz (a), variable temperature W Band EPR spectra of **6** measured at 95.5777 GHz (b), and variable temperature W Band EPR spectra of **3** measured at 94.321 GHz (c)*

The variable temperature W Band spectra of **15** are shown in Figure 104 (a), and the comparisons with the single wheels **6** and **3** are shown in Figure 104 (b) and Figure

104 (c) respectively. The sharp feature at 3658 mT in the spectra of **15** decreases in intensity at high temperatures, mirroring the behaviour of that feature in the spectra of **6**. The feature at 3377 mT in the spectra of **15** grows and remains at high temperatures, and this behaviour also with that feature in the spectra of **3**.

The temperature-dependence of the features of the W-Band spectrum of **15** are not all represented in the temperature-dependence of the features of the W-Band spectra of **6** and **3**, further indicating that there is a non-zero exchange interaction between the wheels.
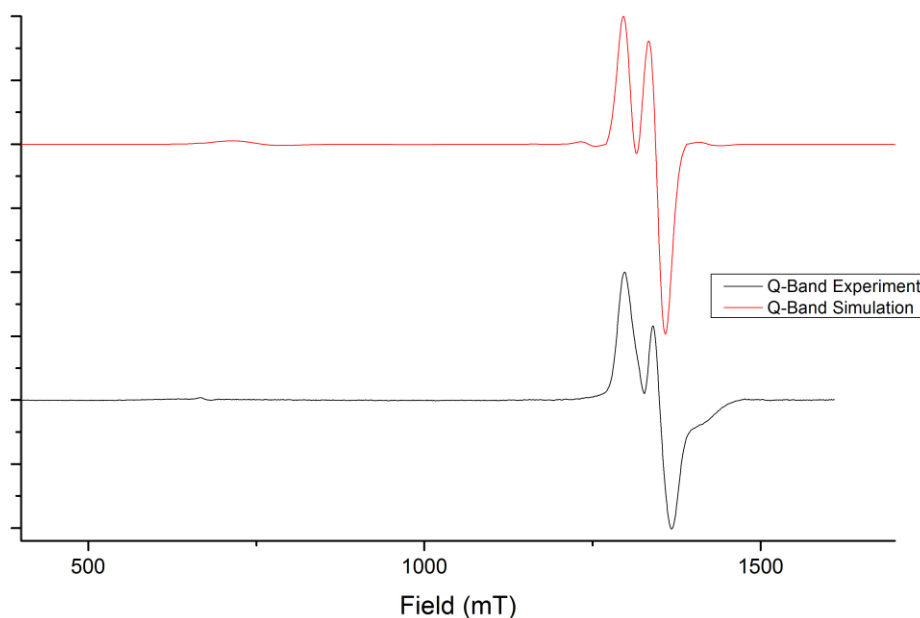
*Figure 105 Q Band spectrum (black) and simulation (red) of **15** at 5 K*

Powder measurements of **15** taken at Q Band show two sharp features at 1294 mT and 1342 mT and a smaller broad feature at 708 mT. The simulation has been found with an inter-ring coupling of $J' = -0.3$ K. This simulation accurately reproduces the positions and relatively intensities of the two sharp peaks, and also the low-field broad feature. Simulations with a positive J' were also investigated, but did not

reproduce the experimental spectrum. The best simulations were found in the range $(-0.5 < J' < -0.2)$ K.
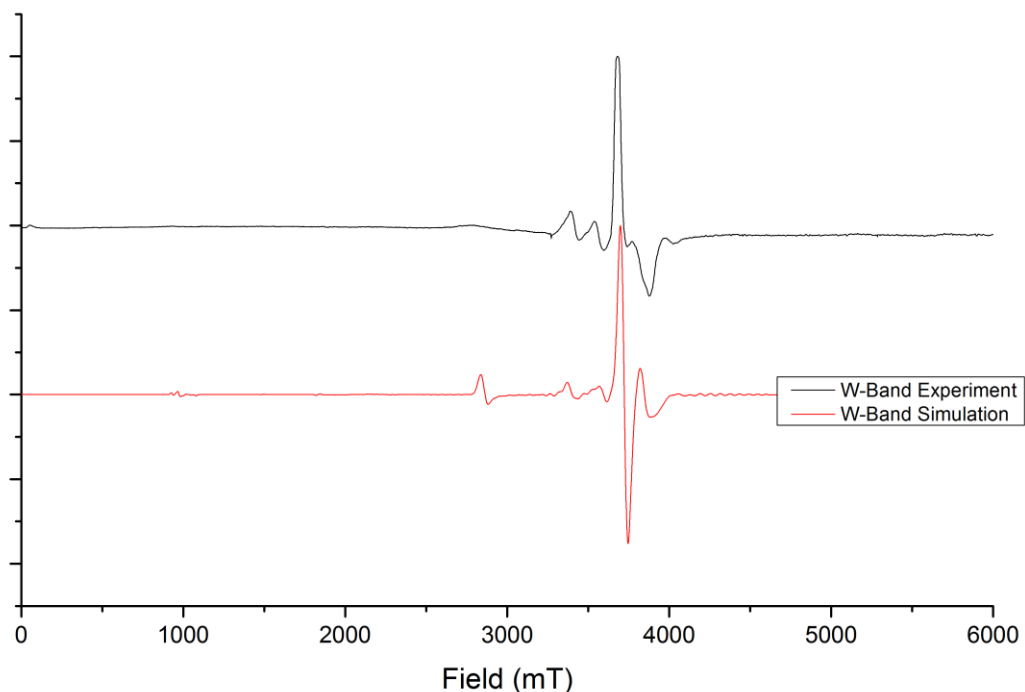
*Figure 106 W Band spectrum (black) and simulation of **15** at 5 K*

The powder spectrum of **15** at W Band shows a sharp feature at 3693 mT, and smaller broader features at 3388 mT, 3538 mT, and 3968 mT.

This spectrum has been accurately simulated with J' = -0.3 K. In principle, the J' parameter has a complex effect upon the spectrum both splitting, shifting and broadening features across the spectrum. In this case, the J' parameter has a strong effect upon the W Band spectrum. With J' = -0.3 K, the sharp central peak and the two features at 3545 mT and 3379 mT are reproduced. The lower field feature at 2755 mT is present in the simulation but it is much broader in the experiment than in the simulation. Positive values of J' were also investigated, but no simulations with positive J' reproduced the experimental spectrum.

Conclusions

Table 16 Inter-ring exchange parameter J' for series of dimers

Green Purple	Cr$_7$Zn **(1)**	Cr$_7$Mn **(2)**	Cr$_7$Ni **(3)**

(4)
Cr$_7$Zn
	(7)
	    $0\ K$
		(8)
		    $0\ K$
			(9)
			    $0\ K$

(5) Cr$_7$Mn	**(10)** $(0.01 < |J'| < 0.05)\ K$	**(11)** $(0.6 < J' < 0.8)\ K$	**(12)** $(1.4 < J' < 1.5)\ K$
(6) Cr$_7$Ni	**(13)** $(0.05 < J' < 0.09)\ K$	**(14)** $(0.1 < J' < 0.3)\ K$	**(15)** $(-0.5 < J' < -0.2)\ K$

For the entire series, the communication between the rings is significantly weaker than the communication within the rings. The Cr-Cr exchange interaction has been found to be $J_{Cr\text{-}Cr} = 20.4$ K in the purple rings, and $J_{Cr\text{-}Cr} = 16.9$ K in the green rings. The Cr-M exchange interaction has been found to be $J_{Cr\text{-}Mn} = 12$ K, $J_{Cr\text{-}Ni} = 12.4$ K for the purple ring and $J_{Cr\text{-}Mn} = 16.6$ K, $J_{Cr\text{-}Ni} = 16.9$ K for the green rings.

Cr$_7$Ni-Cr$_7$Mn shows different behavior if Mn^{2+} is in green with a carboxylate bond or purple with an N-bond.

The inter-ring exchange interaction *J'* is an order of magnitude smaller than this interaction. There is, however, a small but non-zero interaction between some of the rings. The effect of this interaction on the spectroscopic information is subtle and manifests itself in the broadening and slight shifting of resonant peaks.

With the implementation of a full microscopic Hamiltonian, modeling sixteen metal centres, the effects of these features can be accurately simulated.

From a structural perspective, the series of these compounds ought to be modeled with two inter-ring exchange parameters, one for the interaction s_8^p with s_7^g and the other for the interaction s_8^p with s_8^g (see Figure 58). The effects of a single inter-ring communication parameter are already very subtle, but some of the simulations – in particular those of spectra from **12** and **13** may be improved by a more accurate model.

When the Cr₇Zn wheel is purple, the dimers can be modeled as a sum of individual rings with no communication because the only connection is through the diamagnetic ion. When Cr₇Zn is the green component of the dimer, the communication can go only through the adjacent Cr^{3+} ion. As a result of this, there is a very small but non-zero J' for compounds **10** and **13** in Table 16.

A striking result is that one of the dimers (**15**) exhibits ferromagnetic inter-ring coupling while the others exhibit anti-ferromagnetic coupling. Positive values of J' correspond to anti-ferromagnetic interactions in Equation 2. This could be an indication of two communication pathways, one ferromagnetic and one anti-ferromagnetic, the relative dominance of which varies between the series. Alternately, it could also be a feature of the limitation of modeling the individual rings with so few parameters.

The model of the dimers in Figure 58 is an over-simplification of the exchange interactions in the dimer, and this is most likely the origin of the difficulty in obtaining accurate simulations of the EPR spectra.

A more precise model would be to consider a triangle of three non-equal exchange interactions; one between the divalent metal on the purple ring and the Cr ion on the green ring, one between the divalent metal on the purple ring and the divalent metal

on the green ring, and one between the divalent metal on the green ring and the adjacent Cr. This final exchange interaction ought, in principle, to be distinct from the exchange interaction between the divalent metal and the Cr ion on the other side, resulting in two $J_{Cr\text{-}M}$ parameters.

The difficulty in obtaining an accurate simulation also may be due to the large number of free parameters already present in this simple model. The effect of J' upon the simulated spectrum is complex, and every variation in J' also may require a change in broadening parameters as features are shifted and broadened by J'. A thorough investigation therefore requires a large number of independent simulations – in the course of investigating the dimer compounds, over 54,460 independent simulations have been run spanning the possible solution space. The process of analyzing these simulations would greatly benefit from an algorithmic method for comparing the simulation to the experimental spectrum. Any further extension of this model would necessarily run into this same limitation.

References

[1] Deutsch, D.; *Proc. R. Soc. Lond. A*, **1985**, 400, 1818, 97-117

[2] Carthy, L.; *Linking Wheels for use in Quantum Information Processing*, Thesis submitted to The University of Manchester, 2010

Chapter VI – Measurements of [Cr₇*M*]-{Cr₇*M'*}-[Cr₇*M*] heterometallic trimers

The series of heterometallic dimers in Chapter V can be even further extended by introducing a third wheel. A second isonicotinate linker is attached to the opposite side of the green wheel so that the two axial pivalates at the M^{2+} ion are substituted by isonicotinates allowing for a purple-green-purple arrangement of wheels, see Figure 107.
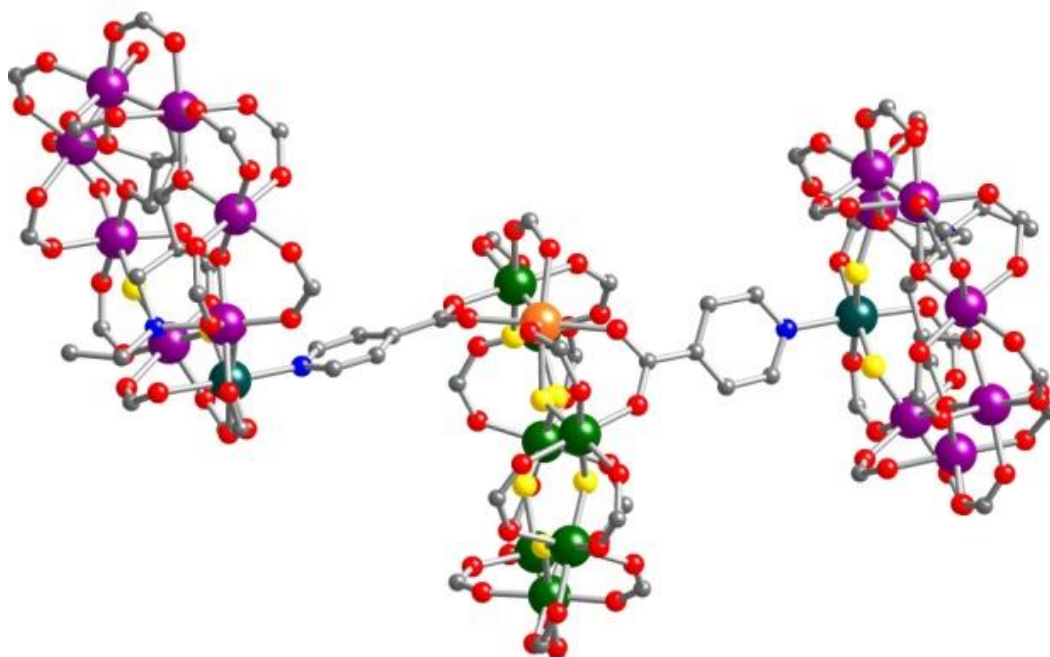
Figure 107 Structure of (C₃H₇)₂NH₂Cr₇MF₈(O₂CCMe₃)₁₄ (O₂CC₅H₄N)₂ [Cr₇M'F₃(O₂CCMe₃)₁₅C₈H₁₄NO₅]₂

EPR spectra of these compounds have been measured at various frequencies. Due to the involvement of 24 spin centres in each of these systems, it is not currently possible to simulate these spectra with a microscopic Hamiltonian. Unless $M = \text{Zn}^{\text{II}}$ in the purple wheel, the dimer shows communication between wheels through this linker, so it is reasonable to expect there to be some communication between all

three wheels in these systems. When comparing the dimer systems to the sum of their respective single wheel spectra, the effect on the spectroscopic data was broadening and subtle shifting of various features. When comparing the trimer systems to their respective dimer systems, the difference is similarly subtle and occasionally imperceptible.

Table 17 Spin properties of trimer systems

16	Cr$_7$Ni(p)-Cr$_7$Mn(g)-Cr$_7$Ni(p)	S=1/2	S=1	S=1/2
17	Cr$_7$Ni(p)-Cr$_7$Zn(g)-Cr$_7$Ni(p)	S=1/2	S=3/2	S=1/2
18	Cr$_7$Zn(p)-Cr$_7$Mn(g)-Cr$_7$Zn(p)	S=3/2	S=1	S=3/2

The spin properties of the trimers studied are outlined in Table 17. In order to ascertain whether there is an exchange interaction, the spectra of the trimer systems will be compared to the linear sum of the composite dimer spectrum and the remaining single wheel spectrum. This takes into account the expected relative magnitude of the contributions from the component wheels of the trimer, and also the effect of the exchange between the wheels in the dimer. Any observed difference between the trimer spectrum and the linear sum of the spectra of the dimer and the single wheel will be due to the additional exchange with the additional wheel.

Based on the study of the dimers, there is not expected to be any exchange interaction between any of the wheels in the spectrum of **18**.

[Cr₇Ni purple] – {Cr₇Mn green} – [Cr₇Ni purple] trimer   16
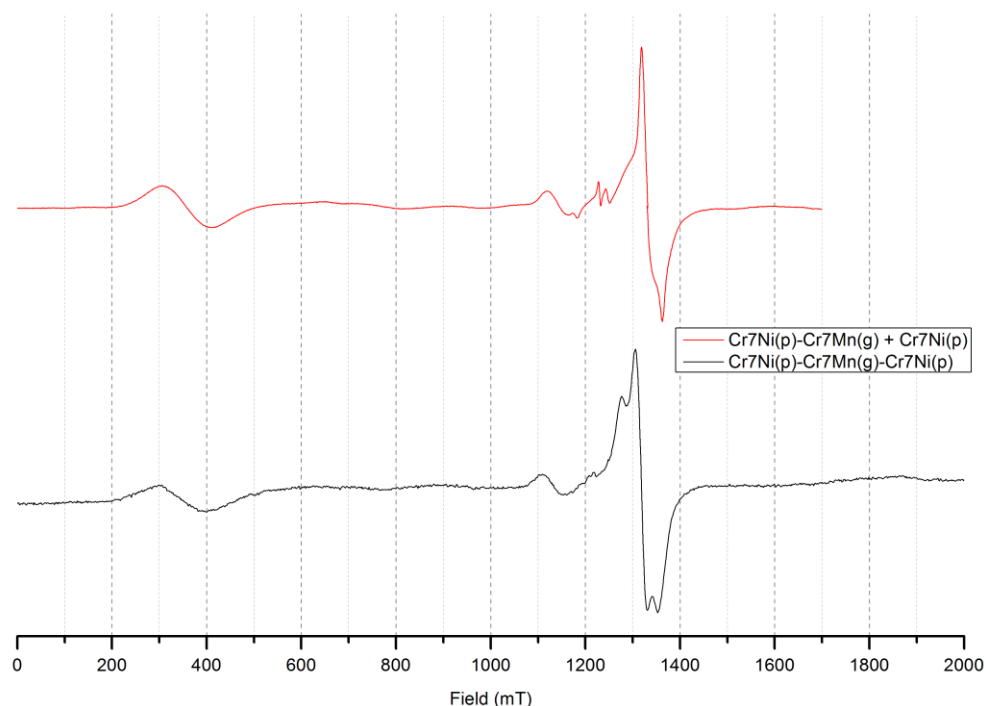
Figure 108 Comparison of 5 K Q Band spectra of the trimer 16 (black) and the linear sum of the dimer 14 and monomer 6 (red)

The spectrum of the trimer in Figure 108 shows generally the same features as the dimer and monomer sum but with some interesting differences. The summed spectrum of **14**+**6** shows some small but sharp and prominent features at 1238 mT, originating from the dimer **14**. There is a small absorption shape at the same position in the trimer spectrum of **16** which may indicate the presence of that feature but with much less intensity and greater broadening. Additionally, the two distinct features that appear in the trimer spectrum at 1280 mT and 1346 mT are shifted to higher field in the linear sum spectrum. The lower field feature in the trimer spectrum is also broader and much weaker compared to the linear sum spectrum.

These subtle differences may indicate some difference in the exchange interaction in the trimer **16** as compared to the model of a dimer **14** with the addition of the spectrum of a non-interacting ring.
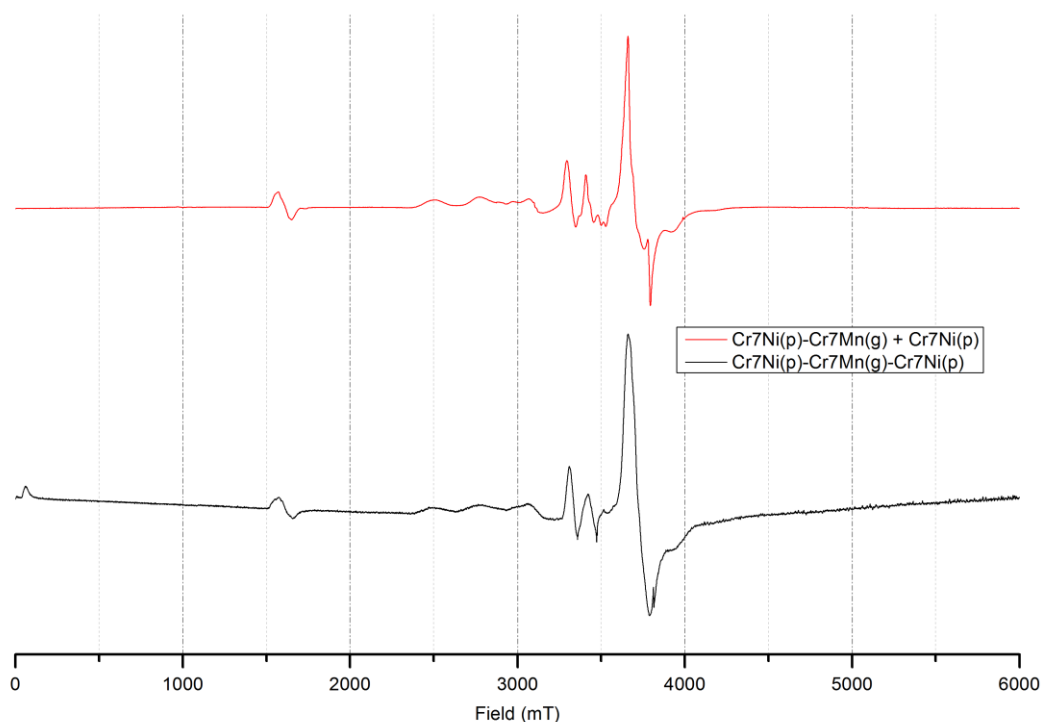
*Figure 109 Comparison of 5 K W Band spectra of the trimer **16** (black) and the linear sum of the dimer **14** and monomer **6** (red)*

Similar to Q Band spectra in Figure 108, the W Band spectrum of the trimer **16** generally shows the same features as the linear sum of the W-Band spectra of the dimer **14** and monomer **6,** see Figure 109. However, the small, sharp double dip feature at 3512 mT in the summed spectrum **14** is entirely absent in the trimer spectrum of **16**. The sharp feature at 3810 mT appears in both spectra but with much less intensity in the trimer spectrum.

The small blip at 61 mT in the trimer spectrum **16** is not a response from a sample, it is a common artefact from the instrumentation.
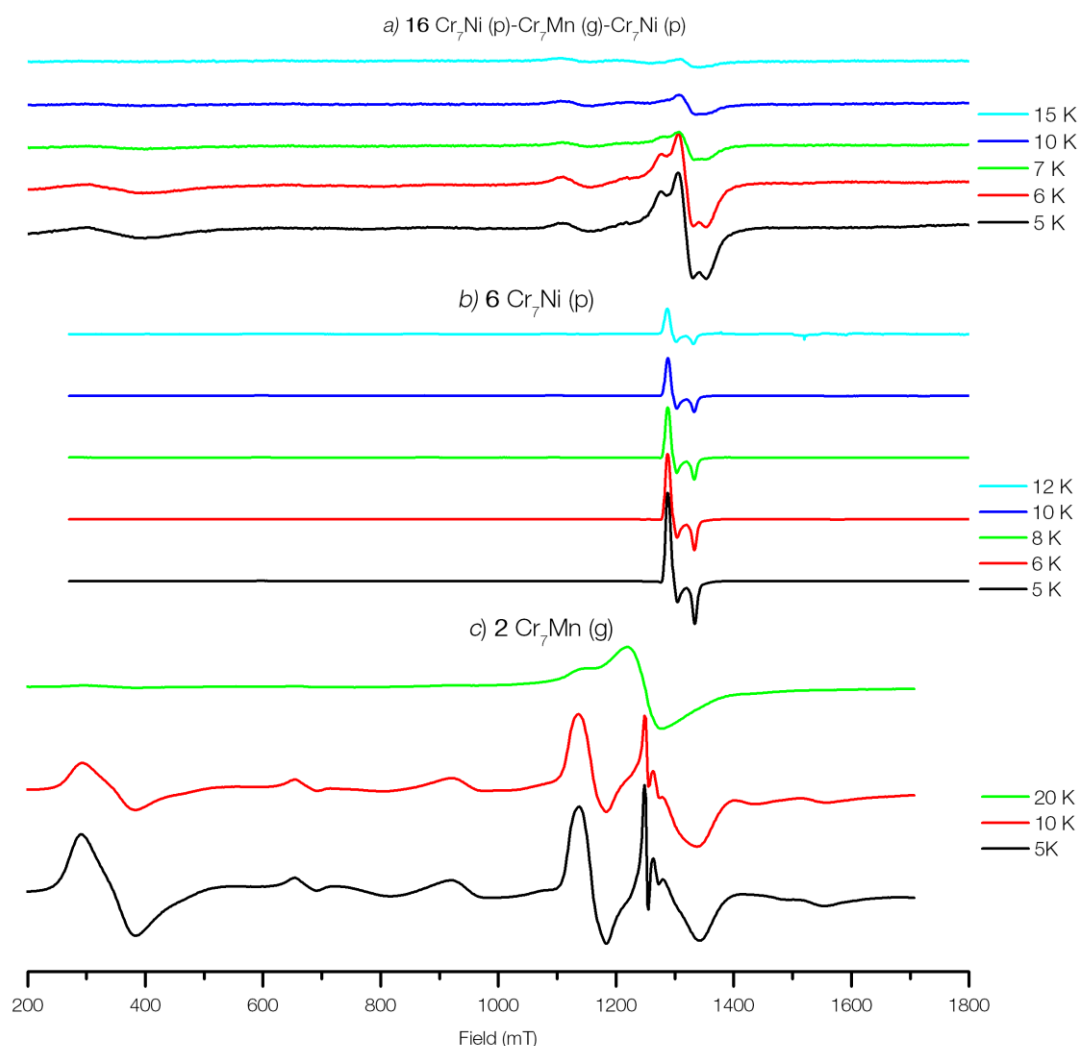
*Figure 110 Variable temperature Q Band EPR spectra of **16** measured at 33.647 GHz (a), variable temperature Q Band EPR spectra of **6** measured at 34.3187 GHz (b), and variable temperature Q Band EPR spectra of **2** measured at 34.0978 GHz*

The variable temperature Q Band spectra of **16** are shown in Figure 110 (a), and the comparisons with the single wheels **6** and **2** are shown in Figure 110 (b) and Figure 110 (c) respectively. The spectra of **16** have three features at 1311 mT, 1328 mT, and 1354 mT, which diminish with increasing temperature. These features broadly correspond to the features in **6**, though significantly broadened. The additional feature at 1280 mT in the spectra of **16** corresponds to the sharp feature in the spectra of **2**, although again significantly broadened. The two features at 1112 mT and and 296 mT in the spectra of **16** also correspond to features in **2**. These features all

diminish in intensity with increasing temperature. While many of the features of the trimer correspond to features in the single wheels, the broadening suggests an exchange interaction that is affecting the spectra.

[Cr$_7$Ni purple] – {Cr$_7$Zn green} – [Cr$_7$Ni purple] trimer   17
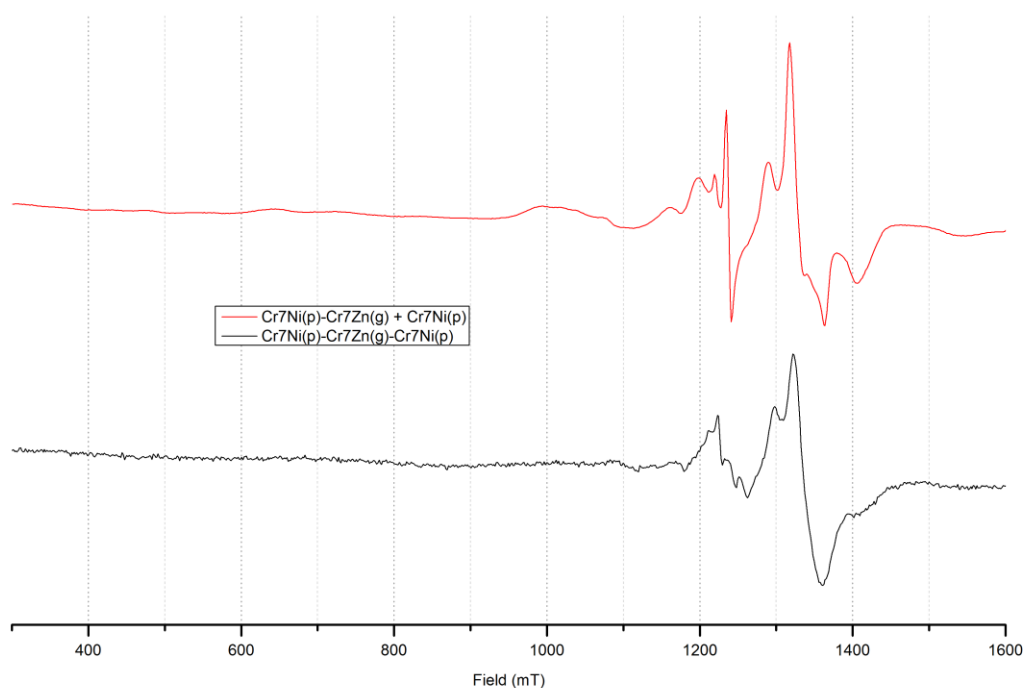
Figure 111 Comparison of 5 K Q Band spectrum of 17 (black) and the linear sum of 13 + 6 (red)

As with trimer **16**, most of the features in the Q-Band spectrum of **17** appear in the linear sum of the dimer **13** and the monomer **6**. There is a notable difference in relative intensities of features. The feature at 1233 mT is present in both spectra but with much less intensity in the trimer spectrum. Additionally, the summed spectrum shows a broad feature at 1001 mT. This does not appear to be present in the trimer spectrum at all, though may be obscured by noise.
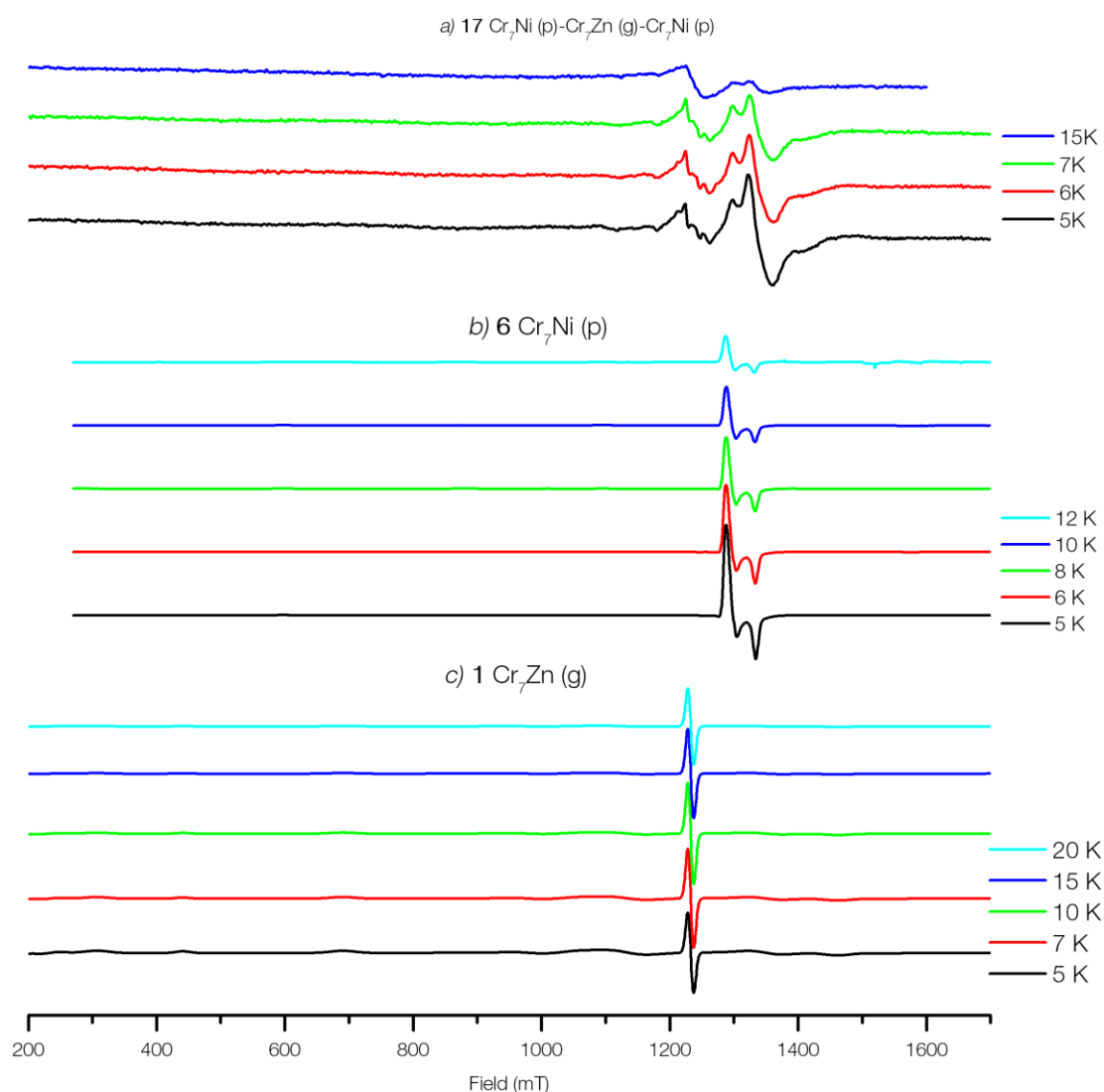
*Figure 112 Variable temperature Q Band EPR spectra of **17** measured at 34.130 GHz (a), variable temperature Q Band EPR spectra of **6** measured at 34.3187 GHz (b), and variable temperature Q Band EPR spectra of **1** measured at 34.1238 GHz (c)*

The variable temperature Q Band spectra of **17** are shown in Figure 112 (a), and the comparisons with the single wheels **6** and **1** are shown in Figure 112 (b) and Figure 112 (c) respectively. The spectra of **17** have a feature at 1293 mT that broadly corresponds to such a feature in the spectra of **6**. The feature at 1320 mT from **17** spans the two features in the spectra of **6,** broadened across that region. These features in the spectra of **17** diminish in intensity with increasing temperature, as

they do in the spectra of **6**. The spectra of **17** have a number of features in the region of 1233 mT, which do not correspond to features in either **6** or **1**.

Additionally, the difference between the spectra of **17** and the linear sum of **13** and **6** suggest that there could be a sizeable exchange interaction between the wheels of **17** that affects the spectra.

[Cr$_7$Zn purple] – {Cr$_7$Mn green} – [Cr$_7$Zn purple] trimer   18
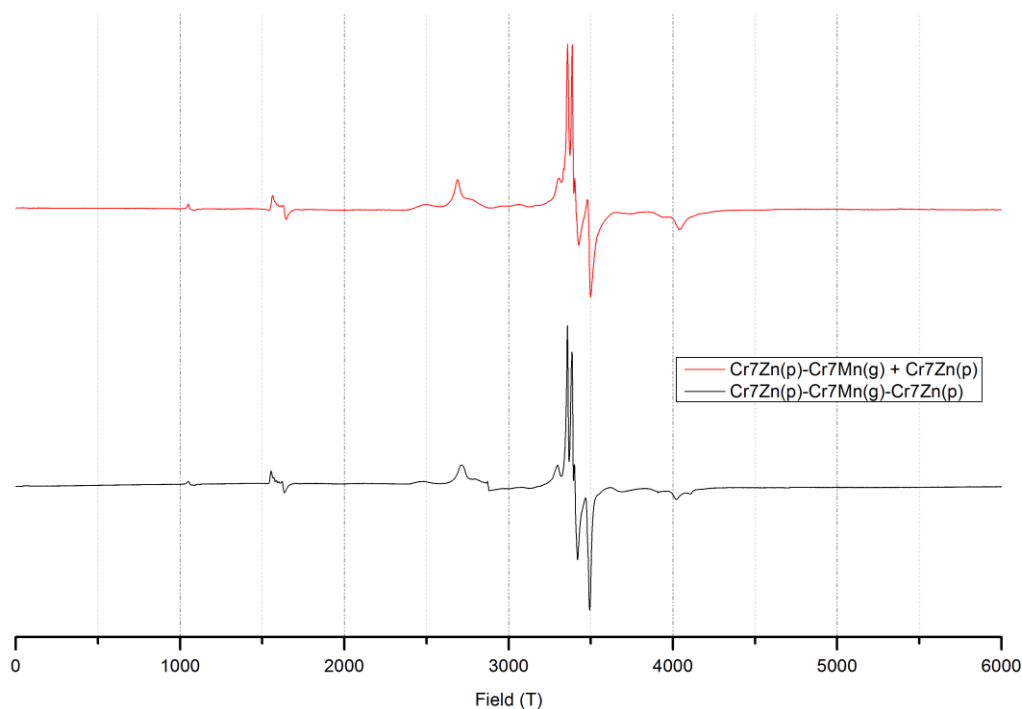
*Figure 113 Comparison of 5 K W Band spectrum of trimer **18** (black) and the linear sum of the dimer **8** and monomer **4** (red)*

The W Band spectrum of **18** is modelled almost identically by the linear sum of the dimer **8** and **4**. There is only a slight discrepancy in the relative intensities of the features at 3385 mT and 3357 mT. This is not surprising, as due to the diamagnetic nature of the single point of linking in Cr$_7$Zn there ought not be any interaction between the rings, as established by the cases where the Cr$_7$Zn purple ring was a component in the dimers in Chapter V.

Conclusions

The investigations into the heterometallic dimers showed that for compounds involving the purple wheel Cr$_7$Zn (**4**) there was no exchange interaction between the wheels. This is also the case for the heterometallic trimers, as the W-Band spectrum of the trimer **18** is identical to that of the sum of the constituent component wheels.

For the cases where the purple-green-purple trimer system is composed of purple Cr$_7$Ni, however, there are clear differences between the trimer spectra and the summed spectra of the component wheels. The spectrum of **17** in particular is notably different to the spectra of its component wheels, indicating some exchange interaction. The spectrum of **16** is also different, but these differences are more subtle.

These observations cannot deduce the relative magnitude of exchange interactions, simulations of the spectra are necessary to obtain numeric values. It is currently not possible to perform simulations of such large spin systems.

Chapter VII - The Problem of Fitting

Simulating complex systems with a microscopic Hamiltonian often results in a large number of parameters to be determined. Some parameters can be fixed by a combination of experimental methods, such as INS, bulk magnetisation and EPR. The most reliable model will be found by fixing parameters from experimental data rather than seeking to fit all parameters by simulation. Even after fixing as many parameters as possible, there will often be some remaining free parameters that must be found by simulation. These may be spin Hamiltonian parameters that describe some physical property of the system, or broadening parameters that describe lineshape.

If there is only a single free parameter to fit, the process is trivial: deduce the expected range of that parameter from literature, and then run numerous simulations varying that single parameter over that range until a fit is found. If there exists a numerical method to compare the simulation to the experimental data, this process is can be entirely automated algorithmically. If there does not, the process of fitting 'by eye' is not difficult – though often time-consuming.

When the number of free parameters is two or greater, the possible solution space becomes vast. It is of course still possible to iterate over all combinations of parameters, but the process of fitting by eye becomes a prohibitively exhaustive endeavour with difficulty in establishing confidence in finding a good fit. The question of whether a particular simulation is the 'best' possible fit is difficult to answer when 'good' is an entirely subjective measure. What is required is a quantifiable metric of 'goodness of fit'.

Least Squares

The standard approach to a fitting routine is to use *least squares*. This method was developed in 1805 by French mathematician Andrien-Marie Legendre to provide ships with a method of navigating in open seas by observing the positions and movement of celestial bodies.[1] As its goodness of fit metric, this routine uses the residual.

$$r_i = y_i - f(x_i) \qquad\qquad\qquad 1$$

The residual is the difference between the actual experimental value y_i and a value calculated by a simulation $f(x_i)$. The least squares method finds the minimum of the sum of the squared residuals

$$S = \sum_{i=1}^{n} r_i^2 \qquad\qquad\qquad 2$$

This approach is the basis of most fitting routines. This can be used for fitting very simple EPR spectra. For example, the EPR spectrum of a spin ½ system, as defined in Chapter I, can be modelled with an isotropic g.
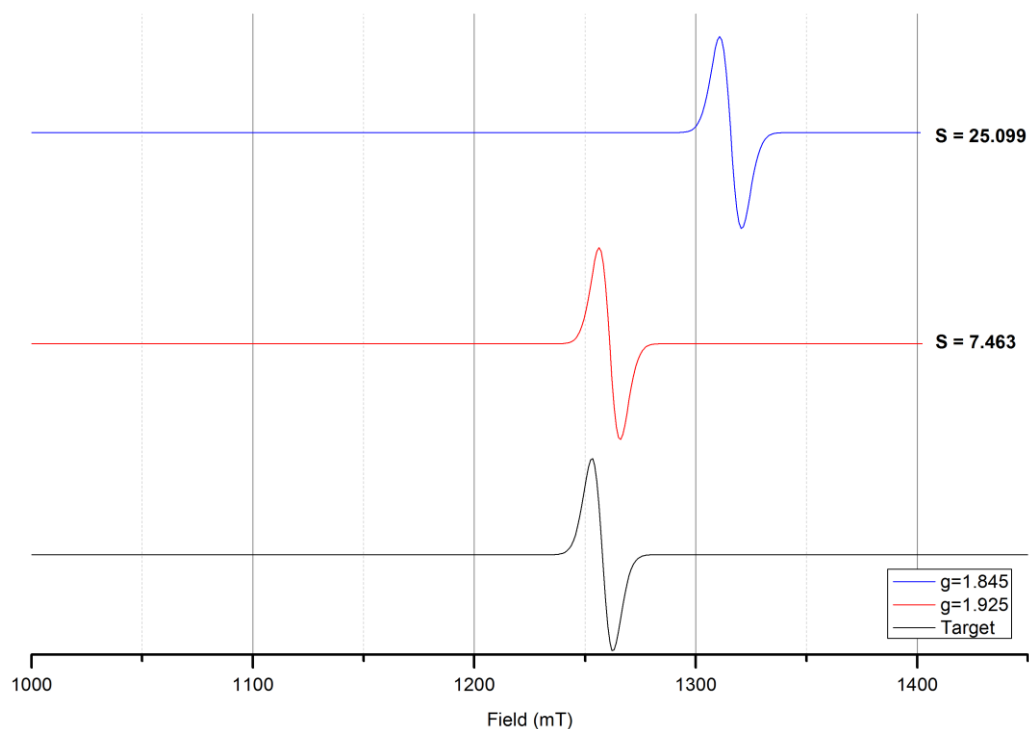
Figure 114 Comparison of some 'target' spin 1/2 spectrum (black) with an unknown g value and two attempted simulations g=1.925 (red) and g=1.845 (blue)

In Figure 114, a 'target' spin ½ spectrum has been generated representing an experimental spectrum with an unknown g value. The problem is to find the g value of this spectrum. Applying equation 2 to a simulation with $g = 1.845$ results in $S = 25.099$, while $g = 1.925$ results in $S = 7.463$ indicating that the latter is a closer fit to the target. If we repeat this process with many more plots, repeatedly calculate S, we can find this parameter value.
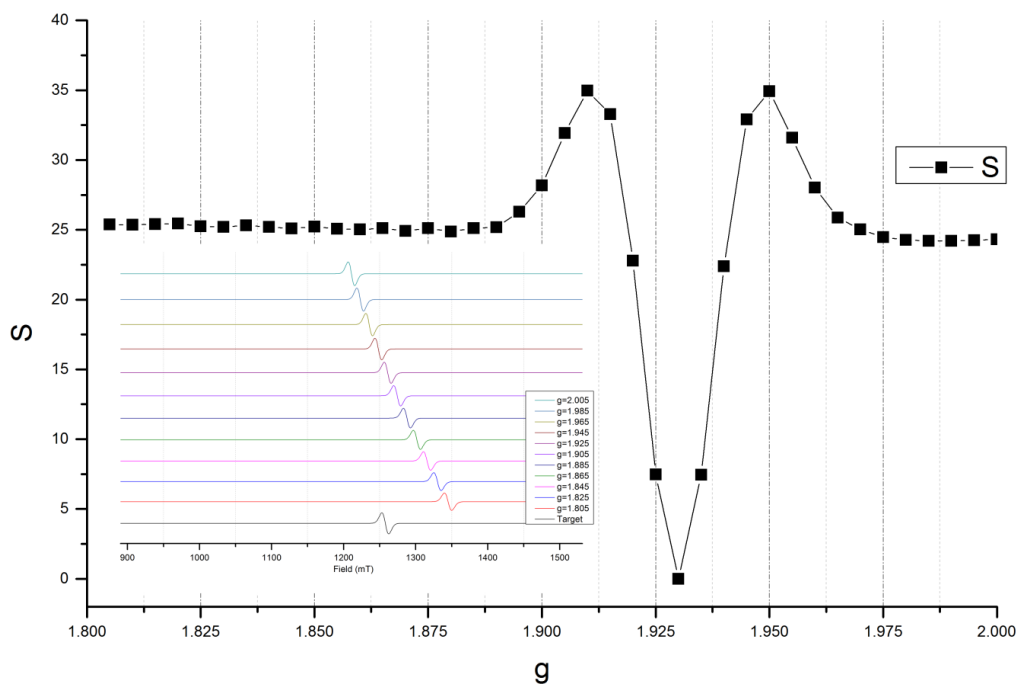
Figure 115 Plot of sum of squared residuals with variation in g, and plot of simulations used (inset)

This results of this process are shown in Figure 115 plotting *S* as a function of *g*. The lower the value of *S*, the 'better' the simulation is according to the least squares routine. The minimal *S* is found at *g* = 1.93.

The process of finding *g* is obviously trivial. The parameter is simple to calculate, and so the process of repeated simulations is unnecessary in real applications. By looking at the inset plot in Figure 115, it is obvious by inspection which plot is best. The purpose of this example is to analyse the algorithm and this has some interesting results for the least squares routine.

In principle, the further a simulation is away from *g* = 1.93 the 'worse' it is. However, in Figure 115 there is no difference in the value of *S* below *g* = 1.88. The least squares routine cannot discriminate between a bad simulation and a very bad simulation. Below *g* = 1.88 or above *g* = 1.98, the residual is being calculated between an isotropic spin ½ spectrum and a straight line and so there will be no

difference in the calculated *S*. This may not seem especially important, but when investigating the effects of more complex parameters upon a simulation it is possible to have no expectation of even the magnitude of the parameter. The investigative process always begins with repeated simulations varying that parameter and attempting to deduce a trend of increasing parameter value with goodness of fit. The least squares routine cannot determine this trend, and so is not useful if the test value of the parameter is very far away from the correct value.

As the simulations approach *g* = 1.93, the 'better' they ought to get. However, the value of *S* increases to a maximum *S* at *g* = 1.91 before decreasing to a minimum. The least squares routine seems to consider that *g* = 1.91 and *g* = 1.95 are the worst possible simulations.
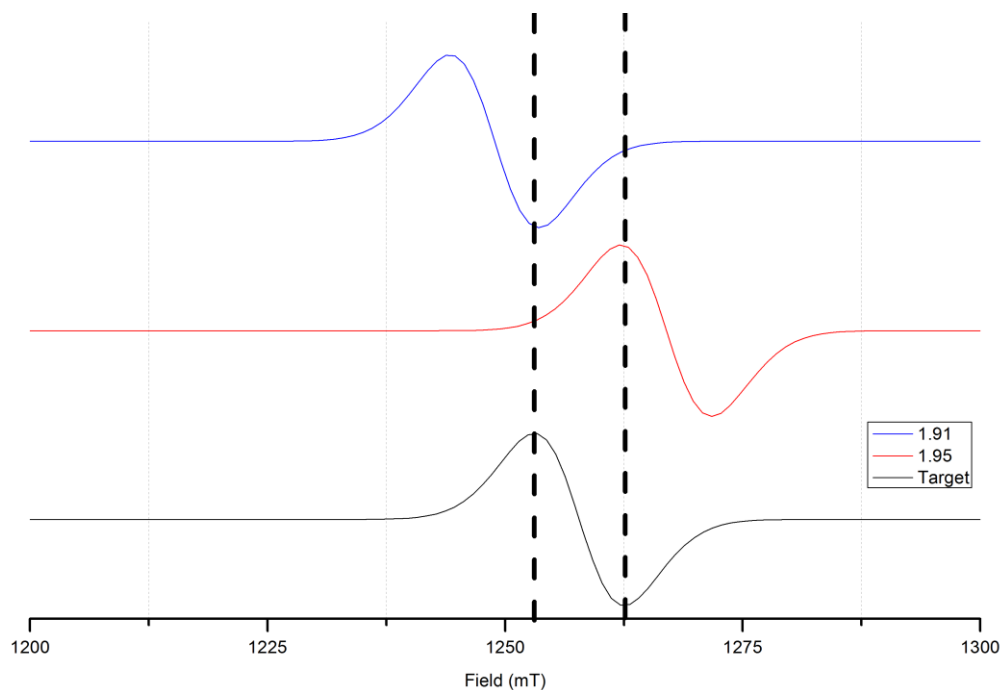
Figure 116 Simulations of the two maximal values of S

The reason for these features is that as at those values of g, the peak of the target meets the trough of the simulated *g* = 1.95, and the trough of the target meets the peak of the simulated 1.91 in Figure 116. At both of these points, the value of the

residual is maximal and so contributes heavily to the value of S. This means that when a simulation is in the region of being very close to correct, there is a huge spike in S giving the appearance of being in the region of a terrible simulation. In Figure 115, this rapidly drops to a minimum. This minimum is only found accurately because of the large number of simulations run across the parameter range. If that number were half as large, it is likely that the range of S would 'skip' over the correct value and the least squares routine would present only the maximal value of S in the region of the correct value. This means that the region of the best simulation would actually appear as the worst possible simulation, according to the least squares routine. Moreover, it means that S is not at all a reliable 'goodness of fit' metric for any single given simulation.

This second failing can be overcome by integrating the EPR spectrum to obtain an absorption spectrum. In a real EPR spectrum, signal to noise ratio is a significant consideration. Any noise reduction algorithms - while trivial – are computationally expensive. This broadening results in a loss of information. Integration is itself a computationally expensive process as well, so this would make a fitting routine considerably inefficient.

The limitations of least squares are apparent even in the simplest possible EPR spectrum and simulation. These problems are only further compounded when applied to real spectra with noise and numerous features, of varying lineshapes and intensities.

Least squares data for Cr$_9$F$_{10}$ QBand simulations using S=3/2 + S=3/2 model
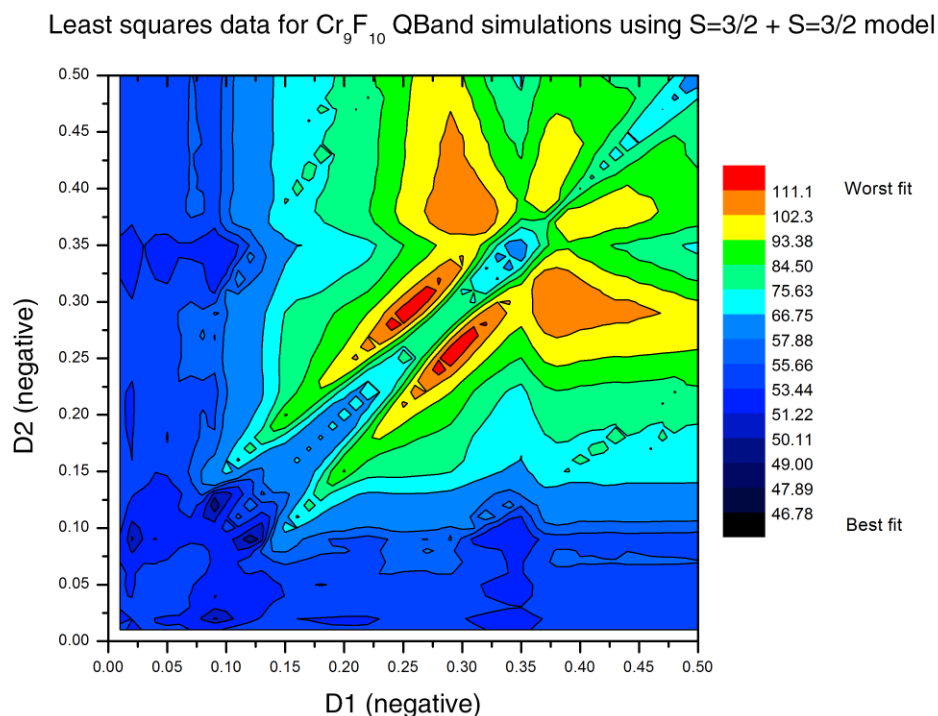
Figure 117 Least Squares map for simulations of [^{i}Pr$_2$NH$_2$][Cr$_9$F$_{10}$(O$_2$C^{t}Bu)$_{18}$]with the model S=3/2 + S=3/2

An optimistic attempt was made to model [^{i}Pr$_2$NH$_2$][Cr$_9$F$_{10}$(O$_2$C^{t}Bu)$_{18}$] as a sum of two S=3/2 states with two different D values, D_1 and D_2. Investigating this model rigorously involved simulating every possible combination of D_1 and D_2. This produced several thousand simulations. The ideal method to analyse these simulations is to calculate S for each simulation and produce a contour plot of S against the two D values as shown in Figure 117. In this plot, the red to yellow should indicate poor fits while blue indicates good fits. The most prominent result is that this plot does not predict any single best simulation, but rather has a wide area of possible solutions. This might be a useful result to reduce the possible solution space, if the predicted areas correspond to a good fit.
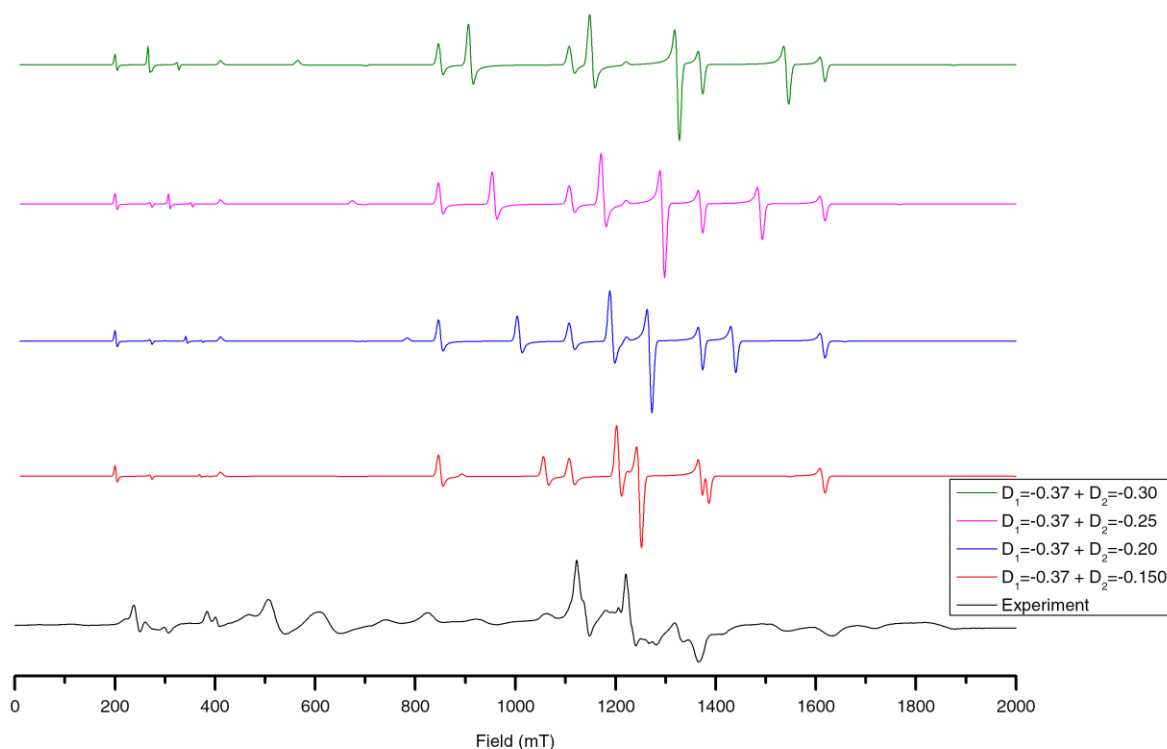
*Figure 118 Attempts at simulating{Cr₉F₁₀} Q Band spectrum (black) with a model
S=3/2 + S=3/2 with two non-identical D values*

A cross section of the simulations with D_1=-0.37 K is shown in Figure 118.

According to Figure 117, they ought to be progressively worse simulations with

increasing D_2. Upon inspection, this is not the case. While none of the simulations

are perfect, the simulation with D_2 = -0.25 K is the closest of the set with the most

features in approximately the correct positions. This is not reflected by the least

squares routine at all.

The value of S is not a good measure of goodness of fit for a given spectrum and

simulation. Despite this, least squares is still used as a measure as part of EPR fitting

routines in packages such as EasySpin [2] and others. [3,4] EasySpin is a MATLAB

toolbox for EPR simulations and contains a variety of methods for automated fitting

of simulations to experimental spectra, generally attempting to search for a global

minimum in the least squares solution space such as the dip in Figure 115. These

techniques do not solve the fundamental problem with least squares, but rather bypass them by some very elegant implementation of non-linear optimisation techniques. These algorithms use the current simulation to determine which parameters to run for the next simulation. They determine whether that simulation is better or worse than the previous one, and use that information to map the solution space to search for a global minimum. The biggest pitfall in these algorithms is finding a local minimum and not being able to escape that region to search for other minima that may be deeper. This corresponds to finding a simulation that appears to be a fairly good fit and optimising the parameters of that simulation, while ignoring the possibility of a much better fit elsewhere with significantly different parameters.

The problem of finding a global minimum, combined with the fundamental limitation of least squares, means that these fitting routines are useful only when searching over a very limited parameter range and very small number of unknown parameters. They also require that the simulation itself be run using the same software package as the fitting routine. This is a very powerful technique if the simulation can be carried out in EasySpin, and a rough simulation has already been determined and the parameters need only be optimised to greater accuracy.

For larger and more complex spin systems, it is more efficient to write custom software for each specific problem rather than general use EPR simulation tools. This software can exploit symmetries unique to the given system to reduce the computational complexity of the problem to minimize memory requirements and calculation time.

More generally, when given one specific simulation it does not give a reliable quantitative answer to the fundamental question: *is this simulation a good fit to the experimental data?*

I propose two different techniques that may produce a reliable goodness of fit parameter for EPR simulations. I set four criteria for this parameter. The goodness of fit parameter must:

- produce one global minimum over the solution space.

- be quick to calculate

- be easily reproducible and verifiable

- be independent of the simulation package

Pixel Mapping

Instead of treating the EPR spectrum as data points and using statistical techniques upon those data points, consider the plot of the EPR spectrum as an image and then using image processing techniques to analyse them. The question of how similar the spectra are becomes one of how similar these images are. The smallest component of a raster image is a *pixel*, or picture element. These pixels are arranged on a regular two-dimensional grid, the height and width of which determines the resolution of the image.

If the EPR spectrum is plotted and exported to an image, this image can be imported back in again computationally as a matrix of pixels. The size of the matrix depends upon the resolution of the image. The matrix consists entirely of values either '255' if that particular pixel is blank and does not contain a segment of spectrum, or '0' if that particular pixel does contain a segment of spectrum, as shown in Figure 119.

Figure 119 Part of the matrix of pixels of an EPR spectrum

The advantage of using a matrix representation of the spectrum is that information about both dimensions is preserved. The least squares routine calculation only includes the y values of the spectrum. The matrix representation includes both dimensions and so may provide a more accurate measure of field-dependent features.
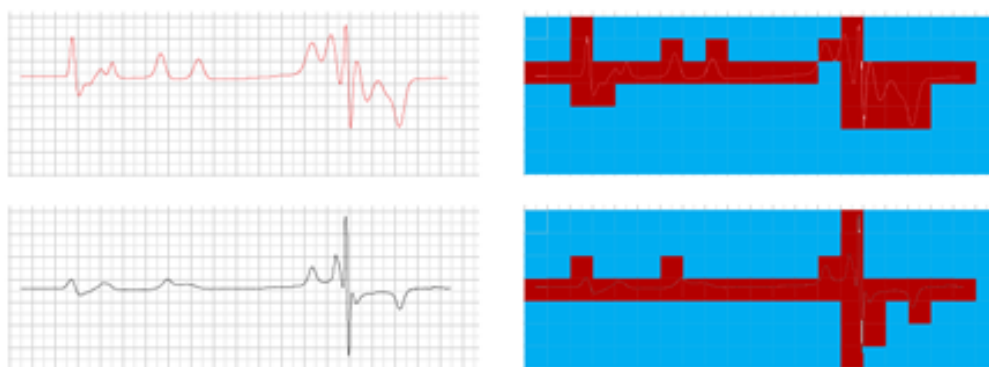
Figure 120 EPR spectra arranged upon a grid (left) and filling of pixel grid corresponding to whether area contains spectrum or not

The EPR spectrum is overlaid on a grid, and if a square contains any segment of spectrum it is filled with red and if it does not it is filled with blue. The results is a highly pixelated version of the spectrum. By reducing the size of the grid in Figure 120, the pixel map becomes a more accurate representation of the original spectrum. However, the size of the matrix grows exponentially with decreasing pixel size and so for efficiency this size must be optimised before any matrix operations can be carried out. The optimisation process involves a simple algorithm that fills in the pixel grid and calculates the number of squares that are filled as a percentage of the total number of squares in the grid. The pixel size is then reduced and the percentage of filled squares is re-calculated. This process is repeated until there is no change in the calculated percentage, ensuring that all features in the spectrum are covered by the size of the pixel but also that the pixel is not unnecessarily small.

Once we have the two spectra in matrix form, there are a few different ways in which to compare them. The most simple is to iterate across the grid and test if one grid has a filled region where the other does not in the same respective position.

Table 18 Pseudocode for pixel grid matrix comparison where d quantifies difference

```
1.  d=0
2.  for i=1:size(MatrixA)
3.      for j=1:size(MatrixB)
4.          if MatrixA(i,j) ~= MatrixB(i,j)
5.              d = d + 1;
6.          end
7.      end
8.  end
```

The pseudocode in Table 18 demonstrates the calculation of the goodness of fit metric d.
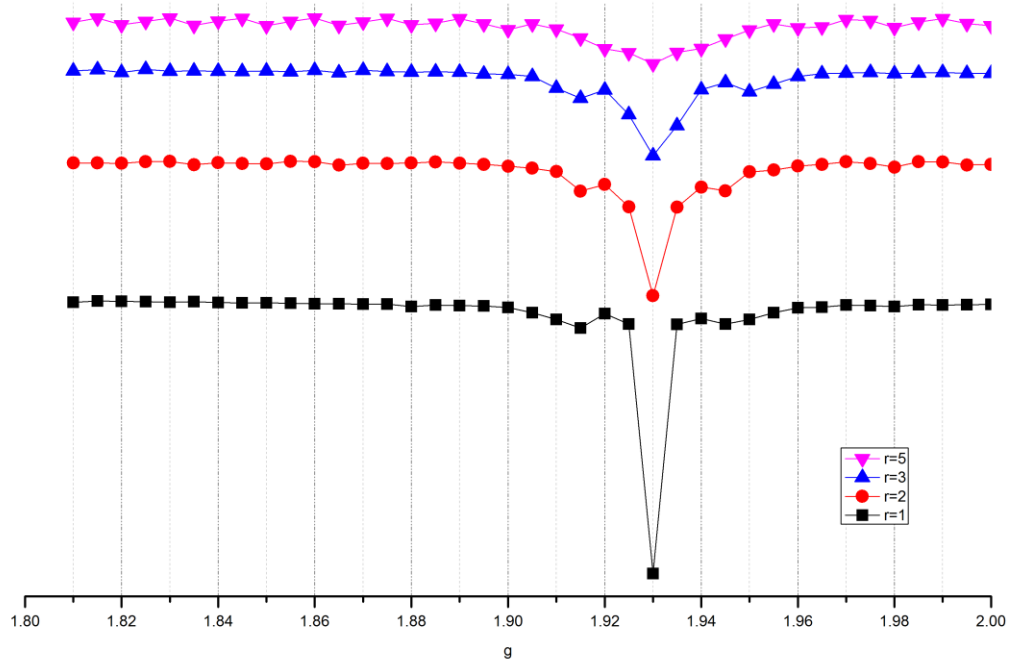
Figure 121 Plot of pixel map metric d for S=1/2 simulations with unknown g, with varying pixel size r=1, r=2, r=3, and r=5

We can apply this algorithm to the same simulations as shown in Figure 115, a simple S=1/2 spectrum with isotropic *g*. Figure 121 shows several different plots of this pixel matrix metric *d*, with different pixel sizes *r*. The black line is a plot with this algorithm run with a 1x1 square pixel, red with a 2x2 square pixel, blue with 3x3 and pink with 5x5. There is a 50.7% performance increase between the 2x2 and 1x1. The most important result is that this simple metric precisely identifies the correct *g* value with a very sharp minimum at *g* = 1.93. This minimum is clear with a pixel size of up to 3x3. This algorithm does not have the misleading maxima surrounding *g* = 1.93 as produced by the least squares method in Figure 115. However, it does produce the same value of the metric below 1.90 and above 1.96 and so exhibits the same difficulty in differentiating between poor and very poor simulations.

The efficiency of the method in Table 18 is highly dependent upon the chosen pixel size and this pixel size is chosen to be the same across the grid. It is possible that this

method could be improved by implementing different pixel sizes across the grid, benefiting from the speed of a large pixel size in flat areas of spectrum and the precision of a small pixel size in areas of sharp features. This would require an algorithm to identify the position of peaks, searching for maximal intensity values across the spectrum.

Using these same pixel map matrices, more nuanced metrics could also be calculated. For example, an element-by-element subtraction of the two matrices would produce a matrix that represents their difference. Some operation upon this difference matrix could yield a viable goodness of fit metric.

However, this pixel mapping method is fundamentally a very brute force method producing quite large matrices. These matrices do mostly consist of zeros, and so some sparse matrix optimisation could conceivably improve efficiency. A more elegant approach to this problem would be the application of some more fundamental mathematical operation upon the spectrum.

Wavelet Transform

A transform is a mathematical operation that finds additional information from a signal. The most well-known of such transforms is the Fourier Transform. The most common application is to transform a signal from a time domain into a frequency domain or vice versa. [5]

Experimental data are usually acquired at discrete intervals, and such signals are transformed into a frequency domain by a Discrete Fourier Transform (DFT). The problem with a Fourier transform is that when a signal is transformed into a different domain, all information is lost about the previous domain. As the EPR phenomenon is fundamentally field-dependent, it would not make sense to Fourier transform the

spectrum. A short-time Fourier transform uses a sliding window over which to perform this Fourier transform, preserving the information about both domains but the length of the window limits the resolution. Wavelet analysis provides information about both dimensions without this limitation.

The first wavelet was proposed by Alfred Haar in 1910, [6] though the term did not exist until proposed by Morlet and Grossmann in 1985. [7] The fast wavelet transform was developed in 1989 by Mallat, beginning the application of this transform in the field of signal processing.[8] Wavelet transforms are comparatively a very recent mathematical development and a very active area of research.

The wavelet transform is defined as

$$\psi(t,s) = \sum_{-\infty}^{\infty} f(x) \frac{1}{\sqrt{s}} \phi\left(\frac{x-t}{s}\right) dx \qquad\qquad \textbf{3}$$

where

- $f(x)$ is the square integrable function to be analysed
- ϕ is a square integrable base wavelet
- t is a translation parameter
- s is a scaling parameter

The value of $\psi(t,s)$ is a measure of the similarity of the functions $f(x)$ and ϕ, which is then translated t units and stretched s times.

The Wavelet Transform works by repeatedly passing a time domain signal through different highpass and lowpass filters, removing maximal and minimal portions of the signal. This process is repeated, continually removing some portion of the signal. Consider a signal composed of frequencies up to 200 Hz. This signal is divided in two, a lowpass and a highpass segment, a process known as *decomposition*.

Table 19 First decomposition of 200 Hz signal

0 – 200 Hz	
0 – 100 Hz	100 – 200 Hz
Lowpass	Highpass

The lowpass portion is decomposed again, resulting in three data sets.

Table 20 Second decomposition of 200 Hz signal

0 – 200 Hz		
0 – 50 Hz	50 – 100 Hz	100 – 200 Hz
Lowpass		

Once again the lowpass portion is chosen and decomposed.

Table 21 Third decomposition of 200 Hz signal

0 – 100 Hz			
0 – 25 Hz	25 Hz – 50 Hz	50 – 100 Hz	100 – 200 Hz
Lowpass			

This decomposition process is repeated until we have a set of signals corresponding to different bands, the number of iterations depending on the complexity of the signal. These decomposed signals can be put together on a 3D plot of frequency vs. time vs. amplitude.

We can know which frequencies exist at given time intervals, but we cannot know which frequency exists at a specific instance of time. This is because of the Heisenberg Uncertainty Principle. The Uncertainty Principle is a quantum mechanical inequality that sets a limit upon the precision of which complementary variables can be known simultaneously. [9] This is a fundamental mathematical limit present in all wave-like systems, irrespective of the limits of an experimental setup. The original formulation of the Uncertainty Principle is that the momentum and position of a particle cannot be determined simultaneously with arbitrary precision. When applied to a time-dependent signal, this means that it is not possible to know which spectral component is present in any given instant of time. We can only know which spectral components are present in a given interval. The uncertainty principle also means that the highpass portion of the spectrum in Table 19 has a more precise time resolution while the lowpass portion has a more precise frequency resolution. [10] The choice of this interval is very important for the resolution of the wavelet transform.

The application of the wavelet transform in equation **3** depends upon the choice of the base wavelet ϕ. The first wavelet proposed was the Haar wavelet, [6] a sequence of square functions that form an orthonormal system. The Haar function $\psi(t)$ is described by

$$\psi(t) = \begin{cases} 1 & 0 \leq t < \dfrac{1}{2} \\ -1 & \dfrac{1}{2} \leq t < 1 \\ 0 & \text{otherwise} \end{cases}$$

with a scaling function $\phi(t)$ as

$$\phi(t) = \begin{cases} 1 & 0 \leq t < t \\ 0 & \text{otherwise} \end{cases}$$

There are four basis vectors for the Haar wavelet, normalised by magnitude

$$
e_1 = \begin{pmatrix} 1/2 \\ 1/2 \\ 1/2 \\ 1/2 \end{pmatrix} \qquad
e_2 = \begin{pmatrix} 1/2 \\ 1/2 \\ -1/2 \\ -1/2 \end{pmatrix} \qquad
e_3 = \begin{pmatrix} 1/\sqrt{2} \\ -1/\sqrt{2} \\ 0 \\ 0 \end{pmatrix} \qquad
e_4 = \begin{pmatrix} 0 \\ 0 \\ 1/\sqrt{2} \\ -1/\sqrt{2} \end{pmatrix}
$$

These basis vectors are the simplest orthogonal square wave signals, and so have extremely low memory requirements. For this reason, they have applications in pattern recognition and image processing. [11,12]

As wavelet transforms are such a recent mathematical development, there has not been much work in the application of wavelets to EPR spectra. In the literature, there is only one attempt at an implementation. Drzewiecki and Sczaniecki have investigated the relation between EPR spectra and the wavelet transform. [13] Their choice of basis wavelet is the Lorentzian basis wavelet

$$
\phi\left(\frac{x-t}{s}\right) = -\frac{4}{\sqrt{\pi}} \frac{\dfrac{x-t}{s}}{\left[1 + \left(\frac{x-t}{s}\right)^2\right]^2}
$$

Hence the wavelet transform becomes

$$
\psi(t,s) = \frac{-4A\sqrt{\pi}\Delta B s^{\frac{3}{2}}}{(s+\Delta B)^3} \cdot \frac{3\left(\dfrac{t-B_0}{s+\Delta B}\right)^2 - 1}{\left(\left(\dfrac{t-B_0}{s+\Delta B}\right)^2 + 1\right)^3} \qquad \textbf{4}
$$

This function has one single maximum at $t = B_0$ and $s = \Delta B$, which satisfies the first criterion I specified for a goodness of fit metric. Drzewiecki and Sczaniecki had an ambitious desire to deduce spectroscopic parameters directly from the wavelet transform, the constants in Equation **4** corresponding to EPR parameters. This would have replaced the need for numerical simulation entirely, as spin Hamiltonian

parameters could be deduced directly from a transform of an experimental spectrum. This appears not to have been successful, and no further research has been reported on using wavelet transforms directly as a tool for simulation. However, the desire for a goodness of fit metric is a much more modest one and the work of Drzewiecki and Sczaniecki produces an interesting result that may have applications in this search.
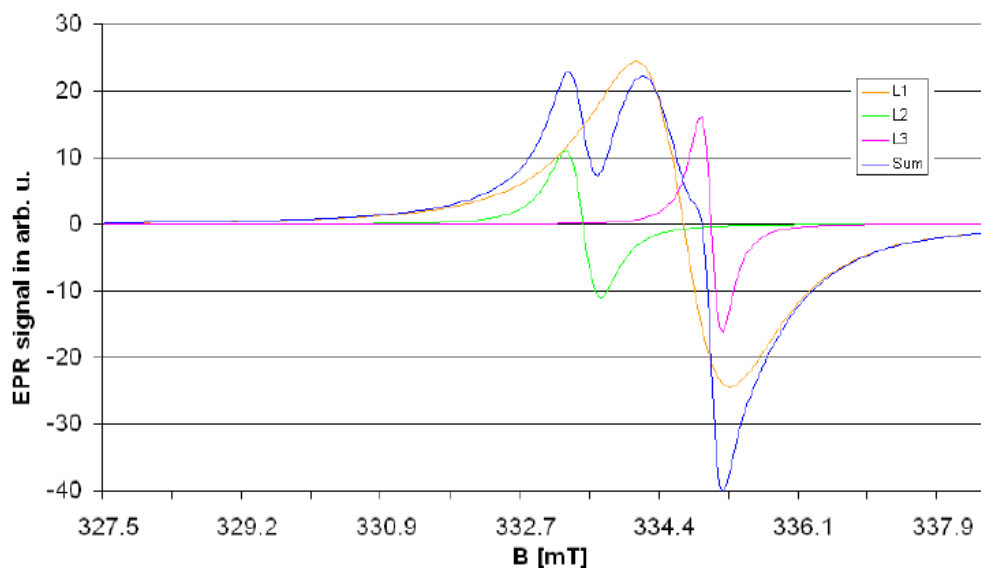
Figure 122 Decomposition of EPR spectrum by wavelet analysis. L1 (yellow), L2 (green) and L3 (pink) are the decomposed signals and the Sum (blue) is the sum of L1+L2+L3 that reproduces the EPR spectrum[13]

The wavelet transform can be used to transform a complex EPR spectrum into different components of the signal. The sum of these components reproduces the original EPR spectrum. While the EPR spectrum is complex, consisting of several overlapping peaks of varying lineshape, the decomposed signals are very simple, see Figure 122.

A fitting routine could be produced that compares the decomposed signals of the experimental spectrum with the simulation. This process would repeatedly find the best fits for each decomposed signal and then report the cross-section where a fit is found for all signals. In this case, least squares may well be an appropriate goodness

of fit metric because it is being used to simultaneously fit dependently multidimensional data. For the first decomposition, least squares will produce numerous misleading minima and maxima. For the second decomposition, least squares will also produce misleading minima and maxima – but in different positions. The true minimum will be the one that is consistent between the two. The actual process will almost certainly not be this simple, as there may be numerous consistent minima but increasing the number of decompositions will reduce the number of consistent minima and focus in on the true global minimum – corresponding to the best fit. In this case, the goodness of fit metric will be the squared sum of the least squares.

The difficulty with the wavelet transform is the choice of basis wavelets. Drzewiecki and Sczaniecki chose the Lorenzian basis wavelet to search for spectroscopic parameters in the output of the transform. This may not be the most appropriate nor the most efficient basis wavelet when simply fitting an experimental spectrum to one already simulated. The Lorenzian wavelet does accurately decompose an EPR signal, and this process would be scalable to the complexity of any spectrum simply by repeated decompositions.

Conclusion

The lack of a reliable goodness of fit metric for EPR spectra is always going to be a problem for the simulation of complex systems. When there is a large number of free parameters, fitting by eye is not a reliable method to rigorously explore a solution space. Moreover, fitting by eye is an entirely qualitative judgement over how good a fit is 'good enough'. The pixel mapping routine is indeed one that works and works better than least squares, but comes at a great cost of computational requirements. The Wavelet Transform is a much more elegant procedure and shows promise in the

decomposition of an EPR spectrum, but a full investigation into basis functions is necessary before implementation of a fitting routine is possible.

References

[1]   Stigler, S. M; The History of Statistics: The Measurement of Uncertainty Before 1900; *Belknap Press of Harvard University Press*, **1986**.

[2]   Stoll, S.; Schweiger, A; *J. Magn. Reson.,* **2006**, 178, 42.

[3]   Kirste, B; *J. Magn. Reson.,* **1987**, 73, 213.

[4]   Misra, S. K; *J. Magn. Reson.,* **1976**, 23, 403.

[5]   Jordan, D.; Smith, P; Mathematical Techniques: An Introduction for the Engineering, Physical, and Mathematical Sciences; *OUP Oxford*, **2008**.

[6]   Haar, A.; *Math. Ann*., **1910**, 69, 331.

[7]   Grossmann, A.; Morlet, *J;. SIAM J. Math. Anal.,* **1984**, 15, 723.

[8]   Mallat, S.; G., *IEEE Trans. Pattern Anal. Mach. Intell.*, **1989**, 11, 674.

[9]   Busch, P.; Heinonen, T.; Lahti, P.; *Phys. Rep.,* **2007**, 452, 155.

[10]   Xu, Y.; Weaver, J. B.; Healy, D. M., Jr.; Lu, J.*IEEE Trans. Image Process.*, **1994**, 3, 747.

[11]   Oren, M.; Papageorgiou, C.; Sinha, P.; Osuna, E.; Poggio, T. *Proceedings of IEEE Computer Society Conference,* **1997**, p 193.

[12]   Lai, Y.; Kuo, C. C. J.; *JVCIR.,* **2000**, 11, 17.

[13]   Drzewiecki, A.; Sczaniecki, *Acta. Phys. Pol. A.,* **2005**, 108, 73.

Chapter VIII - Conclusions and Future Work

The series of purple Cr_7M rings have been modelled with a microscopic Hamiltonian, considering the contribution of numerous spin states and the effects of S-mixing. In order to implement this Hamiltonian, the system is modelled with many fewer parameters than may be expected from first principles. However, the experimental EPR spectra are well reproduced by simulations with this model. The simultaneous implementation of INS and EPR at Q and W Band allows for the determination of these parameters.

This model could be extended by introducing more exchange parameters according to the bridging arrangement; an additional J_{Cr-Cr} corresponding to the bridge with the fluoride and two carboxylates, a different J_{Cr-Cr} for the alkoxide and two carboxylates, a J_{Cr-M} for the bridge with the fluoride and two carboxylates and another different J_{Cr-M} for the bridge with one fluoride and one carboxylate.

While the experimental data on the purple Cr_7M rings is fairly well reproduced with this model, there are a few features that may be improved with a more nuanced exchange picture. An important result from this work is that the determination of exchange parameters can be made based on spectroscopic data, rather than structural arguments. Additional parameters ought only to be introduced when data require it.

Pulsed EPR measurements on the purple Cr_7M rings show that these rings are worthy of further investigation as qubits, as the measured compounds exhibit relaxation times of a similar magnitude to previously studied green wheels and other proposed candidates as qubits.

The same approach was taken to the modelling with the [Cr$_7$$M$ purple] − {Cr$_7$$M$ green} dimers. This was not as successful as with the individual wheels, as the exchange model is far too simple. In this case, the resolution of the data may well warrant the introduction of additional exchange parameters. The simple model does show that the inter-ring exchange is weak but non-zero, an order of magnitude weaker than the communication within the ring. For dimers involving {Cr$_7$Zn purple}, the communication is immeasurably small by EPR spectroscopy and so is set to zero. For dimers involving {Cr$_7$Zn green}, the communication is very weak − an order of magnitude weaker still compared to the dimers of {Cr$_7$M green} and {Cr$_7$Ni green}.

To reproduce the experimental spectra, this model does need to be extended to include additional non-equal exchange interactions.

The family of [Cr$_7$$M$ purple] − {Cr$_7$$M$' green} − [Cr$_7$$M$ purple] trimers has also been measured, but the vast number of spins in this system does not make it feasible to simulate the spectra with a microscopic Hamiltonian. If the model of the dimers needs to be extended to include additional exchange parameters, a microscopic model of the trimers would involve a very large number of free parameters. The complexity of the process of simulating those systems would be enormous.

To simulate complex systems with large numbers of free parameters, there needs to be an algorithmic method to compare and fit the spectra. The fundamental limitations of least squares has been thoroughly investigated, and two alternative approaches proposed.

The pixel mapping algorithm is a brute force and inefficient method, but does demonstrate features that have a significant advantage over the least squares method. This algorithm could be incrementally improved in a number of ways. First, it would presumably be more efficient to implement in the algorithm in a language other than MATLAB. The process of exporting an image to import back in again is the simplest way to generate a pixel map matrix. Once the pixel map matrices are generated, they could be expressed in a more compact format. The matrices are mostly empty, consisting mainly of 0s, and so sparse matrix representations may improve efficiency considerably. I have presented the simplest possible algorithm for comparing the two pixel map matrices: increment a value if there is a difference in equivalent positions. Despite its simplicity, this produces a better goodness of fit metric than least squares. This algorithm is also massively parallelisable because each pair of pixels is independent of every other pair.

Other more nuanced algorithms for comparing the two pixel map matrices may well yield better results, such as a direct subtraction of the two matrices and some calculation on this difference matrix.

A more mathematically elegant method to this problem would be to implement a Wavelet Transform, to decompose the spectrum and repeatedly fit the decomposed parts of the spectra. This method is proposed as a possible solution to this problem, the efficiency of which is currently unknown.

The solution to this problem of fitting has almost certainly already been solved, in some other area of signal processing or fundamental mathematics. The challenge is to find it and implement it for EPR spectroscopy.

Appendix I – Pixel Mapping Algorithm

Chapter 6 details an algorithm for pixel-by-pixel comparison of EPR spectra and simulations. The idea is simple and intuitive, but the implementation has some nuanced complexity that is worth presenting. As this code produces and manipulates matrices, it seemed sensible to use MATLAB to implement this method. MATLAB, originally MATrix LABoratory, is a high level programming language that is especially adept at large matrix manipulations. MATLAB is a proprietary product requiring numerous licenses for numerous toolboxes, so it would make sense to adapt this code for some open source alternative such as FreeMat or Scilab.

There are different parts of this code split up into different classes. The 'main' class specifies the input files and calls the other more general code. In this code, the spectrum to be fitted (usually an experimental spectrum) is designated a 'seed' and the other simulations are designed as 'needles'. The needles all need to be in one folder, separate from the seed. The output is written to a tab delimited file as a list of the needle filenames and the difference metric between that needle file and the seed.

Table 1 'Main' class for Pixel Mapping algorithm

```
1.  needles = dir('S0.5/spcnorm/')
2.
3.  seed = 'S0.5/g/target.spcnorm';
4.  figure
5.  figplot=gca
6.
7.  figure
8.  contfig = gca
9.
10. fighandle(1) = figplot;
11. fighandle(2) = contfig;
12.
13.
14. ww = waitbar(0,'Reticulating splines')
15.
16. for i = 4:size(a,1)
17.     waitbar(i/size(a,1),ww,'Reticulating splines')
18.     g(i) = seekarraycompare(fighandle,2,seed,0,strcat('S0.5/spcnorm/',needle
    s(i).name),0);
19.     B20{i,1} = needles(i).name;
20.     B20{i,2} = g(i);
```

```
21. end
22.
23. filename='testresS0.5_res3.txt'
24. M = B20
25. fid = fopen(filename,'wt');
26. [rows,cols] = size(M);
27. for i=1:rows
28.     fprintf(fid,'%s\t',M{i,1})
29.     fprintf(fid,'%i\n',M{i,2})
30. end
31. fclose(fid)
32.
33. close(ww);
```

This function calls the 'seekarraycompare' function that compares the two pixel matrices and returns a value of the two.

Table 2 'Seekarraycompare' function for comparing pixel map matrices

```
1.  %Function that gives number of how similar two datasets are
2.  function diffval = seekarraycompare(fighandle,resolution,fileone,todifforno
    tone,filetwo,todiffornottwo)
3.
4.  %Import two datasets
5.  ImpDataA = importdata(fileone);
6.  ImpDataB = importdata(filetwo);
7.
8.  %Match x values
9.  [U,V] = matchsets(ImpDataA,ImpDataB);
10.
11. %Generate image matrices for both datasets
12. seekarrayone = makeseekarray(fighandle,resolution,U,todiffornotone);
13. seekarraytwo = makeseekarray(fighandle,resolution,V,todiffornottwo);
14.
15. %Loop through every element (i,j), if elements are unequal then increment
16. %by one
17. diffval = 0;
18. for i=1:size(seekarrayone,1)
19.    for j=1:size(seekarrayone,2)
20.        if seekarrayone(i,j) ~= seekarraytwo(i,j)
21.            diffval = diffval + 1;
22.        end
23.    end
24. end
25.
26. end
```

This is the class that takes the data in the format of a 2 dimensional array and produces the matrix. Some simulations may output an absorption spectrum, and so this function has a flag to differentiate the data.

Table 3 'makeseekarray' class that produces pixel matrix from dataset

```
1.  function seekarray = makeseekarray(fighandle,resolution,DataSet,todiffornot
    )
2.  %If the DataSet contains EPR data, then we don't need to differentiate it.
3.  %If it is absorption data, then we do.
```

```
4.   if ( todiffornot == 1 )
5.   for i=1:(size(DataSet,1)-1)
6.       DataSetDiff(i,2) = (DataSet(i+1,2) - DataSet(i,2))/(DataSet(i+1,1) -
     DataSet(i,1));
7.   end
8.   DataSetDiff(i+1,2)=DataSetDiff(i,2);
9.   DataSetDiff(:,1) = DataSet(:,1);
10.  DataSet = DataSetDiff;
11.  end
12.
13.  %Normalise dataset
14.  DataSet(:,2) = DataSet(:,2) / max(DataSet(:,2));
15.
16.
17.  %Plots the dataset
18.  %figure
19.  %figplot=gca
20.  figplot=fighandle(1);
21.  plot(figplot,DataSet(:,1),DataSet(:,2));
22.  axis(figplot,[min(DataSet(:,1)) max(DataSet(:,1)) -1 1]);
23.  set(figplot,'LineWidth',2);
24.  axis(figplot,'off')
25.
26.  %Exports as an image
27.  saveas(figplot,'eprdata.png');
28.
29.  %Reads image back in again, so we now have an EPR spectrum has a matrix of

30.  %RGB values
31.  EPRimage = imread('eprdata.png');
32.
33.  %imshow(EPRimage);
34.
35.  %This changes the 3 dimensional matrix into a 2 dimensional matrix
36.  for i=1:size(EPRimage,1)
37.      for j=1:size(EPRimage,2)
38.          EPRarray(i,j) = EPRimage(i,j);
39.      end
40.  end
41.
42.  %Sets the size of the squares to be tested
43.
44.
45.  for i=1:resolution:(size(EPRarray,1))
46.      for j=1:resolution:(size(EPRarray,2))
47.
48.          hassignal = 0;
49.
50.          for n=0:(resolution-1)
51.              for m=0:(resolution-1)
52.                  if ((i+n) < size(EPRarray,1)) &  ((j+m) < size(EPRarray,2))

53.                      if EPRarray(i+n,j+m) ~= 255
54.                          hassignal = 1;
55.                      end
56.                  end
57.              end
58.          end
59.
60.          seekarray(int16(i/resolution)+1,int16(j/resolution)+1) = hassignal;

61.
62.      end
63.  end
64.
65.  %figure
66.  %contfig = gca
```

```
67. contfig=fighandle(2);
68. contour(contfig,seekarray)
69.
70. end
```

In order to make these matrices, the data arrays must be the same size. This function first finds the smallest and largest common x value and truncates data outside that region, and then interpolates data between the two.

Table 4 General matchsets function for truncation and interpolation of data

```
1.  function [U,V]=matchsets(A,B)
2.  %This is a function that takes two arrays A,B and matches the closest x
3.  %values of the two arrays.
4.
5.
6.  %First we need to make sure both arrays have the same start point
7.
8.  %Test to find which start point in either array is the largest
9.  if A(1,1) < B(1,1)
10.     match.value = B(1,1);
11.     match.M = A;
12.     match.start = findmatch(match.value,match.M);
13.     A = A(match.start:end,:);
14.
15. else
16.     match.value = A(1,1);
17.     match.M = B;
18.     match.start = findmatch(match.value,match.M);
19.     B = B(match.start:end,:);
20. end
21.
22.
23. %Now we fix the endpoints of the arrays too
24.
25. if (A(end,1) > B(end,1) )
26.     match.value = B(end,1);
27.     match.end = findmatch(match.value,A)
28.     A = A(1:match.end,:);
29. else
30.     match.value = A(end,1);
31.     match.end = findmatch(match.value,B);
32.     B = B(1:match.end,:);
33. end
34.
35.
36.
37. %Now we go element-by-element through the smallest array and find the
38. %closest matching element in the largest array.
39.
40. if (size(A,1) < size(B,1))
41.     for j=1:size(A,1)
42.         match.diffsmallest = 100000000;
43.         match.value = A(j,1);
44.         match.point = findmatch(match.value,B);
45.         %Found the match in the first column of the array, now to fill in
46.         %the corresponding values in all other columns
47.         number_of_columns = size(B,2);
48.         for g=1:number_of_columns
49.             X(j,g) = B(match.point,g);
50.             X(j,g) = B(match.point,g);
51.         end
```

```
52.        end
53.        B=X;
54.  else
55.        for j=1:size(B,1)
56.            match.diffsmallest = 100000000;
57.            match.value = B(j,1);
58.            match.point = findmatch(match.value,A);
59.            X(j,1) = A(match.point,1);
60.            X(j,2) = A(match.point,2);
61.            %Found the match in the first column of the array, now to fill in
62.            %the corresponding values in all other columns
63.            number_of_columns = size(A,2);
64.            for g=1:number_of_columns
65.                X(j,g) = A(match.point,g);
66.                X(j,g) = A(match.point,g);
67.            end
68.
69.        end
70.        A=X;
71.  end
72.
73.  U = A;
74.  V = B;
75.
76.  end
```

Appendix II – Bruker Spectrometer File Format to ASCII conversion

Bruker spectrometers output spectroscopic data in BES3T format. These files are ideally imported into Bruker software such as 'WinEPR Acquisition', but as the files are in a binary format the data cannot be imported into third party software such as Origin or Excel. I have written a short, rapid and extensible Python script to convert this Bruker file format to a more useable ASCII 'plaintext' format.

For each spectrum recorded, a Bruker spectrometer produces two files; a .DSC and .DTA file. The .DSC file is in ASCII tab-delimited format and contains information about the status of the instrument during the experiment, such as microwave frequency and power. This file also contains the maximum and minimum values of field and number of field points collected. The .DTA file is in binary format and contains the data points of the spectrum. The unusual property of this file is that it uses a 'big endian' system. Endianness is refers to how bytes are ordered in memory. A 'big endian' system begin with the most significant digits, just as how numbers are written in languages that write left-to-right. 'Little endian' systems begin with the least significant digit and is adopted by Intel processors, as the process of addition is more efficient with this system. Most Windows applications will expect a 'little endian' format and so this .DTA file will not import correctly.

This Python script imports the .DTA file and converts from a big endian binary format to a little endian ASCII format. The field values are taken from the .DSC file. This script requires both of these files, and outputs the spectrum in a comma-delimited file. For converting a single spectrum, the usage is:

```
conv.py -i [inputfile.DTA] -o [outputfile.csv]
```

To convert all spectra in a folder, the usage is:

```
conv.py -a
```

```
1.  #!/usr/bin/python
2.
3.  import struct
4.  import sys
5.  import getopt
6.  import os
7.  import glob
8.  import csv
9.
10. from itertools import zip_longest
11.
12. def write_to_file(xdata,ydata,outputfile) :
13. #Writes output to file
14.     fileName, fileExtension = os.path.splitext(outputfile)
15.
16.     fout = open(outputfile,'w');
17.     print(str(len(xdata)))
18.     print(str(len(ydata)))
19.
20.     fp = open(outputfile,'w',newline='')
21.     a = csv.writer(fp,delimiter=',')
22.     #Writes header
23.     h = [fileName + ' x',fileName + ' y']
24.     a.writerow(h)
25.     for i in range(0,len(xdata)) :
26.         s1 = xdata[i];
27.         s2 = ydata[i];
28.         r = [s1,s2];
29.         a.writerow(r)
30.
31.     return
32.
33. def generate_ydata(inputfile) :
34. #Extracts the y axis data from the input file
35.     toggle = 2;
36.     ydata = [];
37.     fin = open(inputfile,'rb');
38.
39.     with open(inputfile,'rb') as inh:
40.         indata = inh.read()
41.     for i in range(0,len(indata),8) :
42.         pos = struct.unpack('>d',indata[i:i+8])
43.         ydata.append(pos[0]);
44.     fin.close()
45.     return ydata
46.
47. def generate_xdata(paramfile) :
48. #Extracts the x axis data from the parameter file
49.     fin = open(paramfile,'r');
50.     for line in fin :
51.
52.         p = line[0:4]
53.         #print(p)
54.
55.         if p == 'XPTS' :
56.             xpoints = int(line[5:len(line)]);
57.             print(str(xpoints))
58.
```

```python
59.          if p == 'XMIN' :
60.              xmin = float(line[5:len(line)]);
61.              print(str(xmin))
62.
63.          if p == 'XWID' :
64.              xwid = float(line[5:len(line)]);
65.              print(str(xwid))
66.
67.
68.      xmax = xmin + xwid
69.      xsampling = xwid / xpoints
70.
71.      xdata = [];
72.      for k in range(1,xpoints,1) :
73.          xdata.append(xmin + (xsampling * (k - 1)))
74.        #  print(xdata[k-1])
75.
76.      return xdata
77.
78.
79. def test_files(inputfile,outputfile) :
80.      errors = 0;
81.      #Test if input and output files have been specified properly
82.      if inputfile == '' :
83.          print("You haven't specified an input file!")
84.          print("conv.py -i inputfile -o outputfile")
85.          sys.exit(2)
86.          errors = 1;
87.      elif outputfile == '' :
88.          print("You haven't specified an output file!")
89.          print("conv.py -i inputfile -o outputfile")
90.          sys.exit(2)
91.          errors = 1;
92.
93.      #Test if input file exists
94.      try:
95.          with open(inputfile) : pass
96.      except IOError:
97.          print("input file doesn't exist!")
98.          sys.exit(2)
99.          errors = 1;
100.
101.          fileName, fileExtension = os.path.splitext(inputfile)
102.          paramfile = fileName + ".DSC";
103.
104.          #Test if param file exists
105.          try:
106.              with open(paramfile) : pass
107.          except IOError:
108.              print("parameter file doesn't exist!")
109.              sys.exit(2)
110.              errors = 1;
111.
112.          #Test if is DTA file or not
113.          if fileExtension != ".DTA" :
114.              print("Not a DTA file!");
115.              errors = 1;
116.
117.          return errors
118.
119.
120.
121.      def main(argv):
122.          inputfile = ''
123.          outputfile = ''
124.          doall = 0
125.
```

```
126.        #Get command line arguments
127.
128.            try:
129.                opts, args = getopt.getopt(argv,"hi:o:a",["ifile=","ofile="]
    )
130.            except getopt.GetoptError:
131.                print("You didn't put in enough arguments or something!")
132.                sys.exit(2)
133.            for opt,arg in opts:
134.                if opt == '-h':
135.                    print("conv.py -i inputfile -o outputfile");
136.                    sys.exit()
137.                elif opt in ("-i","--ifile"):
138.                    inputfile = arg
139.                elif opt in ("-o","--ofile"):
140.                    outputfile = arg
141.                elif opt in ("-a") :
142.                    doall = 1;
143.            #Test if user wants to convert all of the files in the folder
144.            if (doall == 1 ) :
145.
146.
147.                tmpfilenames = []
148.                #Go through and generate temporary csv files for all DTA fil
    es
149.                for inputfile in glob.glob("*.DTA") :
150.
151.                    fileName, fileExtension = os.path.splitext(inputfile)
152.                    tmpfile = fileName + ".tmp";
153.                    tmpfilenames.append(tmpfile)
154.
155.                    paramfile = fileName + ".DSC";
156.                    print("\n")
157.                    print(paramfile);
158.                    xdata = generate_xdata(paramfile)
159.                    ydata = generate_ydata(inputfile)
160.                    write_to_file(xdata,ydata,tmpfile);
161.
162.
163.                #Open all of those generated CSV files
164.                handles = [open(filename,'r') for filename in tmpfilenames]

165.                readers = [csv.reader(f,delimiter=',') for f in handles]
166.
167.
168.                with open(outputfile,'w',newline='') as h:
169.                    writer = csv.writer(h)
170.                    for rows in zip_longest(*readers,fillvalue=['']*2) :
171.                        combined_row = []
172.                        for row in rows:
173.                            row = row[:2]
174.                            if len(row) == 2:
175.                                combined_row.extend(row)
176.                            else :
177.                                combined.extend(['']*2)
178.                        writer.writerow(combined_row)
179.
180.                for f in handles:
181.                    f.close()
182.
183.
184.            elif (test_files(inputfile,outputfile) == 0 ) :
185.                fileName, fileExtension = os.path.splitext(inputfile)
186.                paramfile = fileName + ".DSC";
187.                print("\n")
188.                print(paramfile);
189.
```

```
190.            xdata = generate_xdata(paramfile);
191.            ydata = generate_ydata(inputfile);
192.            write_to_file(xdata,ydata,outputfile);
193.
194.
195.     if __name__ == "__main__":
196.        main(sys.argv[1:])
```